Carbon isotopes of methane during the Medieval Climate Anomaly

Analysis of the carbon isotope signature of methane $\delta^{13}CH_4$ during the Medieval Climate Anomaly, and modelling of methane sources from AD $600 - 1600$.

Jonas A. Haller

Submitted in partial fulfilment of the requirements for the degree of
M.Sc. Energy Science and Technology (ETHZ)

Swiss Federal Institute of Technology Zürich (ETHZ)
Institute for Atmospheric and Climate Science
Supervisor: Prof. Reto Knutti

University of Copenhagen (KU)
Niels Bohr Institute (NBI), Centre for Ice and Climate (CIC)
Co-Supervisor: Prof. Thomas Blunier

Zürich, 1 May 2013

This page intentionally left blank.

Acknowledgements

I would like to thank first of all Thomas Blunier for having me accepted for writing my thesis at the Centre for Ice and Climate in his Gaslab team and for his constant support and the fruitful discussions.

I am grateful to Peter Sperlich for setting up the measurement system as it is and the time he took to introduce me into the field of experimental biogeochemistry, explaining me all the parts of the setup at the beginning of my thesis an the continued support during situations with all kind of problems.

I was also very glad for being member of such an awesome team at CIC, where namely Ivana Cvijanovic, Christopher Stowasser, Trevor Popp, Paul Vallelonga, Malte Vinther, Hannah Klempin, Alexandra Messerli and Corentin Reutenauer gave me lots of input and we had inspiring discussions on various topics regarding this thesis and many other things. Thank you very much for proofreading and commenting on it. Also, thank you Ivana, Yongbiao and Mai, for the nice time at the piano together, as well as Corentin, for the many discussions in the lab and outside, his warm laughters that always cheered up my day.

Back in Zürich, thanks go to Alexandra Florin and Claudio Beretta for their support, proofreading and inspiring discussions.

Also a big thank to my brother Sebastian who helped me a lot with various issues at all stages of the thesis, as well as to Alexandra and my parents Katharina and Christoph, who encouraged and supported me throughout.

This page intentionally left blank.

Abstract

Methane is the second most important anthropogenic greenhouse gas, emitted from various anthropogenic as well as natural sources. The contribution of different sources in the past can be inferred from the carbon isotopic signature of methane ($\delta^{13}CH_4$) trapped in ice cores. Here, we report a data series of high-resolution measurements of $\delta^{13}CH_4$ during the time of the Medieval Climate Anomaly, AD $650 - 1300$, measured from two Greenland ice cores, Eurocore and NEEM. The measurement system is presented and various parts of it are described in detail. Furthermore, we discuss different methods for data evaluation. We compare our results to previously measured data and find large differences, the implications of which are analysed in detail in a model. For doing so, we first use a novel smoothing algorithm to create one methane mixing ratio and one isotopic ratio for each hemisphere by combining two Antarctic and 4 Greenlandic ice cores. A two-box-model is then developed and used for analysing changes in biogenic and pyrogenic methane sources from AD 600 to 1600, known as the Late Pre-Industrial Holocene (LPIH). Correlations between these inferred source changes and natural climate variability as well as changes in human population and land use are found and discussed.

This page intentionally left blank.

Contents

Chapter 1

Introduction

Methane is an important, radiatively active and long-lived anthropogenic greenhouse gas. Its sources are linked to human activities and productivity of ecosystems. The atmospheric mixing ratio has increased by more than 150% since pre-industrial times. Therefore its sources, sinks and their changes over time have been subject to many studies, leaving the origin of most recent changes in its atmospheric mixing ratio a subject open to debate. Understanding the sources of atmospheric changes allows to draw conclusions for present and future source changes, while they also serve to understand and corroborate historic events and development. As every class of methane sources bears a more or less unique isotopic signature, changes of sources and sinks can be identified through the analysis of variations of the isotopic signature in the past. In this study we focus in the time of the Medieval Climate Anomaly (MCA, also Medieval Warm Period) which lasted from about AD 950 to 1250.

We analyse carbon isotope signature of methane gas occluded in ice cores from Greenland dating from the MCA and compare our record with most recent measurement over the same time period. With historic data for mixing ratio and isotopic signature from both polar regions, Greenland and Antarctica, it is possible to construct a model over both hemispheres to identify historic changes in source strengths. Changes in anthropogenic sources are often known to a certain degree through written historic records or other environmental proxy data, which can be used for comparison and to corroborate modelling results.

While many workers previously modelled methane sources and sinks, we have for the first time been able to run a fully time-dependent inversion model on complete records of methane mixing ratio and carbon isotopic signature on both hemispheres. We are able to corroborate historic information and identify limitations of a model like this.

In this report we introduce and discuss the utilised concepts (Chapter 2), describe the setup used to measure the carbon isotopic signature of methane in ice cores (Chapter 3), discuss the data evaluation procedure (Chapter 4), before presenting the results of the carbon isotopic analysis (Chapter 5). An inverse model is then developed to identify changes in methane sources (Chapter 6), yielding results (Chapter 7) that are compared to environmental proxy data (Chapter 8). Differences to the record measured by Sapart (2012) [1] at IMAU Utrecht are investigated, and consequences for modelling results discussed in particular.

This page intentionally left blank.

Chapter 2

Background

In this chapter, the greenhouse effect is briefly explained and the contribution of methane discussed (Section 2.1). Some properties of methane and their relevance to life on Earth are presented (Section 2.2), together with the methane budget (Section 2.3), where its sources and sinks are analysed individually. Further, the effects of isotopes on a molecular scale and on various processes are explained together with the corresponding mathematical expressions (Section 2.4), a short briefing about mass spectrometry (Section 2.5) and ice cores (Section 2.6) are given before the nature of the Medieval Climate Anomaly is discussed (Section 2.7).

2.1 The greenhouse effect

Solar radiation (Black body temperature T_{sun}= 5780 K) that reaches the Earth's surface (Black body temperature T_{Earth}=255 K) and is not reflected (depending on the albedo), is absorbed and later re-emitted towards the atmosphere. This mechanism has been understood since 1896, when discovered by Arrhenius [2]. While solar radiation has little infrared content, the Earth's surface radiation is rich in it due to the lower black body temperature (cf. Fig. 2.1). Greenhouse gases (GHGs) in the atmosphere absorb long-wave infrared radiation. During this process, the radiation energy gets absorbed, that is, transformed by exciting the molecules into vibrational modes. There, it remains trapped until it is again released by infrared emission and scattered into all directions, with about a 50% chance to be returned downwards, towards the Earth's surface. With an increased number of molecules participating in this process, there is ultimately more energy stored in the atmosphere and more long wavelength radiation re-emitted towards the Earth, which is referred to as the Greenhouse effect.

2.2 Methane as a greenhouse gas

Methane, as a polyatomic, non-linear molecule composed of $N = 5$ atoms, has $3+3+(3N-6) = 3N = 15$ degrees of freedom, that is, 3 translational, 3 rotational and 9 vibrational modes. The number of vibrational modes is easily determined by ($3N - 6 = 9$).
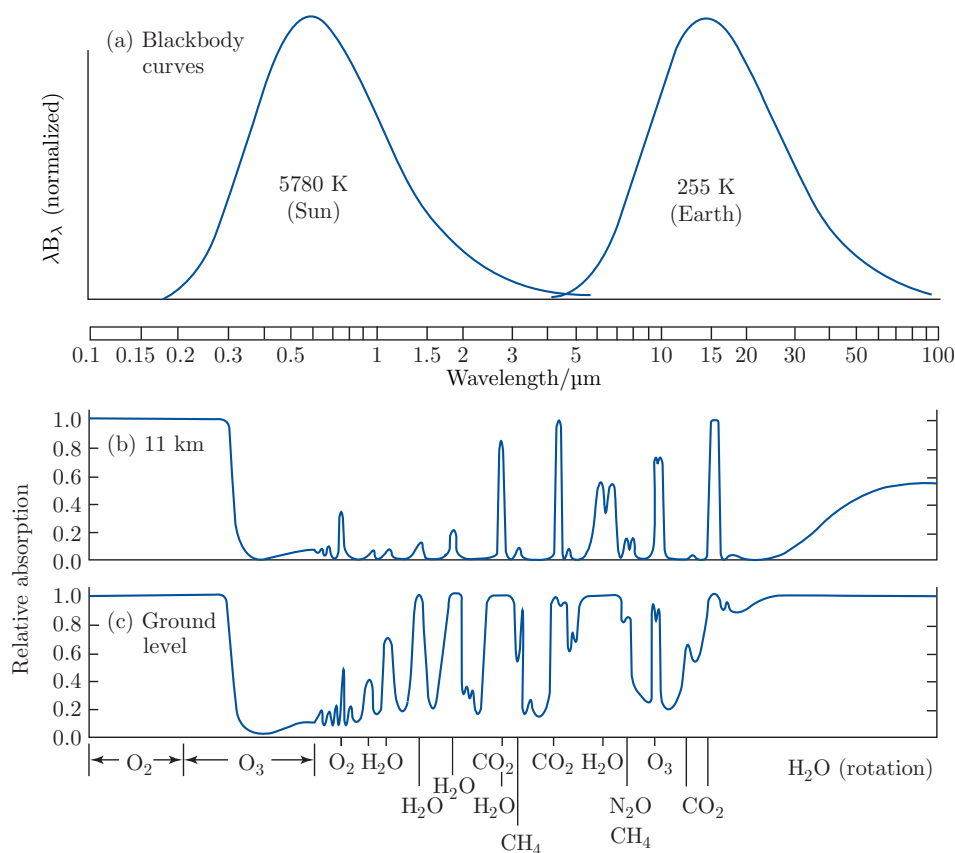
Figure 2.1: (a) Blackbody spectra representative of the sun and the Earth. The intensity scales for the two curves have been scaled to make the areas under the two curves the same; (b) Spectrum of monochromatic absorptivity of the part of the atmosphere above the 11-km level; (c) spectrum of monochromatic absorptivity of the entire atmosphere. Adapted from Goody (1996) [3].

Out of the 9 possible vibrational modes, 6 are infrared (IR) absorbing, and only these induce a change in the molecule's dipole moment (i.e. here: "when the carbon molecule does also engage in the vibration"), cf. Tab. 2.1 and Fig. 2.2.

Table 2.1: Symmetries, Wavenumbers and Absorption activities of the vibrational modes of $^{12}CH_4$ [4]

Symmetry	Modes	Wavenumber [4] ν/cm^{-1}	Activity	Movement of vibration
F_2	3	$\nu_1 = 2920.9$	IR	Wag
E	2	$\nu_2 = 1532.4$	Raman	1 Twist, 1 Scissor
A_1	1	$\nu_3 = 3022.5$	Raman	Symmetric stretch
F_2	3	$\nu_4 = 1308.4$	IR	Asymmetric stretch

The properties in Tab. 2.1 are shown for $^{12}CH_4$. Other isotopologues (cf. Section 2.4) of methane, such as $^{13}CH_4$, show different absorption properties. This behaviour has shown good prospects for laser absorption spectrometry to carry out stable isotope ratio measurements (cf. Section 9.3).

Its six infrared absorbing vibrational modes, and its atmospheric lifetime of 8 years give Methane a Global Warming Potential (GWP) 25 times the one of CO_2 over a 100 years period [5].

F_2 Wag

F_2 Wag

F_2 Wag

E Twist

E Scissor

A Symmetric stretch

F_2 Asymmetric stretch

F_2 Asymmetric stretch

F_2 Asymmetric stretch
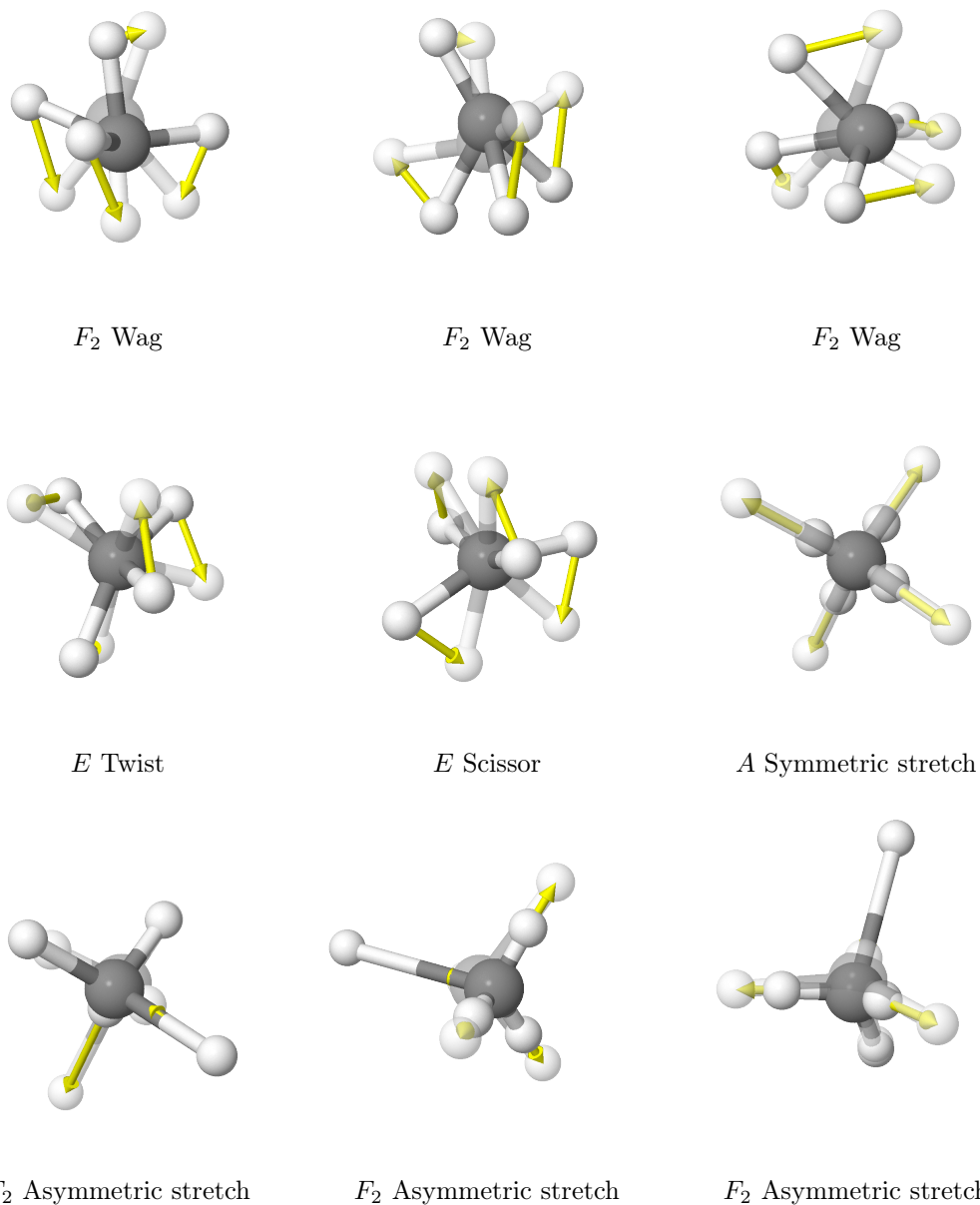
Figure 2.2: The movement of each atom in the $^{12}CH_4$ molecule for each of its nine vibration modes. Notice, how the carbon atom does not move for E and A symmetries, which are therefore Raman but not IR active. (made with "Jmol" and Photoshop).

2.3   Methane budget

The variability of the atmospheric methane mixing ratio had not been discovered until the late 20th century [6], and the understanding of it remains still very limited. A box model of the methane budget is shown in Fig. 2.3. In the coming subsections, the individual sources will be characterised, followed by discussions of the sinks. Readers, unaware of isotopic notions, are advised to first read Section 2.4.
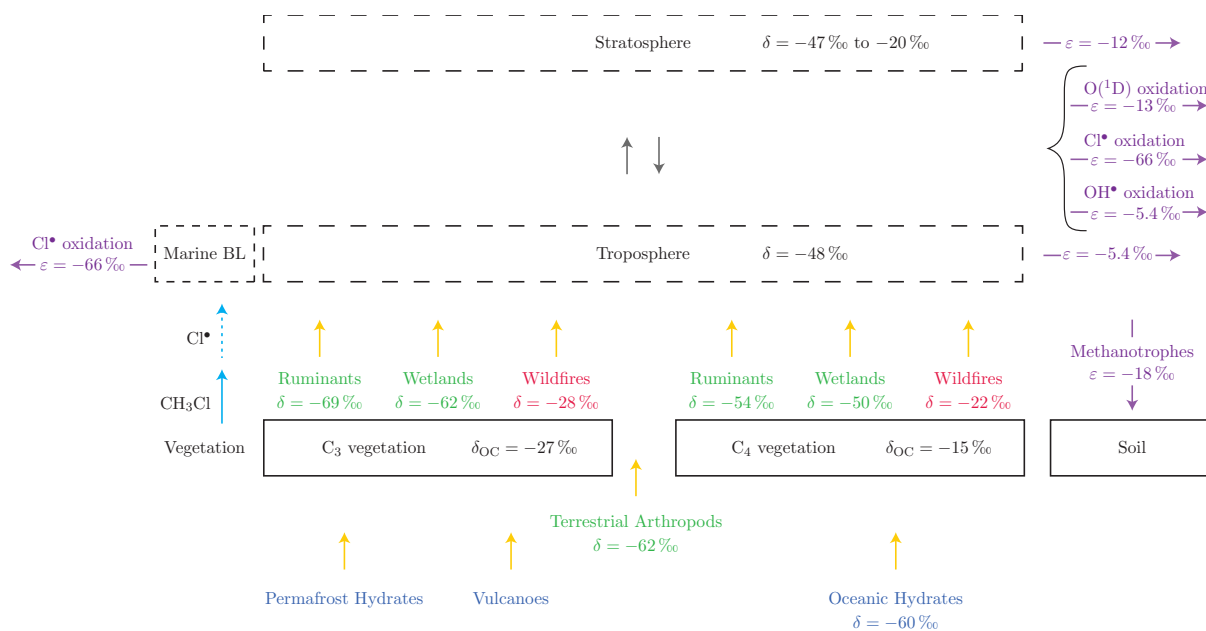
Figure 2.3: Methane budget showing sources and transports (green), sinks (purple) and their isotopic signatures and fractionation factors respectively. Additional compounds that play an essential role are indicated with dashed blue arrows. Data from Schaefer (2008) [7].
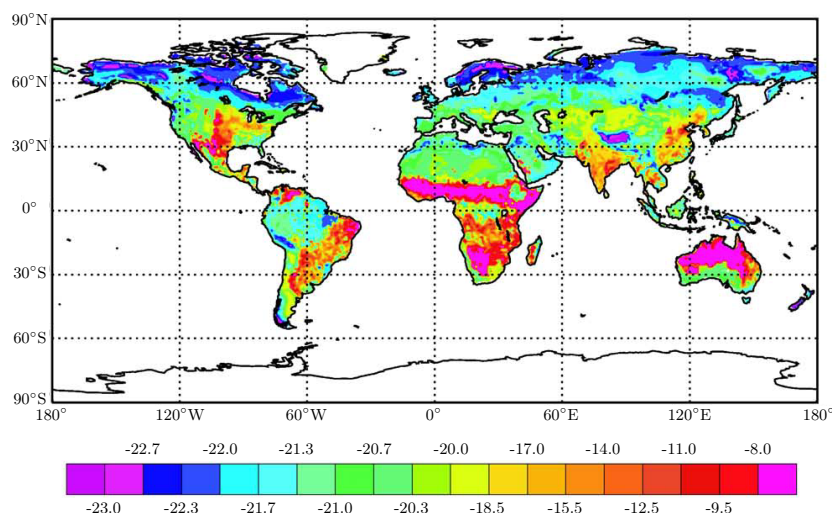
Figure 2.4: Mean Annual δ^{13}C value of plant carbon, (δ vs. VPDB)·1000, resulting from the relative abundances of C_3 and C_4 plants. Adapted from Suits (2005) [8].

Methane budget I: Sources

The different sources of methane have all distinct signatures in δ^{13}C-CH$_4$ and δD-CH$_4$. Fischer (2008) [9] made a compilation of various current sources of methane and their respective isotope signatures, shown in Fig. 2.5. They can be grouped in three distinct classes: biogenic, pyrogenic and geologic sources, depending on the pathway used for transforming organic carbon (OC) into methane. The sinks, which will be discussed in the next section, have a large effect on the isotopes of methane as well, as it can be seen from the comparison of source mix and atmospheric signature in Fig. 2.5.
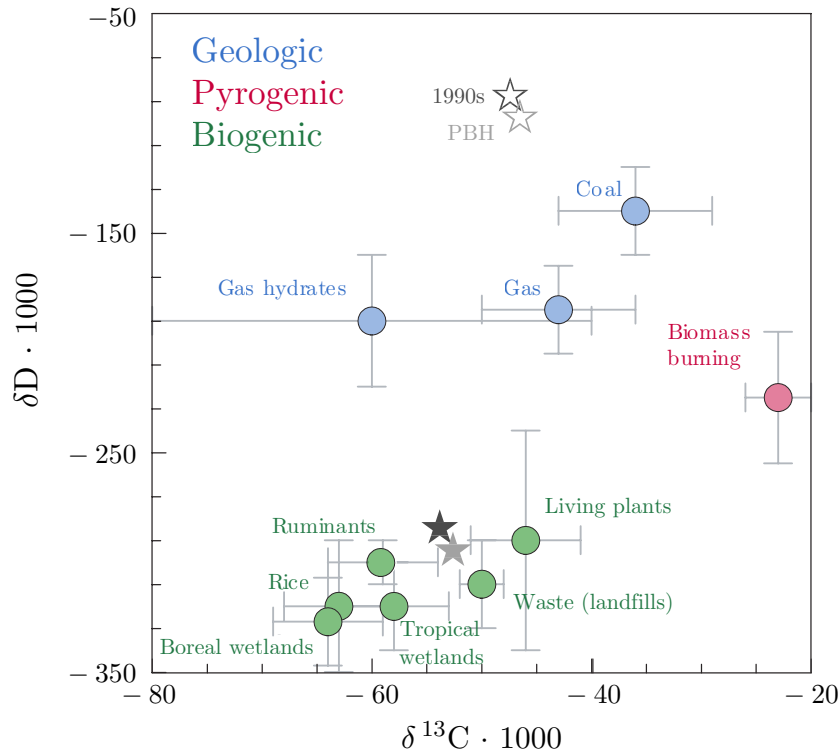
Figure 2.5: Signatures in δ^{13}C (vs. VPDB) and δD (vs. VSMOW) of various methane sources on Earth. Based on a figure from Fischer (2008) [9]. The colours show the nature of the source. The filled pentagram shows the source mix, and the outlined pentagram the signature of the atmosphere for the 1990s (dark grey) and the Preboreal Holocene (PBH, 9 ka ago, light grey).

At the beginning of the (life) cycle of methane, the carbon that will later be released as methane is available as organic matter. The isotopic signature of organic matter from plants allows to distinguish between two families of plants, that is, two different photosynthetic pathways: those who follow the Calvin-Benson-Bassham cycle in photosynthesis (C$_3$) and those who fix carbon with the Hatch-Slack pathway (C$_4$) [7]. The carbon isotope signature of C$_3$ plants ($\delta = -19.2‰$) is lighter than the one of C$_4$ plants ($\delta = -4.4‰$). The mean annual δ^{13}C of plants has been calculated by Suits (2005) [8] and is plotted in Fig. 2.4. These values are valid for the present, while the past distribution must have been somewhat different. The grassland area of C$_4$ plants is said to have been larger ($\sim 75\%$) in the pre-industrial Holocene (PIH) as compared to the present share of ($\sim 57\%$) as reported by Schaefer (2008) [7].

2.3.1 Biogenic sources

Biogenic sources are converting OC into methane by the aid of micro-organisms, and there are two major environments that can be distinguished: digestive tracts of ruminants, and wetlands or flooded soils including rice fields. Recently it has been shown that even some plants are releasing methane by themselves [10]. All of these processes are discussed below.

The two biogenic pathways of methane production involve acetoclastic ($CH_3COOH \longrightarrow CH_4 + CO_2$) and hydrogenotrophic ($CO_2 + 4\,H_2 \longrightarrow CH_4 + 2\,H_2O$) methanogenesis. The substrates for these two are produced from the anaerobic degradation of organic matter using fermentation to acetate, CO_2, H_2 and propionate, as well as other fatty acids [11].

In the model a $\delta_{\mathrm{bio}} = -59.6‰ \pm 2‰$ was used as the source signature for biogenic sources in pre-industrial holocene (PIH) [7], which is in agreement with the values used by other publications [1, 12, 13]. The most important processes of biogenic methane formation are explained below.

Wetlands

In wetlands, the isotopic signature of methane depends on various factors. These are

- production pathway (CO_2-oxidation or acetate fermentation) [14],
- availability of nutrients and organic carbon (the substrate for methane formation) [15],
- water table depth [14, 15] and soil temperature [15],
- gas transport from below the water surface into the air, which results in a characteristic production/oxidation ratio [16, 14].

Considering the strength of the source, Wuebbles (2002) [15] made a review and saw a positive correlation between temperature and CH_4-emissions especially for high latitudes. In contrast, the effect of a change in the water table depth was considered highly uncertain.

Although a change in vegetation and in water table depth can have an impact on the fractionation involved in methane production and release, the effect of these processes always result in a difference smaller than 10‰, according to Popp (1999) [14]. For the later described model, the $\delta^{13}C$ signature for biogenic methane production was assumed to be constant over time.

Rice fields

The quantity of CH_4 produced in rice fields per kg of rice, depends on conditions such as climate, soil characteristics, but also on agricultural practices such as water management, the use of fertiliser and the cultivated rice variety [15]. Fertilisers have been organic for a long time before the 20th century, and they give rise to 50% higher CH_4 emissions than synthetic ones.

Ruminants

The isotopic signature of the ruminants' fodder influences that of the released methane, so that it is $-69‰$ for fodder based on C_3 vegetation and $-54‰$ for C_4 [7, 17]. This 15‰ difference is close to the difference between C_3 and C_4 feed (12‰, cf. Fig. 2.3). The animals' digestion is discriminating with $\varepsilon \sim -41‰$, independent of diet, and also independent of the species [7].

Terrestrial plants

Recent studies by Keppler (2006) [10] have also identified terrestrial plants under aerobic conditions being capable of releasing methane. The estimated source strength of living plants could possibly account for 10 to 25% of total emissions [10]. The uncertainty of this estimate shows that further research is needed to accurately account for this source in budget estimates and simulations.

2.3.2 Pyrogenic sources

Pyrogenic emissions can be of natural origin such as wildfires, or originate from anthropogenic biomass burning and land clearing, which are indistinguishable in their isotope signature. When biomass is burned, CH_4, CO, and other hydrocarbons are mostly emitted during incomplete combustion, such as during smouldering, while CO_2 is emitted from open fires [18]. Since fire is a chemical reaction enriching its products in comparison to its substrates by about $\varepsilon \sim +3‰$, the isotopic signatures for methane emitted from forest fires $(C_3, -25‰)$ and grassland burnings $(C_4, -12‰)$ can be distinguished [7, 19]. In the model, an average source signature of $\delta_{\mathrm{pyro}} = 26.6‰ \pm 2.6‰$ was applied for pyrogenic emissions as estimated by Schaefer (2008) for the PIH [7]. This is a slightly more depleted value than those used by Sapart (2012) [1] (-19 to -25‰) and Lassey (2007) [13] (-25‰).

Biomass burning usually leaves traces in the ecosystem, either as burn scars on surviving trees, or also as charcoal residues in the ground on the spot or in remote sites. Hence, they can be used as a proxy to estimate the pyrogenic contribution to total emissions. Since the emission of CH_4 is concurrent with CO emission, this trace gas has been used as a proxy too. These various proxies are discussed below.

Giant sequoias

At some places, where trees grow very old and conserve burn scars in tree rings, the fire history can quite directly be determined from tree ring data. The species *Sequoiadendron giganteum* (Lindl.) J.Buchholz [20] (*coll.* Giant Sequoia) tree, endemic in California, is one of the largest trees on Earth and can sustain very high fire frequencies [21]. Their records go back to as far as 1000 B.C., cf. Fig. 2.6.
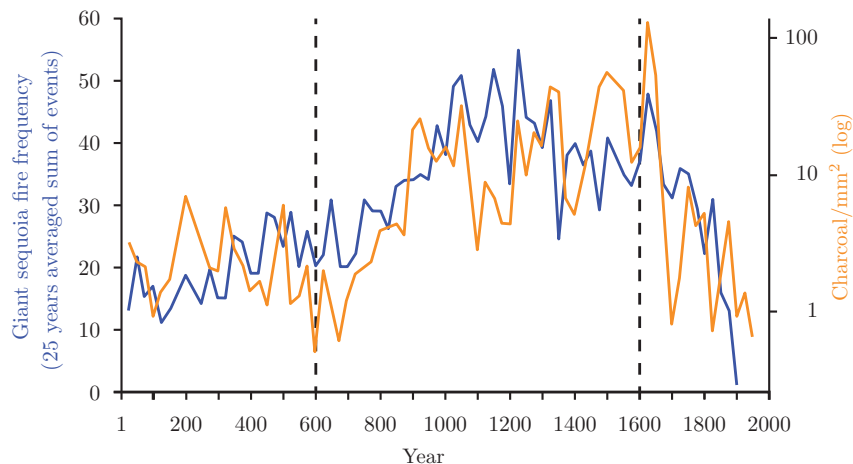
Figure 2.6: Tree ring fire index data from 5 giant sequoia trees from the Sierra Nevada (blue), weighted over 25 years, in comparison with Charcoal data from 4 Sierra Nevada meadows (orange). The two vertical lines at AD 600 and 1600 mark the period modelled in this study. Adapted from Swetnam (2009) [21].

Charcoal indices

Another option to trace fire activity is the use of charcoal indices, these are based on records from stratigraphic sediment cores. one of these records [22], which is not shown here, consists of sediment cores from eight meadows of the Sierra Nevada, California shows similarly an increase in fire frequency around the year AD 1000. However, the peaks do not show up exactly at the same time, and there are fire events that are recorded only in a single record. Moreover, temporal differences of events are high, even between sites only 5 km apart from each other. This leads to the conclusion that fires were not always covering huge areas, even though forests covered much larger areas in historical times as compared to today. Charcoal indices correlating well with data inferred from Giant Sequoia tree rings from the same region corroborate (confirm) the regional relevance of charcoal indices.

Due to their very localised validity, fire index data to be used in this study, should consist of various records from around the globe and latitudinally averaged, as it has been done by Marlon (2008) [23], who analysed various records worldwide "[...] for the first time for large-scale patterns and trends over the past 2000 years". The results are shown in Fig. 2.7 on a global scale and in Fig. 2.8 on a regional level. It is assumed that Charcoal Accumulation Rates (CHAR) measured in lake sediments correlate with carbon released by the burning of biomass [24]. The charcoal influx into lake sediments, or accumulation rates, are sometimes given in Z-scores, that is, converted by subtracting the mean value over a long time span (i.e. here: 2050 years) and dividing by the standard deviation. This shows how the values differ from a long-term average.
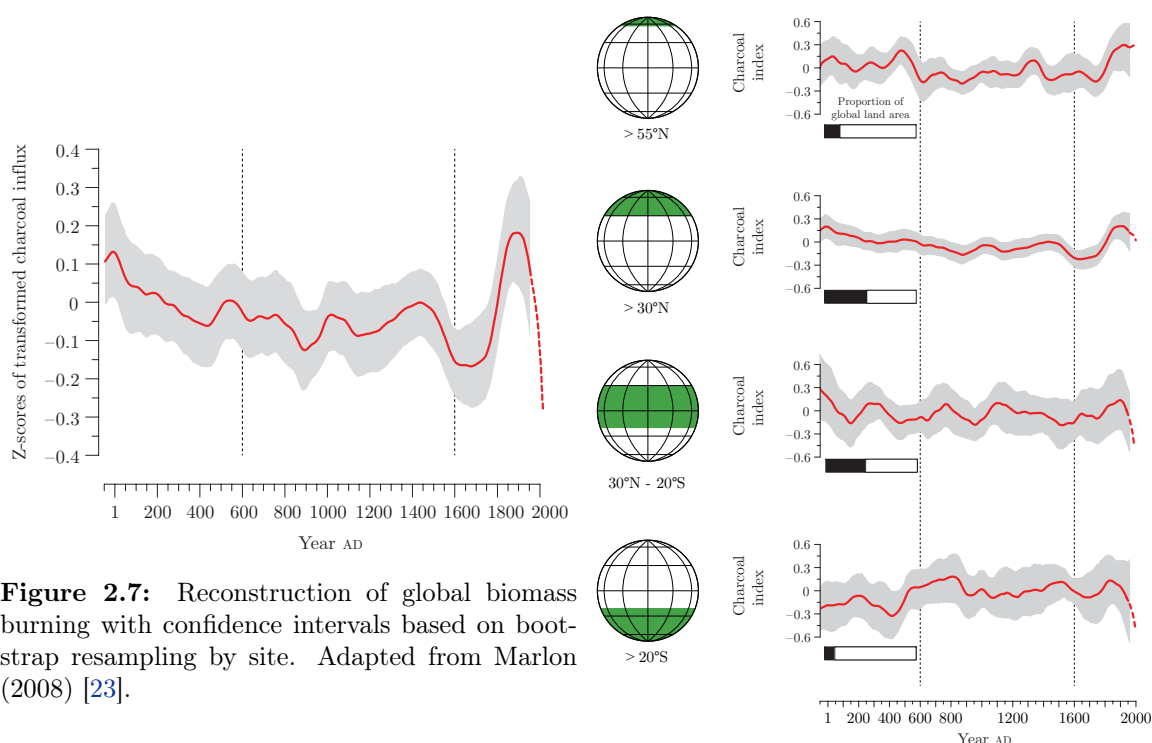
Figure 2.7: Reconstruction of global biomass burning with confidence intervals based on bootstrap resampling by site. Adapted from Marlon (2008) [23].

Figure 2.8: Changes in biomass burning (as in Fig. 2.7). Adapted from Marlon (2008) [23].

CO levels

CO emissions can be used as another proxy for fire activity: Ferretti (2005) [25] compared Antarctic (Law Dome DSS) CO records, from MacFarling (2004) [26], with methane mixing ratios, taking CO as trace gas proxy for (woody) biomass burning in the pre-industrial era [25]. This record together with another one from Greenland by Haan (1996) [27] are shown in Fig. 2.9. Forest fires show a long smouldering phase up to several days, while grass fires burn with large flames and a very short smouldering phase. (Anthropogenic) fuelwood burns in fuel-rich conditions in stoves resulting in high CH_4 emissions, as shown in Table 2.2.

Table 2.2: Emission factor of CH_4 and molar emission ratios of CO/CO_2, CH_4/CO_2 and CH_4/CO. Data from Hao (1993) [18].

Region	CO/CO_2 %	Emission factor g CH_4/kg	CH_4/CO_2 %	CH_4/CO %
Agricultural residues	8.2	2.7	0.44	5.37
Tropical savanna	4.4	1.5	0.24	5.45
Temperate / boreal forest	14.7	6.1	1.05	7.14
Tropical forest	12.4	9.3	1.57	12.66
Fuelwood	10.0	7.6	2.49	24.90

Since the contribution of fuelwood has been rather small in the past, due to little stove use compared to total biomass burning, CO shows good potential to serve as a proxy for pyrogenic CH_4 emissions. Post-emission processes that take place in the atmosphere as well as in firn and ice, do however present some difficulties. This is also reflected by the CO records from the Northern hemisphere that are not comparable to those of the Southern hemisphere. *In situ* photodecarbonylation ($RCHO \xrightarrow{\mu^-} RH + CO$) of dissolved organic matter by Čerenkov radiation, generated by penetrating cosmic muons, has been identified to be a likely source of the higher CO levels in Greenland ice cores. Hence, even excess CO levels (as visible in Fig. 2.9) are likely to track back boreal biomass burnings [28].
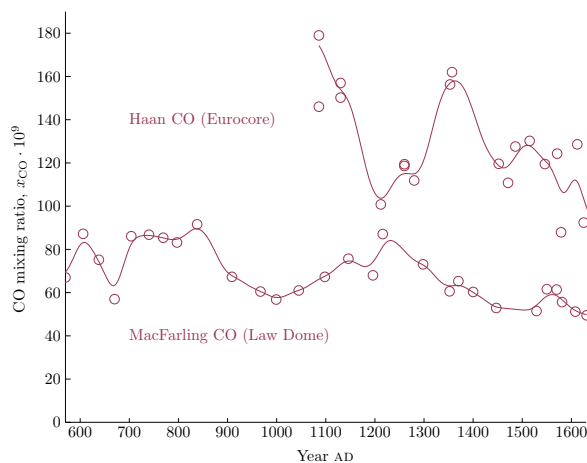
Figure 2.9: CO mixing ratio records from Greenland (Eurocore) [27], and Antarctica (Law Dome) [26], smoothed with $\sigma_0 = 15\,\text{a}$, cf. Section 6.6.

2.3.3   Geologic sources

Geologic sources emit thermogenically produced methane formed in the lithosphere under high temperature and pressure. These can be found in oceanic clathrates and coal mines (coalbed methane) as well as natural gas (leakage). The latter is not discussed in detail, as there was no anthropogenic large-scale natural gas production in medieval times. Nevertheless, gas leaks occurring naturally are accounted for in the model.

Coal mines

Coalbed gas that is released during the mining and processing of coal, consists of up to 95% methane [29], and could thus be an important source that needs to be examined. For doing so, the historical records give indications about the frequency of coal mining in the past: by the year AD 300 coal was mined in China, and was used to heat buildings and smelt metals, so that by in the 11th century, it had become the leading fuel, which was also reported by Marco Polo in the late 13th century. In Europe, coal had been used for a long time, and by the end of the 12th century the Prince Bishop of Liège in the Netherlands granted coal mining rights. By the 13th century, significant amounts of coal were traded and shipped in England. At the same time environmental impact ordinances were passed to control and reduce its use in London, but those were not very effective due to a lack of affordable alternatives. In Germany, at the beginning of the 14th century, the first written transaction included rights to mine coal [30].

Since coal mining activities have thus been reported, the emitted methane quantities have to be assessed. Khalil (1993) [31] mentions an emission of $0.02\,\mathrm{Tg(CH_4)\,a^{-1}}$ coal related emissions in China from the production and use of 1 million tons of hard coal in 1900, rising to $0.38\,\mathrm{Tg(CH_4)\,a^{-1}}$ in 1930 and $12.81\,\mathrm{Tg(CH_4)\,a^{-1}}$ in 1988. Even considering the whole world, it is highly unlikely that the annual amount of coal extracted worldwide by the year 1600 AD would have given rise to any significant methane emissions. Before industrialised large-scale extraction started (in the 19th century), there were no open pit mines for coal extraction at the same scale as today. Hence it seems reasonable to conclude that coal mining emissions were of negligible magnitude until the 18th century at least. In comparison, emissions from rice paddies in China alone amounted to $17.76\,\mathrm{Tg(CH_4)\,a^{-1}}$ in 1900 and $22.99\,\mathrm{Tg(CH_4)\,a^{-1}}$ in 1988 [31].

Clathrates/hydrates

Ocean clathrates constitute a source of methane that can release large amounts of gas at once. They are the result of large-scale sediment slope failures, that is, giant submarine landslides [32], which can give rise to methane release. Bock (2012) [33] developed a model for clathrate pulses, taking account of the strongly negative δ^{13}C-value ($-60‰$) of hydrate methane, which is also reflected in the composition of both benthic and planktonic foraminifera shells, who sometimes exhibit a strongly negative carbon isotopic signature, which is interpreted as a result of massive hydrate dissociation, visible in sediment cores. As he points out, no clear evidence of such events have been found in ice cores, which might also be due to low sampling resolution or smoothing effects in the firn. Moreover, massive methane releases are extremely unlikely for the past 50 ka. Maslin (2004) mentions a slide on the Canadian abyssal plain at around AD 700, but does not further investigate this event [34]. Further research is needed to evaluate the possibility of a (small scale) methane release during this event. Hence, methane pulses have been excluded for the time span considered in the model of this study, since our profile shoes no evidence for such an event, similar to previous work [35].

Small amounts of methane are, however, continuously being released from the sediments. Some methane is getting dissolved, and when the dissolved mass fraction exceeds the solubility, hydrates are formed [36].

Therefore the world oceans contribute also to the atmospheric methane budget by $5 - 10 \, \mathrm{Tg \, a^{-1}}$ [37]. Westbrook (2009) [38] characterised a methane escape along the seabed of Western Svalbard, and quantified the release of this particular location to $0.027 \, \mathrm{Tg \, a^{-1}}$, and a possible source strength around Svalbard of $20 \, \mathrm{Tg \, a^{-1}}$. He argued that a temperature increase could possibly release many tens of teragrams per year. Hence this source is accounted for in the model.

Permafrost in thick ($> 300 \, \mathrm{m}$) permafrost soils are a potential hazard, if temperatures warm over periods longer than $10^3 \, \mathrm{a}$, as reported by Ruppel (2011) [39], who further notes that other research has found that clathrates could be present at depths as shallow as $20 \, \mathrm{m}$, which could then respond to warmer temperatures over much a shorter period of time. The existence of this source is still controversial [39]. Therefore, prospects for future research are great and could lead to a better understanding of this source and its variability over both short ($< 1 \, \mathrm{ka}$) and long ($> 1 \, \mathrm{ka}$) time scales.

The sum of all geologic sources have been accounted for in the model with $50 \pm 20 \, \mathrm{Tg \, a^{-1}}$ [40], distributed mainly the Northern hemisphere [41], where there is a larger area of continents and shallow seas with tectonically active petroleum-bearing sedimentary and geothermal basins. In the model, these emissions account globally for $50 \pm 20 \, \mathrm{Tg \, a^{-1}}$, distributed on the Northern (70%) and Southern (30%) Hemispheres with an average $\delta_{\mathrm{geo}} = -40\text{\textperthousand} \pm 10\text{\textperthousand}$[42].

Methane budget II: Sinks

Commonly, methane sinks are separated into three groups, these being tropospheric hydroxyl radicals $OH^\bullet$ ($\approx 90\%$), methanotrophic micro-organisms in soils ($\approx 5\%$), and stratospheric radicals ($\approx 5\%$) [15]. Recently, a fourth sink, Chlorine radicals $Cl^\bullet$ in the marine boundary layer (MBL), has been suggested [43]. The resulting atmospheric lifetime of methane is about 8 a [5], during which all sinks preferentially remove $^{12}CH_4$ and thus enrich the atmosphere in $^{13}CH_4$. Although changes in $OH^\bullet$ are important, CH_4 changes have been considered to be mainly driven by changing source configurations and strengths. This is also justified, since the abundance of $OH^\bullet$ is largely controlled by CH_4 levels [44]. Therefore, in the model sink rates have been considered constant.

The chemistry of the atmosphere is complex and many of the reactions are closely inter-related [45].

2.3.4 Atmospheric sinks

In the atmosphere, highly reactive radicals, such as hydroxyl ($OH^\bullet$), hydroperoxyl ($HO_2^\bullet$), chlorine ($Cl^\bullet$) and singlet oxygen ($O(^1D)$) are driving most reactions. The mechanisms are radical chain reactions, consisting of radical initiation, propagation and termination. They have been described by Thompson (1996), Houweling (1999) and Logan (1981) [46, 47, 48] and are summarised below. While tropospheric processes account for almost 90% of the global methane sinks [15], stratospheric processes take a smaller share, but show isotopic discrimination affecting the signature in the troposphere. In the following each sink will be discussed, including a discussion of the induced fractionations (ε_i). The sink rates (λ_i) will be discussed in in the modelling chapter, Section 6.7.

Hydroxyl radical

In the troposphere, the most important radical initiation reaction is the photolysis of ozone (O_3) and the reaction of the resulting excited oxygen radical, $O(^1D)$, with water vapour (H_2O).

$$O_3 \xrightarrow{h\nu} O_2 + O(^1D) \tag{2.1}$$
$$O(^1D) + H_2O \longrightarrow 2\,OH^\bullet \tag{2.2}$$

There are various subsequent propagation reactions that can involve a great diversity of compounds, one of which is methane. The oxidation of methane, is followed by a series of reactions that yield formaldehyde (CH_2O) as the first stable product in reaction (2.6).

$$CH_4 + OH^\bullet \longrightarrow CH_3^\bullet + H_2O \tag{2.3}$$
$$CH_3^\bullet + O_2 \longrightarrow CH_3O_2^\bullet \tag{2.4}$$
$$CH_3O_2^\bullet + NO^\bullet \longrightarrow CH_3O^\bullet + NO_2^\bullet \tag{2.5}$$
$$CH_3O^\bullet + O_2 \longrightarrow CH_2O + HO_2^\bullet \tag{2.6}$$
$$HO_2^\bullet + NO^\bullet \longrightarrow OH^\bullet + NO_2^\bullet \tag{2.7}$$

$$CH_4 + 2\,O_2 + 2\,NO^\bullet \xrightarrow{OH^\bullet} CH_2O + 2\,NO_2^\bullet + H_2O \tag{2.8}$$
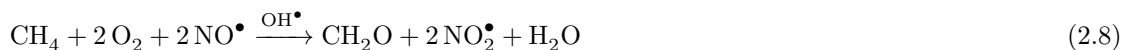
CH_2O undergoes photolysis and subsequent propagation to the final product CO_2 over different pathways, all of them yielding either a $OH^\bullet$ or a $HO_2{}^\bullet$ per CH_2O [49, 50, 51]:

$$CH_2O + OH^\bullet \longrightarrow HCO^\bullet + H_2O \tag{2.9}$$

$$CH_2O \xrightarrow{h\nu} HCO^\bullet + H^\bullet \tag{2.10}$$

$$CH_2O \xrightarrow{h\nu} CO + H_2 \tag{2.11}$$

$$HCO + O_2 \longrightarrow CO + HO_2^\bullet \tag{2.12}$$

$$CO + OH^\bullet \longrightarrow CO_2 + H^\bullet \tag{2.13}$$

$$CO + HO_2^\bullet \longrightarrow CO_2 + OH^\bullet. \tag{2.14}$$

Reaction (2.7), is decisive of the fate of the radicals, and its frequency is governed by levels of nitrogen oxides (NO_x), depending on which, $CH_3O_2^\bullet$, $HO_2^\bullet$, and CH_2O are more or less effectively recycled to $OH^\bullet$, or end in termination of the radical reaction chain. Termination occurs more frequently under low NO_x levels, when the methyldioxyl radical ($CH_3O_2^\bullet$) reduction reaction, (2.5), competes significantly with termination reactions such as reactions (2.15) and (2.16).

$$CH_3O_2^\bullet + HO_2^\bullet \longrightarrow CH_3O_2H + O_2 \tag{2.15}$$

$$2\,CH_3O_2^\bullet \longrightarrow CH_2O + CH_3OH + O_2. \tag{2.16}$$

Therefore, increasing NO_x levels lead to an increase in $OH^\bullet$. Due to a non-linearity however, the reverse is true at high NO_2 levels, above ~ 0.23 ppb [49]. The relative frequency of reactions (2.5) versus (2.15) and (2.16), is determined by the levels of reactive C and N. Hence, there is a highly non-linear response to a change in CH_4 mixing ratio that will also vary across different heights of the atmosphere [52]. Reaction (2.3) has a first-order reaction rate $r = k_1[OH^\bullet]$, where the rate constant, k_1, is only dependent on temperature [53].

The loss can be expressed as:

$$\frac{\partial x_{CH_4}}{\partial t} = -r[CH_4] = -k_1[OH^\bullet][CH_4]. \tag{2.17}$$

In the troposphere, termination reactions such as (2.15) and (2.16) are that important that increasing CH_4 levels lead to a reduction of OH levels [47, 51]. Hence the recycling of $OH^\bullet$ becomes a highly coupled system between CH_4–CO–$OH^\bullet$ as analysed by Prather (1994) [54]. Increases in CH_4 levels in the troposphere, however small, will result in a reduction in $OH^\bullet$ levels, and again increase the CH_4 lifetime [45]. However, Thompson (1996) [46] pointed out that variations in $OH^\bullet$ have not been the driving factor of CH_4 increase in the Holocene [35]. Hence, the atmospheric sink rates are held constant in the model of this study. Although this assumption might not truly hold, further research would be necessary to quantify sink changes.

When speaking about tropospheric removal, it is not entirely clear, where this removal takes place. The $OH^\bullet$ concentration through the troposphere has been modelled by Crutzen (1982) [55] and his findings show that $OH^\bullet$ concentrations are highest in the tropics and lowest at the poles. The *concentration* does not decrease with altitude by more than a factor of 2, which implies a strongly increasing *mixing ratio*, cf. Fig. 2.10.
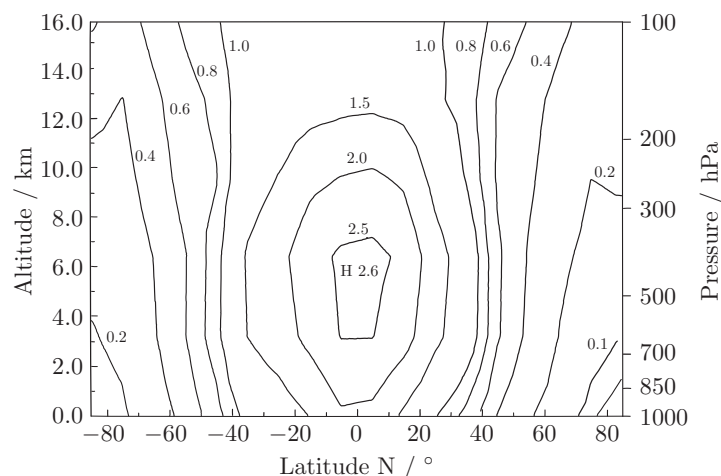
Figure 2.10: Annually averaged OH$^\bullet$ concentrations in the troposphere during the sunlit period of the day in 10^6 molecules OH$^\bullet$ cm^{-3}. Adapted from Crutzen 1982 [55].

Chlorine and singlet oxygen

In the stratosphere (10 km – 50 km asl), the chlorine and oxygen radical reactions are more important, since the abundances of these two compounds are much higher than in the troposphere so that they outweigh the abundance of OH$^\bullet$. Photolysis reactions are enhanced by the presence of the O$_3$-layer and the increased UV-radiation intensity, while water is not as abundant as in the troposphere. Since CFC contributions are responsible for a large part of the presence of Cl$^\bullet$ [56], the contribution of this sink has been much smaller in the past than in the late 20$^{\text{th}}$ century. In 1985 the chlorine mixing ratio was at $3 \cdot 10^{-9}$, of which only 20% was due to naturally produced methyl chloride (chloromethane), CH$_3$Cl [57]. The large fractionation factor of chloride, α_{Cl}, has a great contribution to isotope discrimination. Therefore, their effect cannot be neglected.

The variation in the atmospheric abundance of methyl chloride was long believed to originate mainly from the ocean, with some contribution from biomass burning [58]. However, it has been shown that tropical low land rainforest trees and ferns are contributing a lot, and it was suggested that they could fill a large part of the gap between estimated sinks, 3.5 Tg a^{-1}, and total known sources 1.7 Tg a^{-1} (in Tg a^{-1}: ocean 0.4, biomass burning 0.91, salt marshes 0.17, wood root funghi 0.16 and rice paddies 0.006) [59].

If chlorine is present in its molecular form (Cl$_2$) it forms radicals through a photolytic initiation reaction, similar to ozone, Eq. (2.1),

$$\text{Cl}_2 \xrightarrow{\text{h}\nu} 2\,\text{Cl}^\bullet. \tag{2.18}$$
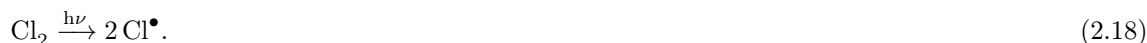
The chlorine radicals, Cl$^\bullet$, propagate in a two stage process [60]:

$$\text{Cl}^\bullet + \text{CH}_4 \longrightarrow \text{HCl} + \text{CH}_3^\bullet \tag{2.19}$$
$$\text{CH}_3^\bullet + \text{Cl}_2 \longrightarrow \text{CH}_3\text{Cl} + \text{Cl}^\bullet. \tag{2.20}$$

Other propagation reactions involve further substitution reactions such as:

$$\text{CH}_3\text{Cl} + \text{Cl}^\bullet \longrightarrow {}^\bullet\text{CH}_2\text{Cl} + \text{HCl} \tag{2.21}$$
$$^\bullet\text{CH}_2\text{Cl} + \text{Cl}_2 \longrightarrow \text{CH}_2\text{Cl}_2 + \text{Cl}^\bullet. \tag{2.22}$$

After and during propagation there are various ways to terminate:

$$CH_3^\bullet + CH_3^\bullet \longrightarrow C_2H_6 \tag{2.23}$$
$$CH_3^\bullet + Cl^\bullet \longrightarrow CH_3Cl \tag{2.24}$$
$$Cl^\bullet + Cl^\bullet \longrightarrow Cl_2. \tag{2.25}$$
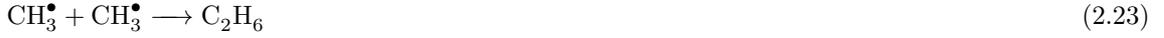
Singlet oxygen initiated from reaction (2.1) can not only react with water, but it can also react with methane by its own. Either way leads to the production of hydroxyl radicals [61]:

$$O(^1D) + CH_4 \longrightarrow CH_3^\bullet + OH^\bullet. \tag{2.26}$$

Table 2.3: Kinetic isotope effect (KIE), α_{KIE}, and lifetimes τ for atmospheric sinks used in model runs.

Sink	Lifetime τ/a	KIE η_{KIE}[a]	Fractionation factor $(\eta KIE = \eta_{KIE}^{-1} - 1) \cdot 1000$	References	
OH		1.0039 ± 0.0004	-3.89 ± 0.40	Saueressig (2001)	[61]
		1.0054 ± 0.0009	-5.37 ± 0.89	Cantrell (1990)[b]	[63]
Cl		1.075 ± 0.005 (223 K)	-69.77 ± -4.31	Saueressig (1995)	[60]
		1.066 ± 0.002 (297 K)	-61.91 ± -1.76	Saueressig (1995)	[60]
		$1.043 \cdot \exp(6.455/T)$	$\cdots$	Saueressig (1995)	[60]
$O(^1D)$		1.013	-12.83	Saueressig (2001)	[61]

The fractionation factors, α_{KIE}, used in models in literature have become more accurate over time thanks to improvements in measurement equipment and setups. Although changes are generally small, it has been reported that these can have a large effect on the $\delta^{13}C$-value of methane in the free troposphere as modelled and reported by McCarthy (2001), who run a model for the two different α_{KIE} values for $OH^\bullet$, from Saueressig (2001) and Cantrell (1990), and ended up with results differing by 1‰ in the free troposphere [64].
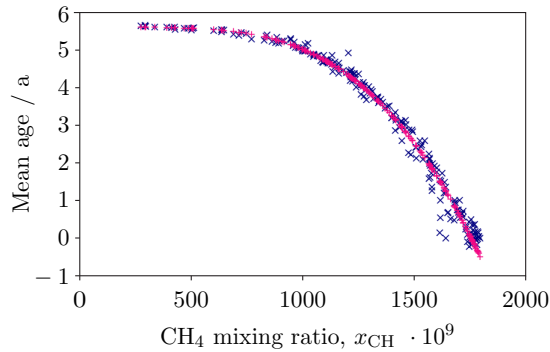
Figure 2.11: Atmospheric mean age of CH_4 against its mixing ratio (red "+"). The original age inferred from the N_2O mixing ratio is shown in blue ("×"). Adapted from Röckmann (2011) [65].

A stratospheric methane lifetime of 6 years is suggested by Röckmann (2011) as shown in Fig. 2.11 [65]. This slightly shorter lifetime as compared to the atmospheric methane lifetime is due to the return of a large part of stratospheric methane to the troposphere. This exchange mass flows across the 100 hPa

---

[a] Many authors (e.g. [62]) are inconsistent with the use of α_{KIE} and $KIE = \eta_{KIE}$, so they mix them up by giving an inverse definition of α.

[b] Saueressig (2001) remarks the high fluctuation in Cantrell's experimental results in relationship with the lower precision [61].

level was assessed in various publications in the past [65, 66, 62]. The presence of mass flow is also visible from the stratospheric mean ages of methane, where a clearly non exponential decay seems to take place, cf. Fig. 2.11.

(a)

(b)

(c)
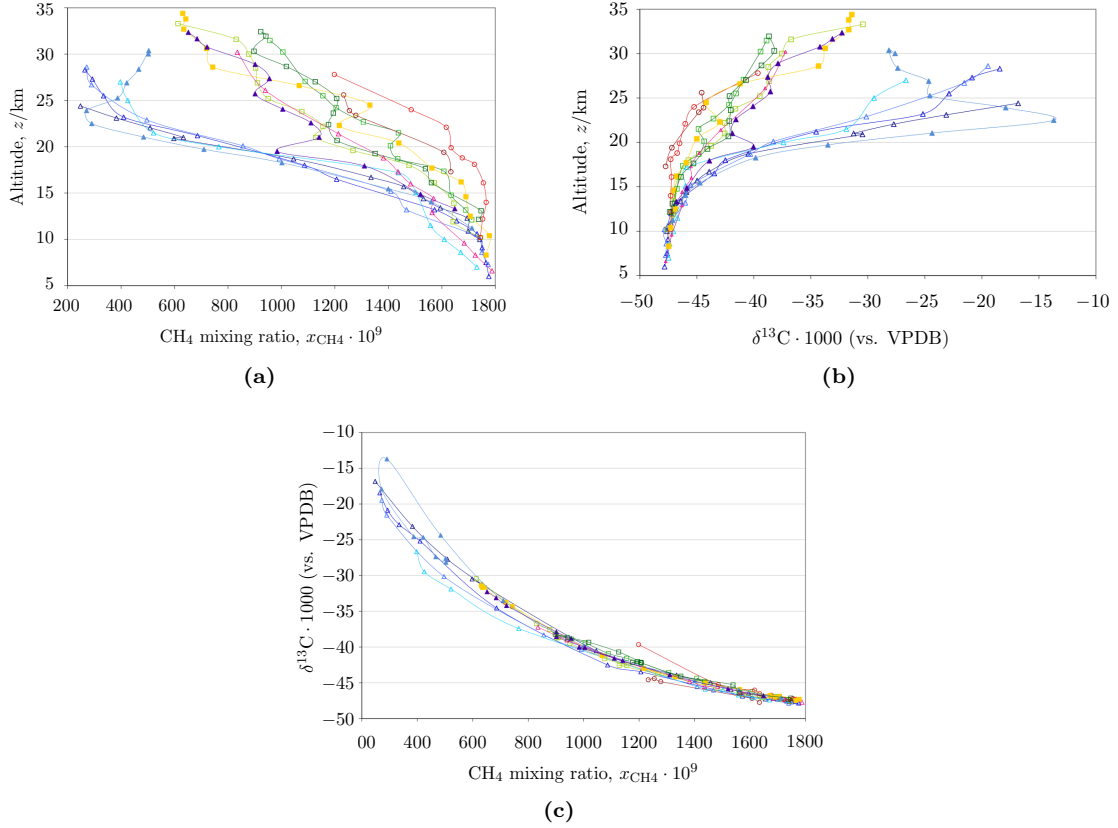
Figure 2.12: CH$_4$ mixing ratio and δ^{13}C signature vs. altitude (a,b), and δ^{13}C signature vs. mixing ratio (c). The different colors show different measurements. adapted from Röckmann (2011) [65].

In the stratosphere, the content and signature of methane varies a lot. While the mixing ratio decreases with height, the signature increases, that is, the higher in the stratosphere, the more enriched the methane is, cf. Fig. 2.12. Since methane is not fully oxidised in the stratosphere, a large fraction returns isotopically enriched to the troposphere, where it has a significant influence on the tropospheric signature.

Since there are many different sink reactions taking place in the stratosphere, at various altitudes with sometimes temperature dependent fractionation factors, it is convenient for modelling purposes to define an *effective* isotope fractionation factor for the stratosphere, weighted by the respective sink fractions, f, as defined by Röckmann (2011) [65, 60]:

$$\alpha_{\text{stra}} = \alpha_{\text{OH}} f_{\text{OH}} + \alpha_{\text{Cl}} f_{\text{Cl}} + \alpha_{\text{O}(^1\text{D})} f_{\text{O}(^1\text{D})} \approx 0.988 \Rightarrow \varepsilon = -12\permil, \tag{2.27}$$

where f_i are the fractions, $f_i \in [0, 1]$, quantifying how much of the total sink each individual sink contributes.

2.3.5 Soil bacteria sinks

Methanotrophic micro-organisms in soils are responsible for a small sink of methane. Like the atmospheric sink, also this sink is enriching atmospheric methane in ^{13}C. A review of measured fractionation factors in soils has been provided by Reeburgh (2007) [42] and is shown in Tab. 2.4.

Table 2.4: Kinetic isotope effect (KIE), $\varepsilon_{\mathrm{KIE}}$, and lifetimes τ for atmospheric sinks used in model runs.

Author	Biome/ data source	$\varepsilon_{\mathrm{KIE}} \cdot 10^3$
Whiticar & Faber (1986)	(model calculations, field data)	-2.0 to -14
Happell (1994)	(swamp floodwater, FL)	-3.0 to -21
King (1989)	(tundra, AK)	-16 (4°C), -26 (14°C)
Tyler (1994)	(forest soil, NH)	-22.2 ± 4
Reeburgh (1997)	(forest soil, AK)	-22 and -25
Snover & Quay (2000)	(grassland, WA)	-17.07 ± 0.97
	(temperate forest, WA)	-18.04 ± 0.4
Sansone & Graham (2004)	(Low O_2 West Mexican Margin waters)	-3.5 to -91[sic!]

In the model an average $\varepsilon_{\mathrm{soil}} = -17.6‰ \pm 3.2‰$ was applied, similar to Mischler (2009). Similar to Miller (2002) [67], the contribution of the two hemispheres were not considered equal: $2/3$ on NH, $1/3$ on SH, resulting in a $\theta_{\mathrm{soil}} = [4/3, 2/3]$, since the mean value still needs to be equal to 1.

2.3.6 Marine boundary layer sink

Methyl chlorine ("chloromethane") distributions have been discussed by Khalil & Rasmussen (1999) [68], who identified the source of methyl chloride to be much larger in the tropics than in higher latitudes, and a little bit stronger in the Northern than in the Southern hemisphere. Methyl chloride undergoes a similar fate as methane, and is being oxidised by OH$^\bullet$ and other radicals. This adds chlorine atoms to the atmosphere that eventually lead to the production of the isotopically strongly discriminating chlorine radicals.

For a long time, it was unclear where the missing sources of methyl chloride could originate from. Khalil & Rasmussen (1999) observed an unusual latitudinal distribution, where high concentrations were observed in the tropics, which is different from the distribution of industrial and other anthropogenic trace gases that have high concentrations in middle Northern latitudes [68]. Later, Yokouchi identified tropical islands as a source [58], and was able to successfully identify tropical vegetation, namely certain types of ferns and large tropical trees, *Dipterocarpaceae*, to be responsible for a large part. Tropical forests alone account for $0.82\,\mathrm{Tg\,a^{-1}}$ [59], that is 23% of the known sinks of $3.5\,\mathrm{Tg\,a^{-1}}$. However, some CH_3Cl emitting plants can also be found in coastal salt marshes [69].

Derendorp (2012) has identified another source to be halophyte leaf litter, accounting for $0.3-2.5\,\mathrm{Tg\,a^{-1}}$. The same report also discussed the temperature dependence of this methyl chloride source [70].
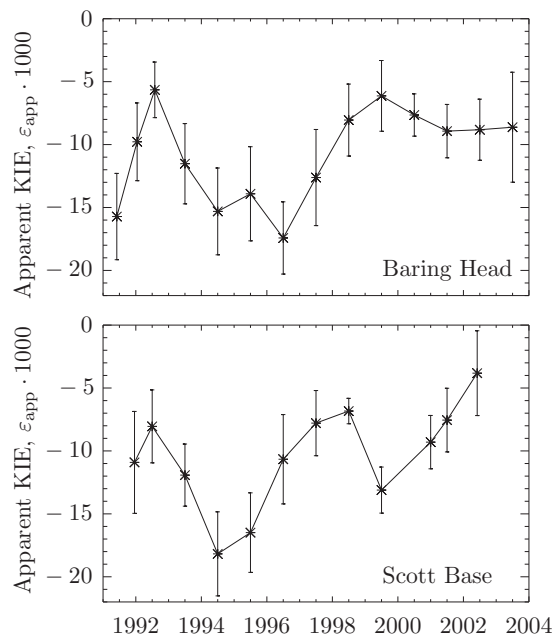
Figure 2.13: Apparent KIEs, $\varepsilon_{\mathrm{app}}$ in New Zealand (Baring Head) and Antarctica (Scott Base). Adapted from Allan (2005) [43].

How these plants and ecosystems and their CH_3Cl emission activity reacts to changes in temperature and humidity is of great interest. Further, the intensity of this methane sink changes so much over time that the apparent ε value for oxidating methane in the free troposphere is affected, as shown by Allan (2005), who reported the discrimination factor of a supposed single atmospheric sink, ε, of the free troposphere to change from -7‰ to -15‰ over a period of less than 10 years [43], cf. Fig. 2.13. Hence he inferred that a chlorine sink originating from the MBL is likely present in addition to $OH^{\bullet}$. Due to the remaining uncertainties, this sink will not be included in the model, but shows great potential for further investigation and modelling pathways, including dynamical variation of its strength.

Allan (2007) suggests hence a tropospheric fractionation factor that combines the effects of $OH^{\bullet}$ and $Cl^{\bullet}$: $\varepsilon_{\mathrm{OH+Cl}} = -6.9\text{‰}$ to account for the large influence of the small chlorine sink. However, our model has shown that too strong of a discrimination would require pyrogenic emissions to be negative on NH, therefore a conservative $OH^{\bullet}$ sink value was used for the troposphere $\varepsilon_{\mathrm{tropo}} = \varepsilon_{\mathrm{OH}} = -3.89\text{‰} \pm 0.4\text{‰}$, similar to Mischler (2009) and Houweling (2008) [71, 72], but different from Sapart (2012) [1], who applied Cantrell's $\varepsilon_{\mathrm{OH}} = -5.4\text{‰}$, cf. Tab. 2.3.

2.3.7 Sea floor anaerobic methane oxidation

Sea floor bacteria have been identified to being able to uptake methane into their metabolisms of anaerobic methane oxidation (AMO) as first suggested in 1976 by Barnes & Goldberg and Reeburgh [73, 74], and successfully identified in 2012 by Joye [75]. This sink is said to be very important for methane in the sea, since it represents a near quantitative sink for upward fluxes originating from sediments as reported by Reeburgh (2007) [42]. However, more research has to be carried out, and this seems not to discriminate against the tropospheric methane signature, since methane that undergoes AMO is being oxidised before reaching the ocean surface. Hence it has not been included in the model.

2.4   Isotopes

The existence of isotopes had been suggested by Niels Bohr already in 1913: "According to the theory, this would mean that the charge on the nucleus, as well as the configuration of the surrounding electrons, was identical in some of the elements, the only difference being the mass and the internal constitution of the nucleus." [76] It was the same year that Soddy had also discovered the same and named them "isotopes" [77, 78]. However, it was not until the discovery of the neutron in 1932 by Chadwick that this mass difference could be explained [79].

For instance, Carbon can exist in the form of 15 different isotopes from ^{8}C to ^{22}C. All of them having 6 electrons and 6 protons, but each of them having a different number of neutrons, thus a different mass. However, only three of them have a half-life time greater than half an hour. These three isotopes and their approximate relative abundances in the present atmosphere are shown in Fig. 2.14.

^{12}C	^{13}C	^{14}C
stable	stable	$t_{1/2} = 5700\,\text{a}$
98.9%	1.1%	$<10^{-12}$

● Proton   ● Neutron   ● Electron
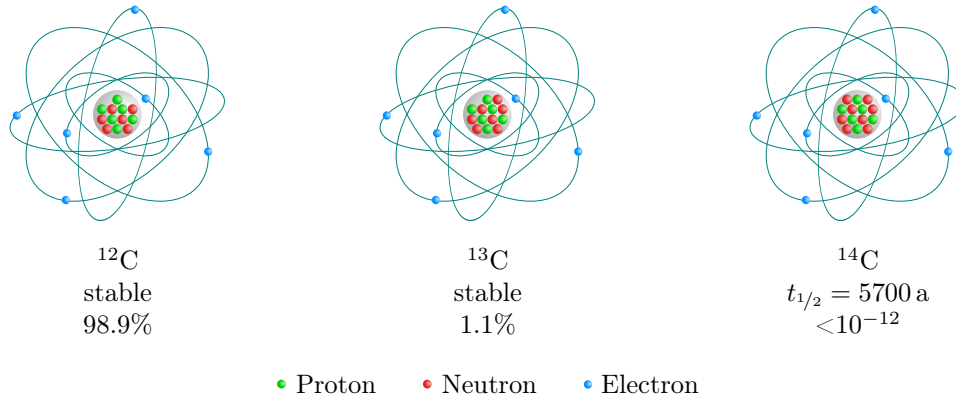
Figure 2.14: Schematic Bohr-Rutherford model [76] of the carbon atom in its common isotopes forms, showing nucleons with orbiting electrons, half-life times, and approximate abundances in the present atmosphere.

2.4.1   Isotope ratios

Two molecules of the same substance and composed of different isotopes are called *isotopologues*[c]. Their *abundances*, F (unitless), are defined as the fraction of the mixing ratio of an isotopologue relative to the total mixing ratio of a compound. The mixing ratio is denoted by x and expressed in m^3/m^3. It has values of around 700×10^{-9} and 7×10^{-9} for ^{13}x and ^{12}x, respectively. The abundance is then given as

$$^{13}F = \frac{^{13}x}{^{12}x + \,^{13}x}. \tag{2.28}$$

The F values come to about 1% and 99% for ^{13}F and ^{12}F respectively. However, it is common to express the *isotope ratio*, R, as the fraction of the abundance of the rare isotopologue over the dominant one:

$$^{13}R = \frac{^{13}x}{^{12}x} = \frac{^{13}F}{^{12}F} = \frac{^{13}F}{1 - \,^{13}F}. \tag{2.29}$$

---

[c] There are also isotopologues of the same gas that share a cardinal mass (e.g., ^{13}CH$_4$ and ^{12}CH$_3$D), these are referred to as "isotopic isobars".

It is interesting to note that the difference between F and R is only very small:

$$^{13}R - {}^{13}F = \frac{^{13}x}{^{12}x} - \frac{^{13}x}{^{12}x + {}^{13}x} = {}^{13}x^2. \qquad (2.30)$$

For this reason, some models in literature use $^{13}F = {}^{13}R$ and $^{12}F = x$, since the rare isotope contributes at much lower order of magnitude to the total mixing ratio.

Changes in isotope ratios through natural processes are only affecting the isotopic abundance at the third significant digit, and hence it is easier to express these changes in relation to a standard. This *relative difference in isotope ratios*, is usually denoted by δ values that are commonly expressed in per mil (‰), compared to international standards:

$$\delta_{std}^{13}C = \frac{^{13}R_{\text{sample}}}{^{13}R_{\text{standard}}} - 1, \text{ where } {}^{13}R_{\text{x}} = \left(\frac{^{13}F}{^{12}F}\right)_{\text{x}}. \qquad (2.31)$$

There have been several attempts to introduce a "quantity of dimension 1" to eliminate the cumbersome expressions of dimensionless quantities per SI guidelines. First, the International Union of Pure and Applied Physics (IUPAP) proposed in 1999 the "uno" with symbol "U" [80]. So, it could be written "$-42.21\,\text{mU}$" for -42.21‰, "$700\,\mu\text{U}$" for $700\,\text{ppm}$, "$23\,\text{nU}$" for $23\,\text{ppb}$ and so on. This would be more of a scientific way to express quantities than using %[d], ‰, ppm, ppb and ppt, "which are language dependent and in some cases ambiguous in their meaning". Hence, "this is to be depreciated" [80]. However, four years later, the "International Committee for Weights and Measures" (CIPM) concluded in its Report of the 16th meeting "that the responses had been almost entirely negative and that [they] recommended dropping the idea" [81]. Eight years later, Brand & Coplen (2012) [82] came up with the "Urey", symbol "Ur", in recognition of Harold C. Urey, an outstanding scientist of the University of Chicago who was the first carry out routine stable isotope analytical measurements. The reaction to this proposal has yet to be seen, but the notation has not yet been widely used.

All δ^{13}C values are nowadays reported versus the standard "VPDB" (Vienna-Pee-Dee-Belemnite). The original standard for expressing carbon-13 isotope ratios was called "PDB" prepared from calcium carbonate extracted from the *rostrum* of a fossil Cretaceous belemnite (*Belemnitella americana*) found in the "Pee Dee" rock formation in South Carolina, USA. This material was chosen for its high ^{13}C/^{12}C ratio compared to most other natural carbon-based substances ($R_{\text{PDB}} = 0.0112372$). Hence, by Eq. 2.31, most other naturally-occurring samples have negative delta values. Its high ^{13}C/^{12}C ratio is not astonishing for its being a petrified organism, since heavier isotopes are more likely to remain in earth until petrification (cf. previous Section 2.4).

The found belemnite was used up quickly, so a synthetic standard was prepared at the IAEA (International Atomic Energy Agency) in Vienna, Austria, which now serves as a reference standard for expressing ^{13}C/^{12}C ratios. The new reference has been reported to have a slightly different isotopic composition as the PDB sample, and is named "VPDB", having an additional "V" as reference to the Vienna laboratory. $R_{\text{VPDB}} = 0.0111802(28)$ as calculated from Chang (1990) and used by Werner (2001) [83]. This is also the value used in this project[e]. Chang determined the signature of the NBS-19 standard. This latter one is used for the *definition* of VPDB $\delta_{\text{NBS-19/VPDB}} = +1.95$‰. However, there is some uncertainty about the value determined by Chang (1990). Coplen (2011) adds that it is preferable to normalise with two international measurement standards, such as "VPDB-LSVEC" [84]. We think, it could be useful to additionally report the absolute value, R, of the assumed isotope ratio of the used standard, in addition to its signature and international reference standard. For the expression of hydrogen isotopes, δD, the "VSMOW" standard (Vienna Standard Mean Ocean Water) is used.

---

[d] The % sign derives from the Italian cento, which was written as $^c/_o$, the slash standing for the "t".

[e] The used working standard has an isotope ratio $R_{\text{ws}} = 0.0107802730$ and is assigned the "known" value of $\delta_{\text{ws}} = -35.771$‰, which implies a $R_{\text{VPDB}} = R_{\text{ws}}/(\delta_{\text{ws}} + 1) = 0.011180199931 \approx= 0.0111802$.

To change between international standards, the following formula is applied:

$$\delta_{\mathrm{sa/S2}} = R_{\mathrm{sa/S2}} - 1 = \frac{R_{\mathrm{sa/S1}}}{R_{\mathrm{S1}}}\frac{R_{\mathrm{S1}}}{R_{\mathrm{S2}}} - 1 = (\delta_{\mathrm{sa/S1}} + 1)(\delta_{\mathrm{S1/S2}} + 1) - 1 = \delta_{\mathrm{sa/S1}} + \delta_{\mathrm{S1/S2}} + \delta_{\mathrm{sa/S1}}\delta_{\mathrm{S1/S2}}. \quad (2.32)$$

2.4.2 Isotope effects on molecular scale

Different isotopes display differences in most chemical and physical properties, which are mainly caused by two consequences of the mass difference:

1. At a given temperature, the kinetic energy of a molecule is defined as a function of its temperature alone, which equals the product of its mass with the square of its speed;

$$E_{\mathrm{kin}} = \frac{f(T)}{2}k_B T = \frac{1}{2}mv^2, \quad (2.33)$$

   where k_B is the Boltzmann constant, f the available degrees of freedom of the molecule, which is temperature dependent, since some higher levels are only achievable at elevated temperatures (details in Appendix A.3). A heavier molecule (isotopologue) will therefore move more slowly than a lighter one (temperature being constant). Quantitatively speaking, if the carbon atoms were to move freely and elementary (unbound) in space, the heavier ^{13}C atoms would move at $\sqrt{12/13} = 96\%$ of the speed of its lighter ^{12}C isotope. However, since in nature, carbon rarely occurs as a gas in its elementary form, but as a molecular compound, the relative mass difference and the resulting difference in speed of isotopologues is smaller. For methane, the molecules with a carbon atom of the heavier isotope move at $\sqrt{M_{^{12}\mathrm{CH}_4}/M_{^{13}\mathrm{CH}_4}} = \sqrt{16/17} = 97\%$ of the speed. This difference in propagation speed influences all the properties involved in the movement of gases, such as diffusivity (lighter molecules will diffuse faster) and collision frequency (lighter molecules will undergo more collisions with other molecules, which allows them to react more often) [85].

2. In classical physics, two atoms in a molecule are separated by a distance r, by the covalent bond. This gives rise to two opposing forces, as proposed in 1931 by John Lennard-Jones [86]: The attractive van der Waals force that increases the closer the atoms come ($F_a \sim r^{-7}$), while the repulsive Pauli force decreases even more quickly the further apart the particles get ($F_r \sim -r^{-13}$). Consequently, the particles will reside separated from each other by the distance at which the resulting force $F = F_a + F_r$ is zero. From Eq. (2.34) and the relationship of force and energy, $F = dE/dr = 0$, it follows that this is the case at the bottom of the energy well (cf. Fig. 2.15).

The Lennard-Jones potential is defined [86] as

$$E_{\mathrm{pot}}(r) = \frac{A}{r^{12}} - \frac{B}{r^6}, \quad (2.34)$$

where A and B are coefficients as a function of the position r_m and the well depth.
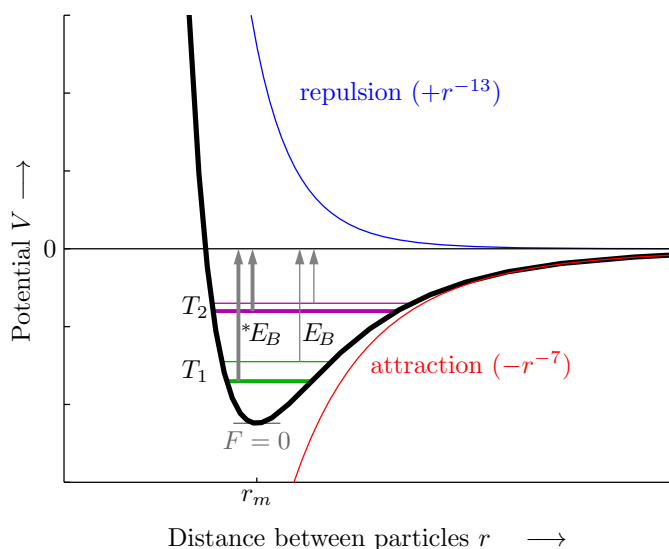
Figure 2.15: Lennard-Jones potential as a function of the distance between particles r for two different isotopes (heavy-line: heavy isotopologue) at two different temperatures ($T_2 > T_1$). (Drawn after Mook (2000) and others [87]).

Due to vibrations, the particle is never at the bottom of the energy well, even not at $T = 0\,K$, as suggested by Einstein and Stern in 1913[f] [88] and further explained by Quantum mechanics with Heisenberg's *uncertainty principle*[g] in 1927 at the *Institute for Theoretical Physics* (now *Niels Bohr Institute*) in Copenhagen [89]. Therefore, the needed energy to take the molecule apart is less than the minimum potential energy at r_m. Different vibrational modes cause the binding energies E_B to be different for each isotope. $^*E_B$ shows the (normal) isotopic effect for the heavier isotope. As the isotopic differences in binding energies decrease with increasing temperature ($T_2 > T_1$), this leads to smaller isotope effects at higher temperatures [87].

In polyatomic molecules, the potential energy to be overcome can under certain conditions be deeper for lighter atoms ($^*E_B > E_B$), and thus the binding energy higher. In this case, the vapour pressure of the heavy species is higher. This phenomenon is referred to as the *inverse isotope effect*. For instance, this is the case for $^{13}CO_2$ with a lesser solubility [90] and higher water vapour pressure [91], or for CH_3D methane with a higher vapour pressure [85]. Due to the prevalent normal isotopic effects, most of the lighter isotopologues of a same molecule can be found in the biosphere, while most of the heavier counterparts will remain on the ground and are eventually petrified in the geosphere.

Methane, being a molecule composed of 5 atoms, can also have some of the hydrogen atoms substituted. The natural abundance of these methane isotopologues as part of the total CH_4 mixing ratio in the present day atmosphere is shown in Table 2.5 [92].

---

[f] Einstein & Stern (1913): At $T = 0$, the energy ϵ of a molecule (e.g. H_2) is expressed by the second Planck formula as:

$\lim\limits_{T \to 0} \epsilon(T) = \lim\limits_{T \to 0} \left\{ \dfrac{h\nu}{e^{\frac{h\nu}{k_B T}} - 1} + \dfrac{h\nu}{2} \right\} = \dfrac{h\nu}{2}$, with Planck's constant h, frequency ν and Boltzmann's constant k_B.

[g] The principle says that for a particle, the more precise its momentum p is known, the less precise its position x is $\left(\sqrt{\left\langle (\hat{x} - x_0)^2 \right\rangle} \sqrt{\langle \hat{p}^2 \rangle} \geq \dfrac{\hbar}{2} \right)$. After a thorough treatment the ground state of the system E_0 can be solved for:

$E_0 = \dfrac{1}{2} \hbar \omega$, where $\hbar$ is the *reduced Planck's constant* and ω the angular frequency of the oscillator.

Table 2.5: Isotopes of methane and their abundances (calculated from [92]).

Isotopologue	Mass (u)	Abundance (%)
$^{12}CH_4$	16	0.98927
$^{13}CH_4$	17	0.01059
$^{12}CH_3D$	17	0.00014

From Table 2.5 it follows that the isotope effect on methane caused by deuterium is only of minor importance as compared to the effect of carbon-13: $(F_{^{13}CH_4})/(F_{^{12}CH_3D}) = 0.0134 = 1.34\%$. But it has a huge potential for determining the methane source, as has been shown by Fischer (2008) [9], cf. Fig. 2.5.

2.4.3 Isotope effects on reactions

Mass-dependent fractionation which occurs in almost all physical and chemical processes, discovered (in 1920) and described by Harkins (1923) [93], are a consequence from what was described in the previous section. They are mathematically described by the *fractionation factor* α, comparing the isotope ratios of a single element in two phases or compounds, educt A and product B of the physical or chemical process (A $\longrightarrow$ B or A $\rightleftharpoons$ B), defined as

$$\alpha_{B/A} = \frac{R_B}{R_A}.\tag{2.35}$$

For example, if methane is formed from CO_2, the fractionation factor for this process is $\alpha = {}^{13}R_{CH_4}/{}^{13}R_{CO_2}$. Since isotope effects are rather small, $\alpha \approx 1 \pm 1 \cdot 10^{-3}$, another value, the *fractionation*, is defined as

$$\varepsilon_{B/A} = \alpha - 1 = \frac{R_B}{R_A} - 1,\tag{2.36}$$

and is, similar to δ values, usually expressed in permill ($1\text{‰} := 1 \cdot 10^{-3}$). This notation is widely used to quantify depletion, ($\varepsilon < 0$) or enrichment ($\varepsilon > 0$) in the rare isotope in reservoir B with respect to reservoir A. This formula can be transformed into a function of delta values that are more commonly used than the R values. The identity in Eq. (2.38), proven in Appendix A.2, is more useful and its approximation is convenient to make estimates:

$$\varepsilon_{B/A} = \frac{\delta_B - \delta_A}{\delta_A + 1} \qquad \approx \delta_B - \delta_A \tag{2.37}$$

$$\Leftrightarrow \quad \delta_B = \varepsilon_{B/A}(\delta_A + 1) + \delta_A \approx \delta_A + \varepsilon_{B/A} \tag{2.38}$$

However, the approximation from Eqn.2.38 does not always hold so well, as it can be seen from Fig. 2.16, the difference increases with increasing magnitudes of both δ and ε.
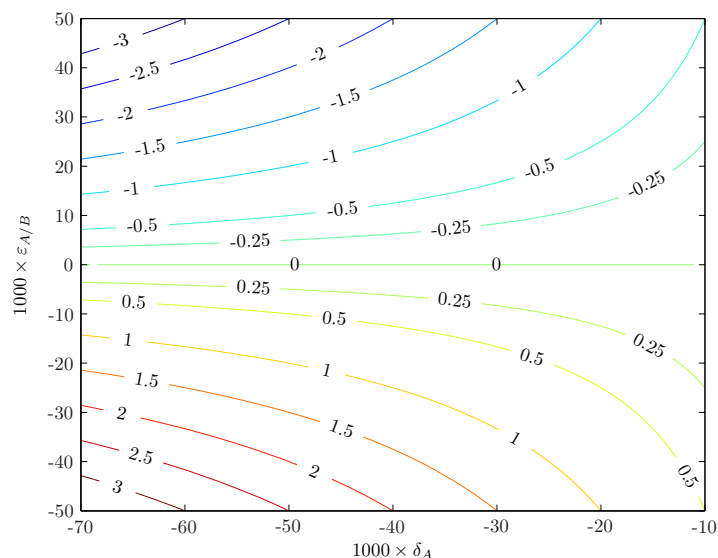
Figure 2.16: Difference between true and approximated δ_B value: $\Delta\delta_B = [\varepsilon \cdot (\delta_A + 1) + \delta_A] - [\delta_A + \varepsilon]$.

There is a distinction between an equilibrium isotope effect and a kinetic isotope effect:

- The *equilibrium isotope effect*, also known as thermodynamic isotope effect occurs in an isotope substitution reaction between compounds A and B, where the asterisk denotes the presence of the rare isotope:

$$^*A + B \rightleftharpoons A + {}^*B. \tag{2.39}$$

Here, the fractionation factor equals the equilibrium constant between compounds A and B for this exchange reaction Eq. (2.39) [87].

$$K = \frac{[A][^*B]}{[^*A][B]} = \frac{[^*B]/[B]}{[^*A]/[A]} = \frac{R_B}{R_A} = \alpha_{B/A} \tag{2.40}$$

- The *kinetic isotope effect*, is a result of irreversible, one-way processes of physical or chemical nature. Such as the Rayleigh evaporation of water (with immediate removal of product vapour), absorption and diffusion of gases, as well as one-way reactions, such as the bacterial decay of plants. The fractionation is mainly characterised by the binding energies of the original compounds [87]. For instance, in the reaction

$$^*A + E \longrightarrow {}^*B + P, \tag{2.41}$$

where educt A and product B contain the element for which the isotopic effect is examined, while educt E and product P do not. The fractionation factor is expressed as the ratio of the reaction rate constants of the reactions with heavier (i) and lighter (j) isotope containing molecules [84][h]:

$$\alpha_{KIE} = {}^ik/{}^jk. \tag{2.42}$$

A special case is the *inverse kinetic isotope effect* that can most commonly be observed in reactions involving hydrogen and carbon atoms [95]. Interestingly, the inverse isotope effect is also present for the case of CH_3D, as reported by Konya (2012) [85].

---

[h] Some authors define a multi-character entity, $KIE = {}^jk/{}^ik = \alpha^{-1}(= \eta)$ [66, 1, 62, 65], while others use α, Eq. 2.42, or $\varepsilon = \alpha - 1$ [71, 62, 94, 13]. Some also take $\varepsilon = KIE - 1$ [65]. And others again take inverse definitions of KIE and α [62, 9].

2.5   Mass spectrometry

With the help of a mass spectrometer, different isotopes can be identified, that is, their ratios in a gas mixture. The mass spectrometer works on the basis of deflection of ionised gas molecules in a magnetic field, and subsequent analysis of their mass to charge (m/z) ratio (cf. Fig. 2.17).
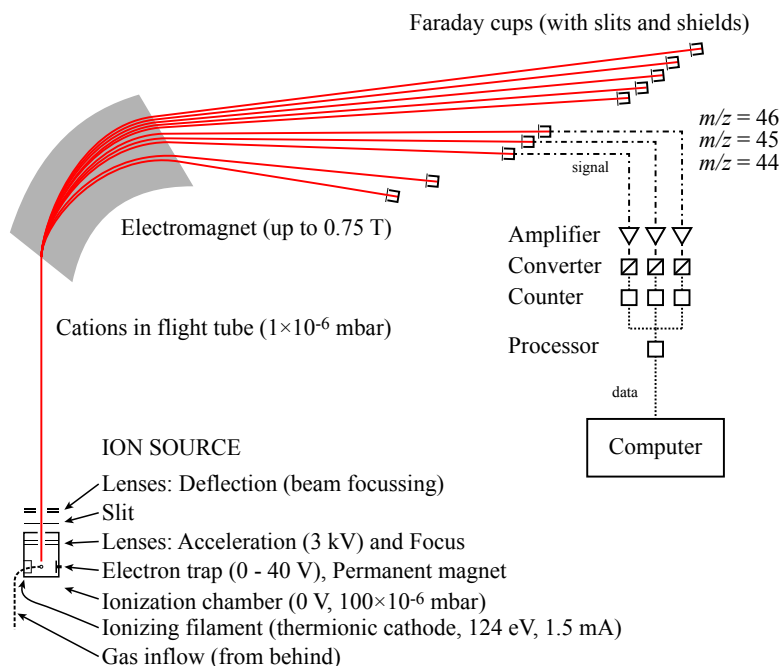
Figure 2.17: Schematic representation of Delta V Plus mass spectrometer (drawn after the information in the information from manual [96]).

The ion source consists of a ionization chamber followed by a lens system. In the ionization chamber, gas molecules are ionised by electrons that originate from an ohmically heated Tungsten filament through thermionic emission: $O=C=O + e^- \longrightarrow O=C=O^{+\bullet} + 2\,e^-$.

Some molecules are "lost" due to double ionization, in which some already-ionised molecules can get ionised to CO_2^{++}, or due to bond dissociation: since, the energy of the electron (ca. 70 eV) is much greater than the energy of the bonds, some parts of the molecule can dissociate, which gives rise to fragment ions and fragment neutrals:

$$O=C=O^{+\bullet} \longrightarrow O^{\bullet} + C=O^+, \quad \text{with } m/z = 28\ (^{12}C^{16}O)\text{ to } 31\ (^{13}C^{18}O)$$
$$O=C=O^{+\bullet} \longrightarrow C=O^{\bullet} + O^+, \quad \text{with } m/z = 16\ (^{16}O)\text{ to } 18\ (^{18}O)$$

$$C=O^+ \longrightarrow C^{+\bullet} + O^{\bullet}, \quad \text{with } m/z = 12\ (^{12}C)\text{ or } 13\ (^{13}C)$$
$$C=O^+ \longrightarrow C^{\bullet} + O^{+\bullet}, \quad \text{with } m/z = 16\ (^{16}O)\text{ to } 18\ (^{18}O)$$
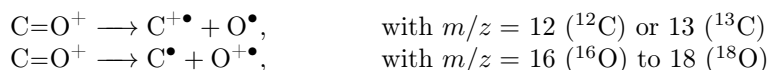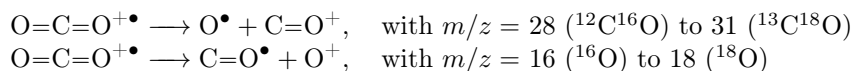
The focus lens system following the extraction lenses aims at focussing the ion beam, so that as many ions as possible will make it through the slit and pass through the magnetic field, which exerts a force to the ions and deviates them from the straight path as a function of their mass to charge ratio (m/z). The CO_2^+ ions hitting a Faraday cup transmit an electric charge that is then amplified in order to balance the abundance of the isotopes collected in the different cups. The analogue ion current signals are then converted into pulses in a voltage-to-frequency converter. The pulses are counted over a preselected

integration time, the result of which is collected by a processor. The bundled data is sent to the *Isodat* software, which performs further calculations and corrections (cf. Section 4.1), to obtain the values for the Carbon isotope abundances.

In our setting, we are running 13 measurements of CO_2 working standard in continuous flow. These are small aliquots from a CO_2 flask with known isotopic composition. The tenth standard aliquot measured serves as the reference peak, meaning that the calculated ^{13}C and ^{12}C ratio then serves as the reference for the *Isodat* programme to calculate the abundances based on the ion counting from the signal processor.

2.6 Ice cores

Ice cores offer a unique opportunity to analyse the atmosphere of the past through air conserved as bubbles or as clathrates dissolved in the ice. On Greenland, there have been several ice core drilling campaigns, starting in 1964 at "Camp Century", a US military base.

The main part of the cores measured in this study are from the Eurocore shallow (304 m) ice core, drilled at GRIP on the Summit without using drill liquid, which is only required for deep cores to prevent closure of the drill hole [97]. And two are from the NEEM core (2538 m) [98], drilled in North-West Greenland, where a bio-degradable drill liquid based on "ESTISOL 240" (coconut oil extract) mixed with "COASOL" was used.

Figure 2.18: Position of drill sites within Greenland [Picture stock of CIC].

Due to differences in accumulation rates, the cores from Antarctica extend much farther into the past (800 ka) [99] than the ones from Greenland (128 ka) [100].

2.6.1 Stable water isotopes

The age of the ice ("ice age") is determined by analysing the ice core and counting the annual ice layers identified by measurements of oxygen and hydrogen isotopes in the ice. The isotopic composition is again given in δ notation, similar to Eq. (2.31):
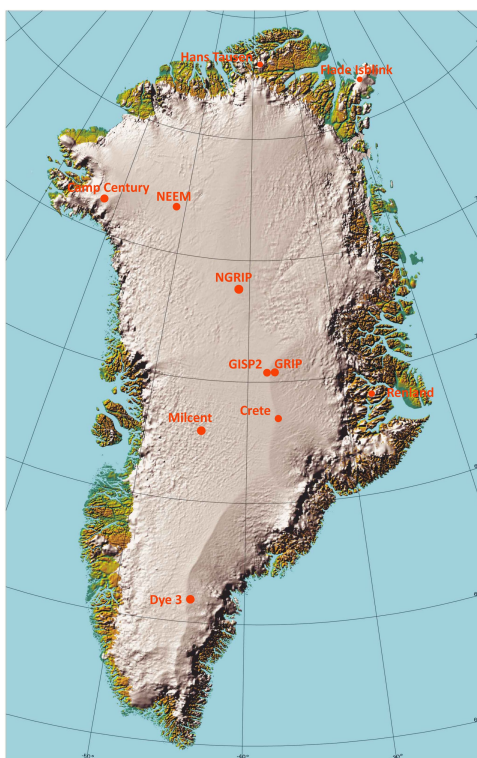
$$\delta^{18}\text{O} = \frac{^{18}R_{\text{sample}}}{^{18}R_{\text{standard}}} - 1, \text{ where } ^{18}R_{\text{x}} = \left(\frac{^{18}\text{O}}{^{16}\text{O}}\right)_{\text{x}} \tag{2.43}$$

$$\delta\text{D} = \frac{^{\text{D}}R_{\text{sample}}}{^{\text{D}}R_{\text{standard}}} - 1, \text{ where } ^{\text{D}}R_{\text{x}} = \left(\frac{^{2}\text{H}}{^{1}\text{H}}\right)_{\text{x}} \tag{2.44}$$

The $\delta^{18}\text{O}$ and δD records show somewhat similar signals and serve as proxy of temperature and the global ice volume. Small differences, calculated through the "deuterium excess", $d = \delta\text{D} - 8\delta^{18}\text{O}$ [101], characterise the conditions at the moisture source (primarily temperature). Snow falling on high elevations on the Greenland ice sheet originates to a large extent from subtropic zones of the North Atlantic Ocean [102]. The air masses rise in altitude and cool down to the dew point temperature, from where further cooling leads to condensation and a preferential fallout of heavy isotopes via Rayleigh condensation. A similar process of Rayleigh sublimation continues also when the solid phase plays an important role [102]. The equilibrium vapour pressure of the light component ($\text{H}_2{}^{16}\text{O}$, p) divided by the enriched one ($\text{H}_2{}^{18}\text{O}$, $p' < p$) gives the fractionation factor $\alpha = p'/p$, which decreases with decreasing temperatures [101]. During the winter, temperatures over Greenland are colder than in the summer, and hence in winter less enriched water remains in the air. This allows counting the peaks (summer) in the record of $\delta^{18}\text{O}$ for dating the upper part of the ice core in combination with various other signals from chemical substances in the snow.

In addition to that, tephra layers consisting of ash from volcanic eruptions, are also a common way of dating ice, and can be used as reference points.

2.6.2 Firn processes

In the previous section it has been explained, how to calculate the ice age. However, for analysing the carbon isotopic signature of methane, the gas age is important, which is not equal to the ice age. Because the age of the ice relates to the age of the snow, and the conversion from snow to firn to ice is a slow process, during a large part of which gases are still in exchange with the atmosphere. That is, in the convective zone (CZ) that ends at $4.5\,\text{m}$ below the surface convective processes dominate and the air is in constant exchange with the atmosphere [103]. Below, in the diffusive zone (DZ), gas is transported by molecular diffusion through the static air column. In the non-diffusive zone (NDZ), gas is no longer exchanged with overlaying layers. The transition from the CZ into the NDZ is the lock-in-zone (LIZ), in where the gas gets closed off into gas bubbles [104].Late research has suggested, that there is a need for a non-vanishing diffusivity in the LIZ [104]. The different zones were identified by the isotope signature of molecular nitrogen ($\delta^{15}\text{N}$), which gets enriched in absence of convection in the diffusive zone, due to the isotopic mass difference (ΔM_{ij}) and according to the barometric formula Eq.(2.45) [105, 106, 103]. The effect of which is shown in Fig. 2.19.

$$\delta_{ij} = \exp\left(\frac{\Delta M_{ij}gz}{RT}\right) - 1, \tag{2.45}$$

where z is depth, g the gravity constant, R the gas constant and T temperature. Since ΔM_{ij} of $^{14}N^{15}N$ is similar to $^{13}CH_4$, the resulting enrichment in $\delta^{13}C$ can be modelled from knowledge of the enrichment in $\delta^{15}N$ and the free air diffusivity of $^{13}CH_4$ relative to $^{14}N^{15}N$ [107].

This leads to three different effects that have to be accounted for: (1) an offset in the gas age compared to the ice age [108, 104], Section 2.6.3, (2) a smoothing of atmospheric variations during the trapping process [37] and (3) an enrichment in ^{13}C due to gravitational fractionation effects by molecular diffusion [109, 105], Section 4.4.
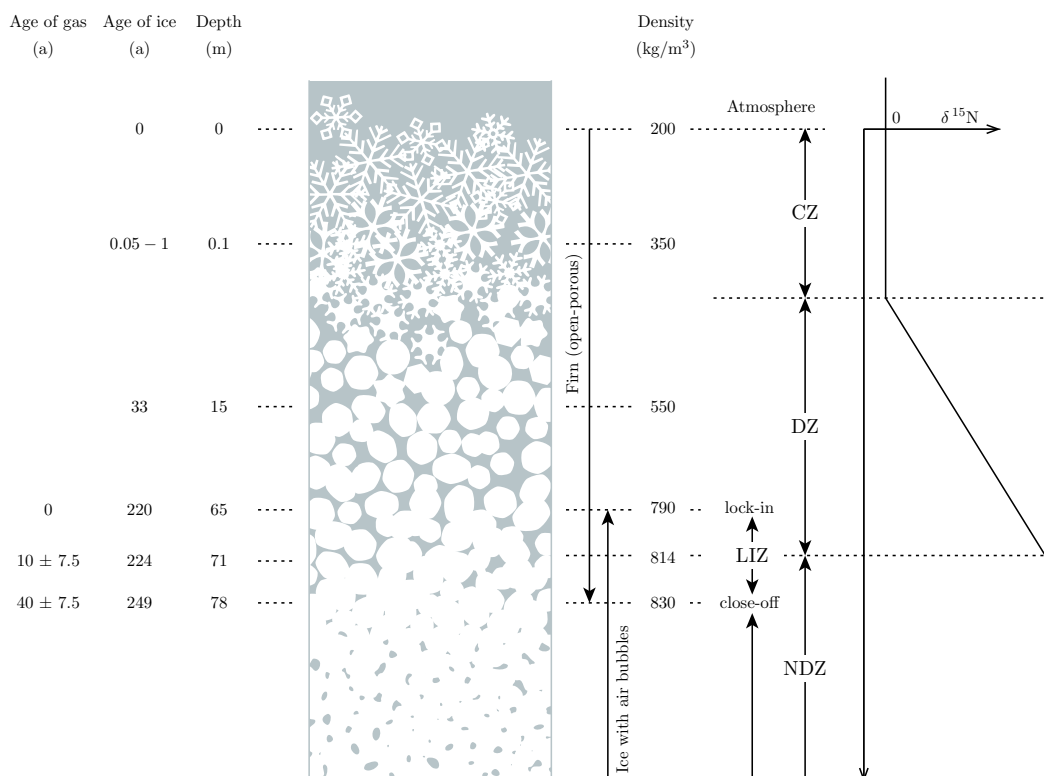
Figure 2.19: Transition from snow to firn to ice at Summit. Drawn according to Blunier (2000) [103] and Buizert (2011) [104].

2.6.3   Time axis correction: Gas age – Ice age offset

The mean gas age to ice age offset, under present climatic conditions for the Eurocore ice core is 210 a as calculated with a diffusion model by Schwander (1993) [106]. Due to diffusive processes, this offset is not a discrete value, but an age distribution with a standard deviation of $\sim$7 a. On the other hand, for NEEM this difference has been modelled with a new multi-tracer method that gives a more complete characterisation of the firn air transport properties, including diffusivity through the lock-in zone. The calculated gas age – ice age difference has been tabulated for each core segment separately by Buizert (2011) [104] and are in the order of 182^{+3}_{-9} a under present climatic conditions.

For the Eurocore ice core, the air showed to get occluded into bubbles mainly between 65 m (lock-in depth) and 80 m (close-off depth) (NEEM: 63 m and 78 m), which corresponds to 790 kg/m³ and 830 kg/m³ respectively [106, 104].

2.7 Medieval Climate Anomaly

The "Medieval Climate Anomaly (MCA)", also known as "medieval warm period (MWP)" or "little climatic optimum", was a warm period around AD 850 – 1300 in Europe and eastern North America, while the North Pacific experienced a cooling. Temperatures in the Atlantic were at least 1 °C above millennial means. Higher temperatures over the Atlantic resulted in increased rainfall over Russia. The sea level rose and fell eustatically at an amplitude of about 0.5 m [110]. The development of temperature in the Southern Hemisphere is less firmly researched, since there is only sparse proxy data available, as reported by Mann (2009) [111], who presents a record for both hemispheres (Fig. 2.20). While in the Northern Hemisphere a warmer period can be identified, an equivalent anomaly is absent in the Southern Hemisphere. Goosse (2006) [112] concluded from modelling that the origin of those warm summer conditions are to a large extent due to a long term cooling [sic!] induced by land-use changes in Europe.

(a) Southern Hemisphere.
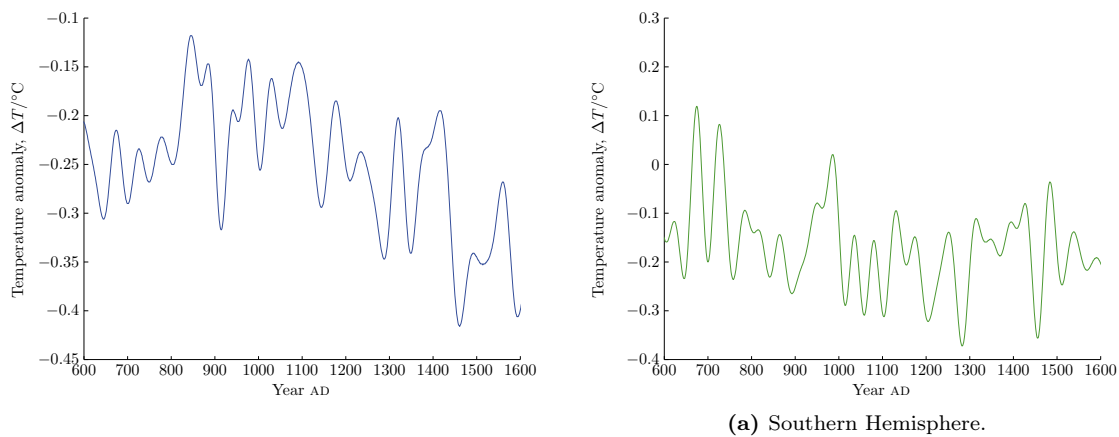
Figure 2.20: Hemispheric temperature reconstructions smoothed with a 40 year low-pass filter. (a) NH reconstruction is based on 6 indicators. (b) SH reconstruction is based on 5 indicators. Data from Mann (2003) [111].

Hughes (1994) [113] analysed tree ring data from all over the world and he found that the climate anomaly manifested itself as a warm period in Europe from AD 1200 – 1375 and from AD 1475 – 1550 and AD 1600 – 1675, as well as in Fennoscandia from AD 1375 until 1550. However it was impossible to conclude, with the data they had, that there was anything more significant than relatively warm conditions in some parts of the globe during some parts of the year. Similar results were reported by Seidenkrantz (2008) [114] who reports "severe cooling" in the Labrador region from AD 700-1100, which they attribute to a reduction in Atlantic water entrainment, with resulting conditions prevailing until 1500. However, Cook (2002) [115] analysed tree ring data from New Zealand and concluded to have identified an MCA *sensu lato* also on the Southern Hemisphere, namely from AD 1137 – 1177 and AD 1210 – 1260. These 40 and 50 year periods are, however, not of the same extend as it was in Europe. Furthermore, he reports a cold period from AD 993 to 1091. For South America, on the other hand, Kellerhals (2010) [116] analysed an ice core from the Andes on Ammonium and reports a warm period from AD 1050 to 1300.

Ljungqvist (2010) [117] and Moberg (2005) [118] further analysed temperature deviations during this period on the Northern hemisphere, the reconstructed temperature anomaly is shown in Fig. 2.21. The warmperiod is present in a similar way as in Fig.2.20.
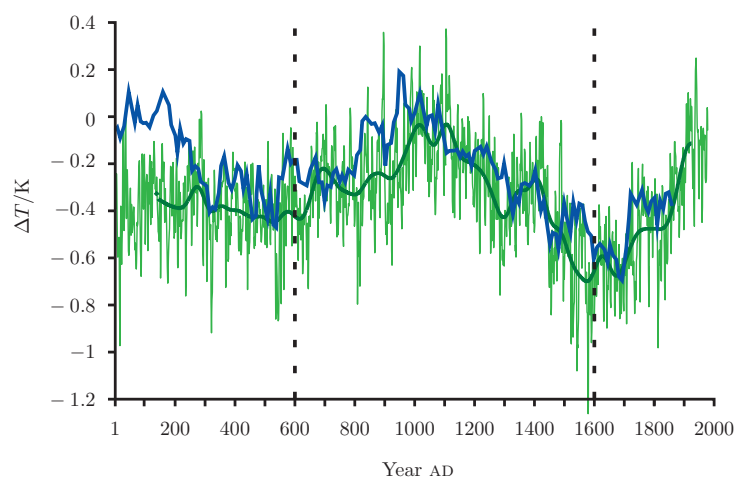
Figure 2.21: Estimation of Northern extratropical temperature variations relative to the 1961–1990 mean (blue) by Ljungqvist (2010) [117], and Northern hemisphere mean temperature variations from a multi-proxy reconstruction (green) by Moberg (2005) [118], where the thick line shows an 80 year smoothed curve.

Part I: Ice Core Analysis
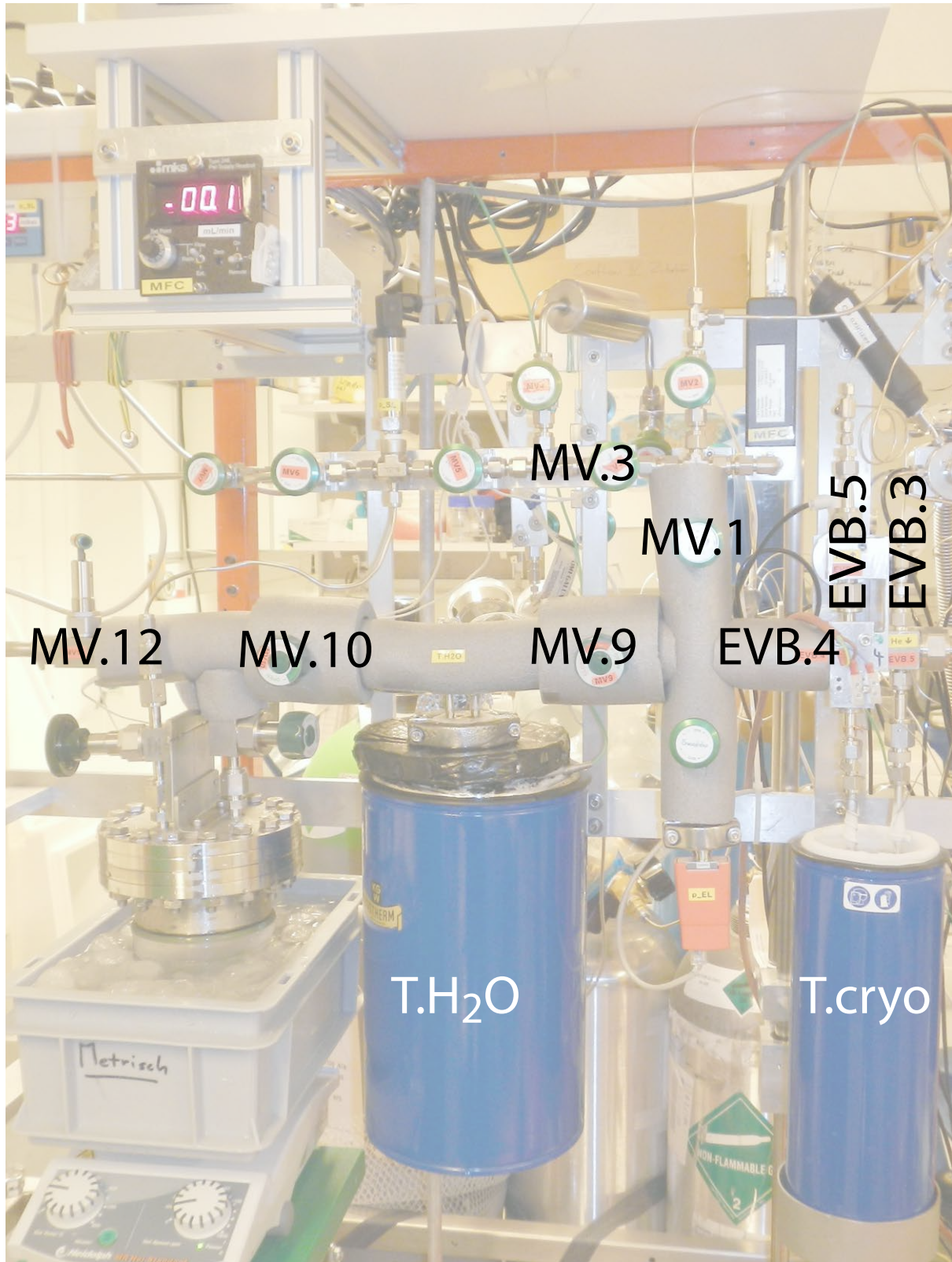
This page intentionally left blank.

Chapter 3

Analytical methods

This chapter deals with the methods used for analysing the isotope signatures of ice cores, which starts with the procedure of preparing ice cores to analyse them (Section 3.2), continues with a presentation of the composition of used gas standards (Section 3.3), and gives a description of every part of the measurement setup (Section 3.4) as well as the full measurement procedure over a day (Section 3.5). In the end a description of a setup to produce bubble free ice is given (Section 3.6).

3.1   Introduction

The setup and procedure used in this study was developed by Sperlich (2013) [119]. Other systems to measure carbon isotopes of methane from ice cores are summarised in Tab. 3.1. With advancing technology, the required ice sample masses have decreased a lot. Various methods have been developed to liberate gas from ice. One being a dry extraction, where the ice is crushed in a vacuum, and another being a wet extraction, where the ice is melted before the released air is trapped, two variations thereof are the melt-purge system, where He gas is bubbled though the melt-water, and the melt-refreeze system, where the melt-water is refrozen again. After the gas extraction, all gases except methane need be removed, the methane is combusted and later as CO_2 injected into the MS.

Table 3.1: Overview over δ^{13}C-CH$_4$ measurement systems reported in literature.

Author	Year		m_{ice}	n_{CH_4}	Precision	Extraction	Analysis[a]
Craig	1988	[120]	25 kg	<120 μmol	0.7‰	melt	C
Sowers	2005	[121]	1–1.5 kg	N/A	0.3‰	melt-refreeze	f-GC-C
Bernard	2005	[121]	1–1.5 kg	N/A	0.3‰	melt-refreeze	f-C-n-GC
Ferretti	2005	[67, 25]	700 g	0.8 nmol	0.08‰	dry	GC-f-C
Schaefer	2007	[122]	100–250 g	0.345 nmol	0.3‰	melt-purge	f-GC-C-n-GC
Behrens	2008	[123]	200 g	0.57 nmol	0.1‰	melt-purge	f-GC-C-n
Sapart	2011	[124]	600 g	<1.1 nmol	0.12‰	dry	f-C-n
Melton	2011	[125]	30–150 g	0.165 nmol	<0.3‰	melt-purge	GC-C-n-f-GC
Sperlich	2013	[119]	200–500 g	<1 nmol	0.1‰	melt	f-GC-C-n-f-GC

3.2   Ice sample preparation

When starting with a sample bag containing parts of an ice core, the core quality was assessed before proceeding with further treatment to decide whether the sample could be used as such, or if the mass was too high or low, so that it could be split into two samples or combined with an adjacent core, if available. After this initial assessment, the cutting took place on a work bench with band saw in a room at $-15°$C. The steps are described in chronological order below.

3.2.1   Ice Cutting

First, the core from the sample bag needs to be cleaned and be cut into pieces that fit into the sample vessel. For doing so, 1–3 mm of each side were removed as they may possibly be contaminated (details, cf. *infra)*, then the cores were cut into pieces of about 10–15 cm length. After cutting a piece, it was cleaned with a synthetic bristle brush[b] and a scalpel. Several scalpel blade shapes have been tested and are discussed later, in Section 3.2.3.

The origin of contamination in the outermost millimetres of a core can be found in drill liquid and post coring processes. A visible contamination was red marker colour used for tagging the cores. The handling of both deep cores (drilled with drill liquid) and shallow cores (drilled without drill liquid) required special attention when sawing them into pieces. For deep cores, it was avoided to touch the "round edge" that was in contact with the drill liquid. Therefore, and in order to prevent the spread of contamination during the handling, this was the first side to be cut on the band saw.

Shallow cores, on the other hand, can be full of cracks that originate from the drill process, when the drill torque was acting on the ice without drill liquid. In this case, it was considered useful to remove these cracks, which was quite laborious: the pieces were generally quite small and sometimes the cracks consisted of skew (neither vertically nor horizontally straight) surfaces, which made it difficult to guide them through the saw blade. In most cases it was easier to hold small ice pieces with two hands, 3 fingers each, to guide the crack through the saw blade instead of sliding it over the metallic bench surface. After sawing, the pieces were cleaned with scalpel and brush and their surface was checked for residual gas bubbles from the crack that had not been cut away.

After the core of the first sample was cut and cleaned, these pieces were placed in one of the pots, which was fetched from the cold freezer room ($-25°$C). A gasket was then laid in between the flanges before moving the pot back to the cold freezer room without closing it by bolts. The table was cleaned to prepare for the cutting of the core of the second sample, which later was put into the pot, equipped with a gasket, covered with the lid and also moved to the cold freezer room. The first sample was then brought back to the warmer freezer, where it was closed with bolts, before the second pot was closed as well. This procedure of closing the bolts of both pots in the end, reduced risks of contamination originating from the somewhat greasy bolts, so that the lab gloves did not need to be replaced after preparing the first sample.

Most of the gaskets were only used once, since it has proven to be difficult to take the flanges apart, when gaskets were reused, and on the other hand, reusing gaskets would also introduce another possible source of contamination and thus uncertainty about contamination. The pots were closed with a torque wrench, as described in Section 3.2.2.

---

[a] Components used in the analysis systems after the N_2,O_2 separation (Preconcentration) prior to the IRMS are shown. These are: combustion (C), gas chromatography (GC), cryofocus (f) and Nafion (n).
[b] Synthetic bristle brushes were available for 20 DKK at the MALING.DK shop on Nørrebrogade.

After closing both vessels, they were placed in the same styrofoam ice core box that was used to bring the pots to the freezer and that had been in the cold freezer ($-25°$C) during sample preparation, which avoided heating up the sample during transport back to the laboratory in the other building. To dampen shocks that could lead to ice cracking or, as reported by Sperlich (2012) [126], lead to fractures in the stir bar, the vessels were fitted into openings cut in the top of a cardboard box so that the glass vessels were suspended inside the cardboard box without touching anything else than the suspension. In the laboratory, the vessels were immediately put into a small chest freezer at $-20°$C.

To minimize contamination possibilities during handling, all samples were handled as much as possible strictly in the same manner.

3.2.2 Flange closing

The flange was then closed with bolts and nuts, each of the two separated from the flanges by a washer. For locking the vessel, the bolts were first tightened by hand, and then fastened three times with a torque wrench; first with a 15 Nm torque, followed twice with a 25 Nm torque. This fastening was not carried out one bolt after the other in turn, but following a special order, such as to achieve the most equilibrated fastening (cf. Fig. 3.1).
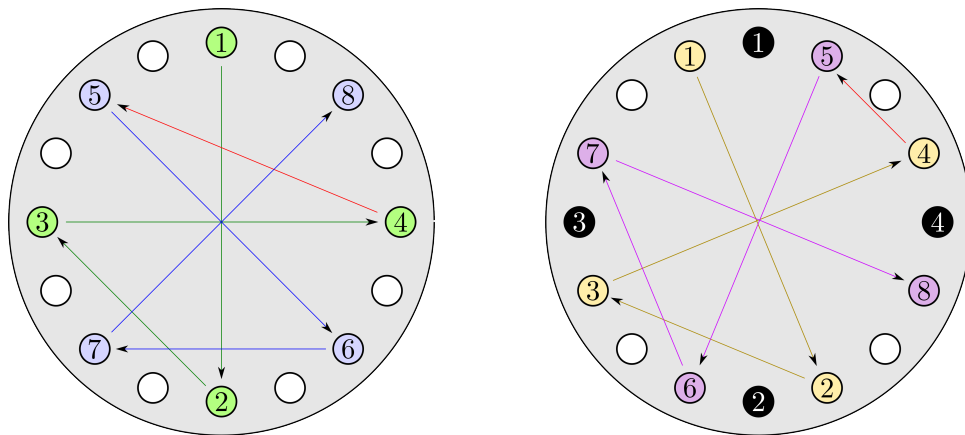
Figure 3.1: The order of closing the bolts: first left 1–8, then right 1–8.

Bolts 1 to 4 had been marked with a marker to provide good orientation: they are marked in green on the left figure, and in black on the right figure.

3.2.3 Blade shapes

Since at one point, new scalpels had to be ordered, some new shapes were tested out: blade shape No. 24 proved to be best suited to our needs, since it allows for being inclined to a very flat angle with respect to the ice. Alternatively, the use of No. 23 can also be recommended, though the blade is a little bit smaller compared to No. 24. But then, No. 11 proved to be of no use, since the straight blade is too small, which gives rise to too steep an angle of attack (the blade cannot be inclined enough, due to the plastic pieces of the handle). Furthermore, the wide, straight blade results in huge friction. The blades are shown in Fig. 3.2.

| No. 24, excellent. | No. 23, good. | No. 11, difficult. |

Figure 3.2: Scalpel blade shapes used (or tested) for ice cutting.

3.3 Gas standards

Several gas standards were used for carrying out the measurements. While some had been produced in-house, others had been bought readily prepared. Specifications and compositions are listed in Table 3.2.

3.4 System configuration

A schematic diagram of the system used for the measurement of the carbon isotopic signature of CH_4 from ice cores is presented in Figs. 3.3 and 3.4. The system consists of several trapping steps, including a cryotrap, a condensible gas trap 3.4.5, two cryofocus traps as well as two GC columns encompassing a combustion oven before the IRMS, which is usually abbreviated with "GC-C-GC-IRMS". A more complete diagram including all unused parts and helium lines is shown in Appendix A.4.

3.4.1 Melt vessel

The previously cut (cf. Section 3.2) ice sample is contained in a $1.25\,L$ melt vessel that is mounted onto the extraction setup with 1/4" VCR fittings. There are two vessels of equal size. In order of not mixing up the flanges and lids, and also to keep track of which ice core was loaded into which vessel, there were two glass stir bars of different lengths, and also two caps of different size to close and protect the connection tube. To track the cores, the long bar and cap and the shorter ones were always paired.

At the end of each day, the vessels were thoroughly washed with ultrapure milliQ-water and Alconox ™Powdered Precision Cleaner No. 1104 (Alconox, White Plains, NY), such as recommended by Mitchell (2011) [133]. After this step, the cleaned stir bars were immediately put back into the vessels, and the lids were put upside down into two glass vessels, so that all of them could be heated over night in a heater at 100°C.

During extraction, the ice core was melted inside the extraction vessel, liberating the relict air bubbles. How this was done is described in Section 3.5.

These footnotes are referred to in Table 3.2.

[c] Measured by Jenk (2012) [128] on dual inlet with ^{17}O correction of Craig (1957) [129].

[d] Measured by Stowasser (2012) [130].

[e] Measured by Sperlich (2012)[131].

[f] CH_4 removed prior to mixing by Sperlich (2012)[131].

[g] No measured value supplied by AirLiquide, but a nominal value is given too for all components (i.e. $x_{CO} = 100\,ppb$).

[h] Written on the same bottle: (-50.28 ± 0.07)‰, together with $x_{CH_4} = 687\,ppb$, from "CH_4 intercalibration"

[i] Value on flask "THC (as CH_4) $\leq 0.01\,ppm$"

[j] Value on flask, "from intercalibration"

Table 3.2: Overview over used gases: Name, Supplier, and Composition. Source of data, if not otherwise stated: supplier data sheet on the flask. Footnotes on page 48.

Gasname [Cyl. no.]	Supplier	Composition (by volume)		$\delta\,^{13}C \times 10^3$
He "Alphagas 1" (carrier, flush)	AirLiquide, Denmark	He H_2O O_2 C_nH_m	$\geq 99.999\,\%$ $\leq 3\,ppm$ $\leq 2\,ppm$ $\leq 0.5\,ppm$	
O_2 "Alphagas 1" (combustion) [266376]	AirLiquide, Denmark	O_2 H_2O C_nH_m	$\geq 99.998\,\%$ $\leq 3\,ppm$ $\leq 0.5\,ppm$	
CO_2 N48 [127] (working standard) [40339]	AirLiquide, Denmark	CO_2 H_2O O_2 C_nH_m N_2 CO	$\geq 99.998\,\%$ $\leq 3\,ppm$ $\leq 2\,ppm$ $\leq 1\,ppm$ $\leq 6\,ppm$ $\leq 1\,ppm$	-35.410 ± 0.012[c]
GIS (calibration) [CB08909]	Sperlich (2012)[e] Mixed *ibid.*	 "Synthetisk Luft" CH_4	 Balance 431 ppb[d]	 -42.21 ± 0.04[e]
"Synthetisk Luft" LAB LINE 5.0	Strandmøllen, Denmark	N_2 O_2 C_nH_m H_2O CO_2 CO	$79.1\,\%$ $20.9\,\%$ $\leq 3\,ppm$[f] $\leq 3\,ppm$ $\leq 1\,ppm$ $\leq 1\,ppm$	
CH_4 N45 [132] [224715]	AirLiquide, Denmark	CH_4 (*cf. infra*)	$\geq 99.995\,\%$	-56.37 ± 0.04[e]
Biogenic CH_4 [55742]	Biogas plant, Northern Germany	CH_4 Undetermined composition		-39.56 ± 0.04[e]
AL (quality control) [4633A] (measured composition)	AirLiquide Denmark	N_2 N40 O_2 N45 Ar N50 CO N18 CO_2 N45 CH_4 N25 N_2O N25	Balance $20.97\,\%$ $0.9698\,\%$ $\approx 100\,ppb$[g] $277.2\,ppm$ $686.7\,ppb$ $273.9\,ppb$	 -49.44[h]
NEEM (additional) [CA08271]	Scott-Marrin Inc., Riverside, CA, USA	Air CH_4 CO NO_x SO_2	Balance 1840 ppb[i] $\leq 0.01\,ppm$ $\leq 0.001\,ppm$ $\leq 0.001\,ppm$	-47.31 ± 0.05[j]
CH_4 N45 [132] (additional) [224715]	AirLiquide, Denmark	CH_4 N_2 O_2 H_2O CO_2 other C_nH_m	$\geq 99.995\,\%$ $\leq 15\,ppm$ $\leq 5\,ppm$ $\leq 5\,ppm$ $\leq 1\,ppm$ $\leq 20\,ppm$	-39.56 ± 0.04[e]

Figure 3.3: Ice extraction part of setup, continued to the right in Fig. 3.4.
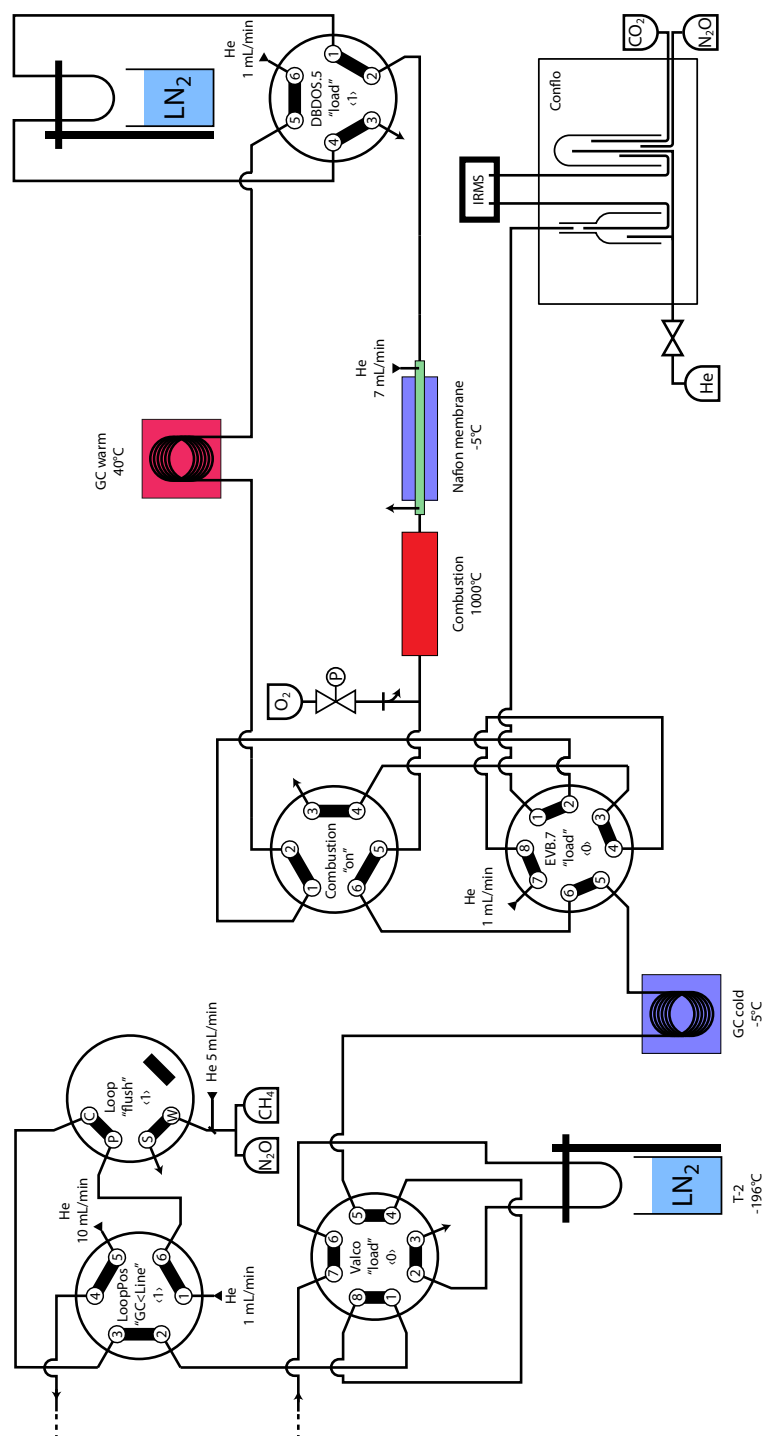
Figure 3.4: Analytical part of setup (GC-C-GC-IRMS). Abbreviations explained in Tab. **??**.

3.4.2 Water trap

A recipient (stainless steel, 45 mm OD, 20 cm heigh) filled with glass beads (diameter $d = 2$ mm) was first cooled in a dewar filled with dry ice-cooled ethanol for at least two hours (during the sample preparation), and is used to freeze out water vapour originating from the sample pot during melt-extraction. Higher levels of dry ice result in a lower trap temperature, since the density of ethanol decreases monotonically with temperature, unlike water, and hence warm ethanol rises to the surface, leading to thermal stratification. The increased viscosity at low temperatures further inhibits mixing, which results in a thermal gradient along the trap if the dewar is not filled with dry ice blocks to the top, cf. Fig. 3.5.
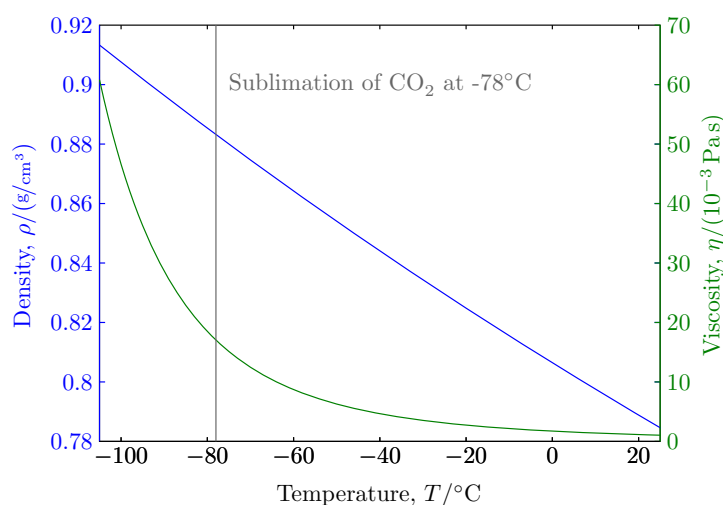
Figure 3.5: Density and viscosity of Ethanol as a function of temperature.

However, even after the water trap some water still remains in the extraction stream, since the freeze-out occurs at around $-78°$C, at which temperature the saturation vapour pressure of water vapour over ice e_i is 9.86 Pa (0.0986 mbar) using the formula[k] of Murphy and Koop (2005) [134].

3.4.3 Cryotrap

The cryotrap has to quantitatively collect all gas extracted from the melt vessel (ice core samples) or from the water trap (standard gas injections), and it is also the starting point of the gas chromatography and combustion part of the setup (GC-C-GC). It consists of a recipient filled with 1.5 g of "HayeSep® D 60/80" (from Supelco, Bellefonte, PA, USA) [119], which makes it adsorb gases when cooled, and desorb them when heated up again. The trap was cooled in liquid nitrogen for more than eight minutes, before the inlet valve is opened to adsorb the gas to be analysed. The adsorption proceeded until a pressure of 0.11 mbar was reached in the extraction line. After which it was heated up with a heating wire to 50°C. At this point, three helium pulses further encouraged the gas to desorb again.

---

k $\log(e_i) = \{9.550426 - 5723.265/T + 3.53068 \cdot \log(T) - 0.00728332T\}$ Pa, as from Murphy and Koop (2005) [134].

3.4.4   CO oxidation column

After being released from the cryotrap, the gases flow through a CO oxidation column. This is necessary, since carbon monoxide, CO, elutes about simultaneously with methane form the GC column (cf. *infra*), which makes the two hard to separate using this technique (GC columns). Therefore, CO has to be oxidised earlier to avoid interference from oxidised CO with the combusted CH_4 to be analysed.

The CO oxidation column working with "Gold 1% on titanium dioxide extrudates (AUROlite™ Au/TiO$_2$)" (by Strem Chemicals, Newburyport, MA, USA), heated to 60°C, is a creation of Sperlich (2013) [119]. It is insensitive to moisture, which allows for quantitative conversion even in the presence of water vapour, as it is the case in ice extraction systems like this. Other laboratories use Schütze reagent and moisture sensitive Sofnocat and Hopcalite.

Using this technique draws the oxygen required for oxidation from O_2 and N_2O [135].

$$CO + N_2O \longrightarrow CO_2 + N_2 \tag{3.1}$$

$$CO + \frac{1}{2}O_2 \longrightarrow CO_2 \tag{3.2}$$

Hence one could think that the use of this catalyst is not suitable, if the isotopic composition of N_2O is to be analysed. However, considering the mechanisms explained below, the fractionation incurred from the reaction with N_2O is in fact negligible.

While N_2O does not dissociate on gold crystallites (average size $\sim 2-3\,nm$) in the absence of a reducing agent (such as CO) [136], it reacts in its presence with kinetics following the Langmuir–Hinshelwood relationship [135]. Oxidation with O_2 and N_2O proceed on a different pathway involving different adsorption sites, however apparent oxidation barriers are the same according to Walther (2008) [135]. Hence it can be assumed that their respective consumption for the oxidation of CO is proportional to their initial mixing ratios, which are assumed as $x_{N_2O} = 274 \cdot 10^{-9}$, $x_{O_2} = 210 \cdot 10^{-3}$, with $x_{CO} = 100 \cdot 10^{-9}$.

It can be calculated that only very little N_2O reacts,

$$x_{N_2O,react} = x_{CO} \frac{x_{N_2O}}{x_{O_2} + x_{N_2O}} = 130 \cdot 10^{-15}. \tag{3.3}$$

Even if one assumes that this reaction would fractionate strongly with, say, $\varepsilon = -0.060$, the apparent change would still only be a negligible amount of about

$$\frac{x_{N_2O,react}}{x_{N_2O}} \cdot \varepsilon = -28.6 \cdot 10^{-9} = -28.6 \cdot 10^{-6}‰. \tag{3.4}$$

. This catalyst also catalyses methane oxidation at low temperatures, but since this reaction does not take place below 130°C [137], Methane measurements are left unaffected. Hence, the use of this catalyst is well suited to use with this setup. This has also been tested by Sperlich (2013), who confirms quantitative conversion to take place as required.

3.4.5   Condensible Gas Trap (CGT)

After the CO being oxidised to CO_2, the gases are trapped in a Condensible Gas Trap (CGT), whose temperature can be varied, since it consists of a U-shaped 1/8" tube filled with Hayesep D, around which a heating wire is wound. The U-tube itself passes through a recipient that can be filled with (impure) Helium or be evacuated. The recipient again is submerged into liquid nitrogen (hereafter: LN$_2$) at

$-196°C$. The combination of the heating wire and the absence or presence of Helium as convective heat transfer medium allows for a dynamic temperature setting, as the heating wire is controlled with a PID.

The temperature can either be set manually with a switch on the hardware interface or in the *Isodat* software that controls the mass spectrometer (MS). From *Isodat*, the temperature can be set to the fixed set point 2 ("S2") or to the variable set point 1, whose value can be changed by a script[1].

First the CGT was cooled to for 4:40 min at $-154°C$, during which time O_2 and N_2 passed through the TCD (cf. nest section), while condensible gases, namely CO_2, CH_4, N_2O and also Kr were retained. The temperature of the trap was then increased to $-128°C$, to sweep up residual air constituents, similar to what was reported by Umezawa (2009) [138], although they reported the optimum low temperature of a similar trap in their system to be $T \leq -130°C$, at which temperature they observed quantitative CH_4 adsorption, whereas they reported lower MS peak heights with higher $\delta^{13}C$ values at $-120°C$. They included a second temperature at $-83°C$.

After the separation completed in 400 seconds, the temperature was risen in steps, first to $-20.7°C$ and then to $33.1°C$, which released the gases and transported them in a He flow of 10 mL/min through the chemical trap (next section) into the capillary trap, "cryofocus" which was submerged in LN_2 10 seconds before.

3.4.6 Thermal Conductivity Detector (TCD)

At the same time as the condensible gases were retained on Hayesep D in the CGT, N_2 and O_2 passed over them and were blown out through the TCD, a Micro-Volume Thermal Conductivity Detector (VICI, Valco Instruments Co. Inc.) that measures the amount of current required to maintain a filament at a constant temperature as gases of varying thermal conductivities pass it. Changes in conductivity are measured only by the change in current required to keep the filament at a constant temperature [139]. The change in current was recorded by the aid of a LabView application and saved to a file, the evaluation of which is presented in Section 4.9.

3.4.7 Chemical trap for water and CO_2

The gases that are transported from the CGT to the first cryofocus, pass through a chemical trap that consists of a glass column (6.2 mm outer diameter (OD), 4 mm inner diameter (ID) and 495 mm length) filled with CO_2 consuming sodium hydroxide on support, encompassed by a layer of water absorbing magnesiumperchlorate hydrate on both sides.

The first layer of Magnesiumperchlorate Hydrate (Anhydron Hydrate, $Mg(ClO_4)_2$, VWR 1.05873.0500) reacts with the remaining water vapour that was not frozen out in the thermal water trap.

The hydration reaction of magnesium perchlorate and its water vapour equilibria are given as [140]:

$$Mg(ClO_4)_2 + 6\,H_2O \rightleftharpoons Mg(ClO_4)_2 \cdot 6H_2O. \tag{3.5}$$

---

[1]

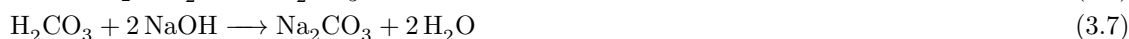For switching between S1 and S2, valve EVB.8 is used. The temperature setting function is

```
_SetCalc("TrapTemp/CalculatingDac 1", -10);
```

where the temperature value is not really accurate and has to be adjusted iteratively, until the read out shows the desired set point value (e.g. -10 corresponds to $-20.7°C$). NB: this relationship has a considerable drift over time, it is good to check the values during the extractions.

Anhydrous magnesium perchlorate was first described as a drying agent in 1922 by Willard and Smith, after extensive testing, also against its tri hydrate version [141].

The CO_2 trapping layer consisting of sodium hydroxide, is encompassed by two layers of the afore described water trap. The substance used is not, as usually referred to, as "Ascarite II", which is a registered trademark by Thomas Scientific (Swedesboro, NJ), but "Sodium hydroxide on support", produced by Merck KGaA (Art. Nr: 1.01567.0250).

$$CO_2 + H_2O \longrightarrow H_2CO_3 \tag{3.6}$$

$$\underline{H_2CO_3 + 2\,NaOH \longrightarrow Na_2CO_3 + 2\,H_2O} \tag{3.7}$$

$$CO_2 + 2\,NaOH \longrightarrow Na_2CO_3 + H_2O \tag{3.8}$$

3.4.8 Pre-combustion cryofocus

Since not all CH_4, N_2O (and Kr) take the same amount of time to be released from the CGT and to be purified in the chemical trap, the gases have to be collected and focussed before releasing them into the cold GC column, where the transit time through the GC column will be critical to separate the gases. Hence it is of utmost importance to release them focussed into this column.

The first cryofocus consists of a 55 cm section of GC column (CP-Pora-Bond Q, 0.25 mm ID, 3 μm film thickness, Varian #CP7348) that can be submerged into LN_2.

3.4.9 Cold GC column

The cold gas chromatography (GC) column consists of 25 m GC column cooled in ethanol to $-5°C$ (CP-Pora-Bond Q, 0.25 mm ID, 3 μm film thickness, Varian #CP7348). And serves the purpose of separating N_2O from CH_4. The N_2O is injected into the mass spectrometer as is, which was, however, not part of this study, while methane needs to be combusted first.

3.4.10 Combustion oven

In the combustion oven, methane is combusted at $1000°C$ with an additional oxygen (cf. Tab. 3.2) bleed-in:

$$CH_4 + 2\,O_2 \longrightarrow CO_2 + 2\,H_2O. \tag{3.9}$$

It is assumed that the relationship between three oxygen isotopes, characterised by the "exponent" λ (cf. Section 4.1) remains the same through all mass-dependent processes taking place on Earth and is the same as in natural O_2. This has its practical relevance in the combustion of CH_4 to CO_2: the isotopic composition of the bleed-in oxygen is unknown, but the resulting oxygen signature of CO_2 from combusted methane is assumed to be similar to that of natural CO_2. This makes sense, since the combustion of CH_4 to CO_2 involves mass depended fractionation. However, as reported by Kaiser (2008) [142], the exponent λ can take values between 0.501 and 0.5303 for certain types of reactions. Nevertheless, even if the assumed factor would not be totally accurate, the resulting error would be similar for calibration standards and samples. The effect of this assumption are discussed in Section 4.1.

The combustion oven is equipped with 8 wires (3 Ni (99.994%), 3 Cu (99.9999%) and 2 Pt (99.997%), similar to what has been reported by Fischer (2008) [9], and also by Behrens (2008) [123], who used CuO,

NiO and Pt wires and re-oxidise the wires weekly. This last step differs from what is done in this setup, where a oxygen bleed provides new oxygen constantly to the combustion oven, which probably prevents eventual oxygen fractionation resulting from the metal oxides that would influence the molecular mass of the CO_2.

3.4.11 Post-combustion gas drying (Nafion)

Since the post combustion gas consists of a large fraction of water, this needs to be removed before injecting it into the mass spectrometer to avoid interferences. Therefore, the gases pass through a "Nafion" membrane, which is highly permeable to water. During this process, the post combustion gases (i.e. CO_2) get dried [143]. To increase the efficiency of the drying process, a counter current Helium flow of $7\,\mathrm{mL/min}$ is installed, while the Membrane is hold at $-5°C$ in a constantly cooled ethanol bath.

3.4.12 Post-combustion cryofocus

The combusted gases cannot not yet be injected into the mass spectrometer right after they have been dried though by passing through the Nafion membrane. First, the δ^{15}N-N_2O and δ^{18}O-N_2O measurements on the MS need to finish, and this is why the CO_2 from CH_4 gets trapped in a post-combustion cryofocus trap.
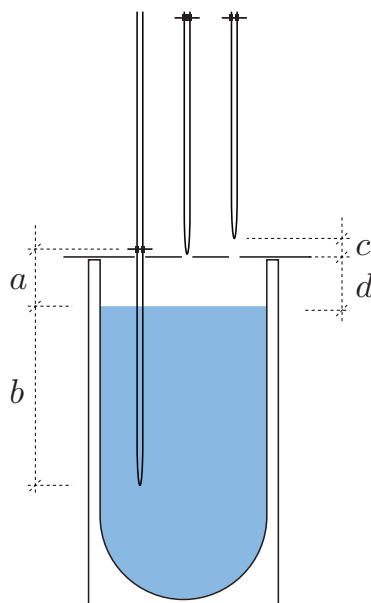
Figure 3.6: LN$_2$ dewar at cryofocus trap. Left: cooling position, middle: earlier upper position, right: later upper position.

This second cryofocus trap was built with a $55\,\mathrm{cm}$ long, $250\,\mathrm{\mu m}$ O.D. capillary. The initial setup, as described by Sperlich (2013) [119] included a $0.1\,\mathrm{mm}$ Nickel wire (Puratonic|r, 99.994%, metal basis) introduced into the capillary to increase trapping efficiency, similar to what was reported by Behrens (2008) [123] and Brand (1995) [144], who included a Ni wire for easing adsorption and providing a higher surface area in order to achieve quantitative trapping. During a test, we observed the trapping efficiency

(MS peak area) to be dependent on the fill height (expressed in terms of available head space, d) of the LN_2 dewar into which it is submerged. There are two distances (cf. Fig. 3.6) that were identified to play a role, these are,

1. the length of the capillary being submerged into LN_2 ($\approx 2d$, actually: $l_{cap} - 2a$),

2. the distance between the LN_2, or the cool headspace and the bottom of the capillary (b, c).

The first has an effect on how much CH_4/CO_2 resublimates on to the inner walls of the capillary. And the second determines how fast the gas elutes from the trap.

We noticed a highly non-linear behaviour at too low distances in the over head space of the dewar, d in Fig. 3.6. This makes sense, since distance c was initially very small, and therefore cold N_2 vapour was still able to cool the capillary even though it was no longer submerged.

In order to prevent this effect from affecting the measurement results, a constant head space height of $7.5 - 8\,\mathrm{cm}$ was maintained by refilling the dewar always at the same time for each run, while the fill height was controlled with a PID.

3.4.13 Warm GC column

The temperature of the warm GC column (CP-Pora-Bond Q, 25 m, 0.25 mm ID, 3 µm film thickness, Varian #CP7348) determines the retention time of the gases. It is hold at a constant temperature of 40°C. The inverse isotope effect (cf. Sec. 2.4.2) in GC columns [145], where the heavier $^{13}CH_4$ moiety elutes faster than its carbon-12 counterpart, is absent in this case, as it can easily be seen in the mass spectrograms, Fig. 3.7: ions with mass-to-charge ratio 45 (red) peak before the 46 ratio counterparts (green).
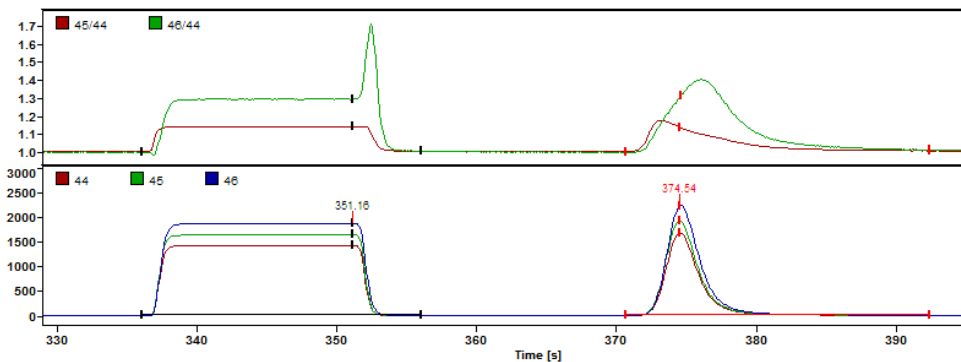
Figure 3.7: Instantaneous ratio (top) and intensity in mV (bottom) of mass-to-charge ratios: working standard peak (left) and sample peak (right).

Sperlich (2013) successfully tested the system against a possible Krypton interference ($x_{Kr} \sim 1 \cdot 10^{-6}$ [146]) that can result from double ionised $^{86}Kr^{2+}$ with $m/z = 43$. Schmitt (2013) [147] reported interferences with CO_2 from combusted CH_4 that could influence the neighbouring cups of $m/z = 44, 45, 46$ if it would not be separated in the GC columns.

3.4.14 Open split

Before the mass spectrometer, there is an open split setup that runs in *continuous flow* ("Conflo"). Helium is continuously streamed out and transports either gas from the GC-C-GC side or reference gas into the ion ratio mass spectrometer (IRMS). The setup is shown in Fig. 3.8. It has been setup by Sperlich (2013) [119], who also noticed that this part of the setup is very sensitive to temperature variations, consequently, it is in a styrofoam box.
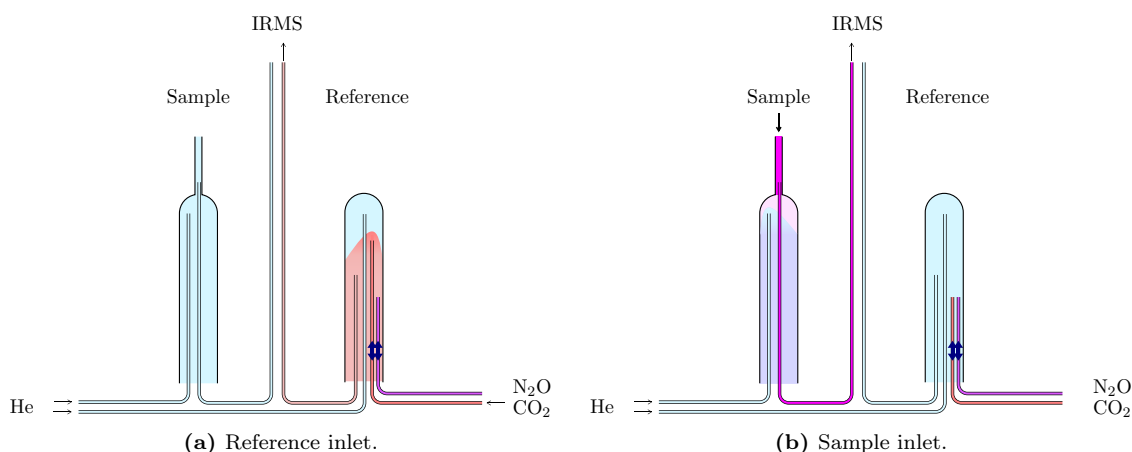
Figure 3.8: Open split with sample and reference side, shown in the two different configurations.

The sample side shows an open tube, where the sample is being quantitatively and undiluted injected, while as on the reference side CO_2 (and N_2O) gets diluted before injection into the isotope ratio mass spectrometer (IRMS). The CO_2 and N_2O inlet capillaries are moves up and down to inject or bypass injection. The tubes are hanging downwards, such as to prevent impurities from falling into them.

3.4.15 Mass spectrometer

The mass spectrometer measures 10 CO_2 reference peaks with the CO_2 working standard prior to the sample measurement, of which the second last, no. 9, serves as reference peak, that is, the measured sample charges ("areas"), for $m/z = 44$, 45 and 46 are multiplied by factors, such as to match the calculated $\delta^{13}C$ signature with the known standard signature, $\delta^{13}C_{CO_2} = -35.771‰$.

3.4.16 Helium source

A cylinder of grade 5 helium (purity 99.999%) is used. It is further purified with additional purifiers, both produced by "Valco Instruments Co. Inc." Vici, Schenkon, Switzerland:

- HP2, where the purification substrate is a non-evaporable gettering alloy,
- P100-1, (Agilent part # 5182-3467), where a multiple bed column is used.

3.4.17 Pressure sensors

Two pressure sensors are installed in the setup. One being on the "extraction line", the other one being on the "standard line", cf. Fig. 3.3.

Extraction line

The model APG100-LC from Edwards used here, comes with a table of pressure as a function of voltage. a cubic spline has been created to follow this dataset. For doing so the data was first logarithmised and then processed in MATLABwith the `spline` function. Such as to use it in LabView. However, since LabView does not offer the possibility of executing scripts the code needs to be translated into the graphical LabView language. The found parameters are given in Appendix **??**.

Standard line

The pressure sensor on the standard line is a linearly reading analogue gauge (PAA-21S, Edwards, edwardsvacuum.com) branched to a display ("SPE 670–030", Schwille). The sensing of the pressure drifts over time. But it can easily be re-adjusted as described in the user manual.

3.5 Measurement procedure

The carried out procedure was the same as the one later described by Sperlich (2013) [119]. In the appendices some practical advice and hints for future similar studies are given, Appendix A.5.

3.5.1 Sequence

Gas samples

Every standard gas extraction started with flushing of the cryopump (T.cryo) with Helium for 5 minutes, followed by an evacuation of 5 minutes, after which the cryopump was submerged into LN$_2$ for 9 minutes. During the first 5 of these 9 minutes, the cryopump was barely cooled, followed by 3 minutes of cooling during which the MFC was flushed such as to get fresh well mixed standard gas and eliminate eventual contaminating residues in the subsequently injected gas into the water trap that followed the flushing in the last one of the 9 cooling minutes. The injection was timed and carried out manually. With a mass flow rate of 60 cm^3/s, the introduced volume in mL was equal to the number of seconds injected. The gas was then extracted onto the cryopump by opening the valve in *Isodat*. The extraction proceeded for 11 minutes after which a pressure of about $p = 0.11$ mbar was reached in the extraction line, at which point the GC-C-GC-IRMS sequence was launched in *Isodat*.

Ice samples

For ice sample the procedure was very similar, but began much earlier, when the pot was mounted already earlier and evacuated for 20 to 35 minutes, while the vessel was standing in an ice-water bath. This bath in turn was prepared even earlier, to allow for a thorough mixture and an equilibrated temperature. During this evacuation of the sample, the outer most layer of ice crystals sublimated. The cryopump

was cooled for 8 minutes, after which the sample was melted using a *bain-marie* technique, that is, the vessel was heated from all sides though submersion into warm water at 60°C. In order of having water at the right temperature, it needed to be prepared a little bit earlier. At the start of the melting process, the temperature of the water was verified again and written into the lab journal.

Already during the melt process, the gas was extracted constantly onto the cryopump such as to reduce the contact time of water and gas. Quite unlike what was reported by Behrens (2008) [123] or Mischler (2009) [71]. The melt process having completed, the pan was immediately removed and exchanged against a water bath, as soon as the last ice bits had melted (cf. Appendix A.5 for hints on how to do it). The stirrer was launched at 750 rpm for the long stir bar and 1000 rpm for the short one. When melting cores of shallow depth, where the gas had not yet undergone clathrate formation, so called "bubbly ice", the stirring has no visible effect on the pressure evolution, while for ice from greater depths (such as measured by Sperlich (2013)), the pressure increased again for a few seconds after the beginning of stirring. Once the pressure reached $p = 0.11$ mbar, the GC-C-GC-IRMS sequence was launched in *Isodat*.

The time needed for an extraction cycle to complete on the extraction part of the setup was 41 minutes, after which the sample was entering the analysis section of the setup (GC-C-GC-IRMS), while the extraction section was already preparing for the next sample.

At the end of an extraction day, the melt vessel is cleaned (cf. Section 3.4.1), the water from the water trap is transferred to another water trap and both GC columns are heated out at 80°C until the next measurement day, to avoid the deposition of water or drill liquid. The water trap is dried by heating it up to 150°C while pressurised at 1500 mbar. The temperature is reached after 5 minutes, and after another 5 minutes, it is then evacuated, though which action the water gets transferred into another water trap. By doing so, the analytical water trap does never have to be opened, which prevents contamination.

Standard gas injections

Standards were measured daily for calibration and quality control purpose. In order to follow the principle of identical treatment ("IT principle") [83], these full air standards were also extracted onto the cryotrap. However, the injection did not take place into the extraction vessel, but into the water trap. Eventual errors resulting from this not-identical treatment were corrected for in the size correction, Section 4.2. A standard volume of 40 mL was injected and measured for all standard measurements in the daily routine as discussed in the next section.

3.5.2 Daily measurement routine

While samples and standard gases are measured according to the procedure discussed in the previous section, there is also a clear routine including calibration standards and blank measurements. Before and after measuring samples, three standard injections of 40 mL (GIS) are measured for the daily calibration (cf. Section 4.3). After each sample, the system extracts without having a gas injected or a sample molten, which serves to detect outliers and to verify the systems leak-tightness and extraction efficiency. In between the samples, 40 mL of the standard gas (AL) are measured as to control the systems accuracy. This daily routine is summed up in Table 3.3.

Some hints and how to avoid classical pitfalls during the work on the system in the laboratory are given in Appendix A.5.

Table 3.3: Daily routine of measurements.

Gas	Purpose
3× GIS	Calibration
Sample 1	Measurement
Blank 1	Outlier detection
AL	Quality control, accuracy
Sample 2	Measurement
Blank 2	Outlier detection
3× GIS	Calibration

3.6 Bubble free ice

Bubble free ice, used for the calibration of the size correction (cf. Section 4.2) was created on the equipment developed by Buizert (2009) [148] in the freezer at $-15°C$. First, the vessel was filled with milliQ-water, which was then evacuated with a pump to around 10^{-1} bar for 15 minutes with huge out-gassing, before the vessel was heated for a few hours, while pumping continued. During this heating process, the water was stirred with a magnetic bar to accelerate the out-gassing process. Two different bars showed totally stunning results. With the small stir bar, the water surface was totally still even when the stir bar rotated at full speed. This makes the super-heated water (at 30°C) "explode" from time to time, cf. Fig. 3.9, which resulted in plenty of water being sucked out of the vessel towards the pump,
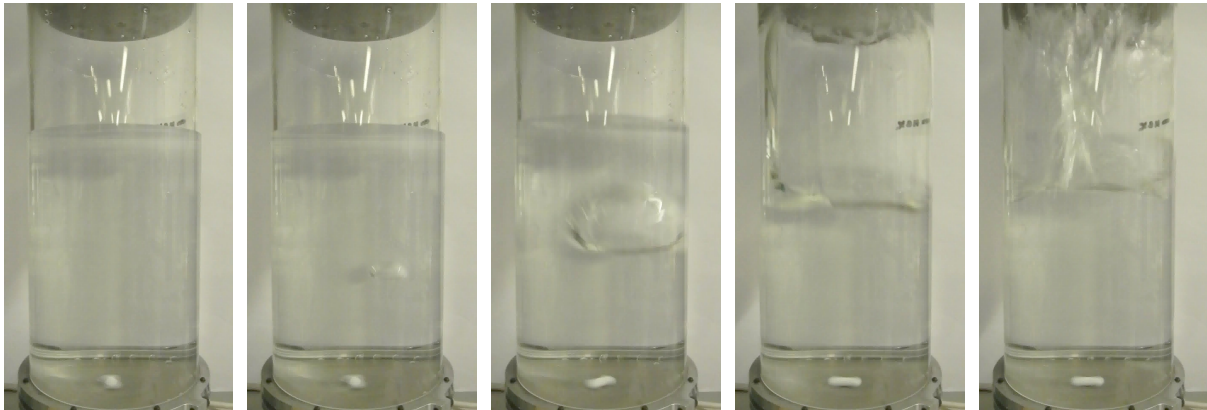
Figure 3.9: BFI vessel getting evacuated while being stirred with small stir bar, showing a superheated water "explosion". The pictures are each 69 ms apart, total duration of sequence 0.55 sec.

and lead to a huge amount of water frozen out in the water trap. So that after 150 minutes evacuation, the trap was covered with ice on all sides. When using the long stir bar, the water featured a nice vortex that effectively prevents super-heating and speeds up the out-gassing process, cf. Fig. 3.10. Even after three hours evacuating, the water trap contains almost no water. After the out-gassing process, the vessel is sealed by closing the valve and brought to the freezer, where it is left over-night, so that it has some time to cool to a temperature somewhere between 0 and 4°C. This is achieved by a heating sleeve being put over the vessel. This sleeve is then very slowly lifted up during the freezing phase, in which the ice freezes from the bottom to the top. This process takes a few days.

Comparing the ice produced using the two different stir bars, there is a remarkable difference in ice quality. With the small stir bar, there were always some residual bubbles in the ice, while the ice was absolutely clear, showing not a single bubble, when the long stir bar was used.

Figure 3.10: BFI vessel getting evacuated while being stirred with long stir bar, showing a small vortex on the surface.

Chapter 4

Data evaluation methods

In this chapter, the evaluation of measured data is explained, specifically, the different offset corrections and some possible sources of errors are discussed. The nomenclature used in this section is presented in Tab. 4.1. And the expression follows Coplen (2011) [84]: i.e. δ values are never multiplied by 1000, since $1\text{‰} := 1 \times 10^{-3}$.

Table 4.1: Nomenclature of measured values.

Symbol	Meaning	Unit
Variables		
δ	Deviation in isotope ratio of ^{13}C (δ^{13}C)	-
	compared to the VPDB standard (if not otherwise specified)	
A	"Area" (voltage peak integrated over time) from IRMS	Vs
$\mathring{\delta}$	Known value (standards), corrected value (samples)	-
$\hat{\delta}, \hat{A}$	Measured values (δ: corrected for δ^{17}O, cf. Section 4.1)	-, Vs
$\Delta\delta$	Offset in δ value	-
Indices		
s	Sample (ice core or standard gas over BFI)	
k,$\{1-6$,m,e$\}$	Calibration standards (GIS gas) (no.$1-6$, morning ($1-3$), evening ($4-6$))	
y	Any gas standard gas of known signature (GIS, AL, NEEM, etc.)	
x	Blank (extraction of the void volume following the sample run)	

Calibrations and corrections have to be carried out due to errors originating from various levels of the extraction and measurement system, and are discussed in the order of the measurement procedure:

1. correction for isotopologues with the same mass to charge ratio but different isotopic composition, known as isobaric interference (δ^{17}O correction) (carried out automatically by the by the software),

2. methane volume size correction,

3. daily calibration with a full air standard undergoing the same procedure as the sample [83],

4. correction for the gravitational enrichment occurring in the firn,

5. correction for the offset of CIC calibrations in comparison with other laboratories.

4.1   Isobaric oxygen interference correction ($\delta^{17}O$)

The software connected to the mass spectrometer, *Isodat 3.0* by *Thermo Fisher Scientific*, evaluates the measured spectrograms. Since there are various gas isotopologues with the same mass possible (isobaric species), the values for the individual abundances have to be calculated by solving a system of equations, using the measured values. The abundances of CO_2 isotopologues in the VPDB standard are shown in Table 4.2.

Table 4.2: Abundance of VPDB-CO_2 isotopologues [142].

Isotopologue	Mass (u)	Abundance (%)	Share of isotopologues with same mass (%)
$^{12}C^{16}O_2$	44	98.4	100.0
$^{13}C^{16}O_2$	45	1.095	93.4
$^{12}C^{17}O^{16}O$	45	0.0770	6.6
$^{12}C^{18}O^{16}O$	46	0.411	99.8
$^{13}C^{17}O^{16}O$	46	0.000856	0.2
$^{12}C^{17}O_2$	46	0.0000151	0.004
$^{13}C^{18}O^{16}O$	47	0.00457	96.6
$^{12}C^{18}O^{17}O$	47	0.0001607	3.4
$^{13}C^{17}O_2$	47	0.0000001674	0.0004
$^{12}C^{18}O_2$	48	0.000429	99.6
$^{13}C^{18}O^{17}O$	48	0.000001788	0.4
$^{13}C^{18}O_2$	49	0.00000477	100.0

From the counter in the IRMS, cf. Fig. 2.17, the abundances of the different masses to charge ratios are known to the *Isodat* software: ^{44}R, ^{45}R and ^{46}R. These values are used to calculate the elemental isotope ratios ^{13}R, ^{17}R and ^{18}R, referring to $^{13}C/^{12}C$, $^{17}O/^{16}O$, $^{18}O/^{16}O$ respectively. Since mass 44 consists only of $^{12}C^{16}O_2$, it involves none of the three R values and will not help solving the system. Hence, the problem translates into solving a system of equations as:

$$^{45}R = {}^{13}R + 2\,{}^{17}R \tag{4.1}$$

$$^{46}R = 2\,{}^{18}R + 2\,{}^{13}R\,{}^{17}R + {}^{17}R^2 \tag{4.2}$$

This system being underdetermined, one more equation is needed to solve for the three unknowns. There are several ways of determining this system: one would be to take one of the additional isotope ratios, ^{47}R, ^{48}R or ^{49}R. This option has, however, little prospects, due to the small intensity tainted with a large relative error. A second option would be to measure the isotopic composition of the used oxygen, similar to what was done for other studies with CO_2, where it was converted to O_2 in order of measuring it directly [149, 150, 142]. But the by far easiest option, and the most commonly used one, is to take advantage of the mass-dependent fractionation of oxygen isotopes, where there is a linear relationship between the enrichment in ^{17}O and ^{18}O, expressed by an empirical parameter λ and a proportionality constant κ (usually designated with A):

$$^{17}R = \kappa\,{}^{18}R^\lambda \tag{4.3}$$

For this mass-dependent fractionation, a value of λ, as well as a value for the proportionality constant κ has been determined by various authors including Kaiser (2008) [142], who provides an excellent review, the values of which are shown in Tab. 4.3. While some authors chose $\lambda = 0.5$ for simplicity, and since

this also corresponds to the theoretical value, since the mass difference between ^{18}O and ^{16}O is twice as large as between ^{17}O and ^{16}O, which results in the theoretical value $\lambda = 0.5$. Many authors have carried out experiments to determine an empirical value of λ. These are shown in Tab. 4.3.

Table 4.3: Published oxygen isotope ratios of VPDB, and the corresponding λ values derived for the ^{17}O correction of mass spectrometric CO_2 isotope measurements. Adapted from Kaiser (2008) [142].

$^{17}R/10^{-6}$	$^{18}R/10^{-6}$	λ	$\kappa/10^{-3}$	Reference	
379.95	2079	0.5	8.333	Craig (1957)	[129]
410.85	(2088.35)	0.516	9.9235	Santrock (1985)	[151]
380.8	2088.35	0.5	8.333	Allison (1995)	[152]
388.02	2088.39	0.52	9.6061	Werner & Brand (2001)	[83]
395.11	2088.35	0.528	10.2768	Assonov & Brenninkmeijer (2003)	[153]
380.58	2088.24	0.528	9.8993	Valkiers (2007)	[154]
391.08	2088.37	0.528	10.172	Kaiser (2008)	[142]

In our measurements, the parameters from "Santrock, Studley and Hayes" (1985) [151], commonly referred to as "SSH", with $\lambda = 0.516$, has been used, similar to what Carter (2011) [155] suggests. He reports that this algorithm is believed to be more mathematically exact and more realistic in its approach, as compared to the values and algorithm of Craig (1957) [129], $\lambda = 0.5$. Verkouteren (2004) [156], on the other hand, is more in favour of applying Craig's $\lambda = 0.5$ for historical constancy reasons, as this value serves for maintaining the inter-comparability of past and future measurement results. Others again use Assonov & Brenninkmeijer's (2003) [153] $\lambda = 0.528$. In past $\delta^{13}C$-CH_4 measurements, different values have been used by different laboratories, cf. Tab. 4.4.

Table 4.4: ^{17}O corrections used in $\delta^{13}C$-CH_4 measurement systems reported in literature, cf. text.

Author	Year		^{17}O correction
Craig	1988	[120]	Craig (N/A)
Sowers	2005	[121]	SSH
Bernard	2005	[121]	SSH
Ferretti	2005	[67, 25]	Craig
Schaefer	2007	[122]	Assonov (no clear mention)
Behrens	2008	[123]	Craig
Sapart	2011	[124]	N/A
Melton	2011	[125]	Assonov (no clear mention)
Sperlich, This study	2013	[119]	SSH

The system of equations is conventionally solved through the Newton-Raphson algorithm. However, in 2003, Schlüter introduced an algorithm with much of a better performance that has later been patented in various countries [157].

The difference between the two algorithms has been quantified by changing the methods used for the $\delta^{17}O$ correction from SSH [151] to Craig [129]. The difference of the two methods resulted in a difference of 0.1146(17)‰ for an individual measurement (40 mL GIS) and 0.1515(27)‰ (40 mL AL). The offset is thus signature dependent. Taking into account the applied corrections (cf. *infra*), this reduced to $\delta_{\text{Craig}} = \delta_{\text{SSH}} + 0.0301(189)$‰. Hence it can be concluded that the effect is about one third of the average total standard aberration of the measurement. And not really a large concern for the moment.

Table 4.5: Carbon and oxygen isotopes in natural CO_2.

Isotope	Abundance
^{12}C	98.9%
^{13}C	1.1%
^{16}O	99.76%
^{17}O	0.04%
^{18}O	0.2%

The IRMS measures the mass-to-charge ratio of ion currents with m/z=44, 45, and 46. These are dominated by the most abundant ions, i.e. $^{12}C^{16}O_2^+$, $^{13}C^{16}O_2^+$, and $^{12}C^{16}O^{18}O^+$ respectively, cf. Tab. 4.5, where the relative abundances of each isotopologue is shown.

Laboratories and producers of IRMS have chosen to use different corrections over time. This resulted in systematic differences between the raw values measured and the derived ratios between various laboratories [142].

4.2 Size correction

Two size effects are affecting the measured $\delta^{13}C$ signature at the same time:

- dependency on the amount of methane gas entering the mass spectrometer, ("pressure effect", increases with sample size),

- contribution of leaked-in gases (the "blank") (relative importance of effect decreases with increasing sample size).

In a test with a pure CH_4 gas, the isotopic signature measured by the IRMS showed a dependency on the peak area of the combusted CH_4. This dependency is due to the combined effect of possible fractionation processes before and during combustion, the relative contribution of gases leaking into the injected sample as well as the so called "pressure effect" [83] in the mass spectrometer, which results from a dependency of the measured ratio on the size of the major ion beam.

The sum of all size effects depending on the CH_4 peak size, A, is quantified by the offset, D, between the measured value of a standard gas (y) extraction over molten water from bubble free ice (BFI), $\hat{\delta}_y$, to its known value $\mathring{\delta}_y$. Since it's true value is unknown, but the measured value is just a measurement of it, it is designated as $\hat{D}$.

$$\hat{D}_{\delta,y} = \hat{\delta}_y - \mathring{\delta}_y. \tag{4.4}$$

With a statistically sufficient number of BFI measurements, the dependence of the offset, $D_{\delta,y}$, on the sample area measured by the IRMS, A_y, can be investigated (cf. Fig. 4.1). The figure suggests a somewhat linear dependence, which can be expressed by a linearly fitted curve, as in Eq. 4.5.

$$D_{\delta,\text{size}}(A_s) = m \cdot A_s + b \tag{4.5}$$

The parameters m and b of this correction have been determined by Sperlich (2012) [126] and again during this study using a total of 28 and 14 measurements respectively, whereof the number of measurement with the injected gases (GIS, AL, NEEM) were (12, 9, 7) and (5, 6, 3) respectively.
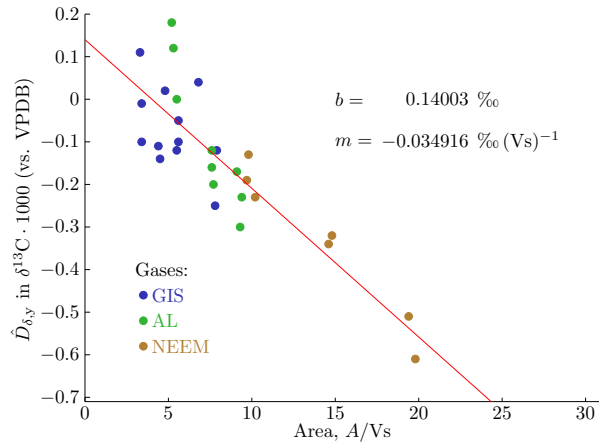
(a) Sperlich (2012) [126]
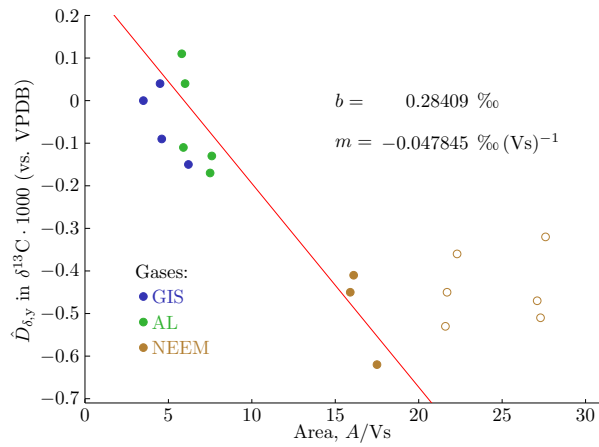
(b) This study.
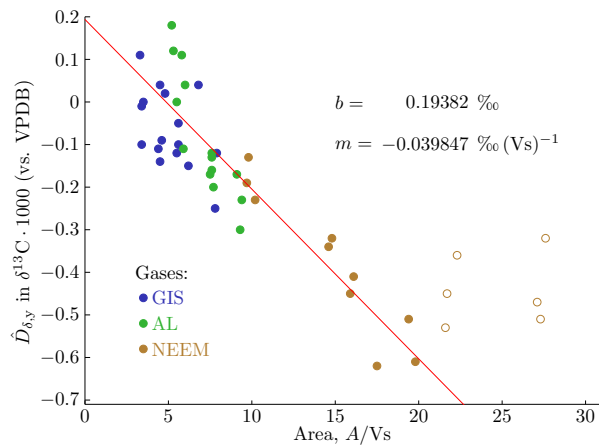
(c) Both sets combined.

Figure 4.1: Measured offsets to the known values $\hat{D}_{\delta,\mathrm{y}}$. Specifications of gases, cf. Tab. 3.2. The outlined points have areas larger than $20\,\mathrm{Vs}$ and have been excluded. Red line: linear fit through valid data.

Table 4.6: Parameters of the size correction as determined through measurements by Sperlich (2012) and in this study.

Name	Slope $(m/\mathrm{As})\cdot 1000$	δ-axis offset $b \cdot 1000$	Measurement period
Sperlich (2012) [126]	-0.034916	0.14003	15.05.12–25.06.12
This study	-0.047845	0.28409	09.10.12–13.11.12 (AL, GIS)
			03/04.01.13 (NEEM)
Combined	-0.039847	0.19382	[all of the above]

The parameters b and m were calculated using linear regression,

$$b = \frac{\sum Y \sum X^2 - \sum X \sum XY}{n \sum X^2 - (\sum X)^2}, \tag{4.6}$$

$$m = \frac{n \sum XY - \sum X \sum Y}{n \sum X^2 - (\sum X)^2}, \tag{4.7}$$

where X and Y were A_s and $\hat{D}_{\delta,\mathrm{y}}$ respectively, and n the number of observations used for the fitting.

In order to correct for this offset, one could simply determine the offset out of the measured sample area, i.e. $D_{\delta,\mathrm{size}}(A)$. Since the δ value for the sample is calibrated with the 6 GIS standard measurements $(\bar{\delta}_k, \bar{A}_k)$ in the same manner as for the construction of this linear regression curve , one can also correct for eventual inconsistencies in the standard size, which are likely as the standard injections were sized manually. By calculating the difference of the offset of the standards and the offset of the sample, the true size dependent correction is found.

$$\Delta'_{\delta,\mathrm{size}}(\bar{A}_\mathrm{k}) - \Delta'_{\delta,\mathrm{size}}(\hat{A}_\mathrm{s}) = [m \cdot \bar{A}_\mathrm{k} + b] - [m \cdot \hat{A}_\mathrm{s} + b]. \tag{4.8}$$

This simplifies to Eq. (4.9), since the Δ-axis offset, b, cancels out:

$$\Delta_{\delta,\mathrm{size}}(\bar{A}_\mathrm{k}, \hat{A}_\mathrm{s}) = m \cdot (\bar{A}_\mathrm{k} - \hat{A}_\mathrm{s}). \tag{4.9}$$

This offset correction is hence dependent on the areas of the six calibration standards, $\bar{A}_\mathrm{k}$, as well as the area of the sample, $\hat{A}_\mathrm{s}$, and is subtracted from the measured value of the sample, $\hat{\delta}_\mathrm{s}$. This correction had an average value $(\pm 1\sigma)$ of 0.046(52)‰, maximum value 0.223‰, cf. Tab. 5.1.

Comparison with other studies

Other studies have reported to have also corrected for different sample δ^{13}C signatures [25]. However, in this study, we only apply a correction for the size of the peak area, others have applied a similar correction but applied it onto the peak height, as we conclude from the units of the correction (0.006‰· nA^{-1}). Their maximum correction value was 0.17‰.

There are also other parameters that possibly result in a non-linearity offset similar to the one presented above. These are discussed in Section 9.1.

4.3 Daily drift corrections

To correct for daily drifts in standards, extraction system and the mass-spectrometer, three full air standard gas (GIS) extractions are carried out at the beginning and end of each measurement day. These

standards are then to be evaluated such as to calibrate the system. For doing so, we used the approach introduced by Sperlich (2013) [119], which is discussed in the next section, followed by the discussion of the approach by Werner & Brand (2001) [83] and the proposal and discussion of a other possibilities. Previous publications have reported different calibrations based on a single set of measurement (Fischer (2008) [9]) or on six consecutive measurements of CH_4 (Behrens (2008) [123]).

4.3.1 Standard approach by Sperlich (2013)

Since there are many standard gases involved in our measurement system, Sperlich (2013) [119] developed a correction system based on Werner & Brand (2001) [83]: on every measurement day, three standard measurement are carried out before, as well as after the sample measurements. The morning and the evening standards are averaged, and these two values averaged again. Normally this has the same effect as average all six values at once, but sometimes, one measurement is missing or invalid, in which case it is important to equally weigh the morning and the evening.

$$\bar{\delta}_k = \frac{1}{2}\left(\frac{1}{n_{\mathrm{m}}}\sum_{i=1}^{n_{\mathrm{m}}}\delta_{k,i} + \frac{1}{n_{\mathrm{e}}}\sum_{i=1}^{n_{\mathrm{e}}}\delta_{k,i}\right) \tag{4.10}$$

From the calculated daily average, the daily offset is calculated:

$$\Delta_{\delta,k}(\bar{\delta}_k) = \bar{\delta}_k - \mathring{\delta}_k \tag{4.11}$$

The value of this offset is neither dependent on the sample's measured composition, $\hat{\delta}$, nor its area, A_{s}. NB: Since all values are reported against VPDB, this correction does not need any additional terms (such as a product of δs), as it would be necessary for a change in the international reference standard, against which measurements are reported, cf. Eq.(2.32).

Instead of averaging over morning and evening, the samples could be corrected with the standards immediately following or preceding the series of standards only. Or, a line could be fitted through the 6 offsets, or through the two daily averages $\Delta_{\delta,k_{\mathrm{m}}}$ and $\Delta_{\delta,k_{\mathrm{e}}}$.

This offset correction is more of an empirical nature than based on physical phenomena, such as leak-in rates (i.e. bottom-up approach).

4.3.2 Correction proposed by Werner & Brand (2001)

The correction as proposed by Werner & Brand (2001) [83] uses the δ values of the blank measurements to correct for the blank contribution by subtracting their contribution to the isotopic signature of the sample weighted by the area (although it is not mathematically sound to subtract delta values weighted by area, the incurred error that could be avoided using F notation is of the order of $1 \cdot 10^{-3}$‰, and thus neglectable):

$$\begin{cases} \hat{\delta}\hat{A} &= \mathring{\delta}\mathring{A} + \delta_{\mathrm{x}}A_{\mathrm{x}}, \\ \hat{A} &= \mathring{A} + A_{\mathrm{x}} \end{cases}, \tag{4.12}$$

$$\Rightarrow \mathring{\delta} = \frac{\hat{\delta}A - \delta_{\mathrm{x}}A_{\mathrm{x}}}{\hat{A} - A_{\mathrm{x}}}. \tag{4.13}$$

This approach has the significant shortcoming that the δ values measured are not precise for too small sample areas. This is why, the measurements were not corrected using this approach. However, using calibration measurements, the correct δ_{x} could be determined, which is discussed in the next section.

4.3.3 Alternative approach

If one assumes the offset originating only from the methane leaking into the line during the extraction, the measured ratio can be decomposed into

$$\hat{R} = \frac{{}^{13}\mathring{n} + {}^{13}n_x}{{}^{12}\mathring{n} + {}^{12}n_x}, \tag{4.14}$$

of which all four variables on the right side are unknown. However, from Eq. 2.29, and since the measured charge "areas" are the closest measure of the amount of methane molecules present, $n \propto FA$, which can be expressed as

$$\hat{R} = \frac{{}^{13}\mathring{F}\mathring{A} + {}^{13}F_x A_x}{{}^{12}\mathring{F}\mathring{A} + {}^{12}F_x A_x} = \frac{\frac{\mathring{R}}{\mathring{R}+1}(\hat{A} - A_x) + \frac{R_x}{R_x+1}A_x}{\frac{1}{\mathring{R}+1}(\hat{A} - A_x) + \frac{1}{R_x+1}A_x}, \tag{4.15}$$

where $\mathring{A}$ denotes the standard area originating from the sample, and A_x for the contribution of the leak-in.

From the four variables in Eq.(4.15), $\hat{A}, A_x, \mathring{R}$ and R_x, there is only one unknown, R_x, while the others can be quantified using results of the blank (A_x) and daily standard extractions ($\hat{A}, \hat{R}, \mathring{A} = \hat{A} - A_x$). The true ratio of the standard, $\mathring{R}$ is known since it is a property of the used gas, while R_x remains unknown, since the measured value lacks in precision and accuracy due to its small area A_x. Hence we can solve the equation for R_x:

$$R_x = \frac{\mathring{R}(\hat{A} - A_x) - \hat{R}(\hat{A} + \mathring{R}A_x)}{\hat{R}(\hat{A} - A_x) - (A_x + \mathring{R}A)}. \tag{4.16}$$

Now, that the isotope ratio of the blank is known, the R-value of the sample can be compensated for it, where R_V is R_{VPDB}:

$$\mathring{R}_s = \frac{{}^{13}\hat{F}_s A_s - {}^{13}F_x A_x}{{}^{12}\hat{F}_s A_s - {}^{12}F_x A_x} = \frac{\frac{R_V(\hat{\delta}_s+1)}{R_V(\hat{\delta}_s+1)+1}A_s - \frac{R_x}{R_x+1}A_x}{\frac{1}{R_V(\hat{\delta}_s+1)+1}\hat{A}_s - \frac{1}{R_x+1}A_x} \tag{4.17}$$

$$= \frac{A_s R_V(R_x+1)(\hat{\delta}_s+1) - A_x R_x(R_V(\hat{\delta}_s+1)+1)}{A_s(R_x+1) - A_x(R_V(\hat{\delta}_s+1)+1)} \tag{4.18}$$

Finally, if one transforms this into delta notation, the effective delta value of the sample becomes:

$$\mathring{\delta}_s = \frac{\mathring{R}_s}{R_V} - 1. \tag{4.19}$$

This approach requires the area A_x of an extraction without gas ("blank") to be known. One option would be to assign A_x the area of the blank extraction right after the sample, which in turn would be required to be clear, i.e. no residual gases from the previous extraction should be present. This could be ensured by evacuating it before the blank extraction. However, evacuating the blanks is not feasible, as it allows for the determination of outliers. In two tests, multiple consecutive blank extractions were carried out, and as the results have shown, the blank area of the second blank increased ($+26\%$ of the original area) or stayed the same (-0.2%). Hence this seems to be a reasonable approach to take. The second option would be to use an average blank area for A_x that is determined once, but this approach does not really solve the problem, since exactly this variation of the blank area is one of the parameters that this correction wanted to address. The third option would be to extract another blank after the sequence, which could then serve as reference area for the most recent measurement but not the previous one.

During this correction, a size dependent correction is applied, which now competes with the sample size correction from Section 4.2 that already included blank contributions, hence it was not possible to use this approach. If it would be used in future studies, the size correction would have to be calculated anew using the same correction for its parameter determination as for the measurements of ice samples. Due to this, this procedure was not taken for the evaluation of the results, but for maintaining consistency the Sperlich (2013) approach was used.

This correction had an average value ($\pm 1\sigma$) of 0.580(129)‰, maximum value 0.756‰, cf. Tab. 5.1.

4.4   Gravitational enrichment correction

Diffusion in the firn layer enriches the methane though gravitational effects by

$$\Delta_{\delta,\text{firn}} = 0.28 \pm 0.03‰, \tag{4.20}$$

which quantifies the gravitational enrichment and diffusion in the firn layer, based on a model of molecular diffusion and gravity for Eurocore by Schwander (1993) [106], cf. also Section 2.6.

However, it is basically incorrect to express a gravitational enrichment with an addition of an offset Δ_δ. Instead, an enrichment factor ε would be more appropriate, since the occurring fractionation is a process whose magnitude depends on the atmospheric signature. This was recently researched by Buizert (2013) [107], who introduced a formula for the gravitational enrichment factor ε, depending on the rate at which the mixing ratio changes over time, the firn tortuosity and the gas species.

4.5   Offset against an absolute reference

When measurements of different laboratories are compared against each other, they have all to be based on a common standard. In recent papers, e.g. Sapart (2012) [1], Bern has been chosen as the reference. Hence this offset was determined against the Bern laboratory through the calibration with a specific ice core bag (B30, 1750) in their report.

$$\Delta_{\delta,\text{B30}} = -0.66‰ \tag{4.21}$$

This practice eases international intercomparability and collaboration, and has also been reported by Behrens (2008) [123] from NIWA (New Zealand), who applied corrections to based on the measurements of the Heidelberg laboratory.

However, the IMAU laboratory of Sapart (2012) and the CIC laboratory do not have an offset between each other. For this reason it was chosen not to apply a correction.

$$\Delta_{\delta,\text{inter}} = 0.00‰ \tag{4.22}$$

4.6   Summation of corrections and offset corrections

Since none of the above corrections' values depend on the sample's measured signature, $\hat{\delta}_\text{s}$, or its area, A_s, and all of these result in a correction to be subtracted, all of them can be subtracted in any order, thanks to the cumulative property of succeeding subtrahends.

The final equation used is

$$\mathring{\hat{\delta}}_{\mathrm{s}}(\hat{\delta}_{\mathrm{s}}, \hat{\delta}_{\mathrm{k}}, A_{\mathrm{s}}, A_{\mathrm{k}}) = \hat{\delta}_{\mathrm{s}} - \Delta_{\delta,k}(\hat{\delta}_{\mathrm{s}}, \hat{\delta}_{\mathrm{k}}) - \Delta_{\delta,\mathrm{size}}(A_{\mathrm{s}}, A_{\mathrm{k}}) - \Delta_{\delta,\mathrm{firn}}(-\Delta_{\delta,\mathrm{inter}}) \tag{4.23}$$

$$\mathring{\hat{\delta}}_{\mathrm{s}} = \hat{\delta}_{\mathrm{s}} \tag{4.24}$$

$$- m \left[\frac{1}{2} \left(\frac{1}{n_{\mathrm{m}}} \sum_{i=1}^{n_{\mathrm{m}}} A_{\mathrm{k},i} + \frac{1}{n_{\mathrm{e}}} \sum_{i=1}^{n_{\mathrm{e}}} A_{\mathrm{k},i} \right) - A_{\mathrm{s}} \right] \tag{4.25}$$

$$- \left[\frac{1}{2} \left(\frac{1}{n_{\mathrm{m}}} \sum_{i=1}^{n_{\mathrm{m}}} \delta_{\mathrm{k},i} + \frac{1}{n_{\mathrm{e}}} \sum_{i=1}^{n_{\mathrm{e}}} \delta_{\mathrm{k},i} \right) - \mathring{\delta}_{\mathrm{k}} \right] \tag{4.26}$$

$$- \Delta_{\delta,\mathrm{firn}} \tag{4.27}$$

$$(-\Delta_{\delta,\mathrm{inter}}) \tag{4.28}$$

4.7 Estimation of standard deviation

Standard deviations can be understood and calculated from two different perspectives, one being the bottom-up approach, that is, the source of the errors are analysed and quantified individually, then through error propagation the total error is calculated. The other approach is more of a top-down approach, that is, the effective total error is estimated from the final values of calibration measurements. The top-down approach is more easy to assess and yields directly the standard deviations, therefore only this one is discussed in the following.

The standard deviation was estimated using the formula for the estimation, s, of the standard deviation:

$$s = \sqrt{\frac{1}{N-1} \sum_{i=1}^{N} (\delta_{k,i} - \mu)^2}, \quad \text{where} \quad \mu = \frac{1}{N} \sum_{i=1}^{N} \delta_{k,i}. \tag{4.29}$$

The estimation was applied onto the standard measurements δ_k, where $N = 6$. The estimated standard deviation of a result of a formula was then calculated using Gaussian error propagation, cf. Appendix A.7. The resulting estimators are plotted in the graph of Fig. 5.2 and 5.4 as 1σ error bars to both sides, up and down, of the point.

4.8 Possible sources of errors

Two different possible sources of errors that lower the capacity of mass spectrometers to give accurate methane isotopic measurements at a precision of $0.01\permil$ have been identified by Werner & Brand (2001) [83], these are discussed in the following.

4.8.1 Isobaric interferences of CO_2H^+

Traces of water and other protonation agents can cause ion/molecule reactions in the ion source and result in isobaric interference of CO_2H^+ ($m/z = 45$) [83]. To mitigate these interferences, and to ensure

that not "no" water molecule can make it to the ion source, there is a warm GC column right before the mass spectrometer, that is, after the combustion process that includes the oven the Nafion membrane and the last cryofocus.

4.8.2 Exchange of oxygen atoms of burnt CH_4

The burnt CH_4 that is measured in the MS as CO_2, would be able to exchange its oxygen atoms other than the one created during combustion, if it were in contact with water. However, in the present system, the possibility of such an exchange is further minimised by the use of a the warm GC column.

4.8.3 Isotopic composition difference of sample and reference

The full air standard used to calibrate the system should always be as close as possible, such as to minimize errors resulting from the balancing of the major ion beam, by which the readings of the minor beam will be different. This error source will vary over time, since the response of the measurement channels will never be perfectly linear [83], also, the $\delta^{13}C$ value of the standard varies over time due to gravitational enrichment.

In our system, we used GIS standard gas (431 ppb CH_4, $\delta^{13}C = -42.21‰$) for the reference calibration and AL (686.7 ppb CH_4, $\delta^{13}C = -49.44‰$) as quality control standard. From the measured $\delta^{13}C$ values, in Fig. 5.2, it becomes obvious that this choice could have been inverse, since the signature of AL lies closer to the measured one than that of GIS. However, it was decided to measure like this, since this was similar to how Sperlich (2012) [126] has made previous measurements over the same age range. Thanks to this, we were able to apply the same values for the size correction as he did, cf. Section 4.2.

If AL would have been chosen, the difference of the imbalance of the ion-beams towards the working standard would have been more similar between calibration and sample, which could have had a beneficial influence, it does however appear unreasonable to take the single AL measurement that was for quality control as calibration measurement.

The signature of the working standard should in principle leave the measured values unaffected, as both the calibration standard and the sample are measured against the same standard. Hence the imbalance would have the same effect and cancelled out.

4.9 Mixing ratio calculation from TCD data

The methane mixing ratio of ice samples can be calculated from the volume of gas (measured by the TCD) and the amount of methane (measured in the mass spectrometer). The TCD is providing a value, φ, in units of volt seconds (Vs) that can be converted into a volume, V, through calibration with the seven standard gas injections per day, that is, $3\times$ GIS (morning), AL, $3\times$ GIS (evening), $V_{k,i}$. Measured values are denoted with a hat (ˆ):

$$\hat{V}_{sa} = \hat{\varphi}_{sa} \left(\frac{1}{7} \sum_{i=1}^{7} \frac{V_{k,i}}{\hat{\varphi}_{k,i}} \right). \tag{4.30}$$

With the calculated volume the total amount of gas is known. For calculating the methane mixing ratio, the amount of methane, v, needs further to be known. It is again obtained through calibration with the

standard gases, and their known methane mixing ratios from the bottle, x_k:

$$\hat{v}_{sa} = \hat{A}_{sa} \left(\frac{1}{7} \sum_{i=1}^{7} \frac{V_{k,i} x_k}{\hat{A}_{k,i}} \right). \tag{4.31}$$

The mixing ration is then the ratio of methane volume over total gas volume,

$$\hat{x}_{sa} = \frac{\hat{v}_{sa}}{\hat{V}_{sa}}. \tag{4.32}$$

The results of this technique applied onto the acquired measurements are plotted in Section 5.3.2. The area in the blanks is usually so small that it is not even detectable in the TCD recordings.

The recordings are evaluated using a MATLAB script, where the area of the peak is numerically integrated. For doing so, first a background value (the "zero") is determined followed by a script for the integration. The relatively simple script has originally been developed by Buizert (2009) [148], and was refined during this study. It is shown in Appendix B.1.1.

4.10   Special case with two partial extractions

One data point features large error bars at the year 1126 in Fig. 5.4. Is was obtained through summation of two partial extractions, which were due to a leaky valve (EVB.5) that regulates the Helium inflow into the cryotrap, cf. Fig. 3.3 (T.cryo). This resulted in an unusual pressure development during extraction, so that the pressure did not just decrease, but increased again after reaching a certain minimum value. The consecutive blank extraction still contained a considerable amount of methane, which was more than ten times larger (1.78 Vs) than a usual blank (0.113 ± 0.037 Vs, $n=24$), and even the TCD recorded a flow. The δ^{13}C-values were averaged, weighted with their "area" in As. The measured TCD fluxes in Vs were added together.

Chapter 5

Analytical results

In this chapter the results of the measurement campaign and data evaluation are discussed, starting with a report of the core quality assessment, before the corrected isotope values are shown, followed by the discussion of identified outliers.

5.1   Core quality

A total of 24 ice cores from Eurocore (Summit, central Greenland, 72°34' N, 51°27' W), and two from NEEM (77°27' N, −51°3.6' W, cf. Fig. 2.18) have been analysed. Three of the ice cores were large enough to split them into two samples: one was split to provide replicates, and the other two were split into an earlier and a later part. Two adjacent cores were too small to be measured alone, since they had been processed with a melt finger and only a part of the core was available to be used, so that they were combined into one measurement.

There were two blocks of measurements, since cores of good quality were measured first, and only after, the ones of bad quality were processed. These required a larger amount of time for the preparation of each sample than the cores of good quality, since a core could need to be cut into more than 20 small pieces, cf. Fig. 5.1. Samples were picked randomly, not following chronological order, in each of the two measurement blocks.
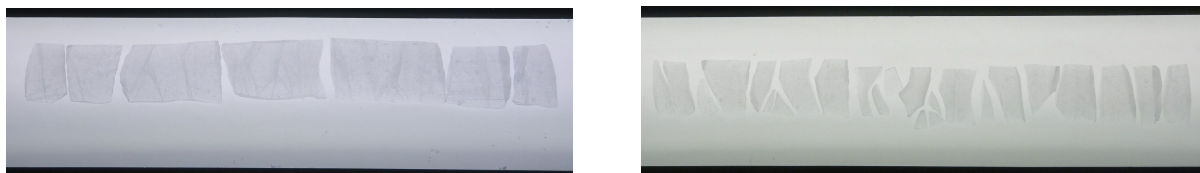
Figure 5.1: Photos of Core EC546 that is full of cracks: before and after cutting.

5.2 Carbon isotope values

The isotope values are reported in Fig. 5.2, where, in addition to the results of this study (blue and outliers in red), the measurements of Sperlich (2012) [126] (in green), and the results of Sapart (2012) [1] (yellow) are also shown.
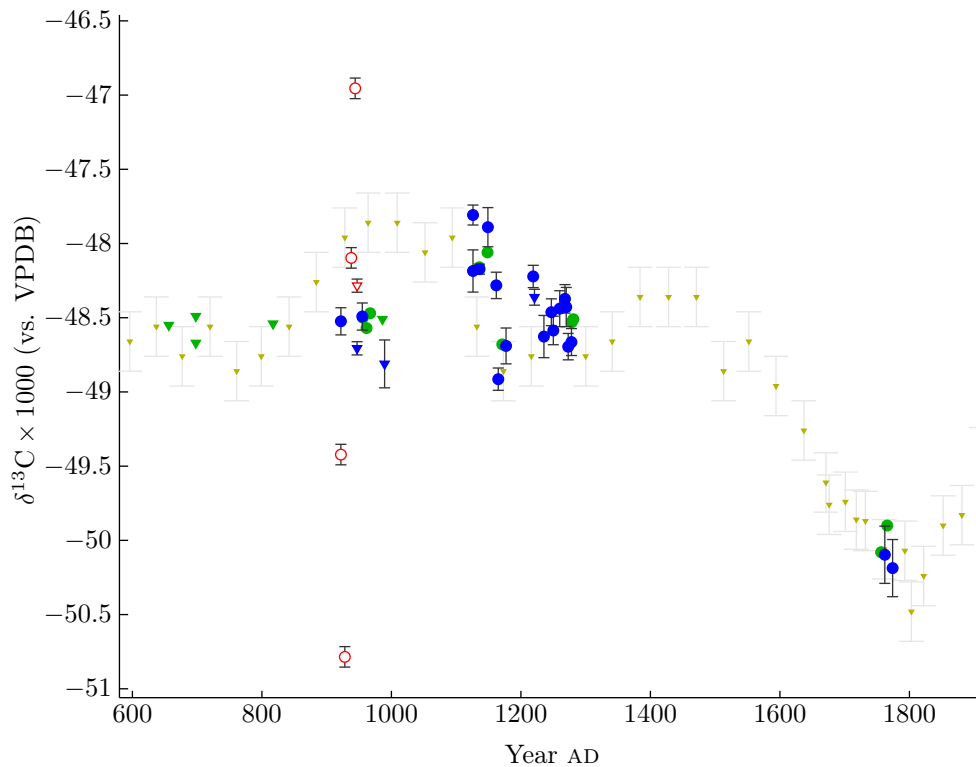
Figure 5.2: Measured carbon isotope signatures of methane, δ^{13}C-CH$_4$: blue (good points), red (excluded, cf. text) and green measured by Sperlich (2012) [126], with 1σ error bars, compared to the record from Sapart (2012) [1] (yellow). The shape of the points denotes the core: circular points are from Eurocore, triangular points from NEEM.

The 1σ error bars were calculated using Gaussian error propagation on Eq. (4.23). The technique is explained in Appendix A.7, where it is applied to the data of the next Section. Some points had to be removed because the blank area was too large or the delta value of the blank was too low. Some of these outliers were confirmed by an anomalous mixing ratio from the TCD (cf. next section).

5.3 Outlier identification

Apart of the measured δ^{13}C-signatures of the sample, some additional measured values are used to identify outliers, caused by errors in the extraction and measurement system or its handling. These are the mixing ratio of the measured sample, and the two MS measurements from the consecutive blank: methane amount (area) and δ^{13}C-signature, if any of the blank values deviated obviously from the general system drift, the measurement of the preceding sample was considered an outlier.

5.3.1 Blank and sample measurements

Sample area and isotopic signature were used to identify outliers. Shown in Fig. 5.3, are the MS values for blanks and samples plotted against their sample number (chronological order). All excluded samples are shown as a red circle, and the ones identified based on a specific measurement value are shown filled in the respective plot. Note the different y-axes scale in the two plots. The low signature of samples 24 and 25 was expected, since they originate from the 18$^{\text{th}}$ century, cf. Fig. 5.2.
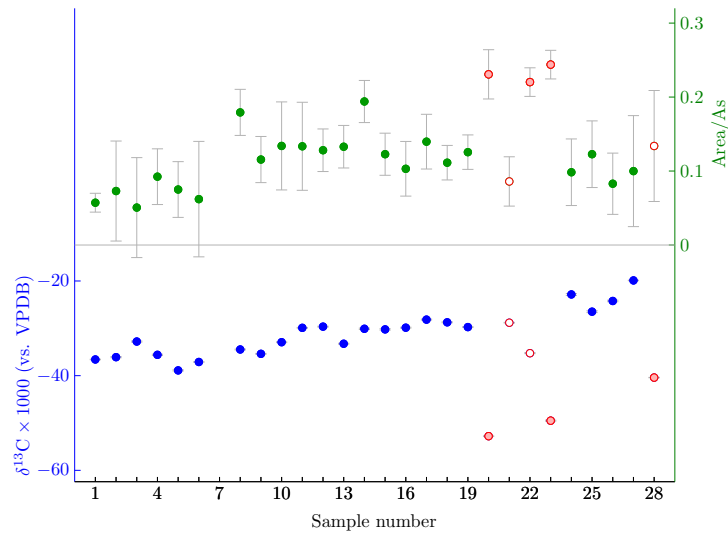
(a) Blank runs following the samples.
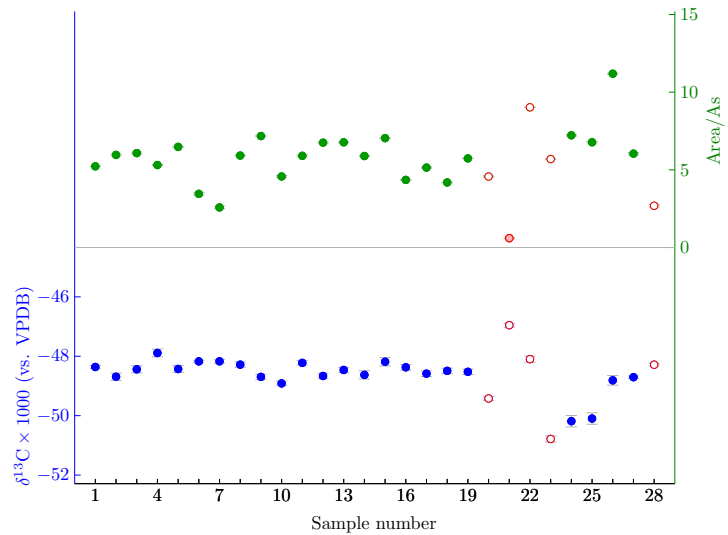
(b) Samples.

Figure 5.3: Measured isotope signatures, δ^{13}C (blue), and MS areas (green) of the blanks (a) and samples (b), with 1σ error bars. In (red): excluded measurement values (cf. text).

5.3.2 Mixing ratio from TCD data

The methane mixing ratios, calculated from TCD data and mass spectrometer measurements (cf. Section 4.9), are shown in comparison to the known mixing ratio record from Rhodes (2013) and Mitchell (2011) [158, 133] in Fig. 5.4. Details about this record and how it was fitted together are explained in Section 6.4.
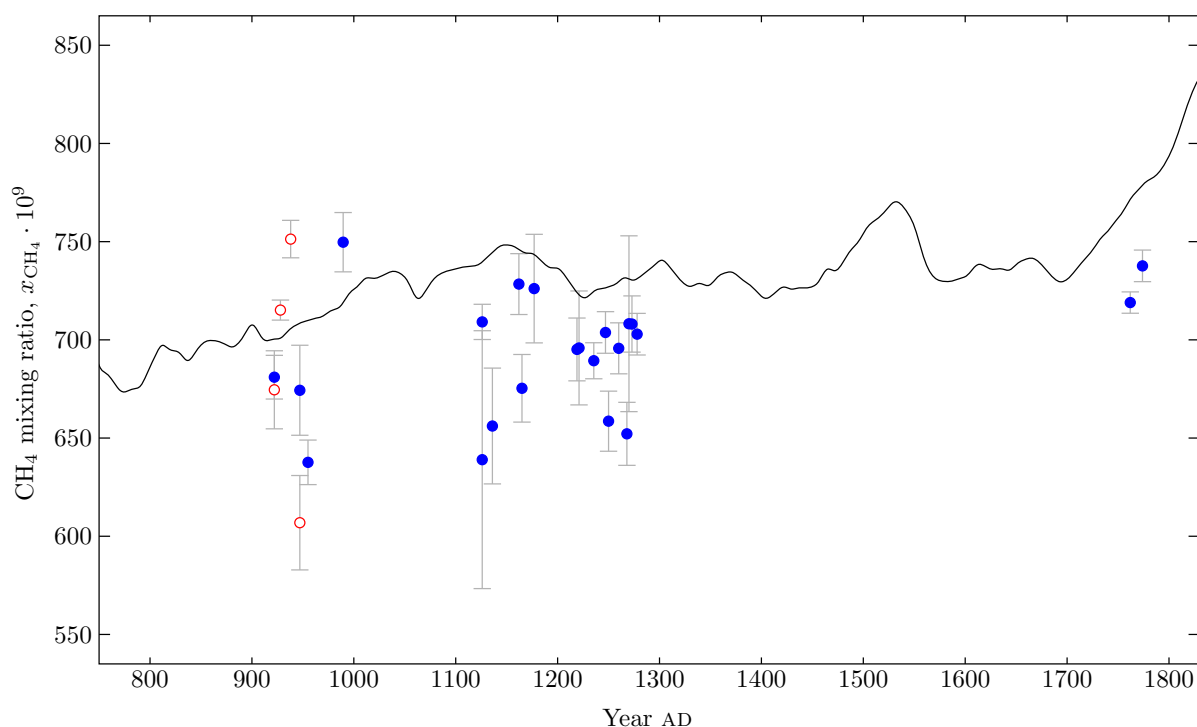
Figure 5.4: Measured mixing ratios, x_{CH_4} (blue) with 1σ error bars, compared to the combined mixing ratio record from Rhodes (2013) and Mitchell (2011) (black line). In (red): excluded measurement values (cf. text).

The error bars (1σ) were calculated using Gaussian error propagation, (details see Appendix A.2). From four plotted outliers, two also show an extreme mixing ratio, in addition to the large blank peaks or extreme $\delta^{13}C$ values in the blank. These points are shown in red. The point at AD 1126 with $x_{CH_4} = 639$ ppb features large error bars, because it was the result of two partial extractions, cf. Section 4.10. For two points, the TCD failed during the measurement, and consequently there is no value shown. One of these points turned out to be an outlier.

The calculated mixing ratios from TCD measurement data lie generally lower than what was previously published. The source of this difference is most likely due to uncertainties and non-linearities in the system. To increase confidence in the measurements, a size correction could be applied to this TCD data, using standards with different mixing ratios and over various injection sizes, similar to the correction applied to δ values explained in Section 4.2.

5.4   Origin of deviations between CIC and IMAU measurements

The cores analysed at CIC, deviate from those measured at IMAU (Sapart), cf. Fig. 5.2. This deviation has not been identified so far, but the following two error sources can be ruled out:

- drifts in the analysis system, since the cores where not measured in chronological order, and the of this study corroborate the points by Sperlich (2012) [126],
- differences between ice cores, since the CIC data is from Eurocore and NEEM.

5.5   Result table

A table with the measurement results of the ice core samples, the blanks, the semi-diurnal averages of the calibration (GIS) standards, the quality control (AL) standards, as well as the results of the TCD evaluation is shown in Tab. 5.1. The most important values are highlighted with blue fill colour, that is, the measured $\delta^{13}C$ with the corresponding standard deviation. The greyed rows contain the outliers, where the abnormal values that identified them as outliers are printed in red.

Table 5.1: Result table. The final value is also adjusted for gravitational enrichment in the firn ($\Delta_{\text{firn}} = 0.28‰$).

Time Code	MS#	Core	Gaseage (Year AD)	A_s (Vs)	$\hat{\delta}^{13}C$ (‰)	$\Delta_{\delta,size}$ (‰)	Δ_{δ,k_m} (‰)	Δ_{δ,k_e} (‰)	$\Delta_{\delta,k}$ (‰)	$\delta^{13}C$ (‰)	$\sigma\delta^{13}C$ (‰)	$\delta^{13}C_{AL}$ (‰)	$\Delta_{\delta,k_{AL}}$ (‰)	A_x (Vs)	$\delta^{13}C_{BL}$ (‰)	m_{ice}/A (g/Vs)	V_{CH_4} (mL)	x_{CH_4} (ppb)	$\sigma(x)$ (ppb)	n_{CH_4} (nmol)
2012-10-23 13:28:32	2116	EC438	1221	5.2274	-47.669	0.015	0.396	0.460	0.428	-48.362	0.054	-49.389	0.021	0.0572	-36.532	59.30	26.61	695.88	29.00	0.75
2012-10-25 14:51:29	2228	EC455	1177	5.9599	-48.096	0.048	0.344	0.379	0.362	-48.690	0.121	-49.438	-0.028	0.0729	-36.116	57.89	30.57	726.10	27.64	0.90
2012-10-25 17:39:35	2234	EC423	1260	6.0781	-47.849	0.052	0.344	0.379	0.362	-48.439	0.121	-49.438	-0.028	0.0506	-32.814	55.94	32.54	695.68	12.97	0.91
2012-10-29 17:14:00	2382	EC466	1149	5.3105	-47.248	0.026	0.469	0.308	0.389	-47.890	0.132	-49.296	0.114	0.0924	-35.594	56.49	-	-	-	.
2012-10-29 21:05:44	2390	EC419	1270	6.4794	-47.827	0.067	0.469	0.469	0.389	-48.428	0.121	-49.296	0.114	0.0750	-38.878	58.65	34.32	708.21	44.76	0.98
2012-10-31 17:21:13	2418	EC471	1136	3.4551	-47.464	-0.027	0.390	0.414	0.402	-48.173	0.034	-49.329	0.081	0.0620	-37.088	-	21.41	656.13	29.48	0.57
2012-10-31 19:47:46	2424	EC475A 1/2		2.5791	-47.490	-0.057	0.390	0.414	0.402	-48.172	0.067	-49.329	0.081				16.71	627.57	32.83	0.42
2012-10-31 20:57:54	2426	EC475A 2/2		1.7790	-46.429	-0.086	0.390	0.414	0.402	-47.111	0.067	-49.329	0.081				11.02	647.78	32.83	0.29
Combination		EC475A	1126	4.3581			0.390	0.414	0.402	-47.808	0.135	-49.329	0.081			91.59	27.73	639.00	65.65	0.71
2012-11-07 16:07:52	2831	EC461	1162	5.9213	-47.456	0.042	0.520	0.656	0.588	-48.282	0.089	-49.241	0.169	0.1793	-34.266	54.04	29.54	728.39	15.48	0.87
2012-11-07 18:35:51	2837	EC418	1273	7.1776	-47.913	0.086	0.520	0.656	0.588	-48.695	0.089	-49.241	0.169	0.1155	-35.177	57.12	36.83	708.06	14.30	1.05
2012-11-12 15:43:46	3073	EC460	1165	4.5737	-47.991	-0.009	0.637	0.630	0.634	-48.914	0.075	-49.237	0.173	0.1340	-32.679	74.34	24.01	675.33	17.20	0.65
2012-11-12 18:06:46	3079	EC439	1219	5.9040	-47.346	0.038	0.637	0.630	0.634	-48.222	0.091	-49.237	0.173	0.1334	-29.643	59.28	30.11	695.13	15.99	0.84
2012-11-13 15:26:29	3097	EC416	1278	6.7526	-47.854	0.066	0.574	0.618	0.596	-48.664	0.091	-49.220	0.190	0.1281	-29.431	56.28	33.92	702.89	10.59	0.96
2012-11-13 17:44:39	3103	EC428	1247	6.7721	-47.654	0.067	0.574	0.618	0.596	-48.463	0.091	-49.220	0.190	0.1329	-33.041	54.64	33.98	703.76	10.59	0.96
2012-11-14 16:35:37	3121	EC432&433	1235.5	5.8897	-47.734	0.036	0.530	0.767	0.648	-48.627	0.142	-49.134	0.276	0.1940	-29.832	73.01	29.95	689.36	9.16	0.83
2012-11-14 18:53:31	3127	EC475B	1126	7.0404	-47.333	0.076	0.530	0.767	0.648	-48.185	0.142	-49.134	0.276	0.1227	-29.957	56.82	34.80	709.14	8.96	1.00
2012-11-19 13:32:53	3291	EC420	1268	4.3552	-47.453	-0.016	0.659	0.590	0.624	-48.373	0.096	-49.016	0.394	0.1030	-29.616	57.40	23.85	652.15	16.05	0.63
2012-11-19 15:47:18	3297	EC427	1250	5.1468	-47.694	0.012	0.659	0.590	0.624	-48.586	0.096	-49.016	0.394	0.1397	-27.911	58.29	27.91	658.59	15.31	0.74
2012-12-06 18:18:25	4095	EC540	955	4.1905	-47.507	-0.018	0.692	0.682	0.687	-48.492	0.091	-49.148	0.262	0.1113	-28.426	79.94	23.89	637.62	11.34	0.61
2012-12-06 20:33:16	4101	EC522B	922	5.7371	-47.593	0.036	0.692	0.682	0.687	-48.524	0.091	-49.148	0.262	0.1255	-29.431	59.26	30.62	681.00	11.12	0.84
2012-12-11 13:22:07	4119	EC522A	922	4.5696	-48.530	-0.008	0.618	0.590	0.604	-49.422	0.069	-49.194	0.216	0.2307	-52.554	59.09	24.07	674.58	19.88	0.65
2012-12-11 15:34:35	4125	EC544	944	0.6023	-45.923	-0.148	0.618	0.590	0.604	-46.955	0.069	-49.194	0.216	0.0859	-28.591	722.24	-	-	-	.
2012-12-19 11:45:06	4142	EC546	938	9.0243	-47.364	0.147	0.641	0.560	0.600	-48.097	0.104	-49.094	0.316	0.2202	-35.031	58.73	42.51	751.31	9.54	1.29
2012-12-19 13:57:52	4148	EC550	928	5.6939	-47.935	0.030	0.641	0.560	0.600	-50.785	0.104	-49.094	0.316	0.2439	-49.289	56.20	28.17	715.16	5.11	0.81
2013-01-05 19:20:00	4208	EC221	1774	7.2222	-49.233	0.081	0.759	0.752	0.756	-50.187	0.193	-48.855	0.555	0.0984	-22.475	54.69	34.56	737.67	8.05	1.03
2013-01-05 21:41:57	4214	EC227	1762	6.7748	-49.127	0.066	0.759	0.752	0.756	-50.097	0.193	-48.855	0.555	0.1227	-26.109	53.14	33.26	719.00	5.43	0.96
2013-01-08 15:58:27	4236	NM498	989.50	11.1905	-47.849	0.223	0.655	0.740	0.682	-48.811	0.161	-48.927	0.483	0.0828	-23.920	53.62	52.94	749.73	15.09	1.60
2013-01-10 16:51:43	4262	NM513-1	947.02	6.0440	-47.737	0.044	0.669	0.709	0.689	-48.706	0.045	-48.917	0.493	0.0999	-19.580	52.95	32.34	674.33	22.93	0.88
2013-01-10 19:13:09	4268	NM513-2	947.02	2.6867	-47.315	-0.073	0.669	0.709	0.689	-48.284	0.045	-48.917	0.493	0.1339	-40.096	89.33	15.97	606.88	24.04	0.39
Average				6.0547	-47.801	0.046	0.567	0.602	0.580	-48.628	0.106	-49.170	0.240	0.1106	-30.842	59.19	31.33	695.44	16.74	0.88
Estimated standard deviation				1.5311	0.499	0.052	0.126	0.140	0.129	0.544	0.042	0.175	0.175	0.0364	4.973	7.31	6.53	29.29	9.33	0.22

Part II: Model

Atmosphere $\lambda_{\mathrm{O(^1D)}}, \alpha_{\mathrm{O(^1D)}}$

$\lambda_{\mathrm{Cl}}, \alpha_{\mathrm{Cl}}$ κ

$\lambda_{\mathrm{OH}}, \alpha_{\mathrm{OH}}$

Pyrogenic

$$Q_{\mathrm{p}} = \frac{Q_{\mathrm{tot}}(\delta_{\mathrm{tot}} - \delta_{\mathrm{b}}) + Q_{\mathrm{g}}(\delta_{\mathrm{b}} - \delta_{\mathrm{g}})}{\delta_{\mathrm{p}} - \delta_{\mathrm{b}}}$$

Soil
$\lambda_{\mathrm{soil}}, \alpha_{\mathrm{soil}}$

Biogenic

$$Q_{\mathrm{b}} = \frac{Q_{\mathrm{tot}}(\delta_{\mathrm{tot}} - \delta_{\mathrm{p}}) + Q_{\mathrm{g}}(\delta_{\mathrm{p}} - \delta_{\mathrm{g}})}{\delta_{\mathrm{b}} - \delta_{\mathrm{p}}}$$
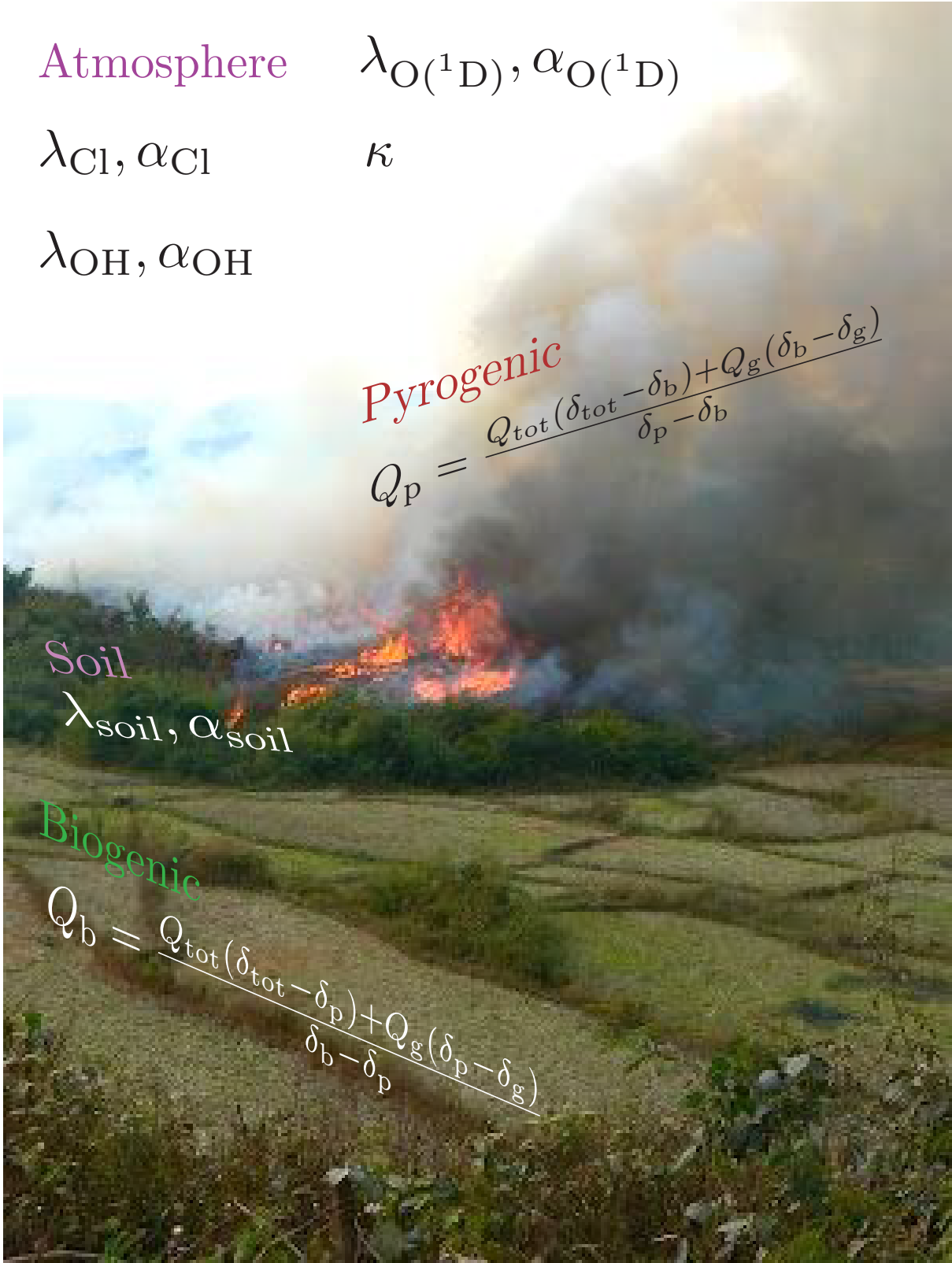
This page intentionally left blank.

Chapter 6

Modelling methods

This chapter presents the methods used in the model. First, a discussion of previous publications and models is given (Section 6.1), then the assumptions used in this model are stated 6.2, followed by the development of the present model 6.3, after which the preparation of time series and the involved smoothing is investigated 6.4 and, at last, the other input values are summarised (Section 6.7. The results are discussed in the next chapter.

6.1 Introduction

The global mass balance of methane in its most general form can be expressed through the mixing ratio, x, sources Q and sink rates λ:

$$\frac{\partial x_{\mathrm{CH_4}}(t)}{\partial t} = Q(t) - \lambda \cdot x(t). \tag{6.1}$$

In this study, a model is constructed that goes beyond the above equation and takes account of the two stable carbon isotopes, both hemispheres, the interhemispheric mixing, as well as various sinks. It provides estimates about the biogenic and pyrogenic emission strengths in each hemisphere. It is based on a general two box model as described in Tipping (2002) [159] and Tans (1997) [160]. Inputs are time series for mixing ratio and isotopic signature, and outputs are the source strengths. Since this is the inverse of the physical sense of mixing gases, where the inputs are given and the mixed ratio is calculated, this approach is termed "inverse modelling".

The methane budget has been the topic of many publications in the past. Early publications on methane mixing ratio variations from ice core data discussed the sources and sinks without knowledge of the temporal variation of isotope signatures (e.g. Khalil (1987) [161], Blunier (1995) [35]), and without constructing complicated mathematical models. In the beginning, data density was sparse and uncertainties large. Hence no evidence was found for statistically or environmentally significant trends between 1500 BC AND AD 1700 [161]. The quality and accuracy of measurements has largely improved since then.

After Craig (1988) [109] showed the significance of carbon isotopes in methane from ice cores, it took another one and a half decade until isotope and mixing ratio data became available with a reasonable resolution over the last two millennia.

Meanwhile many forward models were developed. Following the recognition of the importance of low latitude sources to $\sim$5 ka BP (kiloanni before present, i.e. AD 1975), and the boreal wetland growth thereafter until $\sim$1 ka BP by Blunier (1995) [35], they developed a three-box model in Chappellaz (1997) [162] based on the mixing ratios alone, since no δ^{13}C data was available. The importance of biogenic methane sources was later corroborated through models that made use of δ^{13}C records.

Houweling (2008) [72] presented a forward model including isotope data, based on demographic developments and climatic variations. Their findings came to a reasonable agreement with ice core records ($x_\mathrm{N}, x_\mathrm{S}, \delta^{13}\mathrm{C_S}$). The used data were sparse and the smoothing strong. Hence, there is no detailed model and analysis of changes between AD 600 and 1600. Later, Mischler (2009) [71] developed a forward model to run several scenarios and compare them to actual data of $x_\mathrm{S}, \delta\mathrm{D_S}$ and $\delta^{13}\mathrm{C_S}$, since he considered a fully time-dependent inversion to be too under-constrained to attempt it with the data available at the time.

Finally, Sapart (2012) [1] made an inverse model, which included a time series x_S and δ_N, from which the two missing records (x_N and δ_S) were constructed with an offset. Now, in this study, we develop a fully time-dependent inversion of four measured records, and get source time series for both hemispheres. To our knowledge, this is the first model to include four *measured* time series: mixing ratios and isotope signatures on both hemispheres.

6.2 Assumptions

The model bases on a two box model, where the two hemispheres are separate, vertically and latitudinally well mixed. The implications and validity of this assumption are discussed below.

Hemispheres as separate boxes

The Northern and Southern troposphere have been identified as being two well mixed reservoirs, separated from each other along the equator, as follows from studies on the distribution of tritium in methane (CH_3T) [163]. As long as one does not include further latitudinal boxes, this approach seems to be a reasonable simplification and has been used by many authors in the past.

Vertically mixed hemispheres

The two hemispheres are modelled as two perfectly mixed boxes. However, the perfect mixing is not the case, neither vertically (Fig. 2.12 nor latitudinally. The importance of the vertical variation with altitude (z), is assessed through the barometric law, through which one finds

$$p(z) = p_0\, e^{-z/H}, \tag{6.2}$$

where the parameters are the atmospheric pressure at the surface, $p_0 = 1.013\,\text{bar}$, a scale height $H = \frac{kT}{Mg} = 7.3\,\text{km}$, with the Boltzmann constant $k = 1.38 \cdot 10^{-23}\,\text{J\,K}^{-1}$, the mean atmospheric temperature $T = 250\,\text{K}$, the mean molecular mass of dry air $M = 28.964\,\text{g/mol} = 4.808 \cdot 10^{-26}\,\text{kg}$ and the gravity acceleration $g = 9.81\,\text{m/s}^2$.

The mixing ratio and signature remains fairly constant up to $z = 15\,\text{km}$, until where most of the airmass resides:

$$\frac{\int_0^{15} p(z)}{\int_0^{\infty} p(z)} = 87\%. \tag{6.3}$$

The remaining 13% of the air mass have a considerably different isotopic composition, cf. Fig. 2.12a, induced by the stratospheric sink, but a much lower mixing ratio. This effect, combined with the tropospheric-stratospheric exchange flow, as characterized by Rosenlof (1993) [164], is included in the model through the stratospheric sink term with λ_strat and α_strat.

However, Monteil (2011) [165] introduced in his model a proportionality constant H, by which he scaled the surface mixing ratio to match the atmospheric mixing ratio. He further assumed it to be constant during his 20 year model. In the present model no such correction is applied.

Validity of mixing ratio of gas in ice for the atmosphere

The validity of methane mixing ratios from ice cores to atmospheric surface measurements has been confirmed by matching firn measurements with instrumental atmospheric records [25], and the effect of firn transport and diffusion processes has been assessed by Buizert (2011) [104] and discussed in Section 2.6.2.

6.3 Isotopic budget model

A two-box model approach has been described by Tipping (2002) [159] and Miller (2005) [94]. The methane content of each hemispheres is modelled as a perfectly mixed box, containing an amount of methane molecules, either expressed in number of moles n_{CH_4} or as a fraction of the total size of the atmosphere $x = n_{CH_4}/n_{atm}$. The air exchange between the two hemispheres is described by the exchange time τ_{exc}. This translates into an annual exchange ratio κ,

$$\kappa = \frac{1}{2\,\tau_{exc}}. \tag{6.4}$$

The mass change on each hemisphere, and for each isotopologue, is then given by subtracting the losses and the interhemispheric exchange to the other HS while also adding the exchange mass from the other HS, plus the sinks. As shown in Eq. 6.5 for ^{12}x. A similar expression is used for ^{13}x.

$$\frac{d}{dt}\begin{bmatrix} ^{12}x_N \\ ^{12}x_S \end{bmatrix} = \begin{bmatrix} -\kappa - {}^{12}\lambda_N & \kappa \\ \kappa & -\kappa - {}^{12}\lambda_S \end{bmatrix}\begin{bmatrix} ^{12}x_N \\ ^{12}x_S \end{bmatrix} + \begin{bmatrix} ^{12}\dot{x}_{in,N} \\ ^{12}\dot{x}_{in,S} \end{bmatrix} \tag{6.5}$$

Where x is the mixing ratio of methane with respect to the total size of the atmosphere in mol:

$$\dot{x}_{source} = \frac{\dot{n}_{source}}{n_{atm}}. \tag{6.6}$$

$^{12}\lambda$ and $^{13}\lambda$ are defined as the sum of their constituents, including all different sink processes. As the land mass is unequally distributed over the two hemispheres by about $2/3$ on NH and $1/3$ on SH, the soil sink is weighted according to its hemispherical repartition with $\theta_{soil,N} = 4/3$ and $\theta_{soil,S} = 2/3$ [94], the average of which equals one.

$$^{12}\lambda = \lambda_{OH} + \theta_{soil}\lambda_{soil} + \lambda_{strat} \tag{6.7}$$

$$^{13}\lambda = \alpha_{OH}\lambda_{OH} + \theta_{soil}\alpha_{soil}\lambda_{soil} + \alpha_{strat}\lambda_{strat} \tag{6.8}$$

The model as described before works for forward modelling, when the sources are known. Here, in inverse modelling, two source strengths are solved for: for each step, the remaining amount of methane in each HS is calculated for both isotopes. That is, the sinks and the interhemispheric exchange are applied to the data of the last step. The difference to the amount of methane present in this step yields the total source strength, Q_{tot}, the isotope signature of which allows the determination of individual sources. The model with mathematical expressions is shown in Fig. 6.1.

For the solution, there are two ways, one involves the approximation that the isotope signature of a mixture equals their weighted average, while the other one is mathematically exact. In practice this does not matter, since the error is of the order of 10^{-3}‰, and the resulting difference is not visible on the plot.

Mathematically exact solution

For the exact solution, the calculated total source strengths for each isotope, $^{12}Q_{tot}$ and $^{13}Q_{tot}$, are used to solve for the biogenic and the pyrogenic source strengths on each HS separately. Shown below for the Northern HS, where F_b, F_p and F_g are the ^{13}F abundances of biogenic, pyrogenic and geologic sources respectively, calculated from their δ values: $F = \frac{(\delta+1)R}{1+(\delta+1)R}$, with $R = R_{VPDB}$, as follows from Eq. (2.31).

$$\begin{bmatrix} ^{12}Q_{tot} \\ ^{13}Q_{tot} \end{bmatrix} = \begin{bmatrix} F_b & F_p \\ 1 - F_b & 1 - F_p \end{bmatrix}\begin{bmatrix} Q_b \\ Q_p \end{bmatrix} + \begin{bmatrix} F_g Q_g \theta_N \\ (1 - F_g)Q_g \theta_N \end{bmatrix}, \tag{6.9}$$

$$\sum_i {}^{12}F(\delta_i)\dot{x}_{\mathrm{N},i} \qquad \sum_i {}^{13}F(\delta_i)\dot{x}_{\mathrm{N},i}$$

$$\sum_i \lambda_i \leftarrow \boxed{\begin{array}{l}\text{NH}\\ {}^{12}F(\delta_{\mathrm{N}})x_{\mathrm{N}}\end{array}} \boxed{{}^{13}F(\delta_{\mathrm{N}})x_{\mathrm{N}}} \rightarrow \sum_i \alpha_i \lambda_i$$

$$\uparrow\kappa\downarrow \qquad \uparrow\kappa\downarrow$$

$$\sum_i \lambda_i \leftarrow \boxed{\begin{array}{l}\text{SH}\\ {}^{12}F(\delta_{\mathrm{S}})x_{\mathrm{S}}\end{array}} \boxed{{}^{13}F(\delta_{\mathrm{S}})x_{\mathrm{S}}} \rightarrow \sum_i \alpha_i \lambda_i$$

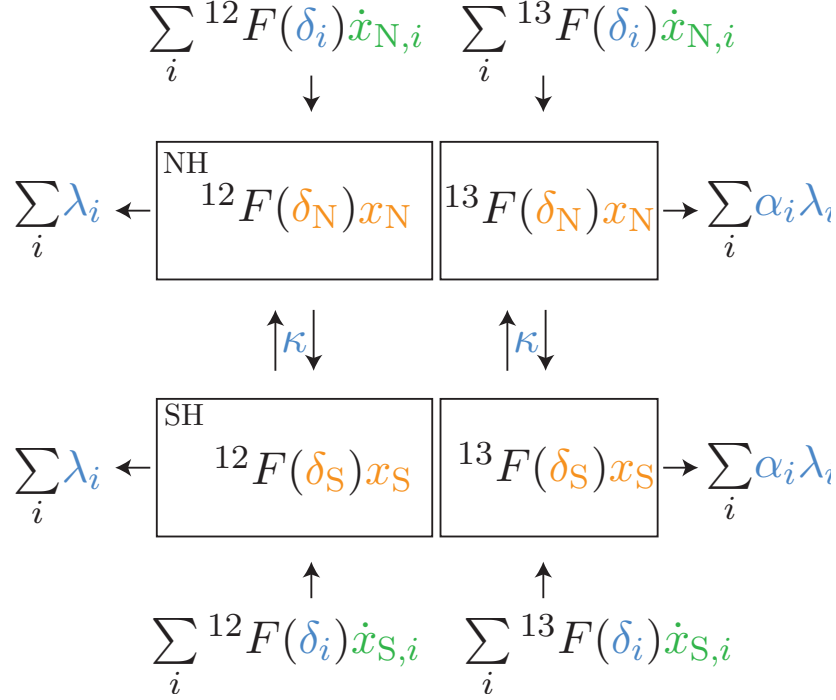$$\sum_i {}^{12}F(\delta_i)\dot{x}_{\mathrm{S},i} \qquad \sum_i {}^{13}F(\delta_i)\dot{x}_{\mathrm{S},i}$$

Figure 6.1: The used model showing the mathematical symbols in colours according to their function: inputs (orange), constants (blue) and outputs (green). $F(\delta)$ denotes F as a function of δ. On each hemisphere, only two of the sources, $\dot{x}_i$, are outputs, while remaining sources are provided as inputs.

The source strengths Q_{b} and Q_{p} result from the reduced row echelon form of the corresponding matrix:

$$\begin{bmatrix} F_{\mathrm{b}} & F_{\mathrm{p}} & {}^{12}Q_{\mathrm{tot}} - F_{\mathrm{g}}Q_{\mathrm{g}}\theta_{\mathrm{N}} \\ 1 - F_{\mathrm{b}} & 1 - F_{\mathrm{p}} & {}^{13}Q_{\mathrm{tot}} - (1 - F_g)Q_{\mathrm{g}}\theta_{\mathrm{N}} \end{bmatrix}. \tag{6.10}$$

Mathematically approximated solution

In the approximated solution, the signature δ of the sources can be used directly, but the signature of the total sources, δ_{tot}, needs to be calculated first: $\delta = \frac{F/(1-F)}{R_{\mathrm{VPDB}}} - 1$.

$$Q_{\mathrm{tot}} = Q_{\mathrm{b}} + Q_{\mathrm{p}} + Q_{\mathrm{g}} \tag{6.11}$$

$$\delta_{\mathrm{tot}}Q_{\mathrm{tot}} = \delta_{\mathrm{b}}Q_{\mathrm{b}} + \delta_{\mathrm{p}}Q_{\mathrm{p}} + \delta_{\mathrm{g}}Q_{\mathrm{g}} \tag{6.12}$$

The geologic sources can be assumed as being constant over the considered time period, and they can be given as an input parameter. To find an expression for Q_{p} and Q_{b} independent from each other, Q_{p} is isolated in order to be substituted:

$$Q_{\mathrm{p}} = Q_{\mathrm{tot}} - Q_{\mathrm{b}} - Q_{\mathrm{g}}. \tag{6.13}$$

This expression for Q_{p} can be substituted into Eq. (6.12) and solved for Q_{b} and similarly for Q_{p}. These are found as

$$Q_{\mathrm{b}} = \frac{Q_{\mathrm{tot}}(\delta_{\mathrm{tot}} - \delta_{\mathrm{p}}) + Q_{\mathrm{g}}(\delta_{\mathrm{p}} - \delta_{\mathrm{g}})}{\delta_{\mathrm{b}} - \delta_{\mathrm{p}}} \tag{6.14}$$

$$Q_{\mathrm{p}} = \frac{Q_{\mathrm{tot}}(\delta_{\mathrm{tot}} - \delta_{\mathrm{b}}) + Q_{\mathrm{g}}(\delta_{\mathrm{b}} - \delta_{\mathrm{g}})}{\delta_{\mathrm{p}} - \delta_{\mathrm{b}}}. \tag{6.15}$$

6.4 Data preparation

Four different data series are needed for the two times two-box model including a separate box for the northern and southern hemisphere, with a box for each isotope. The given data series (Tab. 6.1) were smoothed such as to finally obtain four series in yearly intervals that they can be used in the model, shown in Fig. 6.10. For this, a Gaussian smoothing algorithm was developed and applied. The smoothing of each data series is explained in the following subsections.

Table 6.1: Source data series, used in the preparation process. Grey: disregarded series, cf. text.

Data	Site (Core)	Reference		Age scale	Gas standard
$x_N(t)$	NEEM (2011-S1)	Rhodes (2013)	[158]	[166, 104]	NOAA04 [167]
	GISP 2	Mitchell (2013)	[168]	(Paper in prep.)	NOAA04
$x_S(t)$	Law Dome (DSS)	MacFarling (2004, 2006), Etheridge (1998)	[26, 169] [171]	LD1 [170]	NOAA04
	WAIS (WDC05A)	Mitchell (2011a,2011b)	[172, 133]	WDC05A:2 [71]	NOAA04
	Law Dome (DSS)	Ferretti (2005)	[25]	N/A, possibly [171]	CSIRO94
$\delta_N(t)$	NEEM	Sapart (2012)	[1]	GICC05	VPDB
	GRIP (Eurocore), NEEM	(This study, CIC data)		[173],GICC05	VPDB
$\delta_S(t)$	WAIS	Sowers (2009), Mischler (2009)	[71, 174]	WDC05A:2	VPDB[a]
	Law Dome (DSS)	Ferretti (2005)	[25]	N/A, possibly [171]	VPDB

The record for $x_S(t)$ by Ferretti (2005) showed to have the very same data points as MacFarling, but some of them (very few only) were shifted by a considerable amount. Since MacFarling's data is published online with all other δ^{13}C data from this lab, whereas Ferretti's data are not, it was therefore decided to disregard the mixing ratio data of Ferretti (2005).

As opposed to Mischler (2009) [71], we do not shift the time scales for the isotope data, which they did for 20 years in order to "account for a time lag for atmospheric CH_4 isotopic values to reach equilibrium relative to concentration changes", which they justified with the research by Tans (1997) [160], who developed a forward model and concluded that changes in spatial gradients caused by a varying source configuration need a longer time (20 a) to equilibrate on the isotope signature than on the mixing ratio (2 a). We think it is justified to use the values as is, since the model is supposed to simulate the actual processes taking place in nature.

6.4.1 Northern hemispheric isotope signature

For the NH isotope data, the record of Sapart (2012) [1] is being used as a base line. This record is shown over the entire period of interest in Fig. 6.2.

Now, our δ^{13}C measurement data, can be added to the record and substitute their data at the corresponding times, as shown in Fig. 6.3.

---

[a] Even though Sowers (2009) reports the δ^{13}C values as being expressed against PDB, they are not. The used standard is VPDB. If it were in fact PDB, the values needed to be adjusted for different standards as according to Eq. (2.32). But this would result in an increae of about 5‰, which would make negative emission necessary in the model run.
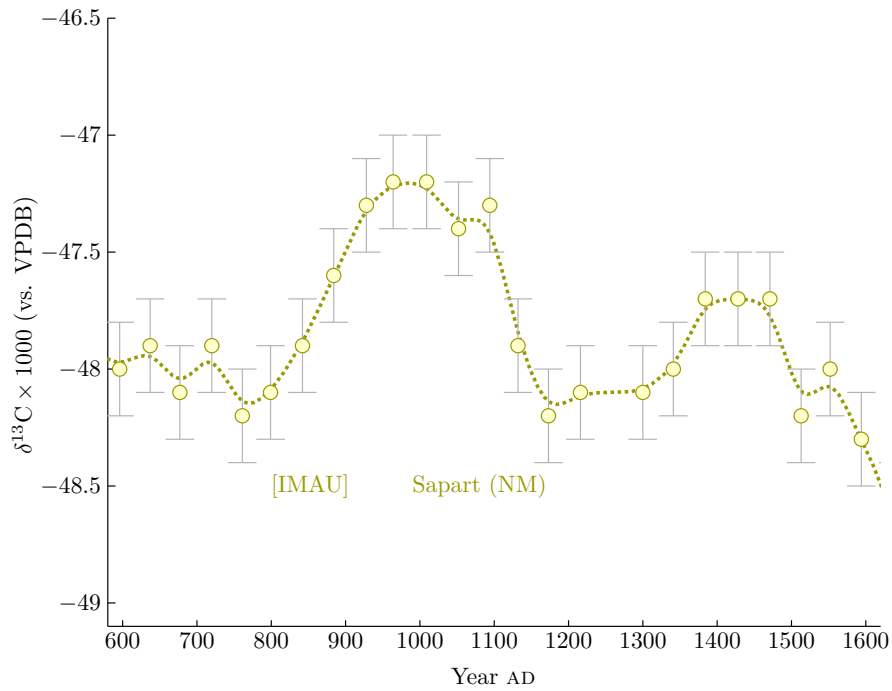
Figure 6.2: Data of Sapart (2012) [1]. The smoothed line was obtained with the area algorithm, using a $\sigma_0 = 20\,\mathrm{a}$.
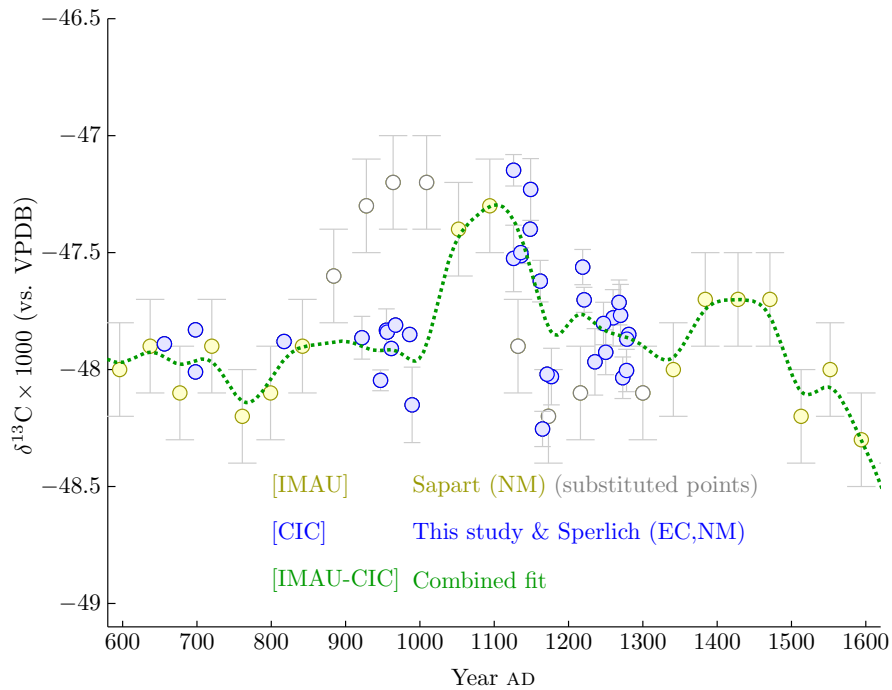

Figure 6.3: Data of Sapart (2012) [1] in yellow, and grey. The outlined grey points were substituted through our data (blue). The smoothed line was obtained with the area algorithm, using a $\sigma_0 = 20\,\mathrm{a}$.

6.4.2 Southern hemispheric isotope signature

The individual records of Southern hemispheric isotope signature, from Ferretti (2005) [25] and Sowers (2009) / Mischler (2009) [174, 71] are shown in Fig. 6.4.
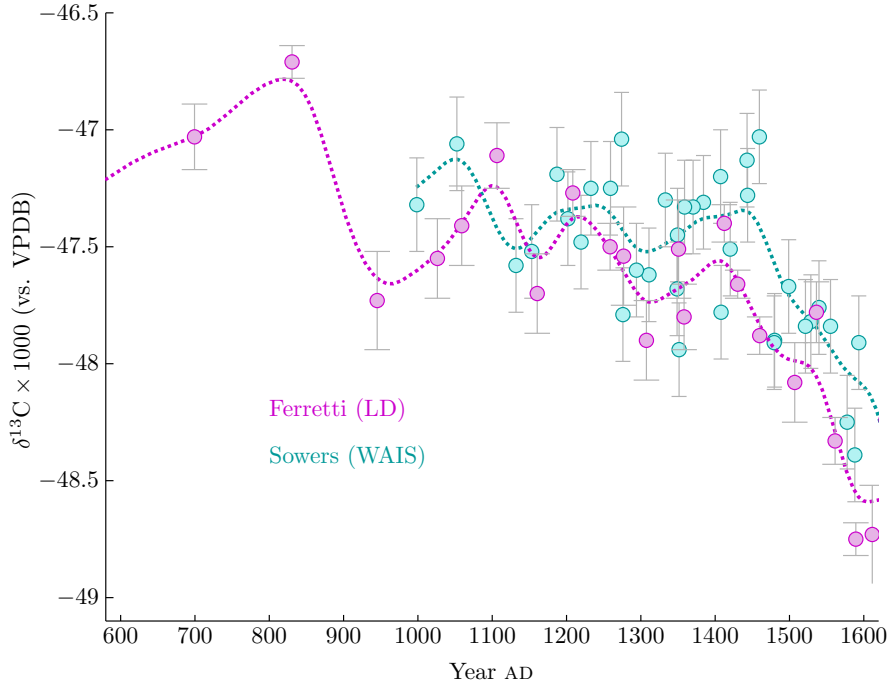

Figure 6.4: The two records of Southern hemispheric isotope signatures.

Unfortunately the record before AD 800 is only based on two values, and thus not very reliable. However we consider it a better solution to include it despite this, instead of constructing a record based on the NH isotope values.

To combine the two Southern hemispheric $\delta^{13}C$ records, the maximum area of overlapping data in the interval of interest ($t \in [t_{\min}, t_{\max}] = [700, 1600]$ AD) was identified by

$$t_{\text{overlap}} = t \in [\max\{\min(t_{\text{LD}}), \min(t_{\text{WS}}), t_{\min}\}, \min\{\min(t_{\text{LD}}), \min(t_{\text{WS}}), t_{\max}\}]. \tag{6.16}$$

The difference between the mean values of the individually smoothed curves over this time period, t_{overlap}, was used to shift both data series by half the offset, after which the series were combined and smoothed together. This approach is justified, by assuming that both the Law Dome points and the WAIS points have a similar validity in time, i.e. assuming that a similar amount of ice was used to measure points of both series.

This approach yields very satisfactory results, as in Fig. 6.5. We have also tried another option that consist in the combination of the individually smoothed curves. But this has the drawback of resulting in dis-continuities at the point ($t = 998$), were the WAIS record begins, which then need to be smoothed out again, e.g. with an additional smoothing that processes the entire combined curve again.
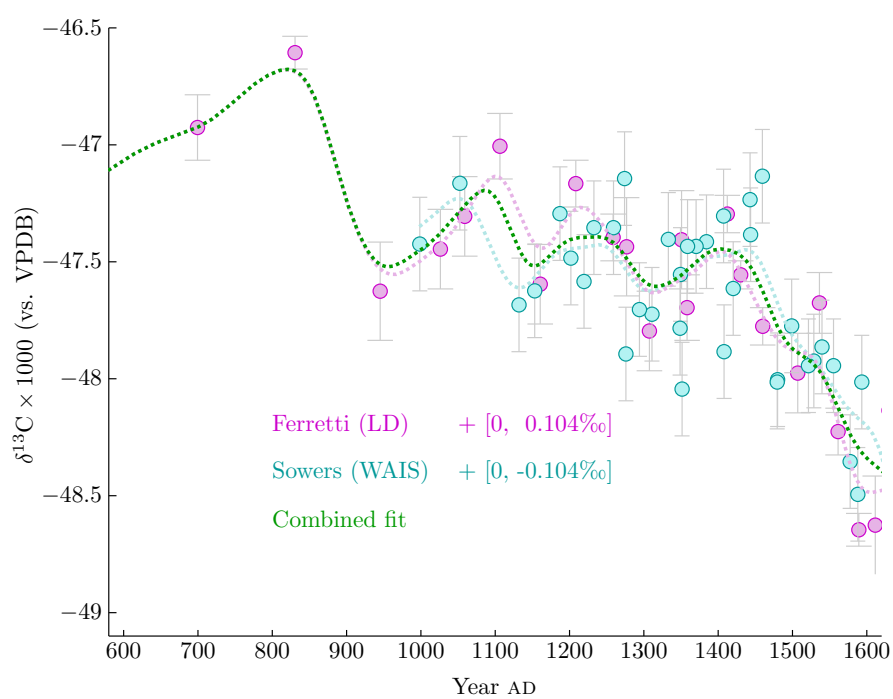
Figure 6.5: Smoothed Southern hemispheric isotope signature records through all points of both records.

6.4.3 Northern hemispheric mixing ratio

The Northern hemispheric mixing ratio data from Continuous Flow Analysis (CFA) by Rhodes (2013) [158] shows considerable parts of missing data. These missing data can be fixed with discrete data from the GISP2D core by Mitchell (2009) [133].

The nature of the smoothing algorithm makes it necessary to remove partial spikes that lie right at the beginning of missing data periods, since the last point will be excessively weighted as compared to the rest of the data series. This was the case for $t = $ AD 710.
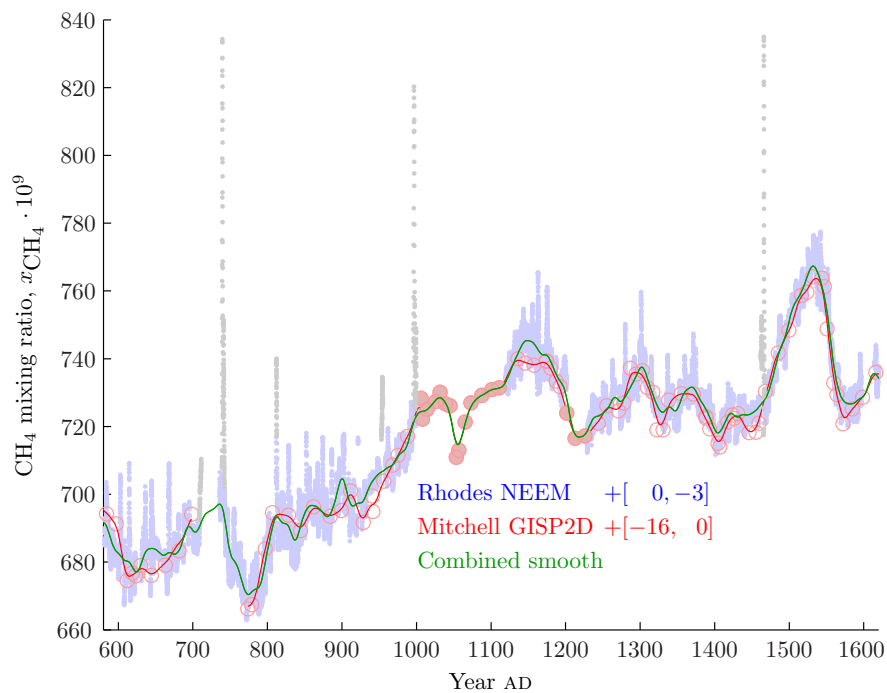

Figure 6.6: Methane mixing ratio on the Northern hemisphere, smoothed using the area algorithm with $\sigma_0 = 5\,a$, the filled GISP2D points have been included in the calculation of the combined smooth (green).

6.4.4 Southern hemispheric mixing ratio

Two data records for the Southern hemispheric mixing ratio were available. Similarly to the SH isotopic signatures, these two series did not show an even distribution over time either. However, unlike the isotopic signature, the points of each series follow a line, and can be fitted nicely on their own, as shown in Fig. 6.7. As it can easily be seen, there seems to be an offset on the time axis, especially well visible in
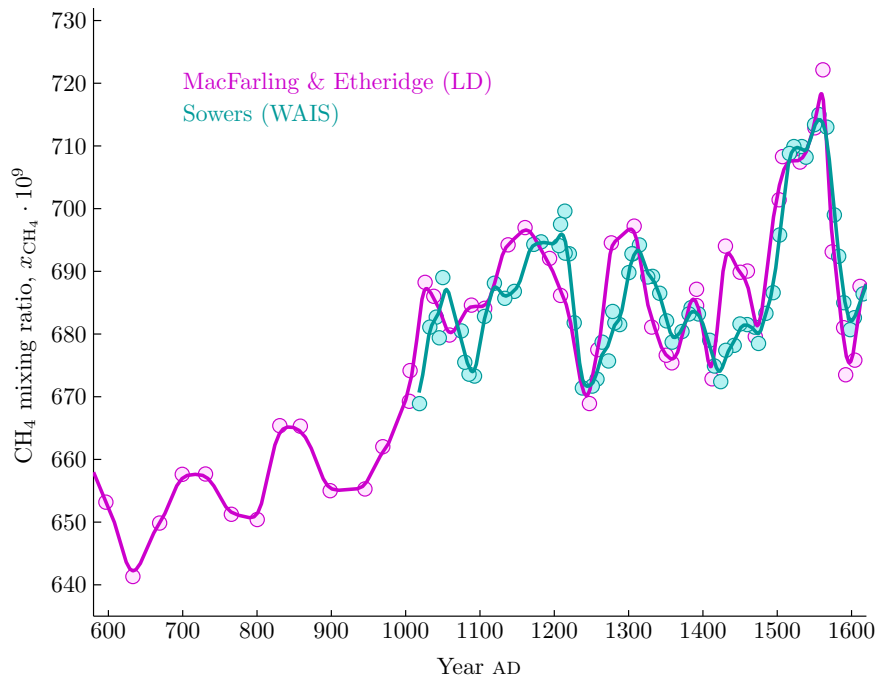

Figure 6.7: Methane mixing ratio on the Southern hemisphere, each smoothed using the area algorithm with $\sigma_0 = 5\,a$.

the first century of the second millennium (AD 1000 – 1100). The offset was determined by eye, using a manual dichotomy approach to find the best fit, and turned out to be 13 years. In regard to the mixing ratio axis offset, the same concept as for the isotopes was used to correct for eventual offsets (difference of means over the investigated period). The offset correction, with its 0.75 ppm, was almost non-existent. For the construction of a unified record, the same concept as for the SH isotopes was tried: concatenate the points and smooth over the new entire set of points. However, due to uneven spacing, this resulted in some awkward results, the strangest shapes of the fitted curve can be found around $t = $ AD 1190 and $t = $ AD 1450, were the fitted curve "sinks" to the lower record, induced by a short gap in the upper record, even though neither of the two records show strange discontinuities. Hence, the obtained smoothing was rejected, cf. Fig. 6.8. A better solution is obtained using the two singly smoothed curves (Fig. 6.7) and combining them through concatenation and smoothing them anew, using the density function algorithm with $\sigma = 5\,a$. The is is necessary, as area weighting would have problems, since the algorithm cannot handle multiple values at the very same t. The obtained smoothing has no strange shapes and looks convincing, Fig. 6.9.
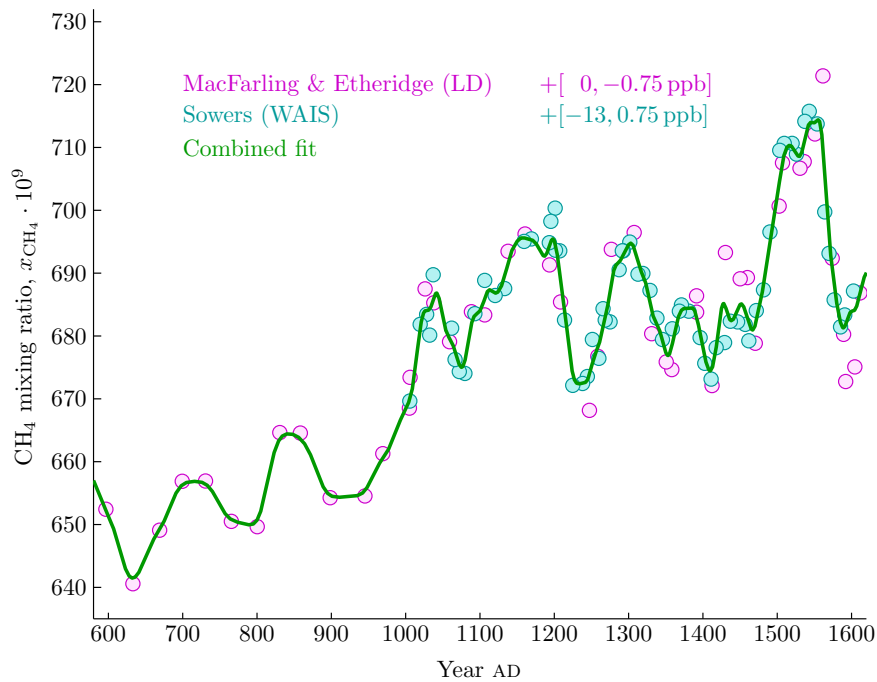
Figure 6.8: Methane mixing ratio on the Southern hemisphere, using all points (shifted!) from both records, smoothed using the area algorithm with $\sigma_0 = 5\,a$.
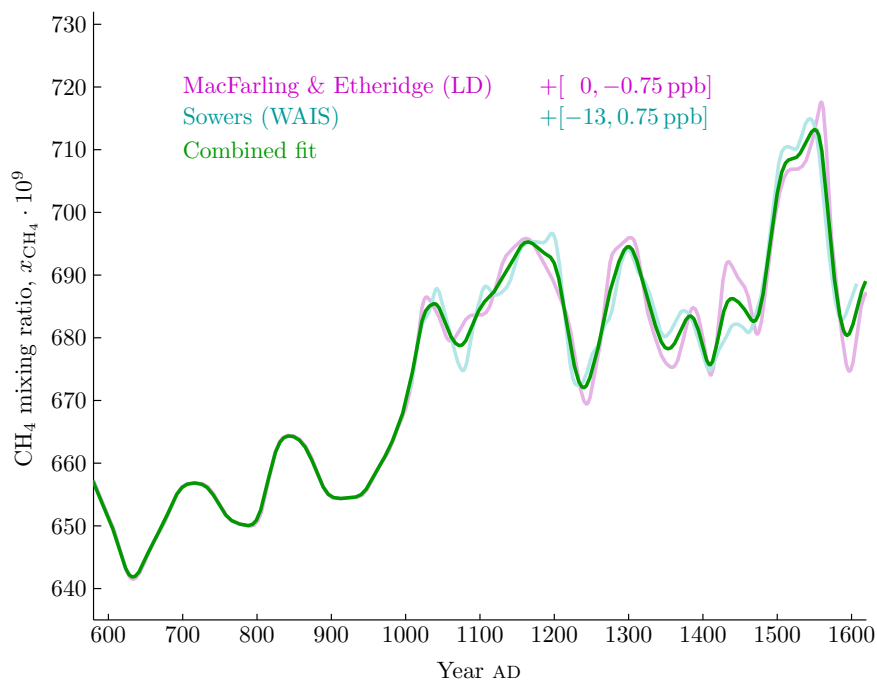

Figure 6.9: Methane mixing ratio on the Southern hemisphere, each record smoothed using the area algorithm with $\sigma_0 = 5\,a$. The smoothed records were combined (2 points at each t) and smoothed again using the density algorithm with $\sigma = 5\,a$.

6.5 The fitted data set

The fitted data series are shown in Fig. 6.10 and already at this point, the differences between the [IMAU] and the [IMAU-CIC] can be analysed.
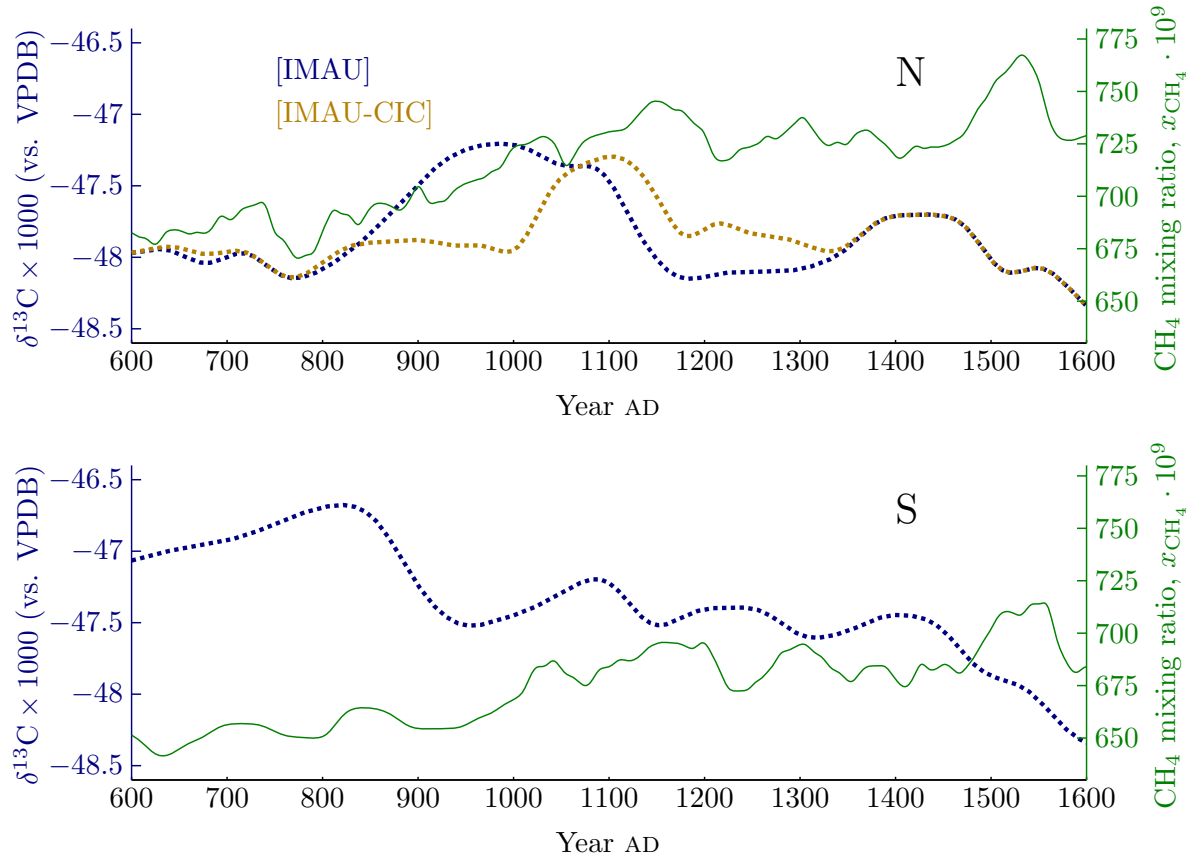

Figure 6.10: Mixing ratio and isotopic records from both hemispheres. Data sources as in Table 6.1.

With [IMAU], an excursion (a rise and subsequent fall) of the carbon isotopic signature is observed between AD 800 and 1150, while [IMAU-CIC] report this excursion to be briefer and occur later, from AD 1000 to 1175. Since the isotopic signature of biogenic emissions is known to be lighter (more negative) compared to the one of pyrogenic emissions, the modelled biogenic emission series resulting from the [IMAU] data can be expected to stay lower for a longer time at the end of the first millennium, when the rising emissions on the North Hemisphere would be mostly due to rising pyrogenic emissions, which is also reflected in a rising mixing ratio, x_{CH_4}. While at the end of the excursion, biogenic emissions can be expected to be higher with [IMAU].

6.6 Gaussian smoothing

A smoothed time series is to be constructed from a dataset with a time array $\mathbf{t}$ and a corresponding value array, $\mathbf{x}$. Each array consists of n elements $x_i(t_i)$. And the smoothed curve $\check{\mathbf{x}}$ needs to have equally spaced time intervals $\check{\mathbf{t}}$. The smoothing will either increase (in the case of sparse discrete measurements) or decrease (for dense CFA measurements) the data density.

For a fixed smoothing window size, σ, the Gaussian probability density function (PDF), ϕ, at time t_j of the smoothing is given as a vector, $\boldsymbol{\phi}$, with a density value for each data point by:

$$\boldsymbol{\phi}(t_j) = \frac{1}{\sigma\sqrt{2\pi}} \exp\left(-\frac{(\mathbf{t}-t_j)^2}{2\sigma^2}\right) \tag{6.17}$$

Finally, the value of the new, smoothed data point, is obtained by taking the dot product of density and values and dividing by the total weight:

$$\check{x}_j = \frac{1}{\sum \boldsymbol{\phi}(\check{t}_j)} \boldsymbol{\phi}(\check{t}_j) \cdot \mathbf{x}. \tag{6.18}$$

This algorithm is widely used, and is a common operation in image processing (2D smoothing over all pixels of an image). The result of this smoothing algorithm is shown in Fig. 6.11a. The density
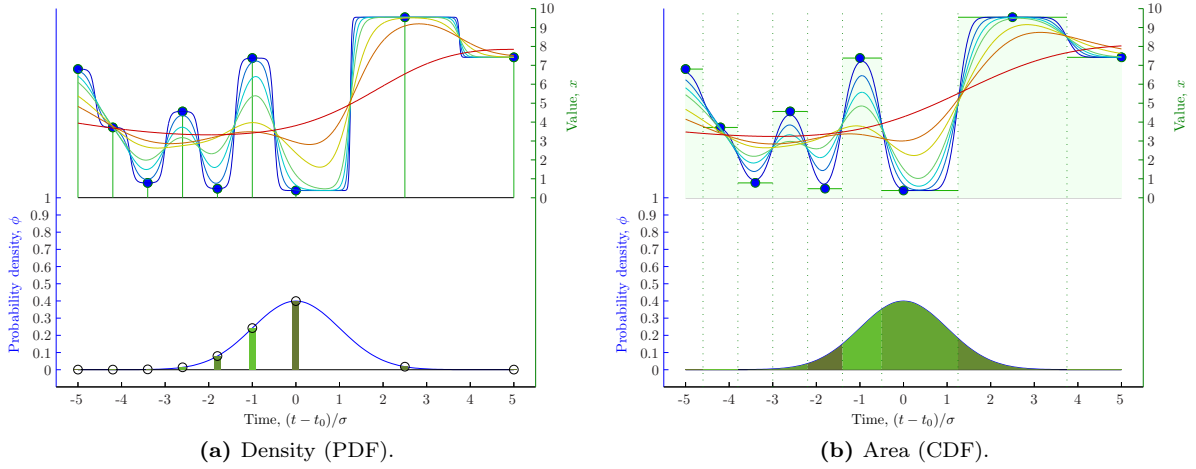

Figure 6.11: Gaussian smoothing using density and area for various sigmas σ of 0.2 (blue), 0.3, 0.4, 0.5 (green), 0.75 (yellow), 1 and 2 (red). The bell curve shows the weighting for the point at $t=0$ for $\sigma=1$ (orange). The bars and areas in various green tones represent the ϕ and Φ values respectively.

algorithm gives good results, if the x-axis resolution is to be kept constant or decreased, and if samples are uniformly spaced. For non-uniformly spaced samples and if the resolution is to be increased (such as if missing points in the concentration from CFA measurements are fixed using some points from discrete measurements), the resulting curve is much less accurate, than with another formula. Instead of weighing each point with its PDF value, it is weighted with the cumulative density area around that point, that is, from the last midpoint between two adjacent point to the next one, i.e. from $\frac{t_{i-1}+t_i}{2}$ to $\frac{t_i+t_{i+1}}{2}$. The cumulative density function (CDF, referred to as "area smoothing") is defined with the error function by:

$$\Phi'(\check{t}_j, t_i) = \frac{1}{2}\left[1 + \operatorname{erf}\left(\frac{t_i - \check{t}_j}{\sqrt{2\sigma^2}}\right)\right], \tag{6.19}$$

where the error function (erf) is defined as

$$\text{erf}(x) = \frac{2}{\sqrt{\pi}} \int_0^x e^{-t^2} \, dt. \tag{6.20}$$

Hence, the resulting cumulative density for each data point $x_i(t_i)$, when calculating the smoothed point $\breve{x}_j(\breve{t}_j)$, is expressed by:

$$\Phi(\breve{t}_j, t_i) = \frac{1}{2} \left[\text{erf}\left(\frac{\frac{t_{i+1}+t_i}{2} - \breve{t}_j}{\sqrt{2\sigma^2}} \right) - \text{erf}\left(\frac{\frac{t_{i-1}+t_i}{2} - \breve{t}_j}{\sqrt{2\sigma^2}} \right) \right] \tag{6.21}$$

The value of the smoothed point is obtained by summing all individual cumulative densities multiplied with their corresponding data points. A division through the total area is still needed, even though the total area under the Gauss curve always equals one: in the beginning and the end, the data points during the first and last 3σ would otherwise be much too low.

$$\breve{x}_j = \frac{1}{\sum_{i=1}^{m} \Phi(\breve{t}_j, t_i)} \sum_{i=1}^{m} \Phi(\breve{t}_j, t_i) x_i. \tag{6.22}$$

This second algorithm produces a curve (Fig. 6.11b) that is smoother for the same window size as the corresponding smooth using density values. Moreover, it gives a less edgy fit and less distortion, e.g. yellow curve at $t = 0.5\,\sigma$. Also have a look at the weight (lower graph) of the point at $t = 2.5\,\sigma$, which in the density algorithm (PDF) is almost zero, while it has a larger weight in the area (CDF) algorithm.

When there is heterogeneous spacing, a too large of a sigma results in too excessive a smoothing over areas with a high point density, while on the other hand a too small of a sigma gives rise to a smoothed curve that looks like a step function: while smoothing proceeds from point $P_1(t_1, x_1)$ to point $P_2(t_2, x_2)$ the smoothing curve would be very close to value x_1 up to midway, $t_m = 1/2 \cdot (t_1 + t_2)$, since the total weight is largely dominated by the fraction of point P_1. At midway, the weights of each of the point are equal and thereafter P_2 dominates. This is true for small sigmas, $\sigma < (t_2 - t_1)$. (An additional example of the difference between the two modes is given in Appendix A.6).

Hence for heterogeneous data samples, a larger sigma should be used, for larger spacing on the t-axis $(t_{i+1} - t_i)$. If the spacing exceeds a certain value, sigma gets adjusted to a $\sigma(t)$, otherwise, the original sigma, σ_0, is used, Eq.(6.24). Since there is one data point more in number than there are spaces in between, the $\sigma(t)$ from the space to the right and to the left of a point is averaged for each point, Eq.(6.23). For the first and (last) point, the space to the right (left) is taken alone, since there is no averaging over two spaces possible.

$$\sigma(t_i) = \frac{\sigma'(t_{i-1}, t_i) + \sigma'(t_i, t_{i+1})}{2} \tag{6.23}$$

$$\sigma'(t_j, t_k) = \begin{cases} \exists\, t_j, t_k & \begin{cases} \frac{t_k - t_j}{\zeta} & \text{for } t_k - t_j > \zeta \sigma_0 \\ \sigma_0 & \text{otherwise} \end{cases} \\ \nexists\, t_j & \sigma'(t_{j+1}, t_{k+1}) \\ \nexists\, t_k & \sigma'(t_{j-1}, t_{k-1}) \end{cases}, \tag{6.24}$$

where ζ is a constant to be determined.

The data being available as an array, `Data[t,x]`, the above equations translate into the following code:

Listing 6.1: The computation of an array of dynamic sigmas as a function of data spacing. (MATLAB)

```matlab
for i=1:length(Data)−1
    dist=Data(i+1,1)−Data(i,1); % d = t_{i+1} − t_i
    if dist>zeta*sigma_0          % d > ζσ_0
        sigma(i)=dist/zeta; % σ' = d/ζ
    else
        sigma(i)=sigma_0;     % σ' = σ_0
    end
end
sigma=[.5 .5]*[sigma sigma(end); sigma(1) sigma]; % sigma being a line vector
```

This algorithm ensures thus a minimum standard-deviation time of $\sigma_{\min} = \sigma_0$ that is increased for time spacings larger than $\zeta\sigma_0$.

A comparison of the smoothed curves and the σ values applied to each point for three different minimal σ values, σ_0, and various ζ values each, is shown in Fig. 6.12. The value of ζ lies at its optimum at around 3, when the value is large enough that the fitted curve no longer touches the data points (e.g. in the figure for $\sigma_0 = 5\,\mathrm{a}$ at $t = 800$), but when it is at the same time small enough to allow for the contribution of each data point to be visible (e.g. in the figure for $\sigma_0 = 5\,\mathrm{a}$ at $t = 1300$). The choice of $\zeta = 3$ makes also sense, since at $\pm 3\sigma$ from the mean, more than 99.7% of total CDF area are included.
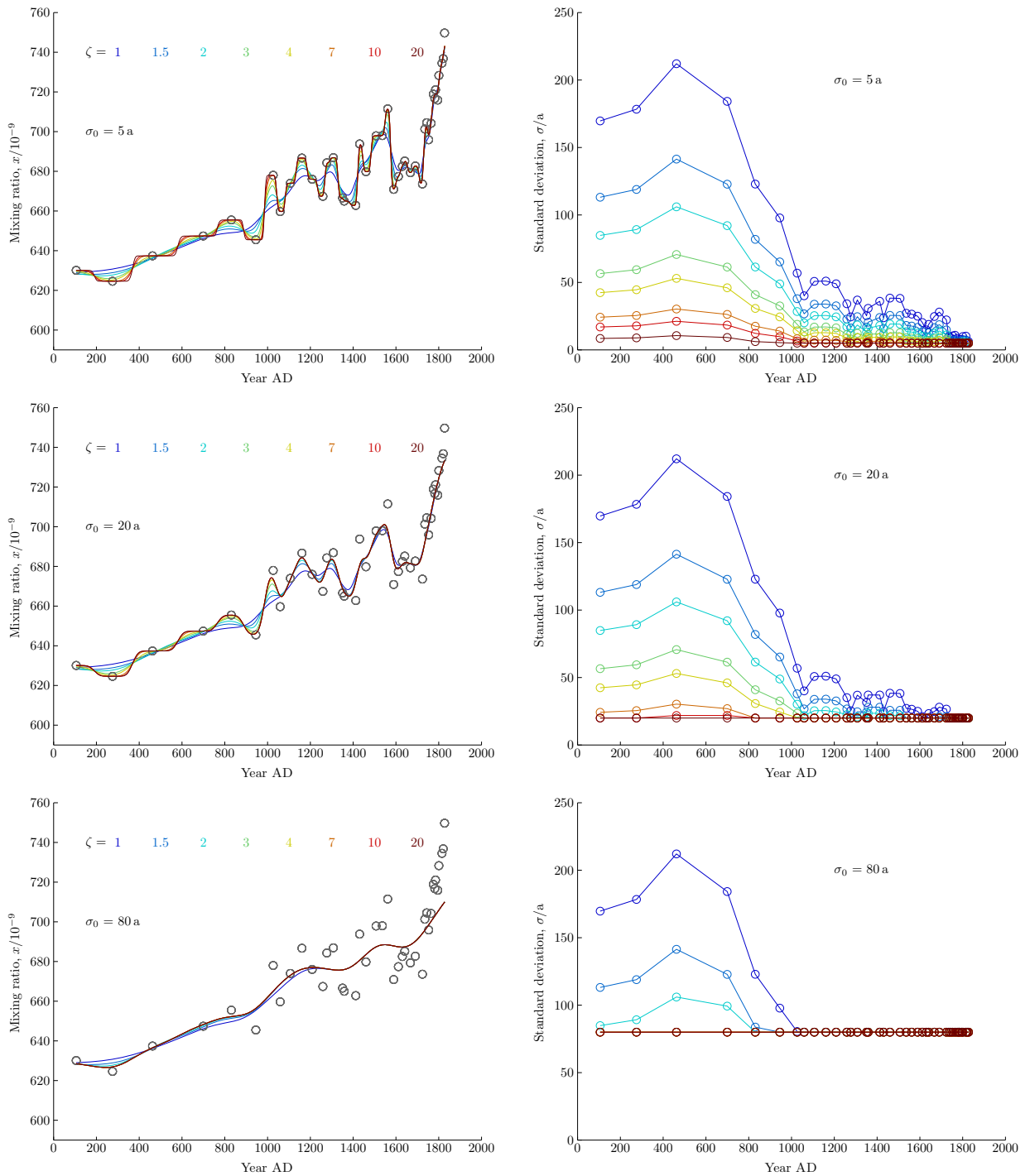
Figure 6.12: Gaussian smoothing using three different minimal sigma σ_0 values, and each of them various ζ values. The fitted curve on the left side, and the corresponding sigmas to the right.

.

6.7 Parameter estimation

6.7.1 Size of the atmosphere, n_{atm}

The size of the atmosphere n_{atm}, in mol, needs to be estimated to be able to relate mixing ratios (in ppm $:= 10^{-9}$) of methane in the atmosphere to its sources, given in teragrams (Tg). There are several ways to calculate the mass of the atmosphere. One of these would be to integrate the pressure over the sphere, and another way is to start with the pressure at ground level $p_0 = 1.01325 \, bar = 101\,325 \, Pa$, with $p = F/A$. The area being the area of the Earth, with a radius of $r = 6370 \, km \Rightarrow A = 4\pi r^2 = 5.1 \cdot 10^{14} \, m$ and hence $F = Ap = 5.20 \cdot 10^{19} \, N$.

This, also equals $F = mg$, where we approximate g as being constant (assuming a constant radius in Newton's general formula $F = G\frac{m_1 m_2}{r^2}$, since the thickness of the stratosphere is negligible compared to the radius of the earth: $60 \, km \ll 6370 \, km = r_{earth}$).

$\Rightarrow m = F/g = 5.3 \, Zg.$ $(1 \, Zg = 10^{21} \, g = 10^{18} \, kg)$

With the average molar mass of air being $M_{air} = 28.97 \, g/mol = 0.02897 \, kg/mol$, the size of the atmosphere is given with $n_{atm} = m/M = 182 \, Emol = (182 \cdot 10^{18} \, mol)$.

6.7.2 Interhemispheric exchange time, τ_{exc}

The interhemispheric exchange time has been estimated by various authors, using the concentrations of different tracer gases to calculate the exchange times.

Table 6.2: Published estimates of interhemispheric exchange time τ_{exc}.

Author	τ_{exc} value	Method	
Junge (1962)	$2 - 3.3 \, a$	CH_3T distribution	[163]
Newell (1969)	$0.87 \, a$	Meteorological observations	[175]
Czeplak (1975)	$0.9 - 1.8$	CO_2 and ^{85}Kr data	[176]
Jacob (1987)	$1.1 \, a$	3D model with ^{85}Kr	[177]
Geller (1997)	$1.3 \pm 0.1 \, d$	SF_6 (surface measurements)	[178]
Levin (1996)	$1.6 - 1.7 \, a$	^{85}Kr (surface measurements)	[179]
Levin (1996)	$1.1 \, a$	^{85}Kr model	[179]

The two box model is based on the assumption that the reservoirs are well mixed and the exchange at the border line is a first-order process [176]. Jacob (1987) [177] pointed out that due to vertical gradients, especially present in the NH, τ_{exc}, values calculated using surface data will be larger than values calculated from vertically integrated data.

The annual exchange ratio, κ_{exc}, is then calculated as $\kappa = \frac{1}{2\,\tau_{exc}}$. If the exchange time is one year, half the mass of each HS will have been transferred to the other HS after a year. If the model has a time resolution of 1 year, the interpolar difference of CH_4 mixing ratio will be set to zero by this mixing during the calculation, and the total interpolar difference has to be a result of the different emission strengths on the two hemispheres, cf. formulae in Section 6.3.

For the model we chose a $\tau_{exc} = 1.0 \, a$, similar to Tans (1997) and Miller (2005) [160, 94]. The value of τ_{exc} was varied in the sensitivity study from $1 \, a$ to $3 \, a$, as the exchange time can never be smaller than the model's time resolution, due to the mathematics of the model.

6.7.3 Atmospheric lifetime of methane, τ_{life}

In Section 2.3.3, the sink fractionation parameters, ε have been discussed. Considering the sink rate, only their relative contribution was mentioned. The sink rate, λ, is calculated from the lifetime τ, which is, in steady state, defined by the total atmospheric mass (m) divided by its annual total source strength ($\dot{m}$): $\tau_{\text{CH}_4} = \frac{m_{\text{CH}_4}}{\dot{m}_{\text{CH}_4}}$. Some estimates of this parameter are shown in Tab. 6.3.

Table 6.3: Estimated vaklues for the atmospheric lifetime of CH_4.

Author		Lifetime, τ_{life}/ a
Ehhalt (1978)	[180]	$2.5 - 11$, most likely 5
Mayer (1982)	[181]	$2.7 - 15$
Chappellaz (1997)	[162]	9.9 for PIH
Denman (2007)	[?]	8.7 ± 1.3

For the model, a τ_{life} of 7 ± 1 a was chosen, the sink strengths of the soil and stratospheric sink have been taken as $\lambda_{\text{soil}} = 0.008\,\text{a}^{-1}$ and $\lambda_{\text{strat}} = 0.006\,\text{a}^{-1}$, which is in agreement with other research, such as Sapart (2012) [1].

Out of the atmospheric lifetime, and the lifetimes of the two minor sinks, soil and stratosphere, the sink rate of the tropospheric sink was calculated:

$$\lambda_{\text{OH}} = \frac{1}{\tau_{\text{life}}} - \lambda_{\text{soil}} - \lambda_{\text{strat}} \tag{6.25}$$

6.7.4 Summary of parameters

The previously determined parameters that were used in the model are summarized in Tab. 6.4 and 6.5.

Table 6.4: Hemispheric variables as used in the model.

Parameter	Unit	Northern Hemisphere	Southern Hemisphere	Comments
x	-	$x_{\text{N}}(t)$	$x_{\text{S}}(t)$	cf. Tab. 6.1
δ	-	$\delta_{\text{N}}(t)$	$\delta_{\text{S}}(t)$	cf. Tab. 6.1
θ_{g}	-	0.7 ± 0.1	0.3 ± 0.1	cf. Section 2.3.3
θ_{soil}	-	$4/3 \pm 1/6$	$2/3 \pm 1/6$	cf. Section 2.3.5

Table 6.5: Global variables as used in the model.

Parameter	Unit	Value	Comments
n_{atm}	Emol	182	cf. Section 6.7.1
τ_{exc}	a	$1.0(+2.0)$	cf. Section 6.7.2
τ_{life}	a	7 ± 1	cf. Section 6.7.3
δ_{b}	‰	-59.6 ± 2.0	cf. Section 2.3.1
δ_{p}	‰	26.6 ± 2.6	cf. Section 2.3.2
δ_{g}	‰	-40.0 ± 10.0	cf. Section 2.3.3
$\dot{m}_{\text{g}}$	$\text{Tg}\,\text{a}^{-1}$	30 ± 20	cf. Section 2.3.3
λ_{OH}	a^{-1}	0.129 ± 0.020	Calculated from τ_{life}, Eq. (6.25).
λ_{strat}	a^{-1}	0.006 ± 0.003	cf. Section 2.3.4
λ_{soil}	a^{-1}	0.008 ± 0.005	cf. Section 2.3.5
ε_{OH}	‰	-3.89	cf. Section 2.3.4
$\varepsilon_{\text{strat}}$	‰	-6 ± 3	cf. Section 2.3.4
$\varepsilon_{\text{soil}}$	‰	-17.6 ± 3.2	cf. Section 2.3.5

Chapter 7

Modelling results

7.1 Modelled source values

The model presented in the last section was run for various sets of time series to construct the time series for the two biogenic and pyrogenic sources on each hemisphere. These time series are discussed in this section. First, the data measured during this study is used to substitute values in the set of Sapart (2012) [1], i.e. the yellow line in Fig. 6.10, (hereafter: [IMAU-CIC]). Next, the obtained results are compared against the unmodified record of Sapart (2012) (hereafter: [IMAU]), and against the constructed source time series shown in the Nature paper of Sapart (2012) (hereafter: [Sapart]). In the end, a study on the sensitivity of the parameters used in this model was carried out.

7.1.1 Using data from this study [IMAU-CIC]

First, a plot of the modelled data is shown in Fig. 7.3. Second, the data is further analysed by calculating the changes in the individual emission source series relative to the average. Sum and difference of the anomalies on the two hemispheres reveal additional information. And third, the setting of the absolute value is discussed.

Change in emissions

Since the absolute values of the emission time series vary depending on the choice of parameters, anomaly plots, where the difference to the millennial average (AD 600 to 1600) is plotted, are much less dependent on the choice of parameters. These anomalies are shown for both hemispheres and both sources in Fig. 7.1.
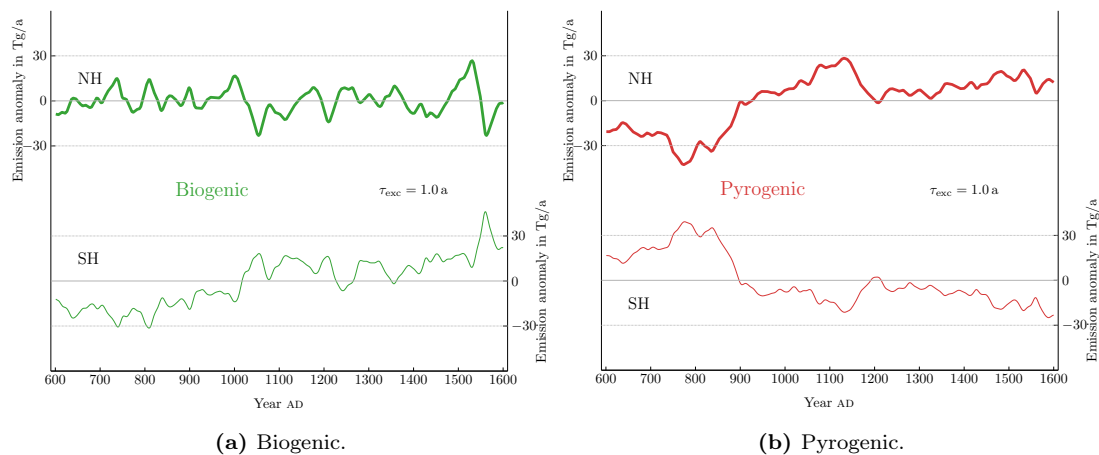

(a) Biogenic.

(b) Pyrogenic.

Figure 7.1: Emission strength anomalies to the mean over the considered period for the NH (thick line) and the SH (thin line).

During the whole time period considered, **biogenic** emissions in the **Northern** Hemisphere are somewhat stable, with visible peaks of around $20\,\mathrm{Tg/a}$ magnitude in AD 730, 810, and 1000. The minimum is reached in AD 1050, and the maximum in AD 1530. This maximum is followed by a steep decline, and a rapid recovery until AD 1600

Meanwhile in the **Southern** Hemisphere, emissions are in a low trend upto year AD 1000, after which they rise abruptly. They stay somewhat constant with a few local minima until AD 1530, when emissions spike high and reach the maximum at AD 1560 and recover again thereafter.

Over the whole 1000 years modelling period, no trend can be identified in the North, whereas in the South, emissions are clearly rising by about $35\,\mathrm{Tg\,a^{-1}}$ over the period.

For **pyrogenic** emissions, the two hemispheres are more "similar and opposite to each other" than they are for biogenic emissions. The North hemispheric emissions feature a decline to AD 780 followed by a **rise** up to AD 1130 a step down to AD 1200 a soft and bumpy rise until AD 1600, while the South hemispheric emission are similar but opposite.

Global sum of change in emissions

The changes observed previously occur almost simultaneously on the two hemispheres but in opposite direction, which suggests an investigation of the sum of both hemispheres' emissions, shown in Fig. 7.2 and discussed below.
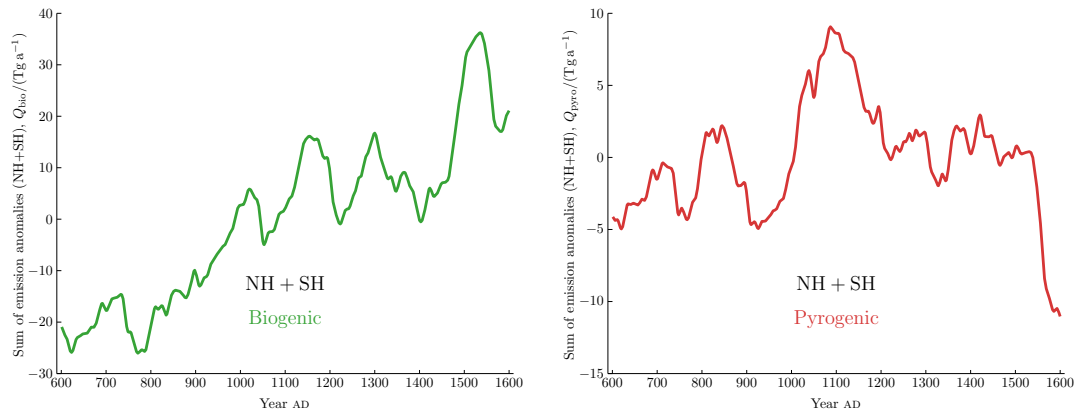

Figure 7.2: Sum of biogenic and pyrogenic source strength anomalies to the mean over the considered period. Notice the different y-axes.

For **biogenic** sources, a much stronger trend becomes visible than what was present in the Southern Hemisphere alone, that is, an increase of about $50\,\mathrm{Tg\,a^{-1}}$. Here, there is a small bump from AD 600 to 800 followed by a period of increasing emissions up to the first of three peaks at AD 1020, 1150 and 1300 followed by a large peak with maximum height at AD 1535.

The sum plot of **pyrogenic sources** shows very low absolute values, as emissions on the two HS are almost equal and opposite. Visible are two small spikes at AD 710 and 820 leading to a steep surge around AD 1100, followed by a smoother decay and a plateau phase prior to a drop to a minimum from AD 1535 to 1600.

Absolute emissions

The model was run with the determined parameters to infer the source strengths of the biogenic and pyrogenic source on each hemisphere, cf. Fig. 7.3.
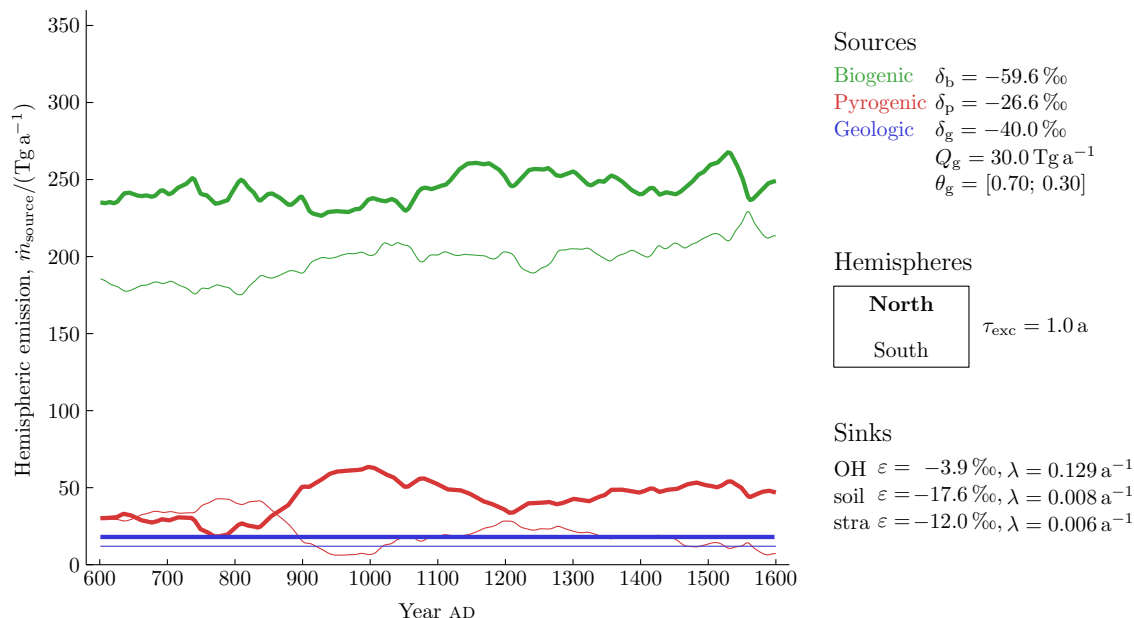

Figure 7.3: Results of model run with the parameters as given in the figure, using the concentration and isotope signatures Table 6.1.

Biogenic emissions are in both hemispheres higher than the pyrogenic ones, which is in accordance with previous research [182, 18, 183, 44]. Pyrogenic emissions in the order of $50\,\mathrm{Tg\,a^{-1}}$ have been reported as well [184, 109]. Moreover, the biogenic source is higher in the North than in the South, which is reasonable, as about 2/3 of the land mass is located on the Northern hemisphere. While pyrogenic emissions are on average higher on the Northern hemisphere, there seems to have been a short lapse of time (AD 600–850), where this was supposedly not the case.

The absolute strength of emissions depends a lot the chosen parameters such as the isotopic signatures and source strengths. These are subject of a more detailed discussion in the sensitivity study in the next section. When running the model on the data set with the original NH δ^{13}C data series, uncorrected to Bern ($\Delta_{\delta,\mathrm{inter}} = 0$), pyrogenic emissions were almost constantly lower in the North compared to the South, and even negative down to $-11\,\mathrm{Tg\,a^{-1}}$ at AD 780. A shift in the hemispheric repartition of neither the soil sink (θ_{soil}), nor the geological source (θ_{g}), was able to increase pyrogenic emissions on the NH. Hence the only left option for correcting this was an offset in the δ^{13}C value, enriching the NH data series or depleting the SH. The values applied for gravitational enrichment showed at least for one of the two δ^{13}C SH datasets (cf. Section 6.4.2) a similar correction to what was subtracted on the NH data set ($\Delta_{\delta,\mathrm{firn,SH}} = 0.31$‰) [71]. Therefore, the offset to an absolute reference was introduced again, taking Bern as the absolute reference for NH measurements ($\Delta_{\delta,\mathrm{B30}} = -0.66$‰), cf. Section 4.5.

7.1.2 Intercomparison with data from [IMAU]

While the last section discussed the modelling results with [IMAU-CIC], the NH δ^{13}C data set including the values measured at CIC, this section compares a comparison with [IMAU], the data from Sapart (2012) alone. The corresponding data sets were plotted in Fig. 7.4. The different isotopic signatures
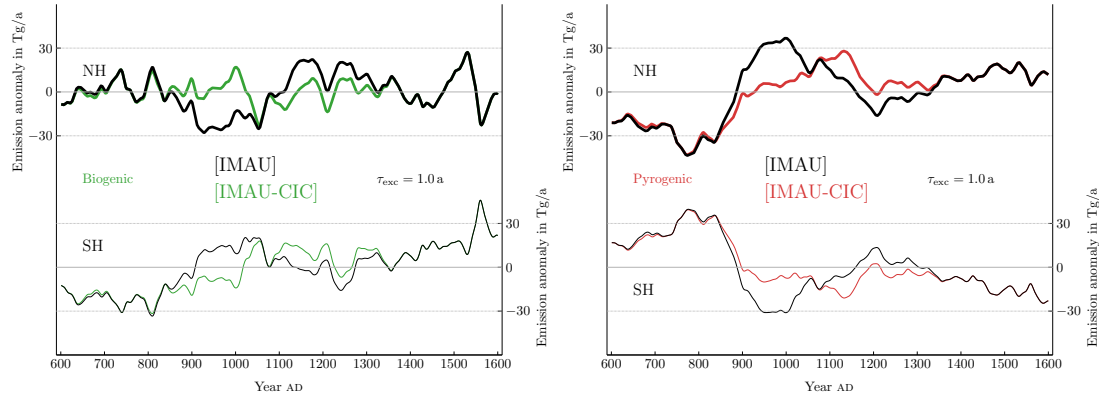

Figure 7.4: The anomalies resulting from [IMAU-CIC] in green/red compared to the data of [IMAU] alone in black.

measured between AD 800 and 1350 have a large impact on modelling results. The **biogenic** model using [IMAU] shows much more variation on the NH, as compared to the results of [IMAU-CIC]. The results with [IMAU] show on the NH show a decline from AD 850 to 920 followed by a surge from AD 1050 to 1150 with a short minimum at AD 1250.

In the modelled **pyrogenic** emissions from [IMAU], there is a positive excursion between AD 890 and 1050 that is absent to that extent in [IMAU-CIC], followed by a period with constantly lower emission strength as compares to [IMAU-CIC] between AD 1100 and 1330.

7.1.3 Nature paper Sapart (2012)

The Nature paper of Sapart (2012) [1], bases its model on two data series only, and constructs the other two from the available ones, that is,

$$x_{\mathrm{N}}(t) = x_{\mathrm{S}}(t) + 40\,\mathrm{ppb} \tag{7.1}$$
$$x_{\mathrm{S}}(t) = \text{WAIS [25] and Law Dome [71, 121]} \tag{7.2}$$
$$\delta_{\mathrm{N}}(t) = \text{[IMAU] in Sapart (2012) [1]} \tag{7.3}$$
$$\delta_{\mathrm{S}}(t) = \delta_{\mathrm{N}}(t) + 0.5\text{‰}. \tag{7.4}$$

This data set (hereafter: [Sapart]), not to be confused with the previously shown [IMAU] dataset, which included all four of its input data series from measured data, while [Sapart] consists of two hemispheres with records of similar shape.

Running the previously established model with the parameters from this study but with [Sapart], results in emissions as in Fig. 7.5. The obtained graphs can again be transformed into anomalies for each source, Fig. 7.6 (**a**,**b**,**e**,**f**). The obtained emission series are in similar shape as the ones presented in the publication of Sapart (2012) (**c**,**d**), but of higher values (cf. 7.5). The absolute figures are said to be misscaled (personal communication with T.Blunier (2013)).
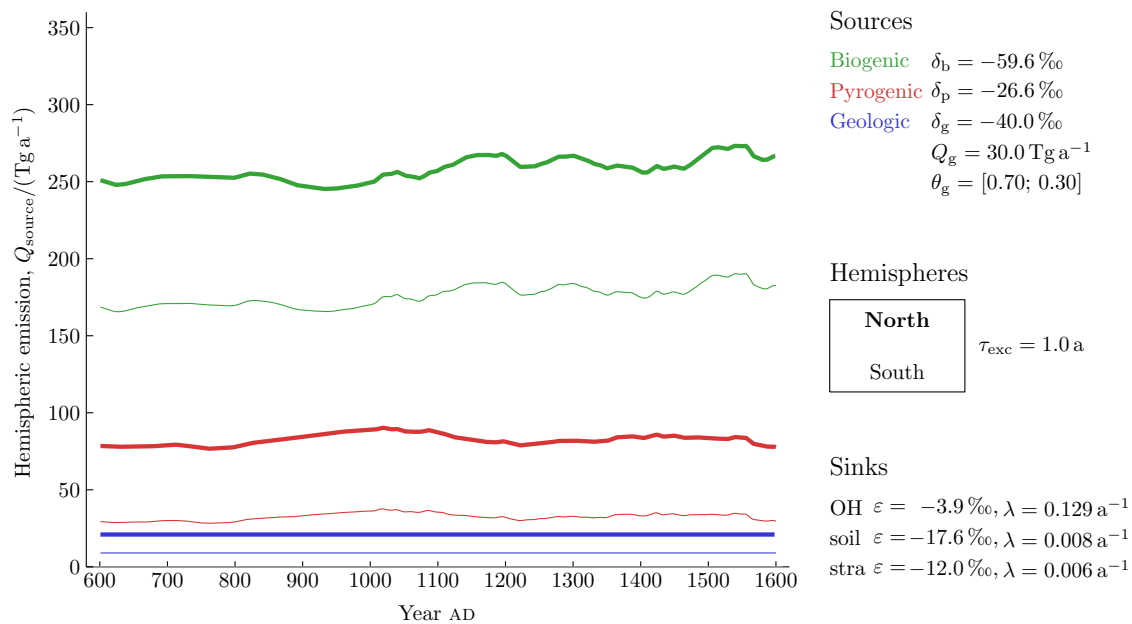

Figure 7.5: Results of model run with the parameters as given in the figure, using similar data series for concentration and isotope signatures as Sapart (2012).

As follows from comparing Fig. 7.5 with Fig. 7.3 for the magnitudes of the emissions, [Sapart] models pyrogenic emissions to be generally higher than what the [IMAU] data set does.
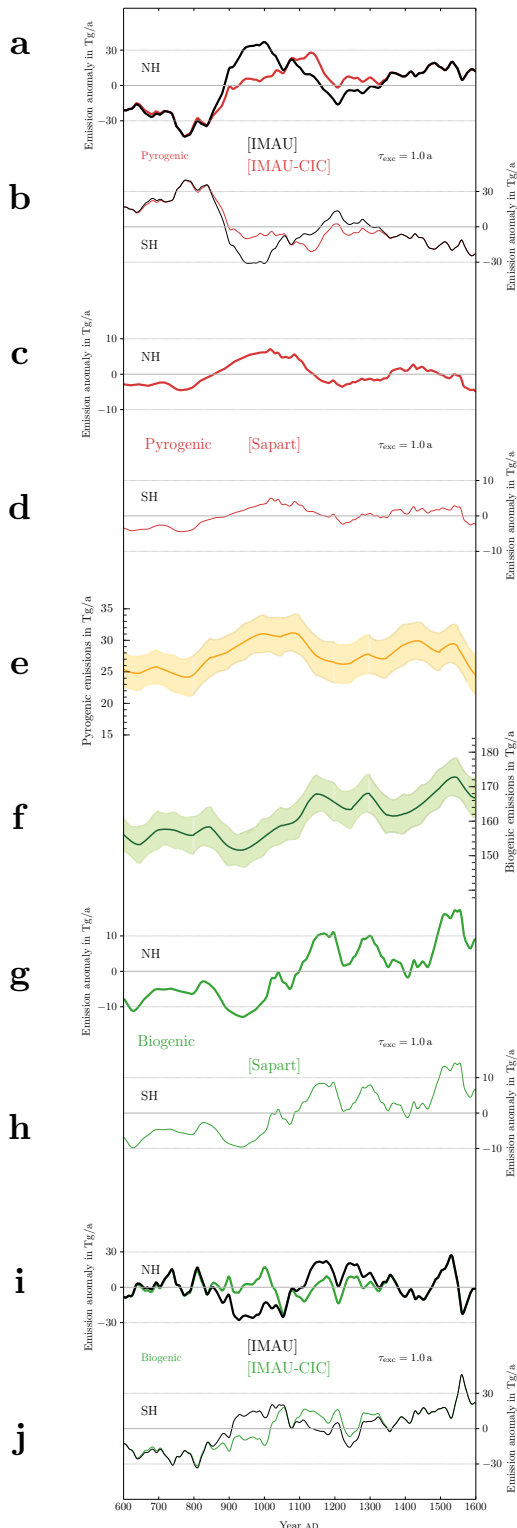
Fig. 7.6 shows an inter-comparison between the model runs with the different datasets previously discussed (**a**/**b**,**i**/**j**), as well as the [Sapart] data series (**c**/**d**,**g**/**h**) and includes the two original plots of Sapart (2012) (**e**,**f**). On the one hand, the original plots confirm the comparability of Sapart's (2012) model and the one of this study.

On the other hand, the comparison between [Sapart] (**c**) and [IMAU] (**a**) (black line) show that [Sapart] infers somewhat similar variations in emissions on the Northern Hemisphere, while the variations on the Southern Hemisphere are inversed.

Regarding the amplitude of the variations, [Sapart] recorded much smaller variations, in the order of 30 Tg/a. (**e**,**f**), while the data sets with four distinct measured data series record differences twice as large (**a**,**i**). Furthermore, the model with [Sapart], infers a highly similar changes on the two hemispheres, while the data other datasets infer a mirrored relation between the two hemispheres.

Figure 7.6: Source strength anomalies to the mean, using the same data as Sapart (2012). Plot (e) and (f) adapted from Sapart (2012) [1].

7.2 Sensitivity study

A sensitivity study has been performed to assess, which parameters have to be most carefully chosen, and what parameters have the largest effect on the outcome of the model. The study has shown that the only parameter that influences the shape of the curve and not only results in a vertical translation is the interhemispheric exchange time, τ_{exc}, cf. Fig. 7.7. That this is not a mere stretch of the curve becomes apparent in the biogenic plot around the year AD 1250, where the local emission maximum changes from one peak to another with the changing τ_{exc}.
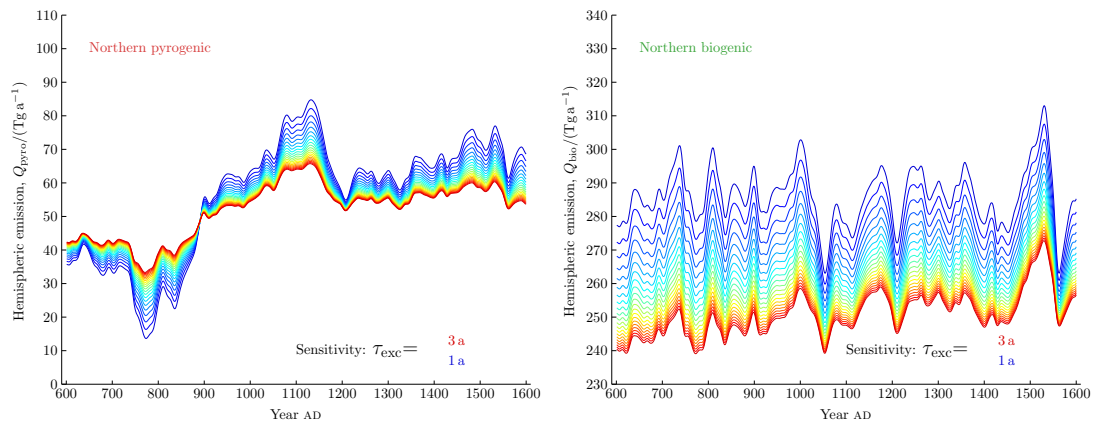

Figure 7.7: Results of sensitivity study with a varying interhemispheric exchange time, τ_{exc}.

The choice of the interhemispheric exchange time, τ_{exc}, seems to be crucial, as from the sensitivity study, Section 7.2. The shorter the time, the more extreme are the changes, and the closer the two hemispheres are to be similar-reversed. The shortest time for exchange that can be used with this model is one year, as this is also the modelling interval. However, when comparing two plots of the global sum of changes with different interhemispheric exchange times, it could be seen that changes do in fact balance each other out, and the plot of sums would remain the same. Not only the sums, would remain the same, but also the differences would just be shifted and remain of the same shape.

The sensitivity plots of the other parameters, as shown in Tab. 6.4 and 6.5 are shown in Appendix A.9.

Chapter 8

Discussion

The modelled time series for the two different sources, biogenic and pyrogenic, are discussed in this chapter and compared to proxy data. Specifically the differences between the [IMAU] and the [IMAU-CIC] data series are analysed. Since environmental proxy data alone cannot explain all the variation in methane emissions, the obtained emission series have been compared anthropogenic records such as land use and population. Those records are presented first, before the subsequent comparison to the globally summed emissions and each hemisphere alone.
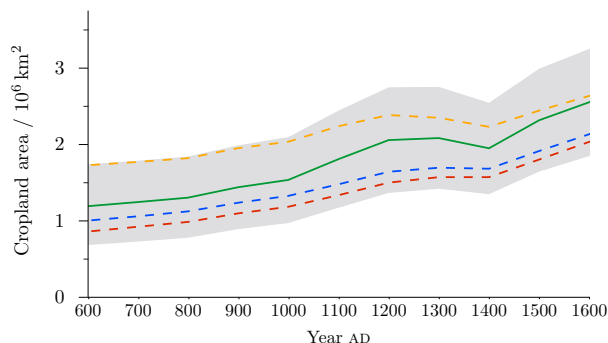
8.1 Anthropogenic landuse change

Figure 8.1: Global estimates of cropland area, using different scenarios:
green: HYDE 3.1 with uncertainty range (grey),
yellow: Ruddimann (4.0 ha/cap in 10k BC),
blue: Nevle and Bird (1.0 ha/cap in 10k BC),
red: Williams (0.43 ha/capita in 10k BC).
Adapted from Klein Goldewijk (2011) [185], wherein the different scenarios are discussed.

The reconstructed historic land-use maps from the History Database of the Global Environment *(HYDE 3.1)* by Klein Goldewijk (2011) [185] are shown in Fig. 8.2. Among the noteworthy developments from AD 500 to 1000 are an intensification in cropland use in Central America, and an East-ward expansion from Europe. Meanwhile in China there is not much change until AD 1000, but thereafter a strong intensification thereafter has been recorded. In the Americas crop land use has further intensified, but declines quickly after the European encounter in the 1500s, although farming in the Americas remained orders of magnitude less important than the other continents. In summary, these maps suggest land use for farming was on a constant rise from AD 600 – 1600.
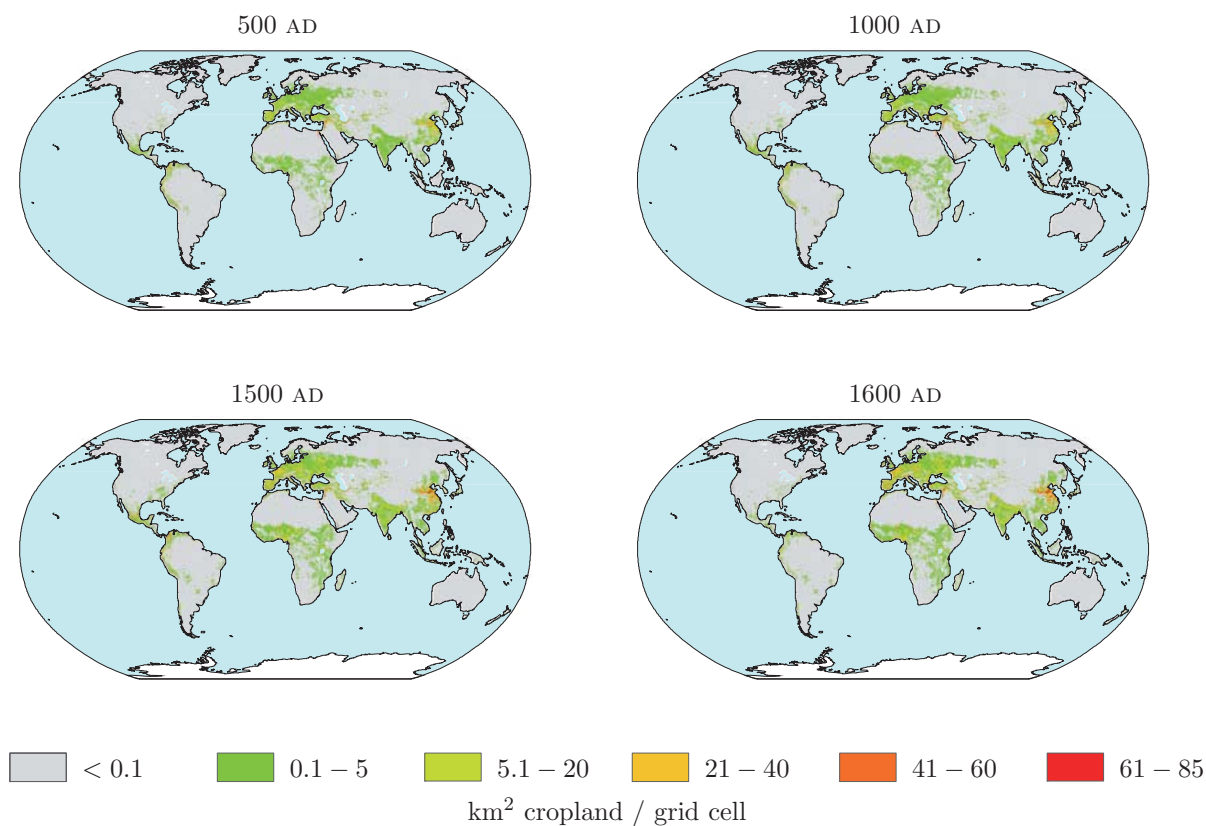

Figure 8.2: Anthropogenic land-use as km^2 cropland / grid cell. Adapted from Klein G. (2011) [185].

Since the maps do not feature a high time resolution the decline in total used cropland area in the 12th and 13th century are not visible, while the plot in Fig. 8.1 does.

The *HYDE 3.1* model also presents maps for pastoral land use, which show a general trend of intensification over the considered period, but they do not account for any pastoral land use in the pre-Columbian Americas, such as buffaloes and bisons in the prairies of the North.

8.1.1 China

In the fourth and third centuries BC, the Chinese started systematic land reclamation and irrigation schemes that converted large areas of natural land into rice paddies. This process was scientifically planned and then continued by subsequent dynasties, reached a climax in the 11th and 12th centuries [186]. At the same time, the population statistics collected during of the Sui, T'ang, Sung, Sung-Ch'in, Ming and Ching dynasties show a surge in population in the 11th century, which coincides with these land conversions [187] (Fig. 8.3).

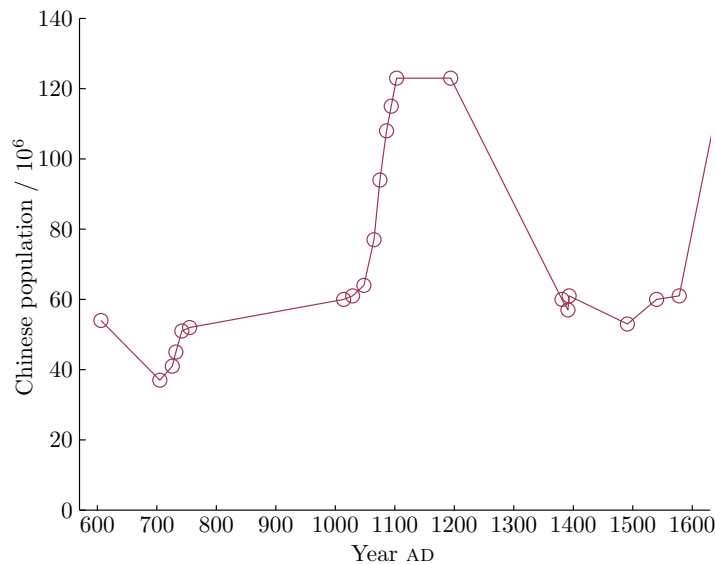**Figure 8.3:** Population statistics of China. Data from Durand (1960) [187].

8.1.2 Americas

The first contact of Europeans with Americans in the late 15th century led to a rapid decrease in population. By the year AD 1650 about 95% of the population had perished [188]. This resulted in a large drop in pyrogenic emissions, as slash and burn practices were wide spread in the Americas [188].

8.2   Model data to proxy comparison

On the following pages, the modelled emission series (**a**,**b**) are compared to environmental proxies that allow for an explanation of observed changes in modelled emission series. The shown graphs are indexed (**a**) to (**j**). All of these proxy series have been shown in either the background (Chapter 2) or the preceding section of this chapter. These are: (**c**) a temperature record [118, 117, 111], discussed in Fig. 2.21 and **??**; (**d**) [185, 187] *HYDE 3.1* land use / Chinese population development, discussed in the preceding section, Figs. 8.3,8.2; (**e**-**g**) Charcoal records [23], discussed in Fig. 2.7 and 2.8; (**h**) CO mixing ratio records from Greenland [27] and Antarctica [26]. In addition, the raw data plots for the respective Hemispheres have been plotted as well, (**i** – **j**).

8.2.1   Comparison of global emissions

The globally summed modelling results are in good agreement with previous research on fire incidence and land use change. This is shown and discussed in Fig. 8.4 and the text column next to it.
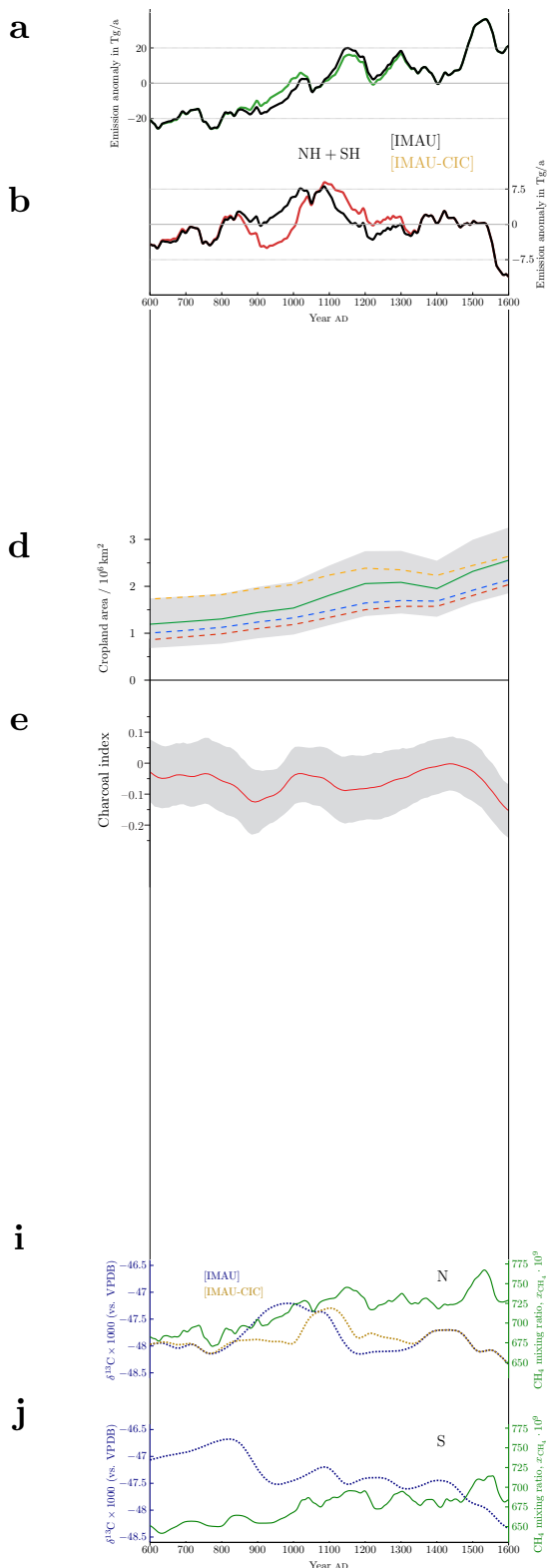
Figure 8.4: Proxy comparison, cf. text.

The cumulative global biogenic and pyrogenic emissions, shown in Fig. 8.4 (**a**) and (**b**), respectively, show a very good agreement with (**c**), the global charcoal index and the cropland use (**e**) from Klein (2011) [185]. Details are discussed below.

The global sum of **biogenic** emissions (**a**) of [IMAU-CIC] differs only minimally from the results with [IMAU]. That is, the increase at AD 875 – 1150 is steeper for [IMAU]. They are in good agreement with land-use statistics for cropland, as reported by Klein Goldewijk (2010) [185] (**e**). The increase until AD 1150 is in good agreement, observing a steeper increase over the period AD 1000 – 1200 than before. The following reported decrease in cropland use is also reflected in the result of this model. Although there is a fair amount of variation, a plateau and minimum at AD 1400 is observed in the results. A subsequent surge until AD 1600 is observed, but much more smoothly in the land-use statistics. Both model runs follow the trends reported by land-use changes. The [IMAU] data could be claimed to follow the pattern better than [IMAU-CIC].

The global sum of **pyrogenic** emissions (**b**), shows variations at a different scale (cf. y-axes scaling), since it is more constant than the the sum of biogenic emissions. Therefore, differences between the two records are much more pronounced. [IMAU-CIC] shows a decrease and local minimum at AD 905 – 925, which is in good agreement with the charcoal record (**e**), whose minimum occurs a little bit earlier at AD 890, but follows a similar trend over a 200 years period. This low frequency of fire events is present in a much more expressed way in the modelling results using [IMAU-CIC] data. Whereas [IMAU] almost omits this local minimum, but leads leading faster to a maximum between AD 1000 and 1100. The corresponding timing is in much better agreement with the charcoal record than the [IMAU-CIC] series. The drop in pyrogenic emissions, inferred to occur in AD 1550, is also observed in the charcoal record, where it begins earlier, at AD 1500. This is in good agreement with the collapse of the American population after the contact with Europeans and the spread of Old World diseases. If charcoal records generally tended to report variations earlier than what is recorded in methane isotopes and mixing ratio, the modelled data from [IMAU-CIC] would be in much better agreement than [IMAU]. Otherwise, neither of the two fits better.
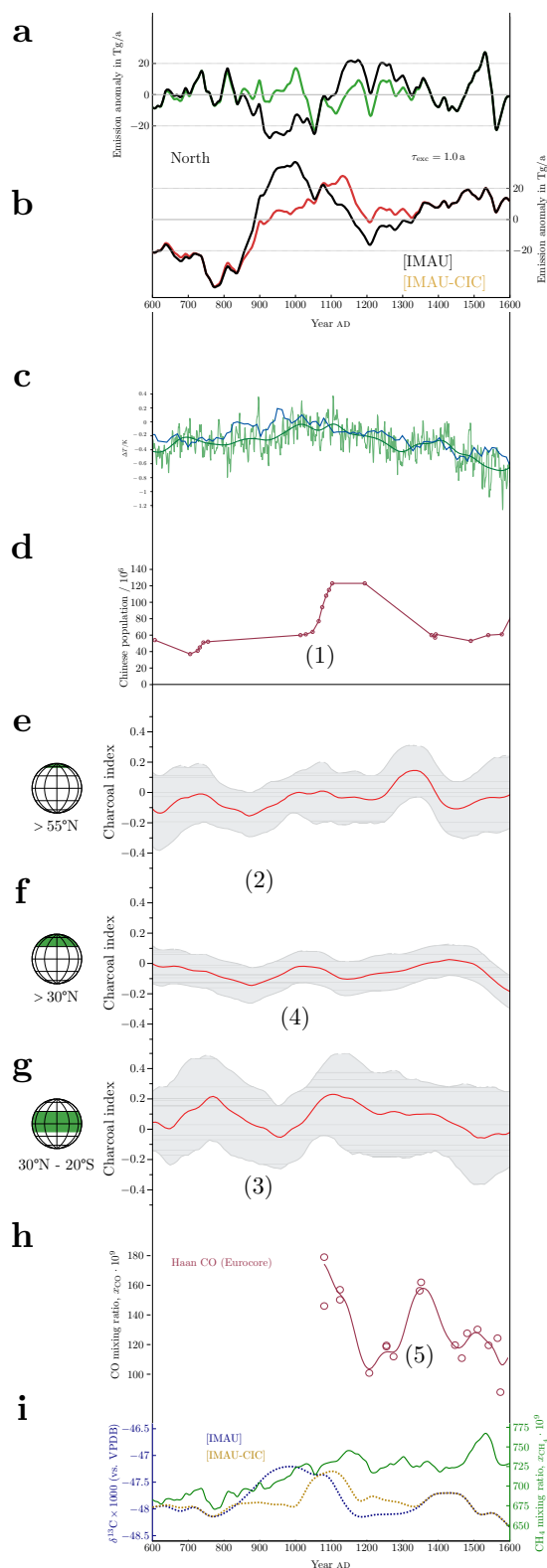
Figure 8.5: Proxy comparison, cf. text.

8.2.2 Comparison of emission series on both hemispheres

After having discussed the global sum of emissions in Chapter 8.2.1, in this section the emission series on each hemisphere are discussed.

Nothern Hemisphere

Northern **biogenic** emissions show a surge from AD 1050 to 1150 with [IMAU], which coincides well with the abrupt rise (1) in Chinese population (**d**) and its reported increase in land use through rice cultivation (Section 8.1.1). On the other hand, no significant correlation with temperature records is observed (**c**).

Northern **pyrogenic** emissions show some correlation with charcoal indices (**e** – **g**). The rise after AD 800 until AD 1000 with [IMAU] shows correlation with charcoal of the Northern extra-tropics (**e**, **f**) (2), while it is in inverse correlation with the tropics (**g**) (3). [IMAU] shows better correlation with a peak at AD 1000 (4), while a continuous increase until AD 1140, such as modelled with [IMAU-CIC] data, is less compatible with the charcoal records.

Also noteworthy, highest latitude charcoal shows some correlation with CO mixing-ratio records from Greenland ice cores (**h**) after AD 1200 (5), while no other correlation can be observed.

Although some correlation with environmental proxies and population was observed in the North, it is generally weak and only applies to parts of the record.
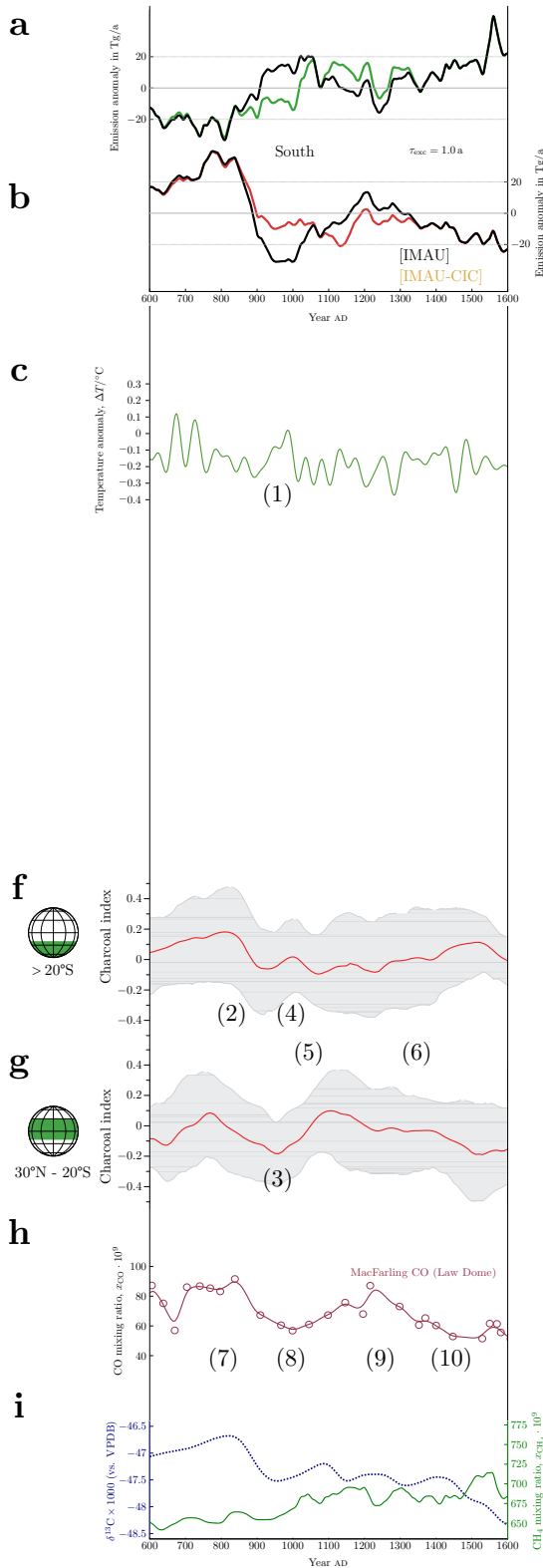
a

b

c

f

g

h

i

Figure 8.6: Proxy comparison, cf. text.

Southern Hemisphere

Southern **biogenic** emissions show an increase from AD 820 to 1050 that begins more steeply with [IMAU], and ends more steeply with [IMAU-CIC]. This correlates to some degree with an excursion (1) in temperature (**f**) as reported by Mann (2003) [111], while the temperature record does not show any other relevant correlation.

Southern **pyrogenic** emissions show good correlations with charcoal indices (**d, e**). First, the maximum around AD 800 is in good concordance with similar maxima in the extra-tropics (2), in the tropics, and in the CO record (7). The decrease in the late 900s with [IMAU] is well reflected in the tropics (3) and with the CO record (8), while [IMAU-CIC] account better for the small increase as reported for the extra-tropics (4) during AD 950 – 1050. On the other hand, [IMAU] resulted in a modelled emission series that correlate better with the increase after AD 1000 (5), which is even more pronounced in the CO records (9). Astonishingly, the steady decline after AD 1200 is not observed in the extra-tropics (6), while it is in the tropics and again in the CO records (10). The extra-tropics contain, however, only very little land mass, which could explain, why charcoal records in the tropics show a better correlation with CH_4 emissions than the extra-tropics.

In the South, correlation to environmental proxies is mainly observed for pyrogenic emissions and charcoal, while biogenic emission show weak correlation with temperature.

8.2.3   Fully time-dependent inversion

To our knowledge, this study presents the first fully time-dependent inversion attempt with two emission time series on each HS as output that also uses four measured time series as inputs. Although some reasonable conclusions can be drawn and the results match with some of the environmental proxy-data series available, the model has only very limited confidence in what concerns the interhemispheric (latitudinal) repartition of sources.

If exchange is stopped totally, $\tau_{\mathrm{exc}} = \infty$, the modelled pyrogenic emissions are similar to the isotopic signature, while biogenic emissions follow the mixing ratio trend on each hemisphere. On the other hand, with complete mixing from each time step to the next, $\tau_{\mathrm{exc}} = 1$, North and South hemispheric pyrogenic emission variations are close to be equal and opposite. Since fire frequencies are very unlikely to be in counterbalance on the two hemispheres, we suggest that a more complex model would be more suited to actually take into account the complexity of the system.

Chapter 9

Outlook

This chapter gives indications about what could be changed and possibly lead to improved results on the current measurement system (Section 9.1) and model (Section 9.2), as well as how advances in other fields could contribute to this field of science (Section 9.3).

9.1 Analytical System

9.1.1 Calibration and control standard signature

The isotopic composition of standard and sample should be as close as possible, as discussed in Section 4.8. The effects were observed from the ^{17}O correction, cf. Section 4.1. For our case, the concentrations and isotopic compositions of the measured samples are actually much more similar to the AL standard than to the GIS standard that was used for calibration. Hence for another measurement of cores with similar values, we suggest using two standards with similar or equal methane mixing ratios and isotopic composition as the current AL standard (AL1 and AL2). AL1 would then be used for referencing (calibration) and AL2 as the quality control standard that accounts for drifts in the standard and is measured between the two samples.

9.1.2 Gas standards in ice

The creation of gas standards from ice in addition to just measuring gas over molten bubble free ice (BFI) has earlier been proven to be impractical, due to gas traces remaining in the water even after evacuating for a long time. With the use of a longer stir bar, this problem was eliminated and the creation of ice standards could be tried again in future experiments. We suggest a top-to-bottom freezing procedure, where after the complete removal of any gas, that is, evacuating and stirring for a few hours, a gas stream is injected below the water surface and a standard gas being introduced, while a constant pressure in the overhead space is maintained. The water would then be frozen top-to-bottom under pressure. To alleviate chances of bursting the vessel, an expansion chamber would probably have to be engineered for the water.

Remaining concerns over this proposals are on the one hand gas residues in not-really-bubble-free BFI, as it was observed in our lab with ice generated by use of the short stir bar and also reported by Bock (2010), who observed changes in their δD signature over bubble free BFI generated through "zone melting" [189]. On the other hand, a further concern is the expansion chamber for allowing top-to-bottom freezing. This is required to retain the gas in the ice, since it would otherwise escape if the bottom-to-top freezing method were applied.

9.1.3 Linearity corrections

One linearity correction has been discussed in Section 4.2, however there have been other labs reporting to apply more than one linearity correction [25]. This could be an area of future research, since it is visible on the plots in Fig. 4.1 that the correction is not only dependent on the area size A, but also the $\delta^{13}C$ signature of the gases: the AL points show a smaller D value for the same A than the GIS points. i.e. they lie slightly more on the right of the graph. It remains unclear, whether this offset D is dependent on the $\delta^{13}C$ signature of a gas and/or the amount of gas injected in addition to the methane peak size, A. These two possibilities are discussed below. In future research, both of them could be analysed and their individual effects be quantified. i.e. it would be possible to apply corrections independently [25] or to construct a multi-dimensional size-correction space, as a function of

- CO_2 peak area, A,

- extracted volume $\propto$ TCD peak size, and

- $\delta^{13}C$ signature.

Dependence on isotopic signature

It has been reported by Ferretti (2005) [25] that a correction for the isotopic signature of a sample has been applied. The reported value was $-0.03‰ \cdot ‰^{-1}$ and was applied to all analyses, which resulted in a maximum value of this correction of $-0.06‰$. This effect was quantified by using three gases spanning $4‰$, measuring their $\delta^{13}C$ difference from their "true" dual-inlet analyses [25].

Dependence on total gas volume

The total gas volume of a sample, varies from core to core. As the extraction is stopped 1:20 min after the pressure has reached 0.11 mbar, the extraction efficiency is likely to vary from sample to sample, depending on the amount (mol) of gas initially present. The the time needed to reach a certain pressure is depending on the sample size. This is easy to notice, during the extraction of gas standards of different sizes.

The extraction efficiency can be calculated from the amount of gas injected, n_i, and the amount of gas left at the end of the extraction n_r, which is itself a function of the final pressure p_f, related over the ideal gas law, $pV = nRT$, where V is the volume of the water trap and the connection tubes.

$$\eta_{\text{extr}} = \frac{n_i - n_f}{n_i} = \frac{n_i - p_f V/RT}{n_i} \tag{9.1}$$

This varying efficiency is likely to invoke a fractionation process. No statistical relevant measurement series has been carried out, but single measurements showed more depleted values for larger gas volumes but similar peak areas. This is also reflected in Fig. 4.1, where the measured GIS points (lower mixing ratio) are more depleted for the same sample size than AL measurements. Since this could also be due to differences in the isotopic signature, more research is needed to be able to make a full conclusion about the importance of these effects.

An additional effect comes into play when ice is extracted, as some water gets trapped onto the cryotrap (cf. Section 3.4.2), which is likely to have an additional effect. The effects of these various processes can be subject of further research.

9.2 Model

9.2.1 Improved Southern hemispheric isotope records

As discussed in Section 6.4.2, there is so far no reliable isotope data series available for the Southern hemisphere before AD 800. When such a record will become available, this will allow for much more confidence in the modelling. The same applies for the mixing ratios of the NH in the early 8th century.

9.2.2 Intercalibration of δ^{13}C series on both hemispheres

To our knowledge, the laboratories of Sowers and Ferretti have not been intercalibrated with CIC/IMAU on δ^{13}C-CH$_4$. If this would be done, various δ^{13}C time series would correspond on the δ^{13}C scale. This could possibly solve the problem of negative emissions in our model.

9.2.3 Marine boundary layer

The effect of the marine boundary layer (MBL) on the discrimination factor of the troposphere could be included, such as to account for the combined effect of the Cl$^\bullet$ and OH$^\bullet$. This could have an effect on model results, if the source variation of CH$_3$Cl can be accounted for and the temporal variation be quantified, since this sink features a strong discrimination as discussed in Section 2.3.6.

9.2.4 Determining time axis offsets for various records

When using various records, a root-mean-square (RMS) algorithm could be used to determine the best fit. A calculation over a predefined range of t offsets and value offsets could be used to determine the optimum t and value offsets that result in a minimum RMS value of the offset of the whole record. (A script is available from the author).

9.2.5   Inclusion of δD records

As it has been shown by Fischer (2008) [9], not only δ^{13}C records, but also δD records give indications about the methane source, cf. Fig. 2.5. The possibilities of having two additional variables as times series to include in the model are huge. The system at CIC is equipped with a pyrolysis stove that has not shown to be functional up to know. Once this setup becomes operational, new measurements from this system will give a boost to the possible modelling possibilities.

9.2.6   Include a model for biomass burning

A model of biomass burning could further be established by combining the records presented in Section 2.3.2, such that a time series of biomass burning could be established for one or both hemispheres, which would allow for the determination of an additional source time series, since one unknown time series is replaced by a data series. This could possibly bring lead to a much better understanding of the climate of the past and its variations.

9.3   Prospects

In this section, some prospects for future improvements in measurement technology and techniques are given. The future availability of the outlined possibilities is only dependent on external factors, such as research being carried out in other fields and laboratories.

In addition to the analysis of ^{13}C and D isotopes in methane, recent and future technological advancements in analytical techniques will make it possible in the future to also analyse multiply-substituted isotopologues. These, isotopologues are of particular interest, since they tell us about the temperature at the emission site of methane [190].

This, however, makes it necessary to analyse the methane in its molecular form without it being combusted to CO_2 or pyrolysed to H_2. Isobaric interferences as from isotopologues make it impossible to analyse this on traditional IRMS mass spectrometers. There are two techniques that will allow for such an analysis: Near-infrared laser absorption spectrometry and IRMS with an increased mass resolving power.

9.3.1   NIR laser absorption spectrometry

Other developments have explored the possibility of using near-infrared laser absorption spectrometry for determining the δ^{13}C ratio to as precise as to $\approx 0.1\permil$ (1σ) at 10% and 1% mixing ratios for methane [191], which is possible to reach after a pre-concentration device. This technique would also allow for the simultaneous analysis of $^{13}CH_4/^{12}CH_4$ and $^{12}CH_3D/^{12}CH_4$. However, the required sample size for a precision $<1\permil$ is in the order of $1\,\mu$mol to $1\,$mmol as reported by Tsuji (2006) [191]. This is still much more than the 0.7 to $1.0\,$nmol[a] we were using in this study.

---

[a] Calculated from volume and concentration data from the TCD (volume) and mass spectrometer (concentration) (cf. Section 5.3.2) with the assumption of a molar volume of $24.47\,L/$mol at $T = 25°$C and $p = 1.013\,$bar.

9.3.2 Increasing mass resolving power on IRMS

Up to now, it has not been possible to measure methane directly, but it always needed be combusted into CO_2 and H_2O, to prevent fragmentation into daughter fragments such as H^+, C^+, CH^+, CH_2^+ and CH_3^+. With new advancements in technology, it could become possible to measure methane directly, and then even detect clumped isotopes thanks to the mass defect: isobaric isotopologues that share a cardinal mass, do not exactly have the same mass. The defect is due to the mass defect, resulting from Einstein's energy–mass equivalence, $E = mc^2$, proposed by Einstein in 1908 and proven by Laue (1911) [192, 193]. Here, E is the binding energy of the atoms to form a molecule and m the resulting mass defect. This mass defect is large enough to manifest on spectrograms of mass spectrometers with a high enough mass resolving power.

The mass resolving power of a mass spectrometer is defined as the ion beam's mass (m) divided by its width (Δm), in equivalent mass units. Calculated as the central portion of the beam containing 90% of its current; this is also referred to as the '5–95% definition' of mass resolving power. Since IRMS usually have a resolving power of around 100, they are unable to distinguish isobaric interfering species. ThermoFisher is developing a new IRMS system, the MAT253-Ultra, with a resolution power of up to 27,000. Thus it could become possible to carry out the methane measurements without the need of combustion, as reported by Eiler (2013) [194]. For comparison, the used ThermoFisher Delta V Plus, has a mass resolution power of 110, as reported in the operating manual on page "5–3" [96].

The prospects for clumped isotopes geochemistry are abundant as shown by Eiler (2007) [190], with astonishing values for methane such as a much higher than expected abundance of CD_4 [195]. However, these measurements need a sample size of 1 µmol of gas because of the limits of counting statistics and transmission (personal communication with J.M. Eiler [196]).

This page intentionally left blank.

Chapter 10

Conclusion

Figure 10.1: "Can we save the atmosphere by burping a little bit less"? Advertisement in front of the Niels Bohr Institute, Copenhagen, 2012.

Our study dealt with agricultural emissions and their impacts, we did not address the cows question, if "the atmosphere can be saved by having [cows] burping less", such as proposed on the advertisement in front of the Niels Bohr Institute. The questions we addressed and the conclusions we find are explained below.

10.1 Analytical Part

In the analytical part, carbon isotope signatures of methane ($\delta^{13}CH_4$) in air from 28 ice cores have been measured. 26 of which from Eurocore (72°34' N, 51°27' W) and 2 from NEEM (77°27' N, $-51°3.6'$ W, cf. Fig. 2.18). There is a strong agreement between NEEM and Eurocore data measured at CIC, also between this study and points by Sperlich (2012) [126]. The cores measured at CIC have been compared to some measured at IMAU by Sapart (2012) [1]: while some of the measured values are in remarkably good agreement (AD 1762 and 1774), in CIC values of 13 cores from the Medieval Climate Anomaly (AD $800 - 1300$).

Different sorts of daily drift corrections have been discussed. And the quality of generated bubble free ice has been improved significantly with the use of another stir bar.

10.2 Modelling Part

A model of the global methane budget was established. Experimental measurement data for methane mixing ratio and carbon isotope signature measured from Greenlandic and Antarctic ice cores was used as input. To have a record in equal time steps, small enough to run the model, the original data was smoothed. Since some data series featured interval with missing data, these were fixed with a novel Gaussian smoothing algorithm that is particularly suited for heterogeneously spaced data series, and can be used for fixing continuous (CFA) data series with sparse data from discrete measurements.

The developed model performs a fully time-dependent inversion, and infers biogenic and pyrogenic emission series on both hemispheres. It was run on two different data sets. One set included the $\delta^{13}C$ signature series measured at IMAU Utrecht, while the other included data measured at CIC. The resulting differences from modelling were analysed and compared with environmental proxies and estimates of human activity.

While the global sum of emissions as modelled has shown some remarkably good concordance with land use estimates and charcoal proxies, such as low pyrogenic emissions in the southern hemisphere around the turning of the millennium, the decline in Northern Hemispheric biogenic emissions due to a population drop in China in the 13th and 14th century, the decline of global pyrogenic emissions after the Columbian encounter in the 1500s. However, the variations of modelled emission series on individual hemispheres can in fact only partially be explained by environmental and historic proxy data. It might be, that for a fully time-dependent inversion to be successful, more research or additional data series would be needed.

Bibliography

[1] C. J. Sapart, G. Monteil, M. Prokopiou, R. S. W. van de Wal, J. O. Kaplan, P. Sperlich, K. M. Krumhardt, C. van der Veen, S. Houweling, M. C. Krol, T. Blunier, T. Sowers, P. Martinerie, E. Witrant, D. Dahl-Jensen and T. Rockmann. *Natural and anthropogenic variations in methane sources during the past two millennia.* Nature, 490(7418):85–88, 2012.

[2] S. Arrhenius. *XXXI. On the influence of carbonic acid in the air upon the temperature of the ground.* Philosophical Magazine Series 5, 41(251):237–276, 1896.

[3] R. Goody and Y. Yung. *Atmospheric Radiation: Theoretical Basis.* OUP USA, 1996.

[4] D. L. Gray and A. G. Robiette. *The anharmonic force field and equilibrium structure of methane.* Molecular Physics, 37(6):1901–1920, 1979.

[5] IPCC. *IPCC Fourth Assessment Report: Working Group II Report "Impacts, Adaptation and Vulnerability".* Fourth Assessment Reportof the Intergovernmental Panel on Climate Change. Cambridge University Press, 2007.

[6] S. F. Singer. *Stratospheric water vapour increase due to human activities.* Nature, 233(5321):543–545, 1971.

[7] H. Schaefer and M. J. Whiticar. *Potential glacial-interglacial changes in stable carbon isotope ratios of methane sources and sink fractionation.* Global Biogeochemical Cycles, 22(1):GB1001, 2008.

[8] N. S. Suits, A. S. Denning, J. A. Berry, C. J. Still, J. Kaduk, J. B. Miller and I. T. Baker. *Simulation of carbon isotope discrimination of the terrestrial biosphere.* Global Biogeochemical Cycles, 19(1):n/a–n/a, 2005.

[9] H. Fischer, M. Behrens, M. Bock, U. Richter, J. Schmitt, L. Loulergue, J. Chappellaz, R. Spahni, T. Blunier, M. Leuenberger and T. F. Stocker. *Changing boreal methane sources and constant biomass burning during the last termination.* Nature, 452(7189):864–867, 2008.

[10] F. Keppler, J. T. G. Hamilton, M. Braß and T. Rockmann. *Methane emissions from terrestrial plants under aerobic conditions.* Nature, 439(7073):187–191, 2006.

[11] G. B. Zhang, Y. Ji, J. Ma, G. Liu, H. Xu and K. Yagi. *Pathway of CH_4 production, fraction of CH_4 oxidized, and ^{13}C isotope fractionation in a straw incorporated rice field.* Biogeosciences Discuss., 9(10):14 175–14 215, 2012.

[12] L. Neef, M. van Weele and P. van Velthoven. *Optimal estimation of the present-day global methane budget.* Global Biogeochemical Cycles, 24(4):GB4024, 2010.

[13] K. R. Lassey, D. M. Etheridge, D. C. Lowe, A. M. Smith and D. F. Ferretti. *Centennial evolution of the atmospheric methane budget: what do the carbon isotopes tell us?* Atmos. Chem. Phys., 7(8):2119–2139, 2007.

[14] T. J. Popp, J. P. Chanton, G. J. Whiting and N. Grant. *Methane stable isotope distribution at a Carex dominated fen in north central Alberta.* Global Biogeochemical Cycles, 13(4):1063–1077, 1999.

[15] D. J. Wuebbles and K. Hayhoe. *Atmospheric methane and global change.* Earth-Science Reviews, 57(3–4):177–210, 2002.

[16] J. P. Chanton. *The effect of gas transport on the isotope signature of methane in wetlands.* Organic Geochemistry, 36(5):753–768, 2005.

[17] F. Klevenhusen, S. Bernasconi, M. Kreuzer and C. Soliva. *Experimental validation of the Intergovernmental Panel on Climate Change default values for ruminant-derived methane and its carbon-isotope signature.* Animal Production Science, 50(3):159–167, 2010.

[18] W. M. Hao and D. E. Ward. *Methane production from global biomass burning.* Journal of Geophysical Research: Atmospheres, 98(D11):20 657–20 661, 1993.

[19] J. P. Chanton, C. M. Rutkowski, C. C. Schwartz, D. E. Ward and L. Boring. *Factors influencing the stable carbon isotopic signature of methane from combustion and biomass burning.* Journal of Geophysical Research: Atmospheres, 105(D2):1867–1877, 2000.

[20] J. T. Buchholz. *The Generic Segregation of the Sequoias.* American Journal of Botany, 26(7):535–538, 1939.

[21] T. W. Swetnam, C. H. Baisan, A. C. Caprio, P. M. Brown, R. Touchan, R. S. Anderson and D. J. Hallett. *Multi-Millennial Fire History of the Giant Forest, Sequoia National Park, California, USA.* The Journal of the Association for Fire Ecology, 5(3):120–127, 2009.

[22] S. J. Anderson, R. Scott Smith. *The sedimentary record of fire in montane meadows, Sierra Nevada, California, USA: A preliminary assessment,* In J. Clark, H. Cachier, J. Goldammer and B. Stocks, editors, *Sediment Records of Biomass Burning and Global Change,* volume 51 of *NATO ASI Series 1: Global Environmental Change,* pages 549–585. Springer-Verlag, Berlin, 1997.

[23] J. R. Marlon, P. J. Bartlein, C. Carcaillet, D. G. Gavin, S. P. Harrison, P. E. Higuera, F. Joos, M. J. Power and I. C. Prentice. *Climate and human influences on global biomass burning over the past two millennia.* Nature Geosci, 1(10):697–702, 2008.

[24] C. Carcaillet, H. Almquist, H. Asnong, R. H. W. Bradshaw, J. S. Carrión, M. J. Gaillard, K. Gajewski, J. N. Haas, S. G. Haberle, P. Hadorn, S. D. Müller, P. J. H. Richard, I. Richoz, M. Rösch, M. F. Sánchez Goñi, H. von Stedingk, A. C. Stevenson, B. Talon, C. Tardy, W. Tinner, E. Tryterud, L. Wick and K. J. Willis. *Holocene biomass burning and global dynamics of the carbon cycle.* Chemosphere, 49(8):845–863, 2002.

[25] D. F. Ferretti, J. B. Miller, J. W. C. White, D. M. Etheridge, K. R. Lassey, D. C. Lowe, C. M. M. Meure, M. F. Dreier, C. M. Trudinger, T. D. van Ommen and R. L. Langenfelds. *Unexpected Changes to the Global Methane Budget over the Past 2000 Years.* Science, 309(5741):1714–1717, 2005.

[26] C. MacFarling Meure. *The Variation of Atmospheric Carbon Dioxide, Methane and Nitrous Oxide During the Holocene from Ice Core Analysis.* Ph.D. thesis, University of Melbourne, 2004.

[27] D. Haan, P. Martinerie and D. Raynaud. *Ice core data of atmospheric carbon monoxide over Antarctica and Greenland during the last 200 years.* Geophysical Research Letters, 23(17):2235–2238, 1996.

[28] A. J. Colussi and M. R. Hoffmann. *In situ photolysis of deep ice core contaminants by Çerenkov radiation of cosmic origin.* Geophysical Research Letters, 30(4):1195, 2003.

[29] W. D. Gunter, T. Gentzis, B. A. Rottenfusser and R. J. H. Richardson. *Deep coalbed methane in Alberta, Canada: A fuel resource with the potential of zero greenhouse gas emissions.* Energy Conversion and Management, 38, Supplement(0):S217–S222, 1997.

[30] C. Cleveland. *Concise Encyclopedia of the History of Energy.* Elsevier Science, Academic Press, San Diego, CA, 2009.

[31] M. A. K. Khalil, M. J. Shearer and R. A. Rasmussen. *Methane sources in China: Historical and current emissions.* Chemosphere, 26(1–4):127–142, 1993.

[32] E. G. Nisbet and D. J. W. Piper. *Giant submarine landslides.* Nature, 392(6674):329–330, 1998.

[33] J. Bock, P. Martinerie, E. Witrant and J. Chappellaz. *Atmospheric impacts and ice core imprints of a methane pulse from clathrates.* Earth and Planetary Science Letters, 349-350:98–108, 2012.

[34] M. Maslin, M. Owen, S. Day and D. Long. *Linking continental-slope failures and climate change: Testing the clathrate gun hypothesis.* Geology, 32(1):53–56, 2004.

[35] T. Blunier, J. Chappellaz, J. Schwander, B. Stauffer and D. Raynaud. *Variations in atmospheric methane concentration during the Holocene epoch.* Nature, 374(6517):46–49, 1995.

[36] W. Xu and C. Ruppel. *Predicting the occurrence, distribution, and evolution of methane gas hydrate in porous marine sediments.* Journal of Geophysical Research: Solid Earth, 104(B3):5081–5095, 1999.

[37] J. Chappellaz. *Ice Core Methods / Methane Studies*, In A. E. Scott, editor, *Encyclopedia of Quaternary Science*, pages 1199–1207. Elsevier, Oxford, 2007.

[38] G. K. Westbrook, K. E. Thatcher, E. J. Rohling, A. M. Piotrowski, H. Pälike, A. H. Osborne, E. G. Nisbet, T. A. Minshull, M. Lanoisellé, R. H. James, V. Hühnerbach, D. Green, R. E. Fisher, A. J. Crocker, A. Chabert, C. Bolton, A. Beszczynska-Möller, C. Berndt and A. Aquilina. *Escape of methane gas from the seabed along the West Spitsbergen continental margin.* Geophysical Research Letters, 36(15):L15 608, 2009.

[39] C. D. Ruppel. *Methane Hydrates and Contemporary Climate Change.* Nature Education Knowledge, 3(10):29, 2011.

[40] G. Etiope, K. R. Lassey, R. W. Klusman and E. Boschi. *Reappraisal of the fossil methane budget and related emission from geologic sources.* Geophysical Research Letters, 35(9):L09 307, 2008.

[41] G. Etiope and P. Ciccioli. *Earth's Degassing: A Missing Ethane and Propane Source.* Science, 323(5913):478, 2009.

[42] W. S. Reeburgh. *4.03 - Global Methane Biogeochemistry*, In D. H. Heinrich and K. T. Karl, editors, *Treatise on Geochemistry*, pages 1–32. Pergamon, Oxford, 2007.

[43] W. Allan, D. C. Lowe, A. J. Gomez, H. Struthers and G. W. Brailsford. *Interannual variation of ^{13}C in tropospheric methane: Implications for a possible atomic chlorine sink in the marine boundary layer.* Journal of Geophysical Research D: Atmospheres, 110(11):1–8, 2005.

[44] J. A. Chappellaz, I. Y. Fung and A. M. Thompson. *The atmospheric CH_4 increase since the Last Glacial Maximum*, volume 45.

[45] M. Prather, R. Derwent, D. Ehhalt, R. Eraser, E. Sanhueza and X. Zhou. *Other Trace Gases And Atmospheric Chemistry.* In *IPCC Second Assessment Report: Climate Change*. 1995.

[46] A. Thompson. *Modeling framework for atmospheric trace gas measurements at the air-snow interface*, In R. C. B. E. W. Wolff, editor, *Chemical Exchange Between the Atmosphere and Polar Snow*, volume I 43, page 225–248. Springer-Verlag, New York, 1996.

[47] S. Houweling, T. Kaminski, F. Dentener, J. Lelieveld and M. Heimann. *Inverse modeling of methane sources and sinks using the adjoint of a global transport model.* Journal of Geophysical Research-Atmospheres, 104(D21):26 137–26 160, 1999.

[48] J. A. Logan, M. J. Prather, S. C. Wofsy and M. B. McElroy. *Tropospheric chemistry: A global perspective.* Journal of Geophysical Research: Oceans, 86(C8):7210–7254, 1981.

[49] S. Hameed, J. P. Pinto and R. W. Stewart. *Sensitivity of the predicted CO–OH–CH_4 perturbation to tropospheric NO_x concentrations.* Journal of Geophysical Research: Oceans, 84(C2):763–768, 1979.

[50] C. J. Luther and L. K. Peters. *The possible role of heterogeneous aerosol processes in the chemistry of CH_4 and CO in the troposphere,* In *Heterogeneous Atmospheric Chemistry*, volume 26 of *Geophys. Monogr. Ser.*, pages 264–273. AGU, Washington, DC, 1982.

[51] D. H. Ehhalt. *Methane in the atmosphere.* In G. M. Woodwell and E. V. Pecan, editors, *Carbon and the Biosphere. Proceedings of the 24 Brookhaven Symposium in Biology*, volume 30 of *AEC Symposium Series*, pages 144–158. United States Atomic Energy Comission, Upton, New York, 1973.

[52] O. A. Søvde, C. R. Hoyle, G. Myhre and I. S. A. Isaksen. *The HNO_3 forming branch of the $HO_2 + NO$ reaction: pre-industrial-to-present trends in atmospheric species and radiative forcings.* Atmos. Chem. Phys., 11(17):8929–8943, 2011.

[53] L. V. Ghanshyam and A. R. Ravishankara. *New measurement of the rate coefficient for the reaction of OH with methane.* Nature, 350(6317):406–409, 1991.

[54] M. J. Prather. *Lifetimes and eigenstates in atmospheric chemistry.* Geophysical Research Letters, 21(9):801–804, 1994.

[55] P. J. Crutzen. *The Global Distribution of Hydroxyl,* In E. D. Goldberg, editor, *Atmospheric Chemistry*, volume 4 of *Dahlem Workshop Reports Physical and Chemical Sciences Research Report*, chapter 17, pages 313–328. Springer Berlin Heidelberg, 1982.

[56] M. Gupta, S. Tyler and R. Cicerone. *Modeling atmospheric delta(CH_4)-C-13 and the causes of recent changes in atmospheric CH_4 amounts.* Journal of Geophysical Research-Atmospheres, 101(D17):22 923–22 932, 1996.

[57] M. J. Prather and R. T. Watson. *Stratospheric ozone depletion and future levels of atmospheric chlorine and bromine.* Nature, 344(6268):729–734, 1990.

[58] Y. Yokouchi, Y. Noijiri, L. A. Barrie, D. Toom-Sauntry, T. Machida, Y. Inuzuka, H. Akimoto, H. J. Li, Y. Fujinuma and S. Aoki. *A strong source of methyl chloride to the atmosphere from tropical coastal land.* Nature, 403(6767):295–298, 2000.

[59] Y. Yokouchi, M. Ikeda, Y. Inuzuka and T. Yukawa. *Strong emission of methyl chloride from tropical plants.* Nature, 416(6877):163–165, 2002.

[60] G. Saueressig, P. Bergamaschi, J. N. Crowley, H. Fischer and G. W. Harris. *Carbon kinetic isotope effect in the reaction of CH_4 with Cl atoms.* Geophysical Research Letters, 22(10):1225–1228, 1995.

[61] G. Saueressig, J. N. Crowley, P. Bergamaschi, C. Brühl, C. A. M. Brenninkmeijer and H. Fischer. *Carbon 13 and D kinetic isotope effects in the reactions of CH_4 with $O(^1D)$ and OH: New laboratory measurements and their implications for the isotopic composition of stratospheric methane.* Journal of Geophysical Research: Atmospheres, 106(D19):23 127–23 138, 2001.

[62] M. C. McCarthy, K. A. Boering, A. L. Rice, S. C. Tyler, P. Connell and E. Atlas. *Carbon and hydrogen isotopic compositions of stratospheric methane: 2. Two-dimensional model results and implications for kinetic isotope effects.* Journal of Geophysical Research: Atmospheres, 108(D15), 2003.

[63] C. A. Cantrell, R. E. Shetter, A. H. McDaniel, J. G. Calvert, J. A. Davidson, D. C. Lowe, S. C. Tyler, R. J. Cicerone and J. P. Greenberg. *Carbon kinetic isotope effect in the oxidation of methane by the hydroxyl radical.* Journal of Geophysical Research: Atmospheres, 95(D13):22 455–22 462, 1990.

[64] M. C. McCarthy, P. Connell and K. A. Boering. *Isotopic fractionation of methane in the stratosphere and its effect on free tropospheric isotopic compositions.* Geophysical Research Letters, 28(19):3657–3660, 2001.

[65] T. Röckmann, M. Brass, R. Borchers and A. Engel. *The isotopic composition of methane in the stratosphere: high-altitude balloon sample measurements.* Atmos. Chem. Phys., 11(24):13 287–13 304, 2011.

[66] J. S. Wang, M. B. McElroy, C. M. Spivakovsky and D. B. A. Jones. *On the contribution of anthropogenic Cl to the increase in $\delta^{13}C$ of atmospheric methane.* Global Biogeochemical Cycles, 16(3):20–1–20–11, 2002.

[67] J. B. Miller, K. A. Mack, R. Dissly, J. W. C. White, E. J. Dlugokencky and P. P. Tans. *Development of analytical methods and measurements of $^{13}C/^{12}C$ in atmospheric CH_4 from the NOAA Climate Monitoring and Diagnostics Laboratory Global Air Sampling Network.* Journal of Geophysical Research: Atmospheres, 107(D13):ACH 11–1–ACH 11–15, 2002.

[68] M. A. K. Khalil and R. A. Rasmussen. *Atmospheric methyl chloride.* Atmospheric Environment, 33(8):1305–1321, 1999.

[69] M. Bill, R. C. Rhew, R. F. Weiss and A. H. Goldstein. *Carbon isotope ratios of methyl bromide and methyl chloride emitted from a coastal salt marsh.* Geophysical Research Letters, 29(4):4–1–4–4, 2002.

[70] L. Derendorp, A. Wishkerman, F. Keppler, C. McRoberts, R. Holzinger and T. Röckmann. *Methyl chloride emissions from halophyte leaf litter: Dependence on temperature and chloride content.* Chemosphere, 87(5):483–489, 2012.

[71] J. A. Mischler, T. A. Sowers, R. B. Alley, M. Battle, J. R. McConnell, L. Mitchell, T. Popp, E. Sofen and M. K. Spencer. *Carbon and hydrogen isotopic composition of methane over the last 1000 years.* Global Biogeochemical Cycles, 23(4):n/a–n/a, 2009.

[72] S. Houweling, G. R. van der Werf, K. Klein Goldewijk, T. Röckmann and I. Aben. *Early anthropogenic CH_4 emissions and the variation of CH_4 and $^{13}CH_4$ over the last millennium.* Global Biogeochemical Cycles, 22(1):n/a–n/a, 2008.

[73] R. O. Barnes and E. D. Goldberg. *Methane production and consumption in anoxic marine sediments.* Geology, 4(5):297–300, 1976.

[74] W. S. Reeburgh. *Methane consumption in Cariaco Trench waters and sediments.* Earth and Planetary Science Letters, 28(3):337–344, 1976.

[75] S. B. Joye. *Microbiology: A piece of the methane puzzle.* Nature, 491(7425):538–539, 2012.

[76] N. Bohr. *XXXVII. On the constitution of atoms and molecules.* Philosophical Magazine Series 6, 26(153):476–502, 1913.

[77] F. Soddy. *Radio-elements and the periodic law.* Chemical News, 107(2770):97, 1913.

[78] F. Soddy. *Intra-atomic Charge.* Nature, 92(423):399–400, 1913.

[79] J. Chadwick. *Possible Existence of a Neutron.* Nature, 129(3252):312, 1932.

[80] International Union of Pure and Applied Physics (IUPAP). *Report on recent Committee activities on behalf of IUPAP by Brian W. Petley September 1998.* http://www.iupap.org/commissions/interunion/iu14/ga-99.html, 1999 (accessed: 20.01.2013).

[81] Consultative Committee for Units (CCU). *Report of the 16th meeting (13 –14 May 2004) to the International Committee for Weights and Measures.* http://www.bipm.org/utils/common/pdf/CCU16.pdf, 2004.

[82] W. A. Brand and T. B. Coplen. *Stable isotope deltas: tiny, yet robust signatures in nature.* Isotopes in Environmental and Health Studies, 48(3):393–409, 2012.

[83] R. A. Werner and W. A. Brand. *Referencing strategies and techniques in stable isotope ratio analysis.* Rapid Communications in Mass Spectrometry, 15(7):501–519, 2001.

[84] T. B. Coplen. *Guidelines and recommended terms for expression of stable-isotope-ratio and gas-ratio measurement results.* Rapid Communications in Mass Spectrometry, 25(17):2538–2560, 2011.

[85] J. Kónya and N. M. Nagy. *3 - Isotopes*, In *Nuclear and Radiochemistry*, pages 27–47. Elsevier, Oxford, 2012.

[86] J. E. Lennard-Jones. *Cohesion.* Proceedings of the Physical Society, 43(5):461, 1931.

[87] W. Mook. *Environmental Isotopes in the Hydrological Cycle: Principles and Applications, 6 Volumes (for Titles See the Abstract Field).* Unesco, 2000.

[88] A. Einstein and O. Stern. *Einige Argumente für die Annahme einer molekularen Agitation beim absoluten Nullpunkt.* Annalen der Physik, 345(3):551–560, 1913.

[89] W. Heisenberg. *Über den anschaulichen Inhalt der quantentheoretischen Kinematik und Mechanik.* Zeitschrift für Physik, 43(3-4):172–198, 1927.

[90] J. C. Vogel, P. M. Grootes and W. G. Mook. *Isotopic fractionation between gaseous and dissolved carbon dioxide.* Zeitschrift für Physik, 230(3):225–238, 1970.

[91] P. M. Grootes, W. G. Mook and J. C. Vogel. *Isotopic fractionation between gaseous and condensed carbon dioxide.* Zeitschrift für Physik, 221(3):257–273, 1969.

[92] P. Quay, J. Stutsman, D. Wilbur, A. Snover, E. Dlugokencky and T. Brown. *The isotopic composition of atmospheric methane.* Global Biogeochemical Cycles, 13(2):445–461, 1999.

[93] W. D. Harkins. *The stability of atom nuclei, the separation of isotopes, and the whole number rule.* Journal of the Franklin Institute, 195(1):67–106, 1923.

[94] J. B. Miller. *16 - The Carbon Isotopic Composition of Atmospheric Methane and its Constraint on the Global Methane Budget*, In *Stable Isotopes and Biosphere Atmosphere Interactions*, pages 288–310. Academic Press, San Diego, 2005.

[95] J. Bigeleisen and M. Wolfsberg. *Theoretical and Experimental Aspects of Isotope Effects in Chemical Kinetics*, In *Advances in Chemical Physics*, pages 15–76. John Wiley & Sons, Inc., 1958.

[96] Thermo Electron Corporation. *DELTA V Plus: Operating Manual.* Bremen, 2005.

[97] T. Blunier, J. A. Chappellaz, J. Schwander, J. M. Barnola, T. Desperts, B. Stauffer and D. Raynaud. *Historical CH_4 record from the Eurocore ice core at Summit, Greenland*. In T. Boden, D. Kaiser, R. Sepanski, F. Stoss and G. Logsdon, editors, *Trends '93: A compendium of data on global change*, pages 244–249. ORNL/CDIAC-65. Carbon Dioxide, Information Analysis Center, Oak Ridge National Laboratory, Oak Ridge, TN, USA, 1994.

[98] D. Dahl-Jensen. *The Eemian ice from the new Greenland ice core at NEEM*. AGU Fall Meeting Abstracts, 2010:A6, 2010.

[99] A. Schilt, M. Baumgartner, T. Blunier, J. Schwander, R. Spahni, H. Fischer and T. F. Stocker. *Glacial–interglacial and millennial-scale variations in the atmospheric nitrous oxide concentration during the last 800,000 years*. Quaternary Science Reviews, 29(1–2):182–192, 2010.

[100] NEEM Community. *Eemian interglacial reconstructed from a Greenland folded ice core*. Nature, 493(7433):489–494, 2013.

[101] W. Dansgaard. *Stable isotopes in precipitation*. Tellus, 16(4):436–468, 1964.

[102] S. J. Johnsen, W. Dansgaard and J. W. C. White. *The origin of Arctic precipitation under present and glacial conditions*. Tellus Series B-Chemical and Physical Meteorology, 41B(4):452–468, 1989.

[103] T. Blunier and J. Schwander. *Gas enclosure in ice : age difference and fractionation*. In *Physics of Ice Core Records*, pages 307–326. Hokkaido University, 2000.

[104] C. Buizert, P. Martinerie, V. V. Petrenko, J. P. Severinghaus, C. M. Trudinger, E. Witrant, J. L. Rosen, A. J. Orsi, M. Rubino, D. M. Etheridge, L. P. Steele, C. Hogan, J. C. Laube, W. T. Sturges, V. A. Levchenko, A. M. Smith, I. Levin, T. J. Conway, E. J. Dlugokencky, P. M. Lang, K. Kawamura, T. M. Jenk, J. W. C. White, T. Sowers, J. Schwander and T. Blunier. *Gas transport in firn: multiple-tracer characterisation and model intercomparison for NEEM, Northern Greenland*. Atmos. Chem. Phys. Discuss., 11(5):15 975–16 021, 2011.

[105] H. Craig, Y. Horibe and T. Sowers. *Gravitational Separation of Gases and Isotopes in Polar Ice Caps*. Science, 242(4886):1675–1678, 1988.

[106] J. Schwander, J. M. Barnola, C. Andrie, M. Leuenberger, A. Ludin, D. Raynaud and B. Stauffer. *The age of the air in the firn and the ice at Summit, Greenland*. Journal of Geophysical Research-Atmospheres, 98(D2):2831–2838, 1993.

[107] C. Buizert, T. Sowers and T. Blunier. *Assessment of diffusive isotopic fractionation in polar firn, and application to ice core trace gas records*. Earth and Planetary Science Letters, 361(0):110–119, 2013.

[108] J. Schwander and B. Stauffer. *Age difference between polar ice and the air trapped in its bubbles*. Nature, 311(5981):45–47, 1984.

[109] H. Craig, C. C. Chou, J. A. Welhan, C. M. Stevens and A. Engelkemeir. *The Isotopic Composition of Methane in Polar Ice Cores*. Science, 242(4885):1535–1539, 1988.

[110] R. Fairbridge. *Medieval Warm Period*, In V. Gornitz, editor, *Encyclopedia of Paleoclimatology and Ancient Environments*, chapter 137, pages 551–554. Encyclopedia of Earth Sciences Series. Springer Netherlands, 2009.

[111] M. E. Mann and P. D. Jones. *Global surface temperatures over the past two millennia*. Geophysical Research Letters, 30(15):1820, 2003.

[112] H. Goosse, O. Arzel, J. Luterbacher, M. E. Mann, H. Renssen, N. Riedwyl, A. Timmermann, E. Xoplaki and H. Wanner. *The origin of the European "Medieval Warm Period"*. Clim. Past, 2(2):99–113, 2006.

[113] M. K. Hughes and H. F. Diaz. *Was there a medieval warm period, and if so, where and when?* Climatic Change, 26(2-3):109–142, 1994.

[114] M.-S. Seidenkrantz, L. Roncaglia, A. Fischel, C. Heilmann-Clausen, A. Kuijpers and M. Moros. *Variable North Atlantic climate seesaw patterns documented by a late Holocene marine record from Disko Bugt, West Greenland.* Marine Micropaleontology, 68(1–2):66–83, 2008.

[115] E. R. Cook, J. G. Palmer and R. D. D'Arrigo. *Evidence for a 'Medieval Warm Period' in a 1100 year tree-ring reconstruction of past austral summer temperatures in New Zealand.* Geophysical Research Letters, 29(14):12–1–12–4, 2002.

[116] T. Kellerhals, S. Brütsch, M. Sigl, S. Knüsel, H. W. Gäggeler and M. Schwikowski. *Ammonium concentration in ice cores: A new proxy for regional temperature reconstruction?* Journal of Geophysical Research: Atmospheres, 115(D16):D16 123, 2010.

[117] F. C. Ljungqvist. *A new reconstruction of temperature variability in the extra-tropical northern hemisphere during the last two millennia.* Geografiska Annaler: Series A, Physical Geography, 92(3):339–351, 2010.

[118] A. Moberg, D. M. Sonechkin, K. Holmgren, N. M. Datsenko and W. Karlen. *Highly variable Northern Hemisphere temperatures reconstructed from low- and high-resolution proxy data.* Nature, 433(7026):613–617, 2005.

[119] P. Sperlich, C. Buizert, C. Sapart, M. Prokopiou, T. Jenk, T. Röckmann and T. Blunier. *An automated setup to measure paleoatmospheric $\delta^{13}C$–CH_4, $\delta^{15}N$–N_2O and $\delta^{18}O$–N_2O in one ice core sample.* Atmospheric Measurement Techniques, (accepted, in press), 2013.

[120] H. Craig, C. C. Chou, J. A. Welhan, C. M. Stevens and A. Engelkemeir. *The Isotopic Composition of Methane in Polar Ice Cores.* Science, 242(4885):1535–1539, 1988.

[121] T. Sowers, S. Bernard, O. Aballain, J. Chappellaz, J.-M. Barnola and T. Marik. *Records of the $\delta^{13}C$ of atmospheric CH_4 over the last 2 centuries as recorded in Antarctic snow and ice.* Global Biogeochemical Cycles, 19(2):GB2002, 2005.

[122] H. Schaefer and M. J. Whiticar. *Measurement of stable carbon isotope ratios of methane in ice samples.* Organic Geochemistry, 38(2):216–226, 2007.

[123] M. Behrens, J. Schmitt, K. U. Richter, M. Bock, U. C. Richter, I. Levin and H. Fischer. *A gas chromatography/combustion/isotope ratio mass spectrometry system for high-precision $\delta^{13}C$ measurements of atmospheric methane extracted from ice core samples.* Rapid Communications in Mass Spectrometry, 22(20):3261–3269, 2008.

[124] C. J. Sapart, C. van der Veen, I. Vigano, M. Brass, R. S. W. van de Wal, M. Bock, H. Fischer, T. Sowers, C. Buizert, P. Sperlich, T. Blunier, M. Behrens, J. Schmitt, B. Seth and T. Röckmann. *Simultaneous stable isotope analysis of methane and nitrous oxide on ice core samples.* Atmos. Meas. Tech., 4(12):2607–2618, 2011.

[125] J. R. Melton, M. J. Whiticar and P. Eby. *Stable carbon isotope ratio analyses on trace methane from ice samples.* Chemical Geology, 288(3–4):88–96, 2011.

[126] P. Sperlich. *$\delta^{13}C$ measurements of EUROCORE ice cores from Greenland.* (personal communication), 2012.

[127] AirLiquide. *Kohlendioxid N48.* http://www.airliquide.de/gasekatalog/pdb/kohlendioxidn48.pdf, 2012.

[128] T. Jenk. *CIC – pure gas & full air standards (10/8/2012).* https://wiki.nbi.ku.dk/w/iceandclimate/index.php?title=File:CIC_gas_standards.pdf&oldid=1519, 2012.

[129] H. Craig. *Isotopic standards for carbon and oxygen and correction factors for mass-spectrometric analysis of carbon dioxide.* Geochimica et Cosmochimica Acta, 12(1–2):133–149, 1957.

[130] C. Stowasser. *Methane concentration measurement of GIS bottle. (personal commmunication)*, 2012.

[131] P. Sperlich, M. Guillevic, C. Buizert, T. M. Jenk, C. J. Sapart, H. Schaefer, T. J. Popp and T. Blunier. *A combustion setup to precisely reference $\delta^{13}C$ and δ^2H isotope ratios of pure CH_4 to produce isotope reference gases of $\delta^{13}C$-CH_4 in synthetic air.* Atmospheric Measurement Techniques, 5(9):2227–2236, 2012.

[132] AirLiquide. *Methan N45.* http://www.airliquide.de/gasekatalog/pdb/methann45.pdf, 2012.

[133] L. E. Mitchell, E. J. Brook, T. Sowers, J. R. McConnell and K. Taylor. *Multidecadal variability of atmospheric methane, 1000–1800 C.E.* Journal of Geophysical Research: Biogeosciences, 116(G2):G02 007, 2011.

[134] D. M. Murphy and T. Koop. *Review of the vapour pressures of ice and supercooled water for atmospheric applications.* Quarterly Journal of the Royal Meteorological Society, 131(608):1539–1565, 2005.

[135] G. Walther, D. J. Mowbray, T. Jiang, G. Jones, S. Jensen, U. J. Quaade and S. Horch. *Oxidation of CO and H_2 by O_2 and N_2O on Au/TiO_2 catalysts in microreactors.* Journal of Catalysis, 260(1):86–92, 2008.

[136] A. C. Gluhoi, M. A. P. Dekkers and B. E. Nieuwenhuys. *Comparative studies of the N_2O/H_2, N_2O/CO, H_2/O_2 and CO/O_2 reactions on supported gold catalysts: effect of the addition of various oxides.* Journal of Catalysis, 219(1):197–205, 2003.

[137] G. Walther, L. Cervera-Gontard, U. J. Quaade and S. Horch. *Low temperature methane oxidation on differently supported 2 nm Au nanoparticles.* Gold Bulletin, 42(1):13–19, 2009.

[138] T. Umezawa, S. Aoki, T. Nakazawa and S. Morimoto. *A High-precision Measurement System for Carbon and Hydrogen Isotopic Ratios of Atmospheric Methane and Its Application to Air Samples Collected in the Western Pacific Region.* Journal of The Meteorological Society of Japan, 87(3):365–379, 2009.

[139] Valco Instruments Co. Inc. *Microvolume Thermal Conductivity Detector Instruction Manual.* Schenkon, 2012.

[140] L. M. Besley and G. A. Bottomley. *The water vapour equilibria over magnesium perchlorate hydrates.* The Journal of Chemical Thermodynamics, 1(1):13–19, 1969.

[141] H. H. Willard and G. F. Smith. *The preparation and properties of magnesium perchlorate and its use as a drying agent.* Journal of the American Chemical Society, 44:2255–2259, 1922.

[142] J. Kaiser. *Reformulated ^{17}O correction of mass spectrometric stable isotope measurements in carbon dioxide and a critical appraisal of historic 'absolute' carbon and oxygen isotope ratios.* Geochimica et Cosmochimica Acta, 72(5):1312–1334, 2008.

[143] K. A. Mauritz and R. B. Moore. *State of Understanding of Nafion.* Chemical Reviews, 104(10):4535–4586, 2004.

[144] W. A. Brand. *PreCon: A Fully Automated Interface for the Pre-Gc Concentration of Trace Gases on Air for Isotopic Analysis.* Isotopes in Environmental and Health Studies, 31(3-4):277–284, 1995.

[145] B. Shi and B. H. Davis. *Gas chromatographic separation of pairs of isotopic molecules.* Journal of Chromatography A, 654(2):319–325, 1993.

[146] N. Aoki and Y. Makide. *The Concentration of Krypton in the Atmosphere – Its Revision after Half a Century.* Chemistry Letters, 34(10):1396–1397, 2005.

[147] J. Schmitt, B. Seth, M. Bock, C. van der Veen, L. Möller, C. J. Sapart, M. Prokopiou, T. Sowers, T. Röckmann and H. Fischer. *On the interference of $^{86}Kr^{2+}$ during carbon isotope analysis of atmospheric methane using continuous flow combustion–isotope ratio mass spectrometry.* Atmos. Meas. Tech. Discuss., 6(1):1409–1460, 2013.

[148] C. Buizert. *Bubble Free Ice Setup (non-published work)*, 2009.

[149] C. A. M. Brenninkmeijer and T. Röckmann. *A rapid method for the preparation of O_2 from CO_2 for mass spectrometric measurement of $^{17}O/^{16}O$ ratios.* Rapid Communications in Mass Spectrometry, 12(8):479–483, 1998.

[150] R. N. Clayton and T. K. Mayeda. *The use of bromine pentafluoride in the extraction of oxygen from oxides and silicates for isotopic analysis.* Geochimica et Cosmochimica Acta, 27(1):43–52, 1963.

[151] J. Santrock, S. A. Studley and J. M. Hayes. *Isotopic analyses based on the mass spectra of carbon dioxide.* Analytical Chemistry, 57(7):1444–1448, 1985.

[152] C. Allison, R. Francey and H. Meijer. *Recommendations for the reporting of stable isotope measurements of carbon and oxygen in CO_2 gas*, In IAEA, editor, *Reference and Intercomparison Materials for Stable Isotopes of Light Elements*, pages 155–162. International Atomic Energy Agency, 1995.

[153] S. S. Assonov and C. A. M. Brenninkmeijer. *On the ^{17}O correction for CO_2 mass spectrometric isotopic analysis.* Rapid Communications in Mass Spectrometry, 17(10):1007–1016, 2003.

[154] S. Valkiers, M. Varlam, K. Ruße, M. Berglund, P. Taylor, J. Wang, M. J. T. Milton and P. De Bièvre. *Preparation of Synthetic Isotope Mixtures for the calibration of carbon and oxygen isotope ratio measurements (in carbon dioxide) to the SI.* International Journal of Mass Spectrometry, 264(1):10–21, 2007.

[155] J. Carter and V. Barwick, editors. *Good Practice Guide for Isotope Ratio Mass Spectrometry.* FIRMS, 2011.

[156] R. M. Verkouteren and D. B. Klinedinst. *Value Assignment and Uncertainty Estimation of Selected Light Stable Isotope Reference Materials:RMs 8543-8545, RMs 8562-8564, and RM 8566, (CODEN: NSPUE2).* National Institute of Standards and Technology Special Publication, (260-149), 2004.

[157] H. Schlüter. *Method for Determining Atomic Isotope Masses.* US2005061965-A1; DE10344239-A1; US7193705-B2, 2005.

[158] R. H. Rhodes, X. Faïn, C. Stowasser, T. Blunier, J. Chappellaz, J. R. McConnell, L. E. Mitchell and E. J. Brook. *Continuous ice core methane measurements from a late Holocene Greenland ice core: atmospheric and in-situ signals.* Earth and Planetary Science Letters, (in press), 2013.

[159] E. Tipping. *Inverse Problems in Atmospheric Constituent Transport.* Cambridge University Press, 2002.

[160] P. P. Tans. *A note on isotopic ratios and the global atmospheric methane budget.* Global Biogeochemical Cycles, 11(1):77–81, 1997.

[161] M. A. K. Khalil and R. A. Rasmussen. *Atmospheric methane: Trends over the last 10,000 years.* Atmospheric Environment (1967), 21(11):2445–2452, 1987.

[162] J. Chappellaz, T. Blunier, S. Kints, A. Dällenbach, J.-M. Barnola, J. Schwander, D. Raynaud and B. Stauffer. *Changes in the atmospheric CH_4 gradient between Greenland and Antarctica during the Holocene.* Journal of Geophysical Research: Atmospheres, 102(D13):15 987–15 997, 1997.

[163] C. E. Junge. *Note on the exchange rate between the northern and southern atmosphere.* Tellus, 14(2):242–246, 1962.

[164] K. H. Rosenlof and J. R. Holton. *Estimates of the stratospheric residual circulation using the downward control principle.* Journal of Geophysical Research: Atmospheres, 98(D6):10 465–10 479, 1993.

[165] G. Monteil, S. Houweling, E. J. Dlugockenky, G. Maenhout, B. H. Vaughn, J. W. C. White and T. Rockmann. *Interpreting methane variations in the past two decades using measurements of CH_4 mixing ratio and isotopic composition.* Atmos. Chem. Phys., 11(17):9141–9153, 2011.

[166] M. Sigl, J. R. McConnell, L. Layman, O. Maselli, K. McGwire, D. Pasteris, D. Dahl-Jensen, J. P. Steffensen, B. Vinther, R. Edwards, R. Mulvaney and S. Kipfstuhl. *A new bipolar ice core record of volcanism from WAIS Divide and NEEM and implications for climate forcing of the last 2000 years.* Journal of Geophysical Research: Atmospheres, in press., 2013.

[167] E. J. Dlugokencky, L. P. Steele, P. M. Lang and K. A. Masarie. *The growth rate and distribution of atmospheric methane.* Journal of Geophysical Research: Atmospheres, 99(D8):17 021–17 043, 1994.

[168] L. Mitchell, E. Brook, J. E. Lee, C. Buizert and T. Sowers. *New Constraints on the Late Holocene Anthropogenic Contribution to the Atmospheric Methane Budget.* in preparation, 2013.

[169] C. MacFarling Meure, D. Etheridge, C. Trudinger, P. Steele, R. Langenfelds, T. van Ommen, A. Smith and J. Elkins. *Law Dome CO_2, CH_4 and N_2O ice core records extended to 2000 years BP.* Geophysical Research Letters, 33(14):L14 810, 2006.

[170] T. D. van Ommen, V. Morgan and M. A. J. Curran. *Deglacial and Holocene changes in accumulation at Law Dome, East Antarctica.* Annals of Glaciology, 39(1):359–365, 2004.

[171] D. M. Etheridge, L. P. Steele, R. J. Francey and R. L. Langenfelds. *Atmospheric methane between 1000 A.D. and present: Evidence of anthropogenic emissions and climatic variability.* Journal of Geophysical Research: Atmospheres, 103(D13):15 979–15 993, 1998.

[172] L. E. Mitchell, E. J. Brook, T. Sowers, J. R. McConnell and K. Taylor. *Methane Concentration and Chronology from the WAIS Divide Ice Core (WDC05A).* Boulder, Colorado USA: National Snow and Ice Data Center., 2011.

[173] T. Blunier. *Timescale for Eurocore ice core (personal communication)*, 2013.

[174] T. Sowers. *Methane Isotopes from the WAIS Divide Ice Core.* http://dx.doi.org/10.7265/N5J67DW0, 2009.

[175] R. E. Newell, D. G. Vincent and J. W. Kidson. *Interhemispheric mass exchange from meteorological and trace substance observations.* Tellus, 21(5):641–647, 1969.

[176] G. Czeplak and C. Junge. *Studies of Interhemispheric Exchange in the Troposphere by a Diffusion Model*, In F. N. Frenkiel and R. E. Munn, editors, *Advances in Geophysics*, volume Volume 18, Part B, pages 57–72. Elsevier, 1975.

[177] D. J. Jacob, M. J. Prather, S. C. Wofsy and M. B. McElroy. *Atmospheric distribution of 85Kr simulated with a general circulation model.* Journal of Geophysical Research: Atmospheres, 92(D6):6614–6626, 1987.

[178] L. S. Geller, J. W. Elkins, J. M. Lobert, A. D. Clarke, D. F. Hurst, J. H. Butler and R. C. Myers. *Tropospheric SF6: Observed latitudinal distribution and trends, derived emissions and interhemispheric exchange time.* Geophysical Research Letters, 24(6):675–678, 1997.

[179] I. Levin and V. Hesshaimer. *Refining of atmospheric transport model entries by the globally observed passive tracer distributions of 85krypton and sulfur hexafluoride (SF6).* Journal of Geophysical Research: Atmospheres, 101(D11):16 745–16 755, 1996.

[180] D. H. Ehhalt. *The CH_4 concentration over the ocean and its possible variation with latitude.* Tellus, 30(2):169–176, 1978.

[181] E. W. Mayer, D. R. Blake, S. C. Tyler, Y. Makide, D. C. Montague and F. S. Rowland. *Methane: Interhemispheric Concentration Gradient and Atmospheric Residence Time.* Proceedings of the National Academy of Sciences of the United States of America, 79(4):1366–1370, 1982.

[182] J. White, D. F. Ferretti, J. Miller, D. M. Etheridge, K. R. Lassey, D. C. Lowe, C. M. MacFarling, M. F. Dreier, C. M. Trudinger and T. v. Ommen. *The global methane budget over the last 2000 years: $^{13}CH_4$ reveals hidden information*, In T. Dawson and R. Siegwolf, editors, *Stable Isotopes as Indicators of Ecological Change*, pages 235–249. Elseiver Academic Press, New York, 2007.

[183] S. Houweling, F. Dentener and J. Lelieveld. *Simulation of preindustrial atmospheric methane to constrain the global source strength of natural wetlands.* Journal of Geophysical Research: Atmospheres, 105(D13):17 243–17 255, 2000.

[184] I. Fung, J. John, J. Lerner, E. Matthews, M. Prather, L. P. Steele and P. J. Fraser. *Three-dimensional model synthesis of the global methane cycle.* Journal of Geophysical Research: Atmospheres, 96(D7):13 033–13 065, 1991.

[185] K. Klein Goldewijk, A. Beusen, G. van Drecht and M. de Vos. *The HYDE 3.1 spatially explicit database of human-induced global land-use change over the past 12,000 years.* Global Ecology and Biogeography, 20(1):73–86, 2011.

[186] G. K. Heilig. *Anthropogenic Factors in Land-Use Change in China.* Population and Development Review, 23(1):139–168, 1997.

[187] J. D. Durand. *The Population Statistics of China, A.D. 2-1953.* Population Studies, 13(3):209–256, 1960.

[188] R. A. Dull, R. J. Nevle, W. I. Woods, D. K. Bird, S. Avnery and W. M. Denevan. *The Columbian Encounter and the Little Ice Age: Abrupt Land Use Change, Fire, and Greenhouse Forcing.* Annals of the Association of American Geographers, 100(4):755–771, 2010.

[189] M. Bock, J. Schmitt, M. Behrens, L. Möller, R. Schneider, C. Sapart and H. Fischer. *A gas chromatography/pyrolysis/isotope ratio mass spectrometry system for high-precision δD measurements of atmospheric methane extracted from ice cores.* Rapid Communications in Mass Spectrometry, 24(5):621–633, 2010.

[190] J. M. Eiler. *"Clumped-isotope" geochemistry—The study of naturally-occurring, multiply-substituted isotopologues.* Earth and Planetary Science Letters, 262(3–4):309–327, 2007.

[191] K. Tsuji, S. Fujikawa, K. Yamada, N. Yoshida, K. Yamamoto and T. Kikugawa. *Precise measurement of the $^{13}CH_4/^{12}CH_4$ ratio of diluted methane using a near-infrared laser absorption spectrometer.* Sensors and Actuators B: Chemical, 114(1):326–333, 2006.

[192] A. Einstein. *Über das Relativitätsprinzip und die aus demselben gezogenen Folgerungen.* Jahrbuch der Radioaktivität und Elektronik, 4:411–462, 1908.

[193] M. Laue. *Zur Dynamik der Relativitätstheorie.* Annalen der Physik, 340(8):524–542, 1911.

[194] J. M. Eiler, M. Clog, P. Magyar, A. Piasecki, A. Sessions, D. Stolper, M. Deerberg, H.-J. Schlueter and J. Schwieters. *A high-resolution gas-source isotope ratio mass spectrometer*. International Journal of Mass Spectrometry, 335(0):45–56, 2013.

[195] E. J. Mroz, M. Alei, J. H. Cappis, P. R. Guthals, A. S. Mason and D. J. Rokop. *Detection of multiply deuterated methane in the atmosphere*. Geophysical Research Letters, 16(7):677–678, 1989.

[196] J. M. Eiler. *Personal Communication*, 2013.

[197] P. J. Mohr, B. N. Taylor and D. B. Newell. *CODATA Recommended Values of the Fundamental Physical Constants: 2010*, In W. M. Haynes, editor, *CRC Handbook of Chemistry and Physics,*, page 1.1. Internet Version 2013. CRC Press, Cleveland, Ohio, 93 edition, 2013.

[198] L. V. Gurvich, V. S. Iorish, V. S. Yungman and O. V. Dorofeeva. *Thermodynamic Properties as a Function of Temperature*, In W. M. Haynes, editor, *CRC Handbook of Chemistry and Physics,*, pages 5.34,. Internet Version 2013. CRC Press, Cleveland, Ohio, 93 edition, 2013.

Title photo: Skåne, Sweden, by Jonas Haller, 2012.
Image on page 81: Photo: Muang Sing, Laos, by Robb Cadwell, 2007. Used with the photographer's permission.

All other figures and schemas are, unless otherwise stated, made by the author himself.

This page intentionally left blank.

Appendix A

Appendix

A.1 Transformation between standards

The relationship between samples against various standards is not apparent on first sight: the value of the sample against standard 1, $\delta_{s/1}$, of standard 1 against standard 2, $\delta_{1/2}$, and the sample against standard 2, $\delta_{s/2}$, are defined as:

$$\delta_{1/2} = \frac{R_1 - R_2}{R_2} \qquad \Leftrightarrow \qquad \delta_{1/2} + 1 = \frac{R_1}{R_2} \tag{A.1}$$

$$\delta_{s/1} = \frac{R_s - R_1}{R_1} \qquad \Leftrightarrow \qquad \delta_{s/1} + 1 = \frac{R_s}{R_1} \tag{A.2}$$

If follows that

$$\delta_{s/2} + 1 = \frac{R_s}{R_2} = \frac{R_1}{R_2}\frac{R_s}{R_1} = (\delta_{1/2} + 1)(\delta_{s/1} + 1) = \delta_{1/2} + \delta_{s/1} + \delta_{1/2}\delta_{s/1} + 1. \tag{A.3}$$

And hence

$$\delta_{s/2} = \delta_{1/2} + \delta_{s/1} + \delta_{1/2}\delta_{s/1}. \tag{A.4}$$

A.2 Epsilon approximation

The identity shown in Section 2.4.3, Eqn. 2.38 is easy to grasp:

$$\varepsilon_{B/A} = \frac{\delta_B - \delta_A}{\delta_A + 1} \tag{A.5}$$

$$\Leftrightarrow \quad \frac{R_B}{R_A} - 1 = \frac{\frac{R_B - R_{std}}{R_{std}} - \frac{R_A - R_{std}}{R_{std}}}{\frac{R_A - R_{std}}{R_{std}} + 1} \tag{A.6}$$

$$\Leftrightarrow \frac{R_B - R_A}{R_A} = \frac{R_B - R_A}{R_A} \tag{A.7}$$

A.3 Degrees of freedom

In Section 2.4.3 the available degrees of freedom to calculate the inner energy are said to be temperature dependent. The following elaborates why.

The available degrees of freedom depend on temperature, since degrees of freedom represent different energy levels, of which higher rotational and vibrational levels are only achievable at elevated temperatures. In this context of calculating the inner energy, the inner ("vibrational") degrees of freedom are counted twice, since oscillations contain kinetic as well as potential energy. Thus, the *maximum* degrees of freedom for methane is $f'_{max} = 3 + 3 + 2 \cdot (3N - 6) = 24$. The number of *available* degrees can be derived from the adiabatic index [a], γ, defined as

$$\gamma = \frac{c_p}{c_v} = \frac{f' + 2}{f'} \Leftrightarrow f' = \frac{2}{\gamma - 1}, \tag{A.8}$$

where c_p is the usually tabulated value, and $c_v = c_p - R$ and $R = 8.3144621(75)\,\mathrm{J\,mol^{-1}\,K^{-1}}$ [197].

Table A.1: Adiabatic indices for Methane, calculated based on $c_p(T)$ from CRC (2013) [198].

Temperature		Heat capacity		Adiabatic index	"Degrees"[b] of freedom
T/K	T/K+273.15	$c_p/(\mathrm{J/mol^{-1}\,K^{-1}})$	$c_v/(\mathrm{J/mol^{-1}\,K^{-1}})$	γ	f'
298.15	25	35.695	27.381	1.304	6.586
600	326.85	52.742	44.428	1.187	10.687
900	626.85	69.137	60.823	1.137	14.631
1200	926.85	81.682	73.368	1.113	17.648
1500	1226.85	90.856	82.542	1.101	19.855

A.4 Setup overview

On the following two A3 pages, the full setup, including the Helium lines (green), unused valves ("Conditioning") and cryotraps ("T-3") as well as the setup for the future δD analysis (Pyro) is shown. An abridged version is shown in Section 3.4.

---

[a]
The adiabatic index is also known as *heat capacity ratio, ratio of specific heats* or *isentropic expansion factor.*
[b] Degrees in quotation marks since $f' = f_{trans} + f_{rot} + 2f_{vib}$, as explained above, while $f = f_{trans} + f_{rot} + f_{vib}$.
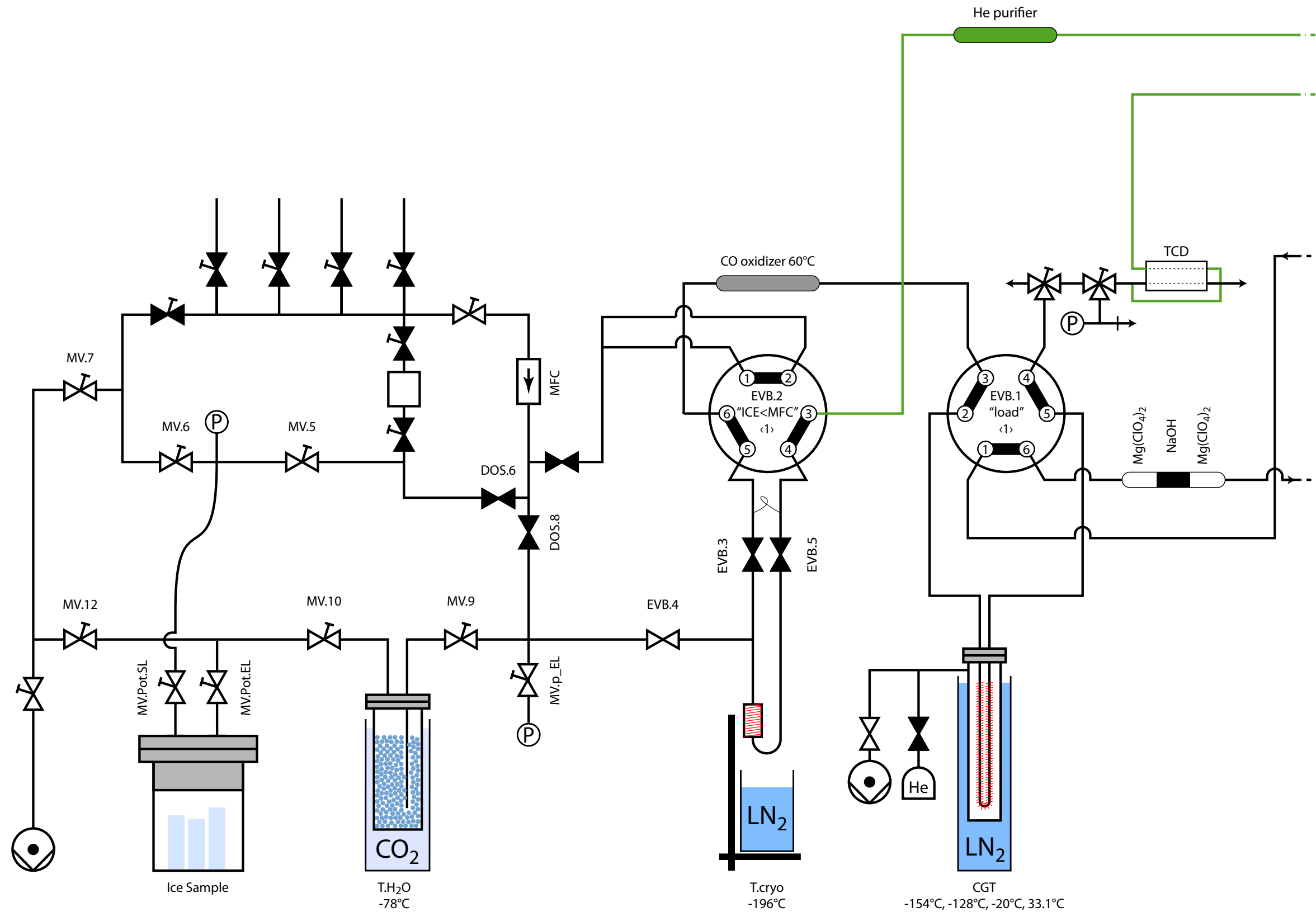
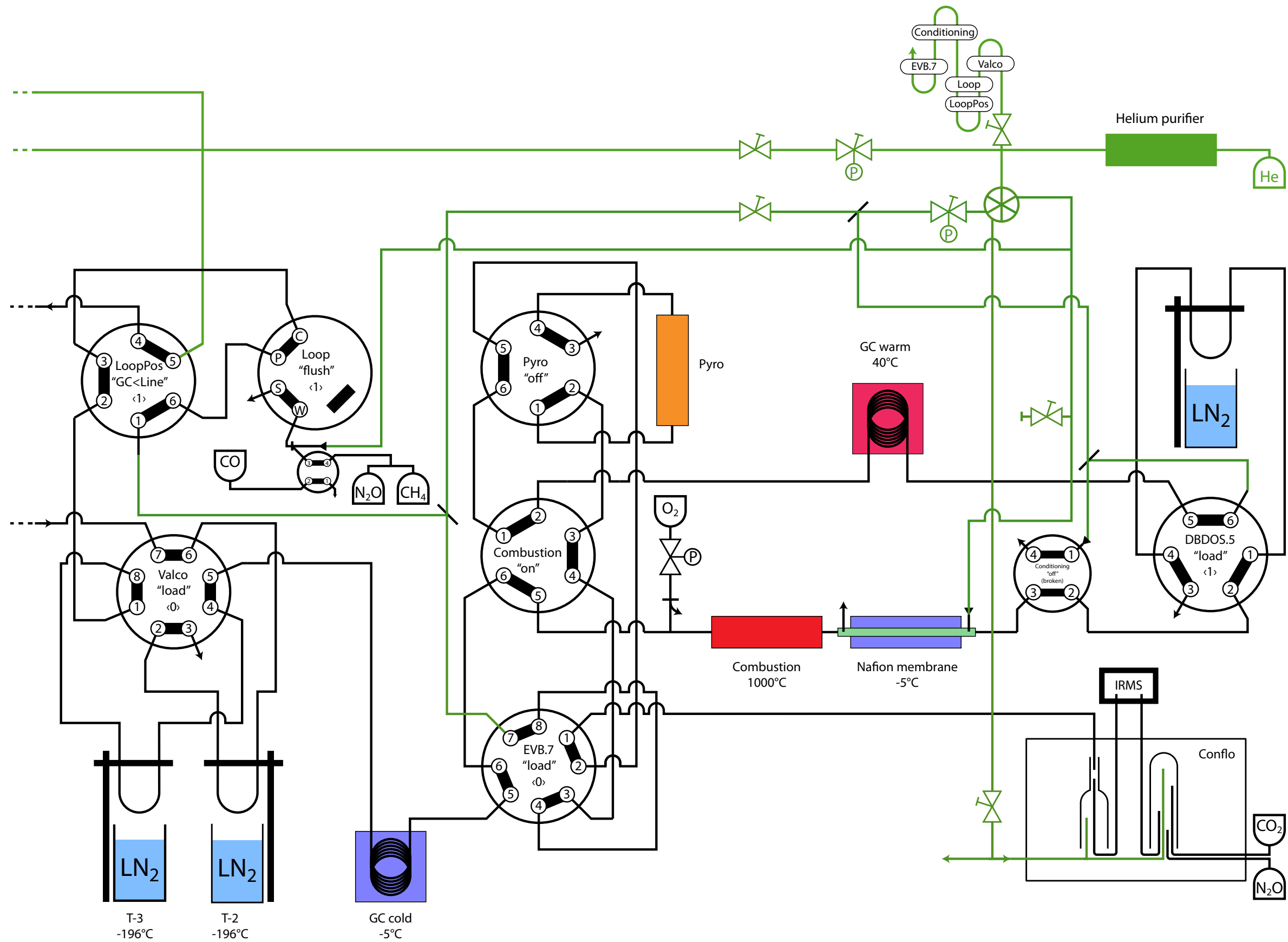**Figure A.1:** Extraction part of setup including He flows (green).

Figure A.2: GC-C-GC-IRMS part of setup, including He flows and unused components.

A.5   Hints and pitfalls

In the following, a few hints are given that help avoiding pitfalls and stress during the lab work.

Exchange ice-water bath with pan

After precooling the cryopump for 8 minutes, the ice-water bath is removed, and the pan on the magnet stirrer are mounted for melting. The stirrer and the base of the pan are together considerably higher than the base of the ice-water containing vessel. Hence, the lab boy must be lowered. Best practice was to lower the lab boy to the level of being able to remove the vessel without moving the lab boy. This will free just enough space to mount the lab boy with the stirrer and the pan on top of it. For doing so, take the lab boy to the side, mount the pan from underneath around the vessel, slide the lab boy with the stirrer back under the pan, cf. Fig. A.3. It kind of looks obvious now, but during the measurement, it can be easily forgotten, by how much of a distance, the lab boy needs to be lowered.
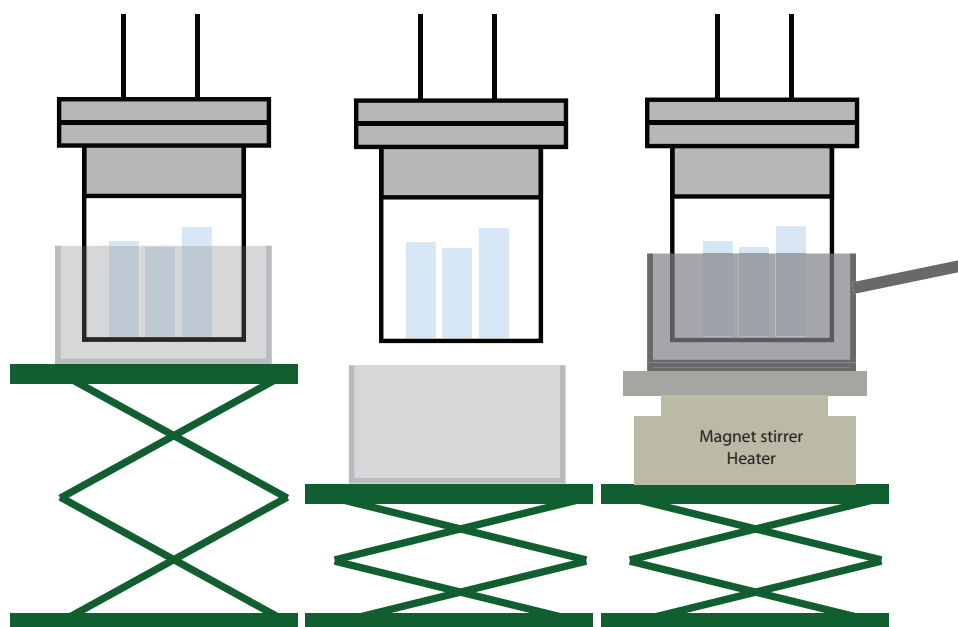

Figure A.3: Exchange of ice-water bath (left) against the pan (right), schematically.

Melt process

During the melting process, the extraction vessel is kept not too close to the base of the pan, to maintain a distance somewhere around 2 cm, to ensure that the base of the vessel is not getting in direct contact with the base of the pan, so that the water of the pot is moving with convection.

After melting

Once the melting is finished, it is useful to cool the heating plate of the stirrer with ice (e.g. ice blocks taken from the ice-water bath). This ensures that the residual heat of the plate does not heat the bottom of the ice water bath, which could raise the water temperature close to the bottom during the subsequent stirring, when the distance between pot and ice-water container must be as small as possible, but not zero. If a too large of a water gap is left between the vessel and the plastic container, the stir bar will not rotate smoothly, but tend to wobble and escape the magnetic field as the rotation speed increases. Only through keeping the vessel close to the container, rotation speeds as high as 750 and 1000 rpm can be reached with the long and short stir bar respectively. The thin, left open water layer allows convective transport of the cooling water, and prevents the pot from getting heated from the residual that nevertheless remains in the stirrer plate.

A.6   Additional smoothing example

An additional example to the smoothing modes presented in Section 6.6 is shown in Fig. A.4 in Fig. A.4.
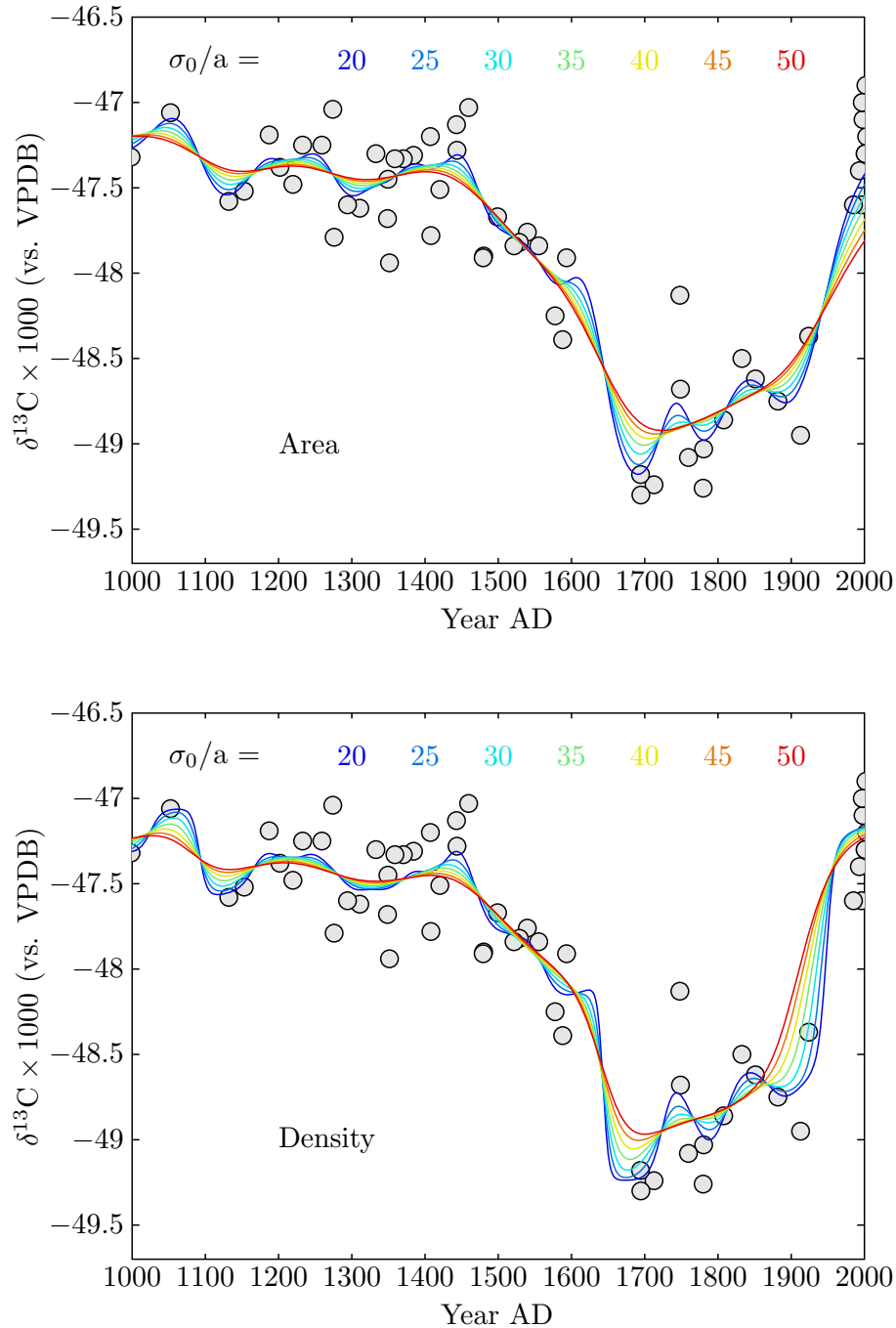

Figure A.4: Gaussian smoothing illustrating the differences of area and density smoothing respectively.

A.7   Variance estimation through error propagation

Eq. (4.32) can be developed and simplified:

$$x_{\text{sa}}(\hat{A}_{\text{sa}}, \hat{\varphi}_{\text{sa}}, \hat{A}_{k,1}, \cdots, \hat{A}_{k,n}, \hat{\varphi}_{k,1}, \cdots, \hat{\varphi}_{k,n}) = \frac{\hat{A}_{\text{sa}} \frac{1}{n} \sum_{i=1}^{n} \frac{V_{k,i} x_{k,i}}{\hat{A}_{k,i}}}{\hat{\varphi}_{\text{sa}} \frac{1}{n} \sum_{i=1}^{n} \frac{V_{k,i}}{\hat{\varphi}_{k,i}}} = \frac{\hat{A}_{\text{sa}} \sum_{i=1}^{n} x_{k,i} \hat{\varphi}_{k,i}}{\hat{\varphi}_{\text{sa}} \sum_{i=1}^{n} \hat{A}_{k,i}}. \tag{A.9}$$

For the calculation of the variance of the function x_{sa}, the coefficient vector, $\mathbf{F}$, is calculated by deriving the function by each variable

$$\mathbf{F} = \nabla x_{\text{sa}} \tag{A.10}$$

$$= \begin{bmatrix} \frac{\partial}{\partial \hat{A}_{\text{sa}}} & \underbrace{\frac{\partial}{\partial \hat{A}_{k,1}} \cdots \frac{\partial}{\partial \hat{A}_{k,n}}}_{\text{n elements}} & \frac{\partial}{\partial \hat{\varphi}_{\text{sa}}} & \underbrace{\frac{\partial}{\partial \hat{\varphi}_{k,1}} \cdots \frac{\partial}{\partial \hat{\varphi}_{k,n}}}_{\text{n elements}} \end{bmatrix} \frac{\hat{A}_{\text{sa}} \sum_{i=1}^{n} x_{k,i} \hat{\varphi}_{k,i}}{\hat{\varphi}_{\text{sa}} \sum_{i=1}^{n} \hat{A}_{k,i}} \tag{A.11}$$

$$= \begin{bmatrix} \frac{\sum x_{k,i} \hat{\varphi}_{k,i}}{\hat{\varphi}_{\text{sa}} \sum \hat{A}_{k,i}} & \underbrace{-\frac{\hat{A}_{\text{sa}} \sum x_{k,i} \hat{\varphi}_{k,i}}{\hat{\varphi}_{\text{sa}} (\sum \hat{A}_{k,i})^2} \cdots -\frac{\hat{A}_{\text{sa}} \sum x_{k,i} \hat{\varphi}_{k,i}}{\hat{\varphi}_{\text{sa}} (\sum \hat{A}_{k,i})^2}}_{\text{n times}} & -\frac{\hat{A}_{\text{sa}} \sum x_{k,i} \hat{\varphi}_{k,i}}{(\hat{\varphi}_{\text{sa}})^2 \sum \hat{A}_{k,i}} & \underbrace{\frac{\hat{A}_{\text{sa}} \sum x_{k,i}}{\hat{\varphi}_{\text{sa}} \sum \hat{A}_{k,i}} \cdots \frac{\hat{A}_{\text{sa}} \sum x_{k,i}}{\hat{\varphi}_{\text{sa}} \sum \hat{A}_{k,i}}}_{\text{n times}} \end{bmatrix}. \tag{A.12}$$

The variance matrix, $\mathbf{K}$, is defined as the variances of the parameters in a diagonal matrix Eq.(A.13), and since the variances of $s^2_{\hat{A}_{\text{sa}}}$ and $s^2_{\hat{A}_{k,i}}$ are equal, the expression simplifies further to Eq. (A.14):

$$\mathbf{K} = \begin{bmatrix} s^2_{\hat{A}_{\text{sa}}} & s^2_{\hat{A}_{k,1}} & \cdots & s^2_{\hat{A}_{k,n}} & s^2_{\hat{\varphi}_{\text{sa}}} & s^2_{\hat{\varphi}_{k,1}} & \cdots & s^2_{\hat{\varphi}_{k,n}} \end{bmatrix}^{\text{diag}} \tag{A.13}$$

$$= \begin{bmatrix} \underbrace{s^2_{\hat{A}} \cdots s^2_{\hat{A}}}_{\text{n+1 times}} & \underbrace{s^2_{\hat{\varphi}} \cdots s^2_{\hat{\varphi}}}_{\text{n+1 times}} \end{bmatrix}^{\text{diag}}, \tag{A.14}$$

where the estimated variances, s^2, are the square of the estimated standard deviations from Eq. (4.29). Now, the variance of x_{sa} can then be estimated by a matrix multiplication:

$$s^2_{x_{\text{sa}}} = \mathbf{F} \mathbf{K} \mathbf{F}^{\text{T}}, \tag{A.15}$$

which can also be expressed as

$$s^2_{x_{\text{sa}}} = \left[\left(\frac{\partial x}{\partial \hat{A}_{\text{sa}}} \right)^2 + n \left(\frac{\partial x}{\partial \hat{A}_{k,i}} \right)^2 \right] s^2_{\hat{A}} + \left[\left(\frac{\partial x}{\partial \hat{\varphi}_{\text{sa}}} \right)^2 + n \left(\frac{\partial x}{\partial \hat{\varphi}_{k,i}} \right)^2 \right] s^2_{\hat{\varphi}}. \tag{A.16}$$

The estimator of the standard deviation, $s_{x_{\text{sa}}}$, is then easily obtained as the square root of s^2. For the calculation of the standard deviation $s^2_{\hat{\varphi}}$ a maximum of 7 measures is taken into account (6 × GIS, 1 × AL), since they are all of a volume of $40\,\text{m}\ell$, while for $s^2_{\hat{A}}$, only the 6 GIS measurement are taken into account, because 40 mℓ AL has a different amount of methane than 40 mℓ GIS, and only identical measurements can be used to estimate the standard deviation.

A.8   Combination of records

Most of the time, there is more than one data set for a given hemisphere and variable. If the datasets are not based on the same scales, time scales and value scales, the curves need to be adjusted with an offset correction against each other. Sometimes, they are even based on the same scales, but still have an offset, in which case, they need to be adjusted too, in order to be able to obtain a meaningful result of the smoothing.

For offsets in the value axis only, this is straight forward: the overlapping times are identified and the average offset between the two curves calculated, after which it is possible to shift both the curves by half the offset towards each other. However, for shifts that include the time axis, it is more difficult, and more computing is required: the range of possible shift is estimated for both time and value over each of which the smoothed curves will be first shifted, and then the overlapping periods identified to calculate the mean offset as root-mean-square. These rms values are saved into a matrix and in the end, its minimal value and the corresponding shift parameters can be detected.

In future work, this method could be applied to determine time shifts more precisely. However, the changes resulting from the introduction of such an analytical approach compared to a manual approach are very small. It is reasonable to conclude that a better determination would not have affected our results significantly.

A.9   Sensitivity study

The plots sensity plots mentioned in Section 7.2 are shown on the next three pages. Most of the parameters have been varied beyond their uncertainty, to make the impact of variations better visible. The relative directions (rising or falling emissions with rising parameter) and magnitude of the influence (on bio and pyrogenic emissions) is of varied nature: a change in some parameters lead to an increase of both Q_p and Q_b, while others (sink reaction rates) result in an asynchronous rise and fall.
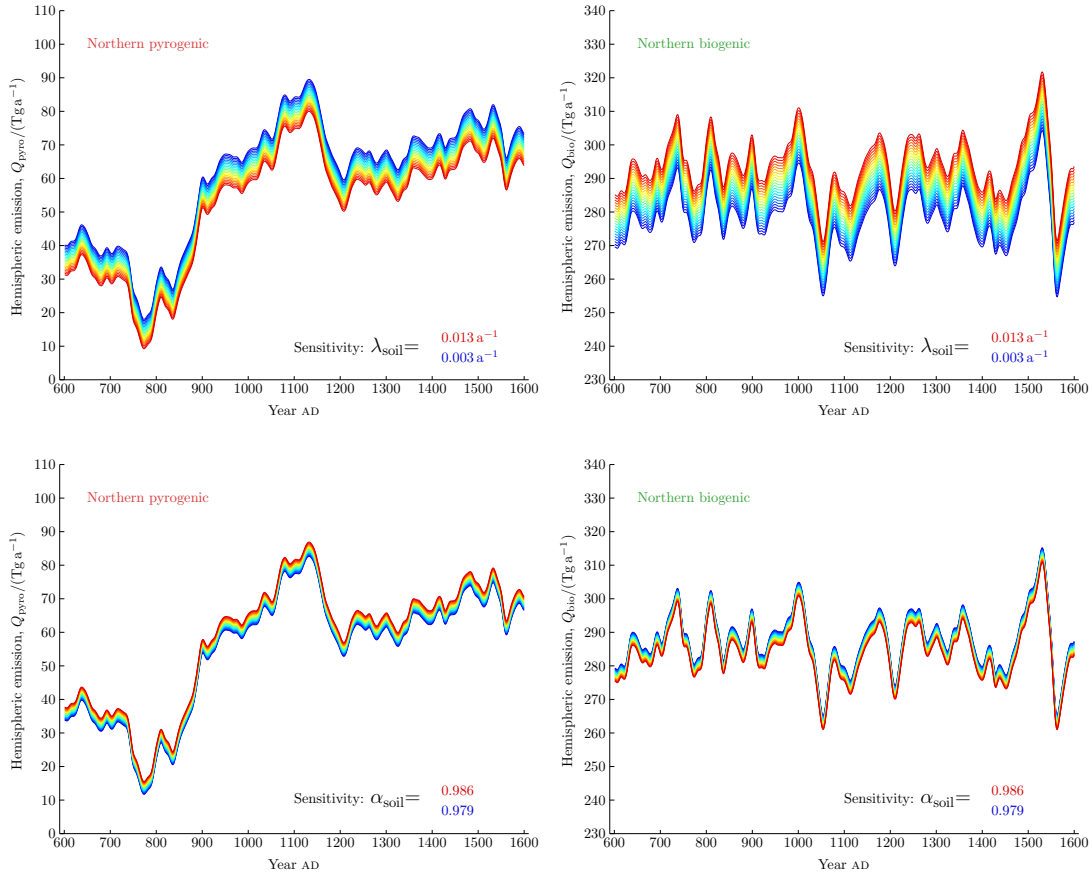

Figure A.5: Sensitivity of two variables as indicated on the plots (1 of 4).
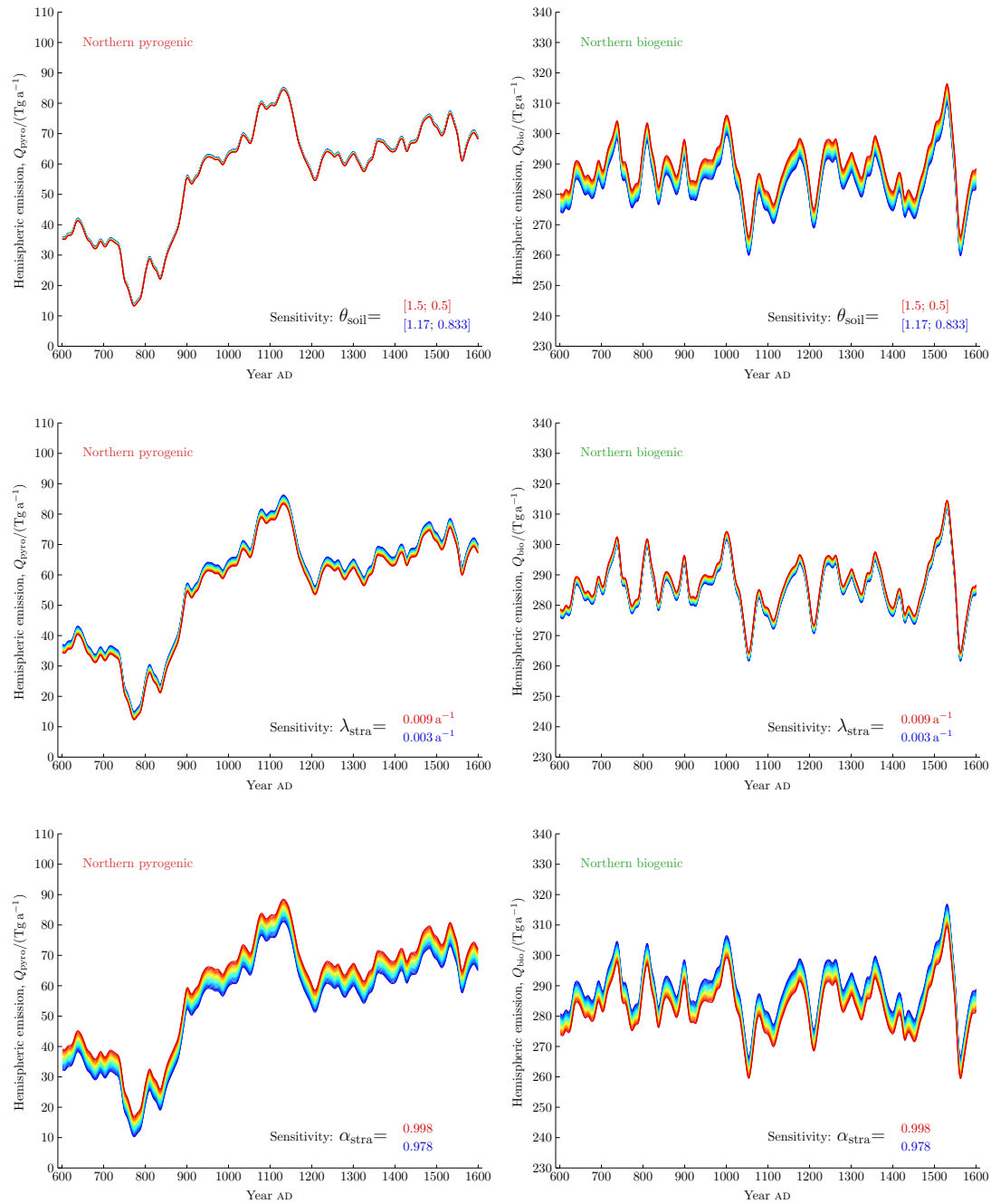
Figure A.6: Sensitivity of two variables as indicated on the plots (2 of 4).
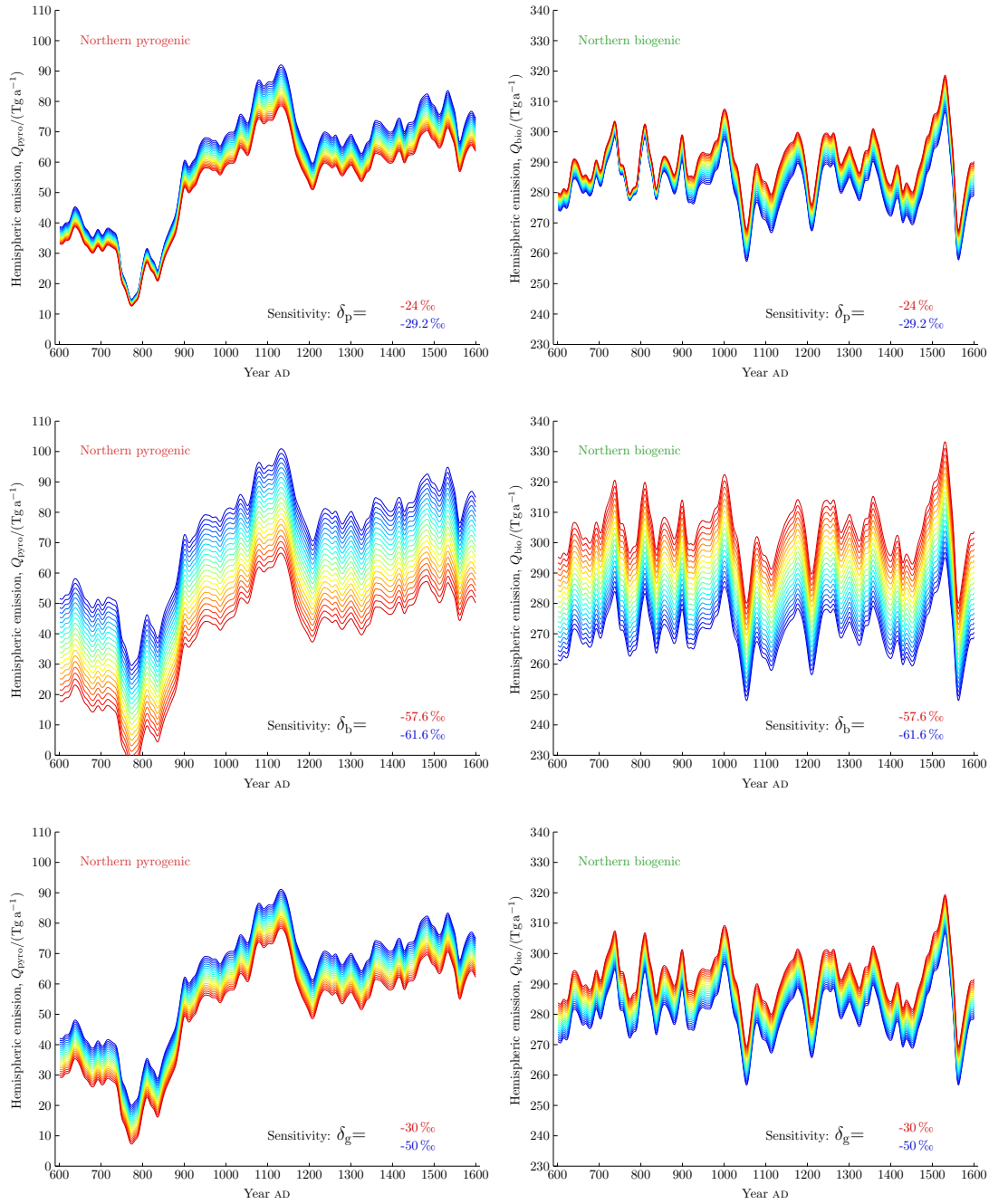
Figure A.7: Sensitivity of three variables as indicated on the plots (3 of 4).
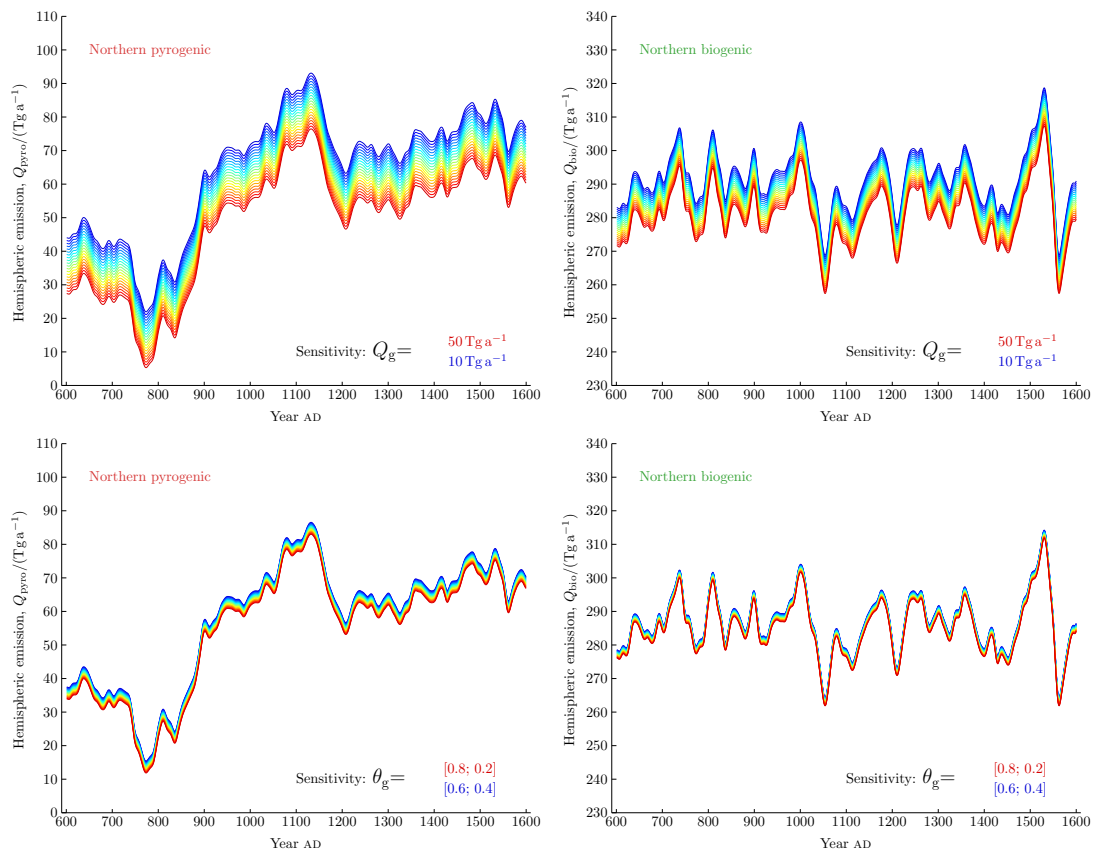
Figure A.8: Sensitivity of three variables as indicated on the plots (4 of 4).

Appendix B

Code listings

In this Section the most essential scripts that were used in the course of this study are listed. The order follows the same system as the report itself: first the analytical scripts, followed by the ones used in the modelling.

B.1 Analytical Scripts

B.1.1 TCD integrator

Listing B.1: Function: TCD file loader, separator and integrator.

```
1  %% Header
2  % Project: Measuring CH4, TCD integration
3  % Author : Christo Buizert, Jonas Haller
4  % Organization: Center for Is og Klima, NBI, Kobenhavns Universitet
5  % Last modified: 2012—12—23
6  % Description: function load sall files as in "dir.txt", wich is generated
7  %              with "dir.bat", then it figures out if there are several
8  %              peaks in one file and integrates every one of them
9  %              separately.
10 %              Files need be named as "TCD_1234_1235_Whatever.txt"
11 %                   first three letters "TCD"
12 %                   on position 10—13 the number of the CH4 MS run
13
14 clear all
15 close all
16 clc
17
18 plotting=1;
19
20 pathname_data=[pwd '\TCD_data\']; % add the path to your data
21 pathname_out= pwd;
22
23 filename=importdata([pwd '\dir.txt'],'\t');
24
25 % select only files with the prefix "TCD"
26 index_TCDfiles=cellfun(@(x) strcmp(x(1:3),'TCD'),filename);
```

```
27  filename=filename(index_TCDfiles);
28
29  %% Test names
30  file_nogood=cellfun(@(x) ¬all(ismember(x(10:13),'0123456789')),filename);
31  file_nogood_i=find(file_nogood);
32
33  for i=1:nnz(file_nogood_i)
34      fprintf('File %d has no good name: %s\n',[file_nogood_i(i) filename{file_nogood_i(i)}])
35  end
36  if nnz(file_nogood_i)>0
37      fprintf('Files will be omitted, fix the name and relaunch.\n')
38  end
39  filename=filename(¬file_nogood); % omitting bad names
40
41
42  % index_TCDfiles=strfind(filename,'TCD'); % strfind returns startpositions of "TCD" within string, else []
43  % index_TCDfiles=¬cellfun('isempty',index_TCDfiles);
44  % filename=filename(¬(index_TCDfiles−1)); % ¬(startposition−1) −> this will only index, where startpositio
45
46  if length(filename)>20 && plotting==1
47      fprintf('\nYour system would probably crash by plotting \n        and keeping open plots from %1.0
48      plotting=0;
49  end
50  % Initialize flag for errors
51  error_plotting = 0; % flag for error (file ends in middle of peak)
52
53  % define tresholds
54  T_detection_threshold = 0.5;    % peaks below this are not detected
55  T_slope1 = 0.005;               % first (rising) slope detection in V/s
56  t_slope2 = 1E−5;%0.0002;        % second (falling) slope detection in V/s % changed by JAH, do not define
57
58  % define smoothing time
59  t_sm1 = 3;                      % smoothing of signal in seconds
60  t_sm2 = 12;                     % smoothing of derivative in seconds
61
62  % Integration
63  t_safety = 5;%5                 % safety margin in peak timing (s)
64  t_BGDtime = 15;                 % time used for background detection in s
65
66  for i=1:(length(filename));%20:30;%33%70:90;%33;1:(length(filename))
67      newData = importdata([pathname_data filename{i}],'\t',23);
68      Raw_data = newData.data; % replaced "TCD_Data(i).Raw_data = ..." 130107 JAH
69      Date = newData.textdata{10}(6:15); %TCD_Data(i).Date = newData.textdata{10}(6:15);
70      Time = newData.textdata{11}(6:13); %TCD_Data(i).Time = newData.textdata{11}(6:13);
71      TCD_Data(i).Timestamp = datenum([Date ' ' Time]);
72
73      time = Raw_data(:,1);
74      Dt = mean(diff(time)); % sampling rate
75      signal = Raw_data(:,2);
76
77      % nums=regexp(filename{i},'\d','match');
78      % fignum=str2num([nums{1:4} nums{9:end}])
79      % figure(mod(filenum,2147483646))
80      % figure(fignum)
81      % plot(TCD_Data(i).Raw_data(:,1),TCD_Data(i).Raw_data(:,2))
82
83      smoothsignal= smooth(signal,30);
84      % TCD_Data(i).difsignal = smooth(smoothdiffJ(smooth(signal,round(30)),.1),round(120));
85      % TCD_Data(i).dif2signal = smoothdiffJ(TCD_Data(i).difsignal,20);
86
87      gr1= smoothsignal> T_detection_threshold;
88      % find(signal(gr2:end)<.3,1,'first');
89      gr12= ( (gr1(1:end−1)−gr1(2:end)) ); %identify falling and rising slopes of peak
90      gr12p=gr12==1; %falling
91      gr12n=gr12==−1; %rising
92      % plot(gr12)
```

```matlab
93
94        N_peaks=sum(gr12p);
95        gr12p=find(gr12p);
96        gr12n=find(gr12n);
97
98        fprintf('File %d contains %d peaks: %s\n',[i N_peaks filename{i}])
99
100       for j=1:N_peaks
101
102           if gr12n(j)>500
103               start_pos=gr12n(j)−500;
104           else % means that the space to the left is < 50 sec
105               start_pos=1;
106           end
107
108           t_start_pos=Dt*(start_pos−1); %first element is at 0 sec −> start_pos−1
109           end_pos=gr12p(j)+3000;
110           if end_pos>length(signal)
111               end_pos= length(signal);
112           end
113
114           try
115
116               signal_peak=signal(start_pos:end_pos);
117               time_peak=time(start_pos:end_pos);
118
119 %               for j=1:N_peaks
120 %                   figure(i*100+j)
121 %                   hold on
122 %                   plot(TCD_Data(i).Raw_data((gr12n(j)−1000):(gr12n(j)+5000),2))
123 %                   plot((gr12n(j)−1000):(gr12n(j)+5000),.2*ones(6001,1),'r')
124 %                   plot(gr12p(j),.5,'ro')
125 %                   plot(gr12n(j),.5,'go')
126 %               end
127               % search peak position (max of smoothed signal)
128               smoothsignal=smooth(signal_peak,round(t_sm1/Dt));
129               [dummy, t_TCDPeak] = max(smoothsignal);
130               Time_peak(j)=TCD_Data(i).Timestamp+(start_pos+t_TCDPeak)/36000/24;
131
132               difsignal = smooth(smoothdiffJ(smooth(signal_peak,round(t_sm1/Dt)),Dt),round(t_sm2/Dt));
133
134               % background detection to the left:
135               % from 10 seconds before TCD peak, until slope steeper than treshold
136               leftb = (difsignal(1:(t_TCDPeak−round(10/Dt))))<T_slope1;
137               p3 = find(leftb,1,'last');
138
139 %               % blank space to the right is from where the slope gets smaller than
140 %               % the treshold until 10 seconds after TCD peak
141 %               rightb = (difsignal((t_TCDPeak+round(10/Dt)):end))>−t_slope2;
142 %               p4 = find(rightb,1,'first')+(t_TCDPeak+round(10/Dt));
143
144               % search start position (slope in smoothed signal)
145               p4 = find(smoothsignal(t_TCDPeak:end)<smoothsignal(p3),1,'first');
146               p4 = p4+t_TCDPeak; % integration end position
147               p1 = p3−round((t_safety+t_BGDtime)/Dt); % start BGD right
148               p2 = p3−round(t_safety/Dt);              % end BGD right
149               if p1<0
150                   p1=1;
151                   fprintf('### File is short: Background calcuated on only %1.1f instead of %1.1f sec. \n',[
152               end
153               p5 = p4+round(t_safety/Dt);              % start BGD left
154               p6 = p4+round((t_safety+t_BGDtime)/Dt); % end BGD left
155
156               leftBGD  = mean(signal_peak(p1:(p2−1)));
157 %                     rightBGD = mean(signal_peak((p5+1):p6)); % changed by JAH, do not define right BG %
158
```

```
159                         %% INTEGRATION as Trapezoid %%%%%%%%%%%%%%%%%%%%%%%%%%%%%%%%%%%%
160    %                Area(i) = Trapezoid(signal(p3:p4)-leftBGD,Dt);
161                     signal2int= signal_peak(p3:p4)-leftBGD;
162    %                      signal2int= signal_peak(p3:p4)-0.5*(leftBGD+rightBGD);
163                     A_int(j) = Dt*( sum(signal2int) -0.5*signal2int(1) -0.5*signal2int(end) );
164                     %%%%%%%%%%%%%%%%%%%%%%%%%%%%%%%%%%%%%%%%%%%%%%%%%%%%%%%%%%%%%%%%%%%
165    %                Area(i) = Trapezoid(signal(p2:p5)-0.5*(leftBGD+rightBGD),Dt) % changed by JAH, do not
166            catch
167                fprintf('### Error in File %d: file ends in middle of the peak? Check plot: %s\n
    Or could it be another error? Comment "Try, Catch...end"\n',[i filename{i}])
168                A_int(j)=NaN;
169                error_plotting = 1; % set flag to plot this one
170                Time_peak=NaN;
171            end
172
173        if plotting || error_plotting
174                %% plotting
175                figure(i)
176                hold on
177                plot(time,signal)
178                try % not available for blank
179                plot(Dt*gr12p,.5*ones(N_peaks,1),'ro')
180                plot(Dt*gr12n,.5*ones(N_peaks,1),'go')
181                plot(Dt*[start_pos end_pos],.2*[1 1],'k')
182
183                plot(time_peak,signal_peak,'k');
184                plot(time_peak,difsignal-.3,'b');
185                % right delimiter (start of integration)
186                plot(time_peak(p3),difsignal(p3)-.3,'go')
187                plot(time_peak(p3)*[1 1],[difsignal(p3)+.1 difsignal(p3)-.4],'k--')
188                end
189                try % points p4, p5, p6 undefined upon error_plotting
190
191                    plot(time_peak,smoothsignal,'g');
192                    % left delimiter (end of integration)
193                    plot(time(p4)*[1 1]+t_start_pos,[difsignal(p3)+.1 difsignal(p3)-.4],'k--')
194                    % plot background average detection zones
195                    plot(time(p1:p2)+t_start_pos,leftBGD*ones(length(p1:p2)),'y','linewidth',4) % left BGD
196    %                    plot(time(p5:p6)+t_start_pos,rightBGD*ones(length(p5:p6)),'y','linewidth',4) %right
197    %                    plot([time(p2) time(p4)],[leftBGD rightBGD],'r','linewidth',1)
198                    plot([time(p2) time(p4)]+t_start_pos,[leftBGD leftBGD],'r','linewidth',1)
199                    xlabel('Time (s)','fontsize',12);%,'interpreter','Latex');
200                    ylabel('TCD signal (V)','fontsize',12);%,'interpreter','Latex');
201    %                        axis([(p1-900)/10+start_pos (p6+1200)/10+start_pos min(signal-.2) max(signal+.2)
202                    text(t_TCDPeak+t_start_pos,.7,num2str(A_int(j)));
203                end
204            end
205            error_plotting=0; % reset error flag
206        end
207
208        if N_peaks ==0
209            j=1;
210            A_int(1)=0;
211            Time_peak=NaN;
212        end
213
214        TCD_Data(i).Area=A_int; % needed to pass the Area into struct Array
215        TCD_Data(i).FilenrCH4= str2num(filename{i}(10:13))*ones(1,j)+(1:j).*.1;
216        TCD_Data(i).Filename= str2num(filename{i}(10:13));%filename{i};
217        TCD_Data(i).i= i*ones(1,j); % for debugging and developping
218        TCD_Data(i).j= j*ones(1,j);
219        TCD_Data(i).Timestamp= TCD_Data(i).Timestamp*ones(1,j);
220        TCD_Data(i).Time_peak= Time_peak;
221        clear A_int Time_peak
222    end
223 % [cell2mat({TCD_Data.FilenrCH4})' cell2mat({TCD_Data.Area})']
```

```
224  fprintf('Thats it!\n')
225
226  % write to file
227  % printable= [cell2mat({TCD_Data.FilenrCH4})',cell2mat({TCD_Data.Filename})',cell2mat({TCD_Data.i})',cell2
228  printable= [cell2mat({TCD_Data.FilenrCH4})',cell2mat({TCD_Data.Area})',cell2mat({TCD_Data.Timestamp})',cel
229  fileID = fopen(['Output_TCD' datestr(now,'YY-MM-DD_HH.mm.SS') '.txt'],'w');
230  for i= 1:size(printable,1)%length(unique(cell2mat({TCD_Data.Area})))+sum((cell2mat({TCD_Data.Area}))==0)-1
231        fprintf(fileID,'%2.1f\t%f\t%f\t%f\n',printable(i,:));
232  end
233
234  fprintf('Finish!\n')
235  % datestr(TCD_Data(12).Time_peak,'YYYY-MM-DD HH:mm:SS.FFF')
```

Auxillary function `smoothdiffJ` used to differentiate numerically is given below:

Listing B.2: Function: Auxillary function to differentiate nummerically.

```
1   %% Header
2   % Authors : Christo, Jonas Haller
3   % Organization: CIC, NBI, KU
4   % Last modified: 2012-12-21
5
6   % smoothdiff(f,dx) differentiates f to x with timestep dx.
7   % df/dx = (0.5/dx)*(f(2:end)-f(1:end-1));
8
9   function out = smoothdiffJ(f,dx)
10
11  if size(f,1) == 1
12      f=f';
13  end
14
15  % to have for each point one value, take double timestep ...
16  out = (0.5/dx)*([f(2:end);f(end)]-[f(1);f(1:end-1)]);
17
18  out(end) = 2*out(end);
19  out(1) = 2*out(1);
```

B.2   Modelling Scripts

The two auxiliary functions to switch between δ values and ^{13}F are given below:

Listing B.3: Function: δ^{13}C to ^{13}F converter.

```
1   function [ F ] = d2f( d )
2   % D2F Converts a 13C delta value vs. VPDB into an abundancy (F)
3   %   D2F(D) calculates the abundancy of 13C out of an isotope signature vs.
4   %   VPDB standard (delta 13C).
5   %   Author: Jonas Haller, Center for Ice and Climate, Copenhagen, 2012
6   R= 0.0111802; % VPDB
7   F=(d+1).*R./(1+(d+1).*R);  %13F = (δ+1)R/(1+δ+1)R
8   end
```

Listing B.4: Function: ^{13}F to δ^{13}C converter.

```matlab
1  function [ d ] = f2d( F )
2  % F2D Converts a 13C abundancy (F) to a delta value vs. VPDB
3  %   F2D(F) calculates an isotope signature vs. VPDB standard (delta 13 C)
4  %   out of the 13C abundancy (F).
5  %   Author: Jonas Haller, Center for Ice and Climate, Copenhagen, 2012
6  R= 0.0111802; % VPDB
7  d= (F./(1-F))./R-1; % δ¹³C = F/(1-F)/R - 1
8  end
```

B.2.1   Smoothing

Listing B.5: Function: Gaussian smoothing using PDF and CDF.

```matlab
1  function TimeArray = GaussSmoothWeighted( sigmaa, dataname, n )
2  %GaussSmoothWeighted performs a Gaussian smoth over density or area.
3  %   GaussSmoothWeighted(SIGMA,DATANAME,N) carries out a smoothing over the
4  %   Data in format [xData yData].
5  %   Smoothing proceeds with a weighted Gaussian algorithm, over
6  %   time DT with a sigma of SIGMA. It either uses the values of the
7  %   probability density function (PDF), if N=1, or those of the cummulative
8  %   density function (CDF) if N=2.
9  %   The function also shows a plot of the fit.
10 %
11 % Authors    : Blunier, Haller
12 % Last edited: 25.02.2013
13
14 % n=0; % way of smoothing: 0 density, 1: area;
15 % clc
16 % clear all
17 % close all
18
19 %% input testing
20
21 % for sigmaa=[5 10 20 40 80]
22 test=0;
23 if test %when used as script (testing)
24     n=1;
25     plott=0;
26 %     nargout=0; % comment when using as function !!!!!!!!!!!!!
27 % %     sigmaa=10;
28     dataname='data/xCH4_S_Ferr.dat';
29     try;close 237;end
30 else
31     plott=0;
32 % if no dataname supplied, choose a file
33     if nargin == 1
34         filename= uigetfile('.txt');
35         n = input('Smooth over area (1) or density(0)? n= ');
36     elseif nargin == 2
37         n = input('Smooth over area (1) or density(0)? n= ');
38     end
39 end
40
41 if nargin < 1
42   disp('Not enough input arguments!');
43 end
44
45 if   ischar(dataname) % || strcmp(class(dataname),'string')
46     filename=dataname;
47       try
48             Data = importdata(filename,'\t');
```

```matlab
49          catch
50              disp('Unable to find file? Check the filename and path!')
51          end
52      else
53          Data= dataname;
54          filename=['GSW_exported_data'];
55      end
56
57
58      % Data:
59      % Time, Value;
60      if isstruct(Data)
61          Data= Data.data;
62      end
63
64      %% sorting of data along time
65
66      [xx ii]=sort(Data);
67      Data=Data(ii(:,1),:);
68
69      %% fitting
70      % zetas=[1 1.5 2 3 4 7 10 20]
71      % zetas=[3 5 10];
72      % col=jet(length(zetas))*.8
73      % for kk=1:length(zetas)
74      %     zeta=zetas(kk);
75      % kk
76      % clear TotWeight
77      % clear TimeArray
78      % clear sigma
79      %%
80
81      L=length(Data);
82      MinTime = floor(min(Data(:,1))); %floor(Data(1,1));
83      MaxTime = ceil(max(Data(:,1)));
84
85      TimeArray = MinTime-4*sigmaa:1:MaxTime+4*sigmaa;  %MaxData;
86      tic
87
88
89      % Adjust sigma if too large a space between two consecutive points: > 4*sigma
90      sigma=zeros(1,length(Data)-1);
91      zeta=3;
92      for i=1:length(Data)-1
93          dist(i)=Data(i+1,1)-Data(i,1);
94          if dist(i)>zeta*sigmaa
95              sigma(i)=dist(i)/zeta;
96          else
97              sigma(i)=sigmaa;
98          end
99      end
100     sigma=[.5 .5]*[sigma sigma(end); sigma(1) sigma];
101
102     if n==0 % PDF smoothing ("density")
103         sigma=sigmaa;
104         for i = 1 : length(TimeArray(1,:))
105             FitTime=TimeArray(1,i);
106             GaussWeight=   exp((-1*(Data(:,1)-FitTime).^2)./(2*sigma^2));
107             Data(:,4)=     GaussWeight;
108             TotWeight=     sum(Data(:,4));
109             TimeArray(2,i)=sum(Data(:,4).*Data(:,2))/TotWeight;
110         end
111     else % CDF smoothing ("area")
112         disp('Calculating ...');
113         for j= 1 : length(TimeArray(1,:)) % calculate weighted point value for each smoothed time
114     %         FitTime= TimeArray(1,j);
```

```matlab
115            xPhi= zeros(length(Data(:,1)),2);
116            dividend=(sqrt(2).*sigma); % this is an array, no needs to be calculated for every iteration again
117            for i= 1 : length(Data(:,1)) % calculate weight for each data point
118                if i== 1
119                    xPhi(i,1)= 1/2*(1 + erf(  ( ( Data(i,1) ) - TimeArray(1,j) )  ./ dividend(i)));
120                else
121                    xPhi(i,1)= 1/2*(1 + erf(  ( ( (Data(i,1)+Data(i-1,1))/2 ) - TimeArray(1,j) )
     ./ dividend(i)));
122 %                 disp(i);
123                end
124                if i== length(Data(:,1))
125                    xPhi(i,2)= 1/2*(1 + erf(  ( ( Data(i,1) ) - TimeArray(1,j) )  ./ dividend(i)));
126                else
127                    xPhi(i,2)= 1/2*(1 + erf(  ( ( (Data(i+1,1)+Data(i,1))/2 ) - TimeArray(1,j) )
     ./ dividend(i)));
128                end
129                xPhi(i,3)= xPhi(i,2)-xPhi(i,1);
130            end
131
132 %            disp(j);
133            TotWeight(j)  = sum(xPhi(:,3));
134            TimeArray(2,j)= sum(xPhi(:,3).*Data(:,2))/TotWeight(j);
135
136        if plott
137            figure(237)
138            hold off
139            plot(Data(:,1),xPhi(:,3)/TotWeight(j),'o') % "jumping balls"
140            hold on
141            plot(Data(:,1),xPhi(:,3),'.') % "jumping balls"
142
143            show_sigma=[-8 -3 -1 1 3 8]*sigma(i);%sigmaa;
144            plot(TimeArray(1,j)+show_sigma,-0.1,'ok') % smoothing poition + sigmas
145            plot(TimeArray(1,j),-0.1,'ok') % smoothing position
146
147            % show bell shape
148            GaussWeight=   exp((-1*(TimeArray(1,:)-TimeArray(1,j)).^2)./(2*sigma(i)^2));
149            plot(TimeArray(1,:),GaussWeight,'-')
150 %              plot(TimeArray(j,1),sum(xPhi(:,3).*Data(:,2)),'-')
151            set(gca,'XLim',[min(Data(:,1)) max(Data(:,1))])
152            set(gca,'YLim',[-.2 1.1])
153 %              figure(33)
154            plot(Data(:,1),sigma,'go-')
155 %              pause(.05)
156            % fprintf('%u\\',j)
157        end
158 %        toc
159 %        tic
160    end
161    disp('finnished calc');
162 end
163
164 TimeArray=TimeArray';%A=permute(TimeArray,[2 1]);
165
166 if n==1
167    mode='area';
168 else
169    mode='dens';
170 end
171
172 ExportFilename = ['GSW_out/OUT_' strrep(strrep(filename,'.dat',''),'data/','') '_' num2str(sigmaa) '_' mod
173 save(ExportFilename,'TimeArray','-ascii', '-double', '-tabs');
174
175
176
177 if nargout==0
178    figure(4000+sigmaa) % Data
```

```
179      hold on
180      plot(Data(:,1),Data(:,2),'o')
181      plot(TimeArray(:,1),TimeArray(:,2),'Color',col(kk,:))
182
183      figure(5000+sigmaa) % total weight
184      hold on
185      plot(TimeArray(:,1),TotWeight,'-','Color',col(kk,:)) % "starting from .6 to 1"
186
187      figure(6300+sigmaa) % sigma
188      hold on
189      plot(Data(:,1),sigma','go-','Color',col(kk,:))
190      set(gca,'YLim',[0,250])
191  end
192
193  i_inbounds= logical((TimeArray(:,1)≥MinTime).*(TimeArray(:,1)≤MaxTime));
194  TimeArray=TimeArray(i_inbounds,:);
195  end
196  % end
197  % end
```

B.2.2   Model

Listing B.6: Script: two box model for CH_4 and $^{13}CH_4$.

```
1   clc
2   clear all
3   % close all
4   %%%% Model
5   % set(0,'defaulttextinterpreter','latex');
6   set(0,'defaulttextinterpreter','none');
7   %
8   a_start=     1013; % start year
9   a_end=       1500; % end year
10
11  %% Data: load data
12  [data_d_N(:,1) data_d_N(:,2)] =  textread('data_fitted/d13C_N_1000-1500.txt', '%n%n', -1, 'headerlines', 0
13  data_d_N(:,2)=data_d_N(:,2)*1E-3;
14  [data_d_S(:,1) data_d_S(:,2)] =  textread('data_fitted/d13C_S_1000-1500.txt', '%n%n', -1, 'headerlines', 0
15
16  [data_x_N(:,1) data_x_N(:,2)] =  textread('data_fitted/xCH4_N_1000-1500.txt', '%n%n', -1, 'headerlines', 0
17  data_x_N = [data_x_N(:,1) data_x_N(:,2)*1E-9];
18  [data_x_S(:,1) data_x_S(:,2)] = textread('data_fitted/xCH4_S_1013-1500.txt', '%n%n', -1, 'headerlines', 0)
19  data_x_S = [data_x_S(:,1) data_x_S(:,2)*1E-9];
20
21  % matrices with dimension [2,1,n] (only one compartment of isotope
22  Dat_d(1,1,:)= data_d_N(logical((data_d_N(:,1)≥a_start).*(data_d_N(:,1)≤a_end)),2);
23  Dat_d(2,1,:)= data_d_S(logical((data_d_S(:,1)≥a_start).*(data_d_S(:,1)≤a_end)),2);
24  Dat_x(1,1,:)= data_x_N(logical((data_x_N(:,1)≥a_start).*(data_x_N(:,1)≤a_end)),2);
25  Dat_x(2,1,:)= data_x_S(logical((data_x_S(:,1)≥a_start).*(data_x_S(:,1)≤a_end)),2);
26
27  Dat_F=[d2f(Dat_d) 1-d2f(Dat_d)]; % full matrices
28  Dat_X=zeros(2,2,length(Dat_x));   % pre allocating
29  for i=1:length(Dat_x)
30      Dat_X(:,:,i)=Dat_x(:,:,i)*[1,1].*Dat_F(:,:,i);
31  end
32
33  %% Define constants
34  n_atm=  1.81E20; % 188 Emol total molecules in atm
35  n_atm_H = n_atm/2; % Emol per hemisphere
36  R_vpdb= 0.0111802;
37  M_CH4=  16.09; %g/mol
```

```matlab
38
39  %% Process values
40  %%% exchange
41  tau_exc= 4; % 1a (Sapart2012)
42  kap_exc= 1/(2*tau_exc);
43
44  %%% Sinks
45  lam_OH=        0.133;    % = 1/tau
46  alp_OH=      1.0054^-1; % = 0.9946
47  lam_soil=      0.008;    % = 1/tau
48  alp_soil=    1.0180^-1; % 0.979 King (1989) in Miller (2005)
49  the_soil=   [2/3; 1/3]; % Miller assumes 2/3 thereof in NH
50  lam_stra=      0.006;    % = 1/tau, Miller: 1/110= 0.009091
51  alp_stra=    1.0120^-1; % cf. also Hein (1997) similar value
52
53  %%% Sources
54  % Qbb  scalar value
55  % Q_b isotopic vector
56
57  % pyrogen
58  d_p = -22E-3;
59  the_p= [.44;.56];% theta_\textup{pyro}
60
61  % biogen
62  d_b = -60E-3;
63  the_b= [.60;.40];% theta_\textup{bio}
64
65  % geologic
66  Qgg = 45E12/(M_CH4*n_atm);% _H); % Tg -> Ur %% Celia % H is not needed, since the theta is deviding it by
67  d_g = -36E-3;
68  the_g= [.70;.30];% theta_\textup{geo}
69
70
71  %% Run (NS,1213,time)
72
73  Q_tot = zeros(2,2,length(Dat_X)); % pre allocating
74  X_sunken = zeros(2,2,length(Dat_X)); % pre allocating
75  X_inverse = zeros(2,2,length(Dat_X)); % pre allocating
76  SQp = zeros(2,length(Dat_X)-1); % pre allocating
77  SQg = zeros(2,length(Dat_X)-1); % pre allocating
78  SQb = zeros(2,length(Dat_X)-1); % pre allocating
79
80  for i= 2:1:a_end-a_start+1
81      %% sinks, these are vectors for 2 HS, 1 isotope [2,1]
82      lam12=lam_OH        + lam_soil*the_soil          + lam_stra;
83      lam13=lam_OH*alp_OH + lam_soil*the_soil*alp_soil + lam_stra*alp_stra;
84
85      X_sunken(:,1,i) = [1-lam12(1)-kap_exc, kap_exc; kap_exc, 1-lam12(2)-kap_exc]*Dat_X(:,1,i-1); % remaini
86      X_sunken(:,2,i) = [1-lam13(1)-kap_exc, kap_exc; kap_exc, 1-lam13(2)-kap_exc]*Dat_X(:,2,i-1); % remaini
87
88      %% sources
89        % calc total source strengths
90      Q_tot(:,:,i)= Dat_X(:,:,i)-X_sunken(:,:,i); % this is the is the total source strength
91      Q_ti= Q_tot(:,:,i);
92      if min(min(Q_ti))<0
93          errortext=sprintf('Year %4.0d has %d (of 4) negative total source strength(s)! -> Improve sink str
94          error(errortext)
95      end
96
97      fQti = Q_ti(:,1)./(Q_ti(:,1)+Q_ti(:,2));
98      d_ti = f2d(fQti(:,1));
99
100     Qbb= (sum(Q_ti,2).*(d_ti-d_p)+Qgg.*(d_p-d_g))/(d_b-d_p);
101     Qpp= (sum(Q_ti,2).*(d_b-d_ti)+Qgg.*(2*d_p-d_b-d_g))/(d_b-d_p);
102
103         %% hemispheric total source calc [N; S]
```

```matlab
104        Q__p(:,1)= Qpp;%the_p*Qpp; % [N; S]
105        Q__b(:,1)= Qbb;%the_b*Qbb; % [N; S]
106        Q__g(:,1)= the_g*Qgg; % [N, S]
107
108        %% isotopic source calc [N12, N13; S12, S13]
109        Q_g(:,:)= Q__g*[(1−d2f(d_g)), d2f(d_g)]; %[12, 13]
110        Q_p(:,:)= Q__p*[(1−d2f(d_p)), d2f(d_p)]; %[12, 13]
111        Q_b(:,:)= Q__b*[(1−d2f(d_b)), d2f(d_b)]; %[12, 13]
112
113        X_inverse(:,:,i)= X_sunken(:,:,i)+Q_p+Q_b+Q_g;
114
115        %% Sum of sources
116        SQp(:,i−1)= sum(Q_p,2);
117        SQb(:,i−1)= sum(Q_b,2);
118        SQg(:,i−1)= sum(Q_g,2);
119   end
120
121   aaa=a_start+1:a_end;
122
123   figure(538)
124   hold off
125   hp(:,1)=plot(aaa,SQp,'LineStyle',':')
126   hold on
127   hp(:,2)=plot(aaa,SQb,'LineStyle','——')
128   hp(:,3)=plot(aaa,SQg,'LineStyle','−')
129   axis([a_start−20,a_end+20,get(gca,'YLim')+[0 1.2E−8]])
130   xlabel('Year \textsc {ad}')
131   ylabel('Hemispheric emission, $\dot{x}_{source}/(ppm\,a^{-1})$');
132
133   set(gca,'XTick',[0:100:2000])
134   set(gca,'Box','off') % right & top ticks off
```